Embedding the DFSZ–Axino in mSUGRA with R–Parity Violation and its implications for Dark Matter

Dissertation
zur
Erlangung des Doktorgrades (Dr. rer. nat.)
der
Mathematisch-Naturwissenschaftlichen Fakultät
der
Rheinischen Friedrich-Wilhelms-Universität
zu Bonn

vorgelegt von
Branislav Poletanović
geb. in
Gummersbach

Bonn 2010

Angefertigt mit Genehmigung der Mathematisch-Naturwissenschaftlichen Fakultät der Rheinischen Friedrich-Wilhelms-Universität Bonn.

1. Gutachter:	Prof. Herbert Karl Dreiner
2. Gutachter:	Prof. Hans-Peter Nilles
Tag der Promotion:	20.12.2010
Tag der Abgabe:	02.11.2010
Erscheinungsjahr:	2011

Ich versichere, dass ich die Arbeit selbstständig verfasst und keine anderen als die angegebenen Quellen und Hilfsmittel benutzt sowie die Zitate kenntlich gemacht habe.

To My Family

Acknowledgements

First of all, I would like to thank Prof. Herbi K. Dreiner for his support and for offering me the possibility to do research on an interesting question in modern physics. During this time I benefited from his expertise and from useful discussions. I also enjoyed our discussions apart from physics.

I would also like to thank Prof. Hans-Peter Nilles for being the second referee. Furthermore I appreciate that Prof. Klaus Desch and Prof. Martin Langer agreed to be the examiners for the final viva.

I would like to thank the *Bonn Cologne Graduate School of Physics and Astronomy* (BCGS), the program *Pro-Motion* of the University of Bonn and the *Sonderforschungsbereich TRR33* for financial support.

I am grateful to my colleques from the Bethe Center for Theoretical Physics. I enjoyed the time at the institute and I had lots of fruitful discussions with members of the Dreiner and Drees group. Here I would like to mention and thank Alessandro Barri, Markus Bernhardt, Nicki Bornhauser, John Conley, Anja Eich, Babak Haghighat, Marja Hanussek, Peter Henseler, Sebastian Grab, Jong-Soo Kim, Olaf Kittel, Tobias Langenbruch, Ulrich Langenfeld, Moritz Meinecke, Tim Stefaniak, Jamie Tattersall and Karina Williams. Of course, I would also like to thank the secretaries Dagmar Faßbender, Eva Zimmermann and Patrica Zündorf. I acknowledge discussions with Manuel Drees.

Special thanks go to Suchita Kulkarni and Marc Thormeier. I had lots of fruitful and interesting discussions with them and in addition thanks to them and Jamie Tattersall for reading parts of my thesis.

Of course, I would like to thank Eduard Reimer, Britta Tzschiesche-Simacek and a lot of other friends who are too numerous to list here. Thank you!

Furthermore I am thankful to the priests Nedjo Janjić and Mladen Janjić for their support and their advices at any time.

I am deeply grateful to my parents, my brother, all other members of my family and especially my beloved wife Dara for their support, influence and love. This would not have been possible without them!

Abstract

We embed the DFSZ axion in supersymmetry with broken R–parity. As Supersymmetry provides hundreds of free parameters we restrict ourselves to the lepton–number violating scenario in minimal supergravity models with baryon-triality B_3. In such models the axino is the lighest supersymmetric particle, it is not stable and its mass is kept to be a free parameter. The axino mixes with the three neutrinos and four neutralinos to form eight mass eigenstates. We introduce an appropiate notation, present briefly the full Langrangian and all axino interactions. This also induces a modification of the renormalization group equations which we compute. Based on this preliminary work we calculate all two– and three–body axino decays to Standard Model particles, *e.g.* leptons and mesons. Depending on the origin of the $\not{R}_p$ operator and the mass of the axino we obtain different final state combinations. Taking this into account we study the corresponding decay widths and branching ratios as a function of the superymmetric unification scale parameters as well as the axino mass. We then in particular focus on the implications for axino cold dark matter. We concentrate on the axino energy density in the light of the WMAP data. These analyses are performed in detail at the benchmark point SPS1a. Representative examples are also chosen for benchmark points SPS2 and SPS4. From this we offer a more general conclusion to other benchmark scenarios.

Contents

1 Introduction

The Standard Model (SM) of particle physics describes in a successful way all known phenomena of elementary particles [1, 2]. Despite this unprecedented triumph the SM faces several problems, see Refs. [3, 4, 5].

One of these problems occurs in the QCD Lagrangian and is called the strong CP problem. Here a supplementary term can be added which does not change the existing Feynman rules. It is parametrized by the $\bar{\theta}$-parameter which is experimentally bounded to be less than $\mathcal{O}(10^{-9})$. This smallness of $\bar{\theta}$ is the strong CP problem and thus a fine-tunning problem, see Refs. [6, 7]. There exist several solutions but the most elegant ones are to set $\bar{\theta}$ dynamically to zero. To do so we need a new $U(1)$ symmetry proposed in the late 1970s by Peccei and Quinn Refs. [8, 9] and an additional scalar field. This field acquires a vacuum expectation value and thus breaks $U(1)_{\mathrm{PQ}}$ spontaneously. Weinberg and Wilczek were the first who discerned that a pseudo Goldstone boson exists which belongs to this broken symmetry, namely the axion, see Refs. [10, 11]. As the axion interactions are highly suppressed it has not yet been discovered, see Ref. [12].

On the other hand around the same time the yet unobserved Supersymmetry (SUSY) was invented to solve other problems of the SM, see Refs. [3, 4, 5, 13]. It represents a symmetry between bosons and fermions where every boson gets a fermionic superpartner and vice versa. Of course, the axion gets a partner as well, the so called *axino* which solves the supersymmetric strong CP-problem.

Particle physics should be considered in a larger context. The axino can solve as well another problem. Cosmologists have set up the Standard Model of cosmology which describes the universe on larger scales and its formation, cf. Refs. [14, 15, 16, 17]. Furthermore observations show the existence of non-luminous matter called dark matter (DM). In the past years cosmology has become a high precision area of research. With the release of the Cosmic Backround Explorer (COBE) and the Wilkinson Microwave Anisotropy Probe (WMAP) satellites the amount of DM could be estimated to a very high accuracy to (21±1) %, see Ref. [18]. It is widely assumed that DM consists of particles which are weakly interacting and electrically neutral as it would have been detected so far.

A possible DM candidate has to be produced in the early universe in a significant abundance [15]. It has to be stable or quasi stable and in the case of SUSY it has to be the lighest supersymmetric particle (LSP) as otherwise it will decay in cascades to it. In SUSY this stability is preserved by the lepton- and baryon-number conservation (R_p R-Parity). In general in the last years plenty of particles have been proposed as possible DM, *e.g.* neutrinos, axions, neutralinos *etc.* See for a nice review Ref. [14] and references therein.. So far it was only proved that neutrinos only contribute to a small amount to the dark matter energy density. Furthermore large experimental efforts have been made to find DM with direct-, indirect-, ground-based or satellite detection methods.

Some collaborations have claimed that they have detected the DM particle but this was recently retracted, Refs. [19, 20, 21, 22].

However, there exist several SUSY models which realize the axino as the LSP. Thus fullfilling the above mentioned constraints make the axino a viable DM candidate, see Refs. [24, 25, 26, 27, 28, 29, 30]. On the other hand, we can add renormalizable interactions to the supersymmetric extension of the SM (SSM) with minimal particle content which do not obey R_p. Hence the LSP and specifically the axino can decay.

In this thesis we exactly focus on this latter scenario: combining the axino with R-parity violation. The axino is realized in the model of Dine *et.al.* (DFSZ) [31, 32] which has not been studied in this case in detail in the literature. There are several issues which have to be analysed. Firstly the lepton number violation can have different sources [33] which in turn leads to different decay channels of the axino. Furthermore SUSY has over 100 parameters. For this purpose, we will briefly introduce the minimal supergravity (mSUGRA) framework in which the axino is embedded, as well as the parameter space points are specified where the analysis is performed [35, 36]. The axino's mass can be kept as a free parameter [34]. We study systematically all possible decay processes to SM particles, *e.g.* to leptons and mesons for axino masses below 500 MeV. Of course, depending on the axino mass not every mentioned particle in a final state is kinematically accesible. A crucial factor is played by the axino Yukawa couplings. To obtain these we derive the appropiate renormalization group equations (RGE) [37, 38] and show that programs like `Softsusy` [39] can be used to compute them. Furthermore the underlying structure of the RGE and the chosen $\not{R}_p$ operator impose further restrictions on the final state combinations of the axino decay. Thus in addition to the already mentioned kinematics different mass regimes will be formed where for example only leptonic- or only mesonic decays are dominant. On the other hand there are also regions where a couple of decay processes compete with each other.

However, we can calculate all decay widths and the according branching ratios (BR). We will argue that the lifetime is comparable to the age of the universe which means that not all axinos have decayed. We use these results to perform a detailed analysis of the axino energy density for different $\not{R}_p$ operators and SUSY parameter space points. We conclude that axinos with masses from 30 MeV to 500 MeV can provide the dark matter of the universe depending on the SUSY parameters.

This thesis is organized as follows. In chapter 2 we give an introduction to the problem of DM. We start with historical evidence where we afterwards present as well the standard model of cosmology and its strong indications of DM. As already mentioned a possible solution to this issue can be found in particle physics. Therefore we give a short list of possible DM candidates. This chapter is concluded by an overview of experiments which try to detect directly or indirectly DM. Chapter 3 presents in detail the embedement of the axino in the mSUGRA model with $\not{R}_p$ and its consequences. As the axino becomes part of the neutralinos we introduce our notation which is used throughout this work. Chapter 4 is dedicted to the computation and the quantitative analysis of the RGE which are changed due to the DFSZ axino. In Chapter 5 we explain very briefly all possible axino decays to SM particles or mesons, respectively. This chapter is devided into two parts. In the first half we investigate all decays which are due to the $LL\bar{E}$ operator. In

the second part decays which are possible because of non-zero $LQ\bar{D}$ operators are shown. Here we focus especially on the implications of quark mixing. Besides the assumption of no mixing among quarks the mixing can be also mainly in the up- or down-quark-sector. In the following chapter 6 we compute the BR of the according decay channels for the SUSY benchmark point SPS1a. Again we show the results devided according to the origin of the $\not{R}_p$ ($LL\bar{E}$ or $LQ\bar{D}$). Chapter 7 is adressed to the question of the axino as DM. Here we introduce the relevant formalism and compute the axino energy density. The investigation of the latter mentioned two chapters is enlarged representatively for two more $\not{R}_p$ couplings to the benchmark point SPS2 and SPS4 in chapter 8. Finally we summarize and conclude in Chapter 9. In Appendix A we introduce some useful relations. Appendix B offers a complete overview of additional Feynman rules of axino interactions which were not shown within the thesis. The explicit calculation of the one loop anamalous dimension and the RGE can be found in Appendix C.

2 The puzzle of Dark Matter

The puzzle of Dark Matter (DM) and its solution is one of the most challenging questions in physics. In this chapter we give a short review of the indications for DM. We also introduce the main aspects of the standard model of cosmology and the related cosmological parameters. Afterwards the most promising DM particle candidates are presented with experiments which hope to find the DM candidate. A nice review can be found in Ref. [14] or in textbooks like Refs. [15, 16, 17]

2.1 Evidences for Dark Matter

The puzzle of Dark Matter came up for the first time in astronomy and cosmology, respectively. The measurement of the radial velocities of spiral galaxies gives the most striking argument for the existence of non-luminous matter. For the determination of the rotation curve astronomers use the 21-cm line of the interstellar hydrogen in combination with the optical Doppler effect. First of all our Milky Way is a good object to study. But other galaxies can also be examined, as the entire galaxy is oberservable and thus measureable. In the latter scenario the orientation of the disk of the galaxy has to be considered.

A priori we know from Newtonian mechanics that the radial velocity of a bound object is given by

$$v(r) = \sqrt{\frac{GM(r)}{r}}\,, \tag{2.1}$$

where G is the Newtonian gravitational constant, r is the distance from the galactic center and $M(r)$ is the total mass within a sphere of radius r. Due to Eq. (2.1) we expect a decrease of the velocity with increasing distance from the galactic centre.

As an example Fig. 2.1 shows the rotational curve of the galaxy NGC 6503. In contrast to the mentioned expected behaviour the curve is constant at a large radius. This can not be explained by the luminous and thus visible matter in the galaxy. Obviously from Eq. (2.1), so the mass profile $M(r)$ has to grow $\propto r$ that a constant velocity is observed. The compelling conclusion is that this flat curve can only be obtained if we postulate the existence of a halo of non-luminous and thus dark matter. Such a measurement for the Milky Way or other galaxies gives similar results. The advantage of this result is that the density distribution of the DM can be deduced.

This first mentioned evidence of DM describes effects on the local scale of galaxies. Our example was restricted to spiral galaxies. The classification of galaxies shows that we have also different types, *e.g.* elliptical- or irregular galaxies *etc.*, see Ref. [17]. We will not go through each type of galaxy and describe possible DM evidences, instead we refer the reader to Refs. [14, 17].

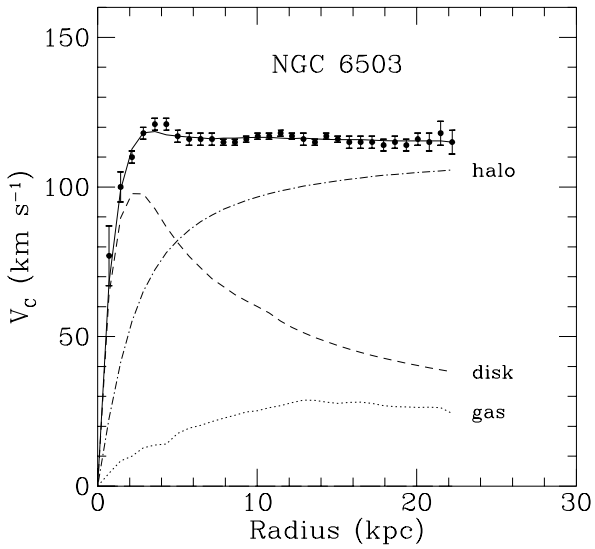

Figure 2.1: This plot shows the rotational velocity vs. the radius of the galaxy NGC 6503. In addition to this you find the contributions of the disk and gas denoted by the dotted and dashed line, respectively. Obviously this explain not the observed curve. The way out is to postulate a dark matter contribution shown by the dashed-dotted line "halo". Picture taken from Ref. [14] but originally published in Ref. [23]

The next larger scale would be to analyse clusters of galaxies, which imply the existence of DM as well. In the early 1930s, Fritz Zwicky measured the radial velocity of galaxies in the Coma cluster, see Refs. [40, 41]. With the mass-to-light ratio and the total luminosity the mass of the cluster can be estimated[1]. Zwicky used the virial theorem as a second method to determine the mass of the cluster. Both methods lead to the conclusion that the Coma cluster contains more mass than observed optically and has to have a certain amount of DM.

Later these conclusions could be also verified using the effect of gravitational lensing [42]. It is one of the predictions of General Relativity (GR) which revealed that the trajectory of any massive particle is influenced by an intense gravitational field. But furthermore the trajectory of photons is also affected by gravitation. The cosmologists take advantage of this effect by looking at nearby massive objects like galaxies or clusters. If we have behind it a bright light source then its light will be deflected by passing the massive object in the foreground. In such a scenario the massive object acts like a lens and bends the light towards the observer and thus the so called "Einstein Rings" would be observable, see Fig. 2.2.

As an example we consider a point-like mass M. In this case the deflection angle is given by, see Ref. [17]

$$\hat{\alpha} = \frac{4GM}{c^2\xi}\,, \tag{2.2}$$

[1]Note that the mass-to-light ratio vary for the different types of galaxies, see Ref. [17].

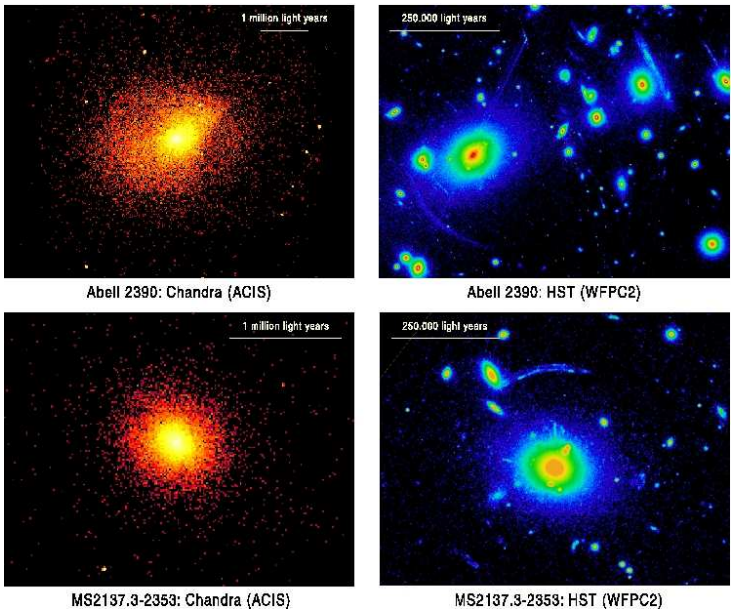

Figure 2.2: Pictures on the left hand side taken from Chandra X-ray and from the Hubble Space Telescope Wide Field Planetary Camera 2 optical on the right. The object on the left is MS2137.3-2353 at z=0.313 and on the right Abell 2390 at z=0.230. On the right hand side you can see the arcs due to gravitational lensing. Of course, an Einstein Ring occurs only in an ideal situation where the background object and the lens are perfectly aligned on the line of sight. If we have a relative position of source and lens we observe these arcs. Taken from Ref. [44].

where the light of the source passes the mass M at a distance ξ. Hence by measuring the deflection angle $\hat{\alpha}$ we can estimate the mass of the foreground galaxy cluster with Eq. (2.2) [45]. Further application methods to proove the existence of DM are, *e.g.* the weak modulation of strong lensing applied on massive elleptical galaxies, see Ref. [14] and references therein.

Up to now we only know that DM exists, not its exact nature. Furthermore it is possible to calculate in each mentioned scenario the amount of DM needed to explain observations. But unfortunately it is not possible to determine the total amount and the kind of DM in the universe. For this it is worth to take a closer look at cosmology. As a natural result from the established standard model of cosmology we get from the recent observations a numerical value for the total amount of DM.

2.2 Standard Model of Cosmology

When we talk about cosmology we have to keep in mind that this part of physics has improved tremendously in the past years. From vague theories and less proved statements it became an area of precise research. The reason is that with the steady improvement of ground- or satelite-based observational experiments, cosmologist were able to get more precise information about the cosmological parameters. Hence they were able to test the proposed theories and to draw a clear picture of the history of the universe.

One of the early discoveries and first steps towards the standard model of cosmology was due to Edwin Hubble in the 1920s, see Ref. [46]. From observation of the Doppler redshifts of the radial velocities of galaxies, he was able to formulate the relation

$$v = H_0 D \,. \tag{2.3}$$

v is the radial velocity, D is the distance to the galaxy and H_0 is the Hubble constant [47]. Eq. (2.3) is named "Hubble's law" after its discoverer and tells us that the larger the distance to a galaxy the higher is its escape velocity. The even simpler conclusion is that the universe is expanding. Going backwards in time we will come to an era where the universe was tiny, dense and hot. The majority of cosmologists agrees that the zero point of the evolution of the universe is the so called "Big Bang", see *e.g.* Ref. [17].

Besides this cornerpoint, we need a more fundamental understanding of the history of the universe. A key to this description is the General Relativity (GR) [49]. From GR we have the Einstein field equation

$$R_{\mu\nu} - \frac{1}{2} g_{\mu\nu} \mathcal{R} = -\frac{8\pi G}{c^4} T_{\mu\nu} + \Lambda g_{\mu\nu} \,, \tag{2.4}$$

with $R_{\mu\nu}$ the Ricci-tensor, $\mathcal{R}$ the Ricci-scalar, $g_{\mu\nu}$ the metric tensor, $T_{\mu\nu}$ the energy-momentum tensor and Λ the cosmological constant. If we neglect for a moment the cosmological constant, which can be interpreted as the vacuum energy density, then we see that the left hand side of Eq. (2.4) reflects the geometry of the universe whereas the right hand side denotes energy content [14]. To find a metric which solves Eq. (2.4) one uses symmetry simplifications which are confirmed by oberservation.

In 1964 Penzias and Wilson discovered the *cosmic microwave background* (CMB) [50] with a temperature of about 3 K for this blackbody. The origin of CMB goes back to the early stages of the universe. After the Big Bang the universe was still hot and dense but with a continous expansion and thus cooling. At a specific point the temperature was low enough that the free electrons were able to combine with the nuclei to form atoms. After the disapperance of the free electrons the photons are not any longer scattered ('last scattering surface'). This directly implies that photons from this era of the universe were able to propagate undisturbed. The CMB exactly consists of these photons which we can observe today.

Of course, since the efforts in the 1960s we have much more sophisticated measurements from the COBE (COsmic Background Explorer) satellite, see Fig. 2.3(a). From the data of the COBE satellite the blackbody temperature was estimated to $T = (2.728 \pm 0.004)$K [51]. This measured spectrum shows the best known blackbody radiation in physics.

Furthermore the data of COBE proved the isotropy on large scales. Another point cosmologist were searching for are anisotropies on small scales. These anisotropies are needed to explain the structure formation. Indeed COBE found the temperature anisotropies and in later experiments the value was determined to $\Delta T/T \sim 10^{-5}$ [17]. If baryons would be the dominant part of matter in the universe this value would be a few order of magnitude larger. This leads to the compelling conclusion that DM exists and plays a crucial role for the structure formation of the universe [17, 14]. A few years later the Wilkinson Microwave Anisotropy Probe (WMAP) satellite was launched and confirmed independently

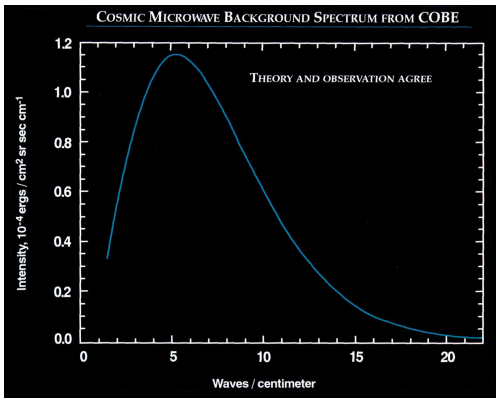

(a) CMB from the Cobe satellite. The blue line shows the expected value. The error bars can not be distinguished from this theoretical values as they are too small. Picture taken from Ref. [52].

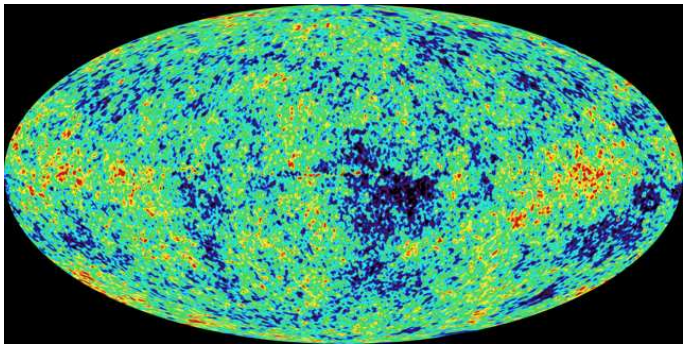

(b) This picture show the CMB anisotropy measuered by WMAP. In this picture the dipole which originates in the relavtive movement of the Earth to the CMB rest-frame. The anisotropies with an amplitude of $\Delta T/T \sim 10^{-5}$ have its origin in fluctuations of the CMB in the era of recombination. Picture taken from Ref. [53].

Figure 2.3: Planck spectrum and the amplitudes of the anisotropies of the CMB

the results of COBE but with a higher angular resolution [17, 14]. Thus we only show the anisotropies obtained by WMAP in Fig. 2.3(b). These anisotropies can have different origins, *e.g.* quantum fluctuations that take place at the time of recombination and are due to CMB fluctuations. For a brief treatment of this question see e.g. Ref. [17].

The compelling bottom line of the COBE and WMAP experiment is that the CMB is highly isotropic. From the isotropy we can conclude the homogeneity of the universe if we assume that without loss of generality there exists no preferred observer. The result that we live in a homogeneous and isotropic universe is called the *cosmological principle*.

With these underlying conditions the metric which describes such an universe and solves the Einstein field equation [49] is given by the Robertson-Walker metric

$$\mathrm{d}s^2 = \mathrm{d}t^2 - a(t)^2 \left[\frac{\mathrm{d}r^2}{1 - Kr^2} + r^2 \mathrm{d}\theta^2 + r^2 \sin^2\theta \mathrm{d}\phi^2 \right] . \tag{2.5}$$

$a(t)$ is the cosmic scale factor with the normalization of $a(t_0) = 1$ for the present time, t is the cosmic time, (r, θ, ϕ) are comoving coordinates and K is the *curvature* with the possible values $K = -1, 0, 1$. These latter three values gives us three different cosmological models namely

- $K < 0$: open universe. The universe expands forever.
- $K = 0$: flat universe, also expanding forever but the limit of the expansion velocity is zero for $t \to \infty$
- $K > 0$: closed universe. After a expansion the universe collapse again.

Inserting the Robertson-Walker metric into the Einstein field equation we end up with the so called Friedmann equation

$$\left(\frac{\dot{a}}{a}\right)^2 = \frac{8\pi G}{3}\rho - \frac{K}{a^2} + \frac{\Lambda}{3}\,, \tag{2.6}$$

where ρ is the energy density of a perfect fluid. Now, introducing the Hubble expansion rate

$$H(t) \equiv \frac{\dot{a}}{a}\,, \tag{2.7}$$

and inserting into Eq. (2.6) with the curvature $K = 0$, we get the definition of the so called critical energy density

$$\rho_{\rm cr} = \frac{3H_0^2}{8\pi G}\,. \tag{2.8}$$

It is convenient to define the dimensionless density parameter Ω which is the ratio of the energy density and the critical density

$$\Omega \equiv \frac{\rho}{\rho_{\rm cr}}\,. \tag{2.9}$$

With this definition the density parameter can be reexpressed as the sum of the radiation (r), matter (m) and vacuum (Λ) densities

$$\Omega := \sum_i \Omega_i \equiv \frac{\rho_\Lambda + \rho_{\rm m} + \rho_{\rm r}}{\rho_{cr}}\,. \tag{2.10}$$

The different Ω_i evolve differently in time. Applying a little bit of algebra, cf. Ref. [15, 16, 17] the expansion equation can be obtained

$$\left(\frac{\dot{a}}{a}\right)^2 = H_0^2\big[a^{-4}(t)\,\Omega_{\rm r} + a^{-3}(t)\,\Omega_{\rm m} - a^{-2}(t)(1-\Omega_{\rm m}-\Omega_\Lambda) + \Omega_\Lambda\big] \tag{2.11}$$

At this point the actual values for the Ω_i are not known. These parameters can be estimated with the WMAP data and the related anisotropy amplitudes. The complete set of information about the amplitudes is contained in the power spectrum. Thus getting the power spectrum we can extract the cosmological parameters [18, 54]. We will only sketch the principle approach of getting the parameter and refer the reader to the complete analysis techniques presented in Ref. [18].

The amplitudes were measured over a complete sphere, *cf.* Fig. 2.3(b). Thus it is convenient to express the amplitude in terms of spherical harmonics $Y_{lm}(\theta,\phi)$

$$\frac{\Delta T}{T}(\theta,\phi) = \sum_{l=2}^{\infty}\sum_{-l}^{+l} a_{lm}Y_{lm}(\theta,\phi)\,. \tag{2.12}$$

One usually defines the power spectrum as

$$C_l \equiv \langle |a_{lm}|^2\rangle \equiv \frac{1}{2l+1}\sum_{m=-l}^{l}|a_{lm}|^2\,, \tag{2.13}$$

see also Ref. [14]. We can plot C_l as function of l. For the extraction of the parameters cosmologists run simulation with usually six parameters to get the best-fit values.

From the analysis of the WMAP data, see Ref. [18] we have

$$\Omega_{\rm b}h^2 = 0.02273 \pm 0.00062\,, \quad \Omega_{\rm CDM}h^2 = 0.1099 \pm 0.0062\,, \quad \Omega_\Lambda = 0.742 \pm 0.030\,, \tag{2.14}$$

where b denotes the baryonic matter density, CDM the cold dark matter density and Λ the contribution of the vacuum. For the Hubble scaling factor [47] the best-fit value is given by

$$h = 0.719^{+0.026}_{-0.027}\,. \tag{2.15}$$

A suprising result is that the largest content of the universe is 'hidden' in the vacuum energy. Hidden in the sense that up-to-date cosmologists are not sure what kind of energy this is. Analogous to DM this energy is called *dark energy* (DE). This outcome of the WMAP analysis is also supported by the theory of Big Bang Nucleosynthesis (BBN). The BBN describes the freeze out of particles as well as the creation of elements in the early phase of the universe after the Big Bang. We will not go into detail of BBN and refer to the textbooks mentioned at the beginning of this chapter. The results of BBN support the above shown result. This motivates that the presented model of the universe is indeed the "standard model of cosmology".

The standard model of cosmology is facing some problems, like the horizon- and flatness problem, see Ref. [15, 17]. The solution to these issues is provided by the extension of the standard model by inflation. This supplement introduces a short phase of the universe where it expands exponentialy and then follows again the law given by the Friedmann equation, see Ref. [15, 17]. This phase leads to a natural solution of the problems and is widely accepted as the enhancement of the standard model of cosmology.

But nevertheless now that we know the total amount of DM and even DE in the universe we have not answered one even more basic question: What is dark matter? The Standard Model (SM) of particle physics does not offer a candidate to answer this question. In the next section we will present some particle physics candidates which are widely discussed as being the DM candidate.

2.3 Dark Matter particle candidates

In the previous sections we reviewed the main aspects and indications for DM. The following sections should give a short overview of the most promising DM particle candidates. This list will of course not be complete neither in the number of particles nor in the argumentation for the mentioned particle. For this see the Physics Report by Bertone *et. al.*, Ref. [14, 55] and references therein, or more specific reviews like Ref. [56] and references therein.

As mentioned, a particle which contributes mainly to DM has not been found, yet. But, large experimental efforts are performed to find it. Of course, for this purpose a vast number of experimental set ups as well as techniques have been introduced. In the next sections we will at first introduce and review some of the particle candidates. Afterwards

we will give an overview about the detection methods, schemes and the experimental prospects and summarize the status quo.

2.3.1 Neutrinos

The Standard Model neutrino was one of the first proposed particles to be non-baryonic dark matter, see Ref. [55] for a nice overview. The basic advantage of neutrinos is that they exist and are detectable. However, a DM candidate has to be massive to be considered. In the Standard Model of particle physics the neutrino has no Dirac mass term as no right handed neutrino is included. Introducing a singlet Majorana neutrino would violate lepton number.

But non-zero neutrino masses seem not to be the problem as there are compelling hints that they are massive. From laboratory experiment the limits on the neutrino masses are [48, 57]

$$m_{\nu_e} < 2 \text{ eV}\,, \quad m_{\nu_\mu} < 0.19 \text{ MeV}\,, \quad m_{\nu_\tau} < 18.2 \text{ MeV}\,. \tag{2.16}$$

An indication that the neutrinos are not massless comes from the observation of neutrino oscillations, see e.g. the results from Sudbury Neutrino Observatory (SNO) collaboration [58]. These oscillations can only be realized if at least one of the neutrino flavours has non-zero mass.

From cosmological considerations of the relic density of neutrinos the contribution to the total density parameter can estimated to [14]

$$\Omega_\nu h^2 = \sum_{i=1}^{3} \frac{m_i}{93 \text{ eV}}\,. \tag{2.17}$$

In this latter expression i denotes the different neutrino flavors. Considering Eq. (2.14) in addition to Eq. (2.17) we can derive that the sum of the neutrino masses should be below 10 eV otherwise the neutrino density would exceed the CDM contribution. Scenarios with larger neutrino masses would lead to an overclose universe, which is not observed.

On the one hand the neutrino mass limits presented in Eq. (2.16) exceed this estimated neutrino mass limit which would exclude the neutrino as CDM candidate. On the other hand from recent tritium β decay experiments at Mainz and Troistk [57] follows an upper mass limit of

$$m_{\nu_e} < 2 \text{ eV} \quad (95\%\text{C.L.})\,. \tag{2.18}$$

The above mentioned neutrino oscillations motivated experiments like e.g. the KamLAND reactor experiment [59] which search for the mass difference of the different neutrino flavors. In combination with the high precision upper limit of the electron neutrino mass cf. Eq. (2.18) we can obtain with the mass difference a better prediction and limit for the neutrino mass itsself in comparison to Eq. (2.16). The solar measurements for the mass difference of the neutrino flavors are given by

$$\Delta m^2_{12} = 7.65^{+0.23}_{-0.20} \times 10^{-5} \text{eV}^2\,, \tag{2.19}$$

whereas from atmospheric measurements we have

$$|\Delta m^2_{13}| = 2.40^{+0.12}_{-0.11} \times 10^{-3}\mathrm{eV}^2\,, \tag{2.20}$$

see Ref. [61]. Hence, the mass differences among the neutrinos are small. Applying the upper neutrino mass limit we can deduce for the neutrino density parameter

$$\Omega_\nu h^2 \lesssim 0.07\,. \tag{2.21}$$

Hence obviously the smallness of the mass difference lead to the conclusion that neutrinos can not provide alone CDM. Thus we have to search on for a viable particle DM candidate.

2.3.2 Axions

In the mid 1970s Polyakov *et. al.* [62, 63] were studying the action of Euclidean Yang-Mills theories and its topological properties. Their specific interest were spacetime dependent field configurations which minimize the action. They found that a solution can be connected to pseudoparticles called instantons. Instantatons have an extensive interpretation. First of all instantons imply a non-trivial vacuum structure where we have possible transitions between vacua states with different quantum numbers, see *e.g.* Ref. [64].

The topological structure of the vacuum leads to a supplement to the QCD Lagrangian [66] of the form

$$\mathcal{L}_\Theta = \Theta \frac{g_s^2}{32\pi^2} G^a_{\mu\nu} \widetilde{G}^{a\,\mu\nu}\,, \tag{2.22}$$

where g_s is the strong coupling, $G^a_{\mu\nu}$ is the gluon-field strength tensor and $\widetilde{G}^{a\,\mu\nu}$ denotes its dual which is given by $\widetilde{G}^{a\,\mu\nu} = \varepsilon^{\mu\nu\rho\sigma} G_{\rho\sigma}/2$. The problem with Eq. (2.22) is that it violates CP. Experimentally to a very high accuracy CP seems to be conserved in QCD. Hence, from this point of view a valid conclusion would be $\Theta = 0$. But the SM includes the electroweak theory where a corresponding term to Eq. (2.22) exists. The electroweak contribution is related to the argument of the quark mass matrix M determinant. Experimentally we have [6]

$$|\bar{\Theta}| \equiv |\Theta + \mathrm{Arg}(\mathrm{det}M)| < 10^{-9}\,. \tag{2.23}$$

The fact that Θ and $\mathrm{Arg}(\mathrm{det}M)$ are *a priori* not related but have to cancel at such a high accuracy is known as the strong CP-problem. A solution to this problem was suggested by Peccei and Quinn [8, 9] which requires a new global chiral $U(1)$ symmetry. This $U(1)$ is named after the two inventors Peccei-Quinn (PQ) symmetry and written as $U(1)_{\mathrm{PQ}}$.

Applying the $\mathrm{U}(1)_{\mathrm{PQ}}$ to the fermion fields of the electroweak Lagrangian we get a contribution of the form of Eq. (2.22)

$$\mathcal{L}_{agg} = \frac{a(x)}{f_{\mathrm{PQ}}/N} \frac{g_s^2}{32\pi^2} G^a_{\mu\nu} \widetilde{G}^{a\,\mu\nu}\,. \tag{2.24}$$

Here $a(x)$ denotes the axion field which is a pseudo Goldstone boson and f_{PQ} is the breaking scale of the underlying PQ symmetry [10, 11]. N denotes the number of quarks

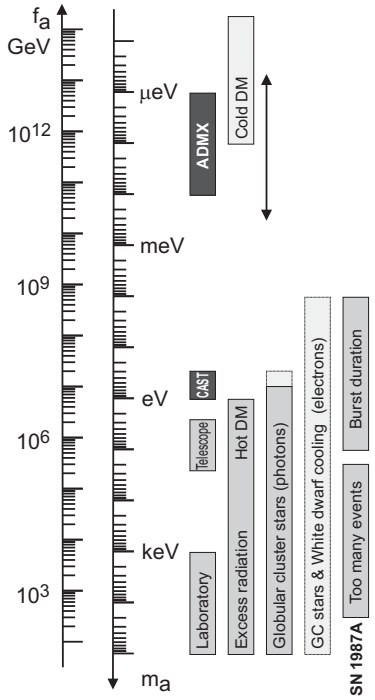

Figure 2.4: This picture shows the parts of excluded regions and sensitivity ranges of the axion-dark-matter-experiment (ADMX) [69] and the Cern Axion Solar Telescope (CAST) [70] for the the PQ breaking scale and the axion mass, respectively. Note, that here $f_{\rm PQ}/N \to f_{\rm PQ}$ was defined, denoted by $f_{\rm a}$ in the plot. The bar with "Cold DM" shows the region where the axion can be CDM motivated by the "misalignment mechanism", see Ref. [56] for further explanations. The "Hot DM" bar comes from constraints from large scale structures. The next two right bars denote constraints which are obtained from model with a axion-photon- and axion-electron coupling, respectively. The bar on the rightmost show exclusion regions inferred from SN 1987A. The bars with the light-shaded grey show bounds from DFSZ axion models. For more details see Ref. [12, 56]. Picture taken from Ref. [12].

which carry non-trivial PQ charges and is related to the realizations of the PQ symmetry discussed below. Combining Eq. (2.22) with $\Theta \to \bar{\Theta} = \Theta + {\rm Arg}({\rm det}M)$ and Eq. (2.24), the value of $\bar{\Theta}$ can be set 'dynamically' to zero dependencing on the related axion potential $V_a(x)$. As the PQ symmetry is not exact and due to instanton effects the axion has a mass, which as we will see is very small [6, 7, 12, 15, 64]. For a full review of the axion theory we recommend the Physics Report of J.E. Kim see Ref. [6] and the contribution of R.D. Peccei to Ref. [7].

There are two most favored 'invisible' axion PQ models. Both models have in common that a new complex scalar field is introduced which is a $SU(2) \times U(1)$ singlet. On the one hand we have a model due to Kim [67] and (independently found by) Shifman-Vainshtein-Zakharov [68]. This model is also often referred to as the KVSZ-, Kim- or heavy quark model. As the latter name implies, one new heavy quark field is introduced which carries the PQ charge. Hence, we have $N = 1$.

On the other hand we have the model of Dine-Fischler-Srednicki [31], and independently

found by Zhitnisky [32]. In the literature this model is called the DFSZ-model. This model requires at least one extra Higgs doublet ϕ in which SM fermions carry PQ charge

$$\mathscr{L} = g\phi^2 H_2^\dagger H_1 + \text{h.c.}\,. \tag{2.25}$$

This is a purely quartic scalar interaction. As we have six SM quarks we have in this model $N = 6$.

Collider searches, laboratory experiments or astrophysical searches have not discovered the axion, yet. But from these efforts a collection of bounds are set up on the PQ breaking scale. A summary of these bounds can be found in Ref. [12] and are visualized in Fig. 2.4 where we have

$$10^9 \text{ GeV} \leq f_{\text{PQ}} \leq 10^{12} \text{ GeV}. \tag{2.26}$$

It is obvious from Eq. (2.24) that such high values for f_{PQ} lead to a high suppression of the axion interactions which makes the axion a weakly interacting massive particle (WIMP). Nevertheless the axion would be very light, *i.e.* in the range of $\mathcal{O}(\text{meV} - \mu\text{eV})$. The latest measurements, see Fig. 2.4 imply that the axion mass can take values such that the axion is a good candidate for cold DM [12]. Experiments like the axion-dark-matter-experiment (ADMX), the Brookhaven-Fermilab-Rutherford-Trieste (BFRT), Cern-Axion-Solar-Telescope (CAST) or Polarizzazione del Vuoto con LASer (PVLAS) search extensivly for the axion. The PVLAS collaboration claimed a discovery of the axion in 2006 [71] which was retracted in 2008 [73]. Hence, to find the axion remains one of the most interesting questions, in particle physics.

The determination of the axion relic density is rather complicated as it is unknown which production process is dominant in the early universe, see Ref. [72]. Despite this problem it is possible to find models where all constraints set up on the axion are satisfied.

2.3.3 Neutralinos

The axion represents an extension of the SM. Besides the strong CP problem the SM suffers from the *hierarchy problem* [74] (*e.g* the calculations of the radiative corrections to the Higgs mass) and the non-unification of the gauge couplings. As one possible solution to these problems the theory of Supersymmetry (SUSY) was set up. We will not perform any kind of review of SUSY as there are many textbooks, reviews and primers, e.g. Ref. [4, 5, 13, 75, 76, 77, 78]. We will work in the framework of the so called Minimal Supersymmetric Standard Model (MSSM).

One of the main aspects of supersymmetry is that the particle content is basically doubled. Each SM particle gets a superpartner with spin that differs by a value of 1/2. In this scope the B and W_3 gauge bosons as well as the higgs bosons H_1^0 and H_2^0 have the fermionic superpartners called bino ($\widetilde{B}$), Wino ($\widetilde{W}$) and Higgsino ($\widetilde{H}_1^0$ and $\widetilde{H}_2^0$). In SUSY these neutral states mix among each other into four mass eigenstates called neutralinos - $\widetilde{\chi}_i^0$ with $i = 1, ..., 4$. One important property of the neutralino is that it is a Majorana particle and thus its own antiparticle. Furthermore due to its origin it is also electrically neutral which makes it a promising DM candidate [79]. The four mentioned states are sorted due to increasing mass: $m_{\widetilde{\chi}_1^0} < m_{\widetilde{\chi}_2^0} < m_{\widetilde{\chi}_3^0} < m_{\widetilde{\chi}_4^0}$. This scenario only holds if we

assume that the lepton- and baryon number is conserved in the MSSM. In the MSSM this fact is reflected by the quantum number called R-Parity. The non-conservation of R-Parity leads to crucial consequences, *e.g.* the neutrinos mix as well with the neutralinos, the lightest supersymmetric particle (LSP) is not any longer stable, see Ref. [33].

The neutralino is a well motivated DM candidate and is widely studied. To perform an analysis of the neutralinos as DM candidate depends crucially on the chosen SUSY parameters. SUSY has over 100 parameters, so it is useful to make restrictions to reduce this number. mSUGRA is one the models which constrains the huge SUSY parameter space, see the work of Kane et al. Ref. [80]. In mSUGRA models a set of boundary conditions at the Grand Unification scale ($M_{\mathrm{GUT}} = \mathcal{O}(10^{16}$ GeV)) is imposed

- Unification of the three gauge couplings, $\alpha_1(M_{\mathrm{GUT}}) = \alpha_2(M_{\mathrm{GUT}}) = \alpha_3(M_{\mathrm{GUT}})$
- Unification of the gaugino masses, $M_1(M_{\mathrm{GUT}}) = M_2(M_{\mathrm{GUT}}) = M_3(M_{\mathrm{GUT}}) \equiv m_{1/2}$
- Universal masses of the sfermions and the higgs mass labeled m_0
- Universal trilinear scalar couplings, labeled A_0

In summary we end up with in total five parameters:

$$\tan\beta,\ m_{1/2},\ m_0,\ A_0,\ \mathrm{sign}(\mu)\,, \tag{2.27}$$

where β is the ratio of the two Higgs vacuum expectation values (vev) and μ is the Higgs mixing mass parameter. SUSY has not been observed, yet, restricting the values of the parameters.

A large amount of neutralinos is pair-produced in the early universe. This should lead to a non-zero relic abundance today. For this purpose programs like `DarkSUSY` [81] or `mircOMEGAS` [82] calculate the relic densities and dark matter properties for a given SUSY model. From these results it is possible to analyse whether e.g. the density parameter is comparable the one of DM. In such a case if the neutralino is the DM the input model provides further restriction on SUSY phenomenology. This gives implications for SUSY searches: the model is testable.

An example for a typical SUSY parameter space scan is shown in Fig. 2.5. For such a scan several constraints have been set the parameters $A_0 = 0$, $\tan\beta = 10$ and a top mass of $m_t = 172.7$ GeV [84] were applied. Further restrictions of the electroweak symmetry breaking and collider limits on the neutral Higgs boson were imposed. For details see Ref. [83]. In conclusion the black line represents regions where the neutralino can provide DM. This region is very narrow due to the precise WMAP measurement. However, Fig. 2.5 represents only one model with one set of SUSY parameters. In Ref. [83] Djouadi *et. al.* show further different combinations of *e.g.* $\tan\beta$ and m_t. Also in these scenarios there exists strips in the $(m_{1/2}, m_0)$ plane where the neutralino can provide the DM of the universe. Hence, despite all these SM and SUSY constraints the neutralino is a viable DM candidate.

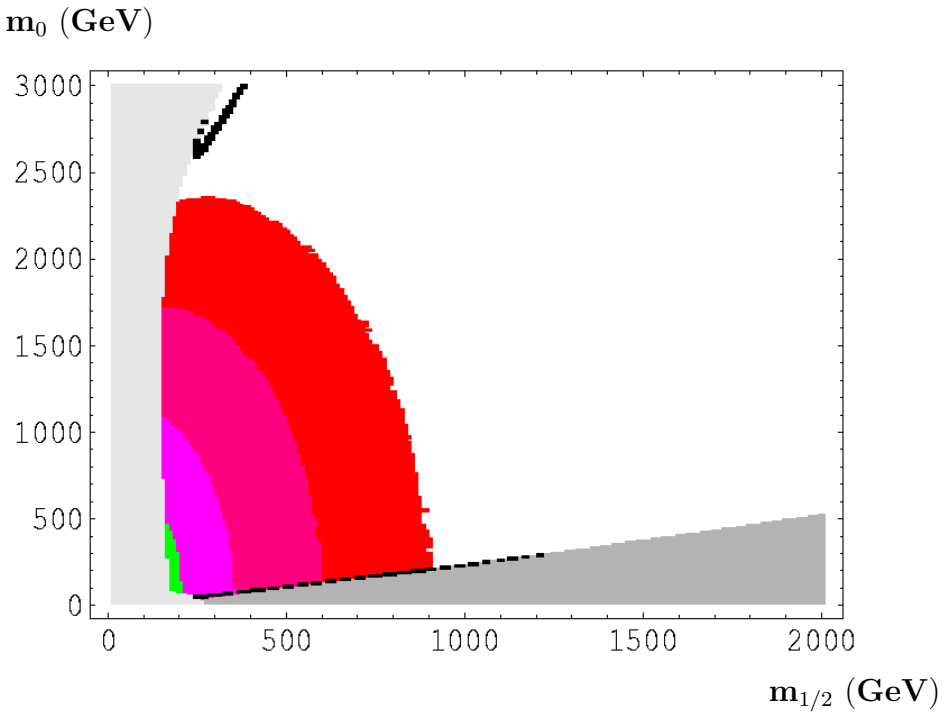

Figure 2.5: The black line shows the regions in the $(m_{1/2}, m_0)$ mSUGRA plane where $0.087 \leq \Omega_{\chi^0} h^2 \leq 0.138$ which coincidents with $\Omega_{\mathrm{CDM}} h^2$ of the WMAP collaboration in 2003, see Ref. [85]. Several parameter space constraints have been imposed: $A_0 = 0, \tan\beta = 10$ and a top quark mass of $m_t = 172.7$ GeV. The light grey area is excluded due to requirements of electroweak symmetry breaking and in the dark grey region the stau ($\tilde{\tau}_1$) is the LSP. The green- and the light pink region are constraint by $b \to s\gamma$ and by LEP searches for the neutral Higgs Bosons, respectively. The red regions are compatible with a SM-like Higgs boson mass of ca. 115 GeV. For more details see Ref. [83] from where the picture was taken.

2.3.4 Axinos

In the MSSM the strong CP problem discussed in Section 2.3.2 persists. The solution is the extension of the MSSM by the PQ symmetry. As consequence the axion gets the fermionic superparter, the axino $\tilde{a}$. The axino is a SM singlet and it can be realised in different ways. We have the KVSZ SUSY models or the DFSZ model. As in the case of the axion, all interactions are suppressed by the PQ breaking scale f_{PQ} which also characterizes the axino as a WIMP. In this section we focus on the KVSZ axino as it was studied intensively in the literature in contrast to the DFSZ model, see Ref. [24, 25, 26, 28]. Furthermore the DFSZ axino will be examined in detail during this thesis. We postpone its analysis to the next chapters.

Most of the literature considers the axino as the LSP under R-parity conservation. Few works consider a scenario where R-parity is broken and the axino decays, see Ref. [26, 29, 86, 87].

The axinos are primarily produced in the early universe after the inflation- and the reheating-phase with temperature T_{R} through $2 \to 2$ scattering processes. The basic question is whether the axino can be produced in such a high amount that it provides the

Figure 2.6: A contour plot for different values of the PQ breaking scale (labeled with f) where $\Omega_{\tilde{a}} = \Omega_{\mathrm{CDM}}$. The parameters are the reheating temperature as well as the axino mass, for details see text. Picture was taken from Ref. [88].

entire DM of the universe. Basic results on this issue were published by Brandenburg et al. [28] where the production rates of the axino and the axino density parameter $\Omega_{\tilde{a}}$ were calculated. Recently published results by Strumia, see Ref. [88], showed that the computations of Brandenburg et al. were incomplete. They lead to a different result for the production process and thus the density parameter

$$\Omega_{\tilde{a}} h^2 \approx 24.8\, g_3^6\, \ln\frac{3}{g_3} \left(\frac{m_{\tilde{a}}}{\mathrm{GeV}}\right) \left(\frac{T_{\mathrm{R}}}{\mathrm{GeV}}\right) \left(\frac{10^{11}\ \mathrm{GeV}}{f_{\mathrm{PQ}}}\right) . \tag{2.28}$$

Inserting these parameters we obtain a contour plot as shown in Fig. 2.6, where the PQ breaking scale, the reheating temperature and the mass were used as free parameters.

From the considerations in section 2.3.2 it is apparent that the PQ breaking scale has a 'window' where the axino can be the DM. The upper value of $f_{\mathrm{PQ}} = 10^{13}$ GeV used in Ref. [88] for Fig. 2.6 has to be implemented with care. Such high values for f_{PQ} result in regions where the DM can be dominantly the axion. Thus smaller values are preferred here.

Furthermore in Fig. 2.6 the axino mass was assumed to be a free parameter. The axino mass depends crucially on the SUSY models and the implementation of the axino in the model, see e.g. Ref. [34, 60]. Chun et al. showed that the axino can take a wide range of masses from a keV up to several GeV.

The red lines shown in Fig. 2.6 denote regions where the axino provides CDM of the universe. In conclusion the axino is a good DM candidate but the details are strongly model dependent.

2.3.5 Other particles

In the last section we have reviewed some of the particle dark matter candidates. As mentioned at the beginning this list is not complete. We left out other particles, e.g. the gravitino, which share in many ways similar phenomenological properties [56]. Besides tha gravitino we have also a sterile neutrino, sneutrinos, light scalar dark matter, Kaluza-Klein states, superheavy dar matter, Q-balls, mirror particles etc. For detailed information of these candidates we refer the reader to Ref. [14] and references therein.

2.4 Detection methods

After clarifying possible DM candidates the question arises whether it is possible that these particles can be observed. In general the searches are divided into two charecteristic methods: 1.) direct detection and 2.) indirect detection. In the next two sections we give a rough overview of these detection principles, see also Ref. [14].

Direct detection

In direct detection experiments a dark matter particle should hit some kind of target material, see Ref. [14]. The deposited energy of the WIMP could then be measured. Crucial points of this kind of DM detection is the knowledge about the density and velocity distribution of the WIMP as well as the cross-section of the WIMP with the target material. The WIMPs have a Maxwell-Boltzmann velocity distribution with a characteristic velocity of $v_0 = 270$ km/sec [14].

- If a WIMP hits a nucleus of the target material it can either scatter elastically or inelastically. In the first case, some energy of the incoming DM particle is deposited in the recoil of the nucleus which is then measured. Typical recoil energies due to the Maxwell-Boltzmann distribution are a few tens of keV.

  A second possibility is the inelastic scattering process where the WIMP does not deposit recoil energy. Instead it interacts with the orbital electrons or with the nuclei. In both cases it leads to an excitation or ionization of the atom or nuclei, respectively.

- Another way of scattering are the spin-dependent or spin-independent processes. In the first case the spin of the WIMP can interact with the spin of the nucleon where the cross section is proportional to $J(J+1)$. Of course, the spin independent scatterings do not interact in such a way. The advantage of the spin independent method is the dependence of the cross section on the mass of the used target nuclei. Thus using a heavier element increases the sensitivity, in contrast to the spin dependent case. In general the spin independent method dominates over the spin independent one.

Many experiments have been built to find the DM particle using direct detection. Some of these experiments consider the fact that the Earth's velocity changes within the year.

It experiences an annual modulation due to motion with respect to the galactic center and the sun, respectively. Thus the Earth's velocity we have [14]

$$v_0 = 220\,\mathrm{km/sec} \cdot \Big[1.05 + 0.07\cos(2\pi(t - t_m))\Big]\,, \tag{2.29}$$

with t_m is approximately the beginning of June and are given in units of years. In Eq. (2.29) the first expression denotes the peculiar velocity through the galaxy of the solar system and the expression in the brackets the modulation due to the earths motion within the solar system, see Ref.[14]. Some experiments attempt to observe the modulation which should lead to about a 7 % variation in the signal. This variation is rather small and thus many of events are needed. Later on we will give a list of experiments which make use of this effect.

Indirect detection

Experiments with the indirect detection method have a different approach. The focus point here lies in the observation of DM annihilation or decay products. As an example we consider Majorana-like DM candidates which annihilate with each other producing detectable particles. In the case of SUSY candidates these annihilation products can be some SM particle. Scenarios where the DM candidate can decay bahve similarly.

Such experiments have to be directed towards regions of high DM densities, e.g. the halo of our galaxy or the sun. Regions with a large amount of matter act like accumulation points of DM. Such points predefine the observable particle as only neutrinos could escape such dense regions in a significant amount.

Besides neutrinos, observations are focused e.g. on gamma-rays, synchrotron radiation, positrons etc. Note that charged particles are deflected in strong magnetic fields which are present in the area with a large amount of matter. In general the fluxes of observations are measured and compared with predicted values. As mentioned earlier, a good knowledge of the dark matter profile e.g. in the halo of the our galaxy is needed. In the literature a lot of halo profiles are examined. The halo profile of Navarro, Frenk and White (NFW) is often used [89]. But keep in mind that such profiles do not provide a reliable density near the Galactic center. However, from the NFW-profile the decay- or annihilation-rates can be calculated and compared with the measured values.

2.5 Experiments

Many experiments have been set up for the direct- or indirect detection of DM. A lot of different techniques are applied in the experimental setups. In the last section, the possibility of elastic- and inelastic scattering for the detection of DM was presented. The discussed recoils associated to scattering processes can be further characterized for the application of detector techniques in direct experiments.

- Phonon: During the interaction of the dark matter particle a part of the energy can be deposited into phonons. Detectors are built such that these phonons can be collected before they thermalize.

- Ionization: The energy transfer of an incoming particle on an electron can be so large that the electron escapes from the nucleon. Small electric fields lead to a drift of the electrons to electrodes where they can be counted. This gives information about the amount of ionization.

- Scintillation: Through energy absorption of an electron within the detector material the electron can be excited to a higher state. If this electron falls back to its ground state it will emit a photon which then can be measured.

Some of the experiments use several of these techniques. CDMSII [90] or EDELWEISS [91] make use of phonons and ionization and XENON100 [19] uses simultaneously scintillation and ionization signals for the detection of DM. At the end of this section we will give a more complete list of experiments which are trying to detect DM directly.

Nevertheless the DAMA/LIBRA and CoGeNT collaborations claimed[2] that they found evidence for DM with a mass in the range of a few GeV , see Ref. [20, 22, 21]. But the XENON100 collaboration recently challenges this result and write in Ref. [19] that they "observe no events." However even this claim was questioned in Ref. [92] from Collar et al. but this criticism was directly rejected by the XENON100 collaboration [93]. Obviously, this controversy is not over.

However, besides the direct detection experiments large efforts are made also in indirect detection experiments. In this case the main aspect is to look for WIMP annihilation- and decay products. The final state particles can be neutrinos, positrons, anti-protons and gamma-rays.

For the detection of gamma-rays in general two technologies are used: space- or ground-based telescopes. The Energetic Gamma Ray Experiment Telescope (EGRET) [94] was the first space telescope in an energy range above GeV. With its observation a catalog of gamma ray sources was created. Its successor is the Fermi Gamma-Ray telescope (FERMI) [95] launched in 2008. It has a higher resolution and will help to identify many high energy sources found by EGRET.

The other possibility to observe high energetic gamma rays is with ground based telescopes. Of course, due to the Earth's atmosphere it is impossible for gamma rays reach Earth based telescopes. The incident gamma rays create a cosmic air shower. This shower in turn is the origin of Čerenkov light. A problem which is related to the ground based observation is that the background radiation must be distinguished from the signal of the source which is analysed. This problem is resolved by computer programs which simulate the atmospheric showers. Some experiments have been built using the detection of Čerenkov light, like e.g. MAGIC [96] or H.E.S.S. [97]. These two experiments are able to measure gamma rays with an energy in the TeV range. Note that MAGIC and H.E.S.S. use different ways to capture the Čerenkov light. MAGIC consists only of one telescope whereas H.E.S.S. is an array of four telescopes.

As mentioned above, besides gamma rays also neutrinos can be produced in dark matter annihilations and thus can be observed. Experiments like AMANDA [98], SUPER-KAMIOKANDE [99] or the not yet finished IceCUBE [98] (successor of AMANDA) use

[2]The DAMA/Libra collaboration found an anual modulation of the signal due to Eq. (2.29)

the Čerenkov light detection as well. The detection of neutrinos has the advantage that neutrinos are weakly interacting. Thus they can travel large distances without affecting their trajectory. On the other hand the observation of neutrinos is more difficult from gamma rays.

In table 2.1 we list some of the major experiments for the detection of dark matter.

Experiment	Detection	Technique	Particles	SD/SI	Ref.
CDMS II	direct	Ionization+Phonons	WIMP	SI	[90]
Edelweiss	direct	Ionization+Phonon	WIMP	SI	[91]
XENON100	direct	Scintillation+Ionization	WIMP	SI	[19]
DAMA/Libra	direct	Scintillation	WIMP	SI	[20]
Zeplin III	direct	Scintillation+Ionization	WIMP	SI	[100]
CoGeNT	direct	Ionization	WIMP	SI	[101]
CRESST	direct	Phonon+Photons	WIMP	SI	[102]
PICASSO	direct	Ionization	WIMP	SD	[103]
DRIFT II	direct	Ionization+Recoil track	WIMP	SI	[104]
EGRET	indirect	space-based-telescope	γ-rays	SI	[94]
FERMI	indirect	space-based-telescope	γ-rays	SI	[95]
PAMELA	indirect	space-based-telescope	$e^+/\bar{p}$	SI	[105]
ATIC	indirect	baloon-based	cosmic rays	SI	[106]
MAGIC	indirect	ground-based/Čerenkov	co. air sh.	SI	[96]
H.E.S.S.	indirect	ground-based/Čerenkov	co. air sh.	SI	[97]
AMANDA	indirect	ground-based/Čerenkov	neutrinos	SI	[98]
ICECUBE	indirect	ground-based/Čerenkov	neutrinos	SI	[98]
ANTARES	indirect	ground-based/Čerenkov	neutrinos	SI	[107]
Super-K	indirect	ground-based/Čerenkov	neutrinos	SI	[99]

Table 2.1: This table shows a list of experiments which try to find dark matter. We indicate whether the experiment in using a direct- or indirect detection method. Furthmore the technique is listed as well as the spin-dependence (SD) or independence (SI). This list is not complete and contains first of all more recent experiments or the last evolution steps of the mentioned experiments.

3 The Axino model

In this chapter we explain briefly how the axion is embeded in SUSY. This automatically leads to the axino. We will describe the tools and the notation used within this work.

3.1 mSUGRA with Baryon Triality

In the previous chapter we the supersymmetric extension of the SM. we shall focus on the Minimal Supersymmetric Standard Model (MSSM).

The SM contains three families of fermionic fields and a complex scalar Higgs doublet H. The SM's external symmetry is based on the Poincaré algebra. Furthermore it has the internal (gauge) symmetry [108]

$$\mathrm{G_{SM}} = SU(3)_C \times SU(2)_L \times U(1)_Y \,. \tag{3.1}$$

Given these ingredients the resulting Lagrangian is fully determined. Restricting oneself to only renormalisable interactions, this Lagrangian has additional (accidental) global symmetries: lepton- and baryon-number.

In order to obtain the supersymmetric Standard Model (SSM) the SM fermionic fields are promoted to left chiral superfields Φ. Similarly the gauge fields are promoted to vector superfields V [109, 110, 111, 112]. This results in the minimal field content

$$L_i,\, \bar{E}_i,\, Q_i,\, \bar{D}_i,\, \bar{U}_i,\, H_1,\, H_2\,; \quad V_Y,\, V_2^{\bar{a}},\, V_3^{\bar{x}}\,. \tag{3.2}$$

Here L_i through $H_{1,2}$ are the chiral superfields of the SSM. $i = 1, 2, 3$ is the generation index; V_Y, $V_2^{\bar{a}}$, $V_3^{\bar{x}}$ are the $U(1)_Y$, $SU(2)_L$, and $SU(3)_C$ vector superfields, respectively. $\bar{a} = 1, 2, 3$ is the index of the $SU(2)$ adjoint representation and $\bar{x} = 1, \ldots, 8$ is the index of the $SU(3)$ adjoint representation.

Given this particle content as well as the external and internal gauge symmetries of the model the most general superpotential is given by [113, 114]

$$\begin{aligned}
W &= W_{\mathrm{P}_6} + W_{\mathrm{LNV}} + W_{\mathrm{BNV}} && (3.3)\\
W_{\mathrm{P}_6} &= \varepsilon_{ab}\big[(\mathbf{Y}_E)_{ij} L_i^a H_1^b \bar{E}_j + (\mathbf{Y}_D)_{ij} Q_i^{ax} H_1^b \bar{D}_{jx} + (\mathbf{Y}_U)_{ij} Q_i^{ax} H_2^b \bar{U}_{jx} - \mu H_1^a H_2^b\big] && (3.4)\\
W_{\mathrm{LNV}} &= \epsilon_{ab}\left[\frac{1}{2}(\mathbf{\Lambda}_{E^k})_{ij} L_i^a L_j^b \bar{E}_k + (\mathbf{\Lambda}_{D^k})_{ij} L_i^a Q_j^{xb} \bar{D}_{kx}\right] - \epsilon_{ab}\kappa^i L_i^a H_2^b, && (3.5)\\
W_{\mathrm{BNV}} &= \frac{1}{2}\epsilon_{xyz}(\mathbf{\Lambda}_{U^k})_{ij} \bar{U}_i^x \bar{D}_j^y \bar{D}_k^z && (3.6)
\end{aligned}$$

Here $a, b = 1, 2$ are indices of the $SU(2)$ and $x, y, z = 1, 2, 3$ indices of the $SU(3)$ fundamental representation. The $(\mathbf{Y}_F)_{ij}$, $F = E, D, U$, are dimensionless Yukawa coupling

matrices. Similarly $(\mathbf{\Lambda}_{F^k})_{ij}$, $F = E, D, U$, are dimensionless couplings. μ and κ are couplings of mass dimension one. See also the notation in [35].

With the superpotential it is possible to compute the Lagrangian using

$$\mathscr{L}_{\text{SUSY}} = -\frac{1}{2}\left(W^{ij}\psi_i\psi_j + W^*_{ij}\psi^{i\dagger}\psi^{j\dagger}\right) - |W^i|^2\,, \tag{3.7}$$

where $W^i \equiv \partial W/\partial\phi_i$ and $W^{ij} \equiv \partial^2 W/\partial\phi_i\partial\phi_j$. Here ϕ and ψ denote the scalar- and spinor-field of the chiral superfield, respectively.

Note that the superpotential does not include any mass terms. To prevent mass degeneracy of the SM particles and their supersymmetric particle counterparts the SSM has to be broken. This is explicitly accomplished by the soft breaking mass terms [4]

$$\begin{aligned}
\mathscr{L}^{\text{SOFT}}_{\text{P}_6} &= -\frac{1}{2}\left(M_3\tilde{g}^\alpha\tilde{g}^\alpha - M_2\widetilde{W}^\beta\widetilde{W}^\beta + M_1\widetilde{B}\widetilde{B} + \text{h.c.}\right) \\
&\quad -\epsilon_{ab}\left(\tilde{\bar{u}}_i\, A^{ij}_u \tilde{Q}^a_j H^b_2 - \epsilon_{ab}\tilde{\bar{d}}_i\, A^{ij}_d \tilde{Q}^a_j H^b_1 - \epsilon_{ab}\tilde{\bar{e}}_i\, A^{ij}_e \tilde{L}^a_j H^b_1\right) \\
&\quad -\tilde{Q}^\dagger_i(\mathbf{m}^{\mathbf{2}}_{\tilde{\mathbf{Q}}})_{ij}\tilde{Q}_j - \tilde{L}^\dagger_i(\mathbf{m}^{\mathbf{2}}_{\tilde{\mathbf{L}}})_{ij}\tilde{L}_j - \tilde{\bar{u}}_i(\mathbf{m}^{\mathbf{2}}_{\tilde{\mathbf{u}}})_{ij}\tilde{\bar{u}}^\dagger_j - \tilde{\bar{d}}_i(\mathbf{m}^{\mathbf{2}}_{\tilde{\mathbf{d}}})_{ij}\tilde{\bar{d}}^\dagger_j - \tilde{\bar{e}}_i(\mathbf{m}^{\mathbf{2}}_{\tilde{\mathbf{e}}})_{ij}\tilde{\bar{e}}^\dagger_j \\
&\quad -m^2_{H_2}H^\dagger_2 H_2 - m^2_{H_1}H^\dagger_1 H_1 - \left(\epsilon_{ab}bH^a_1 H^b_2 + \text{h.c.}\right)\,. \qquad (3.8) \\
\mathscr{L}^{\text{SOFT}}_{\text{LNV}} &= \epsilon_{ab}\left[\frac{1}{2}(\mathbf{h}_{E^k})_{ij}\tilde{L}^a_i\tilde{L}^b_j\tilde{\bar{E}}_k + (\mathbf{h}_{D^k})_{ij}\tilde{L}^a_i\tilde{Q}^{bx}_j\tilde{\bar{D}}_{kx} - D_i\tilde{L}^a_i H^b_2 + \text{h.c.}\right] \\
&\quad +m^2_{\tilde{L}_iH_1}\tilde{L}^\dagger_i H_1 + \text{h.c.} \qquad (3.9) \\
\mathscr{L}^{\text{SOFT}}_{\text{BNV}} &= \frac{1}{2}\epsilon_{xyz}(\mathbf{h}_{U^k})_{ij}\tilde{\bar{U}}^x_i\tilde{\bar{D}}^y_j\tilde{\bar{D}}^z_k + \text{h.c.} \qquad (3.10)
\end{aligned}$$

In Eq. (3.8) M_1, M_2 and M_3 are the gaugino mass terms, with $\alpha = 1, \ldots, 8$ and $\beta = 1, 2, 3$. A^{ij}_u, A^{ij}_d and A^{ij}_e are the scalar couplings with dimensions of [mass]. The $(\mathbf{m}_{\tilde{\mathbf{K}}})_{ij}$, $\tilde{K} = \tilde{Q}, \tilde{L}, \tilde{u}, \tilde{d}, \tilde{e}$, are mass matrices of the according scalar fields and $m^2_{H_2}, m^2_{H_1}$ are the squared masses of the Higgs. b and D_i are bilinear couplings with dimension of [mass]^2. $m_{\tilde{L}_iH_1}$ gives contributions to the slepton Higgs mass matrix. The $(\mathbf{h}_{F^k})_{ij}, F = E, D, U$, are the trilinear scalar couplings corresponding to the Yukawa couplings of the superpotential introduced above.

The terms in W_{LNV} violate lepton-number, the terms in W_{BNV} violate baryon number. Together they lead to rapid proton decay [113, 114, 115, 33, 116]. Thus the simplest SSM is in conflict with experiment: a further symmetry must be added to protect the proton. The standard solution is to impose the discrete multiplicative symmetry R-parity (R_p) [117], which only allows the terms in W_{P_6}. However, it allows for dimension-5 proton decay operators. This is resolved by proton hexality (P_6), leading to the same renormalisable low-energy superpotential [118, 119].

Another possible solution is to impose baryon-triality B_3 [118, 120, 4, 121, 123, 124, 125], resulting in $W_{\text{B}_3} = W_{\text{P}_6} + W_{\text{LNV}}$. P_6 and B_3 are special within the SSM: they are the only discrete gauge anomaly-free symmetries satisfying a minimal set of phenomenological requirements [120, 126, 118]. The advantage of P_6 is that it easily accomodates a dark matter candidate in parts of the parameter space: the lightest neutralino [127, 128]. Other (large) parts of parameter space have a stau as the lightest supersymmetric particle (LSP),

which is not a viable dark matter candidate. If it is stable it would be a charged relic which is excluded [128]. However, in order to obtain light neutrino masses the particle content of the SSM must be extended by one or more singlet chiral superfields. Furthermore, in order to implement the see-saw mechanism, a new physical scale $M_N = \mathcal{O}(10^{10}\,\mathrm{GeV})$ must be introduced [129].

In B_3 models the LSP is unstable. For typical values of the relevant Yukawa couplings the lifetime is short on cosmological time scales. There is thus no natural dark matter candidate.[1] However, the neutrinos automatically obtain Majorana masses without adding further singlets. Through the couplings $\kappa_i L_i H_2 \in W_{B_3}$ they mix with the neutralinos, leading to one massive neutrino. The other neutrinos receive masses through loop corrections [121, 123, 124, 131, 132, 133, 134, 135, 35]. In order to obtain neutrino masses in agreement with the data, we must have $\kappa_i|_{M_W} = \mathcal{O}(10\,\mathrm{MeV})$, see for example Ref. [35]. This seems worse than the original μ–problem [136, 137]. However, this is naturally obtained in B_3 mSUGRA (minimal supergravity) models with universal supersymmetry breaking. κ_i as well as the corresponding soft terms $\tilde{D}_i$ can be rotated to zero at M_{GUT} [131, 138]. $\kappa_i|_{M_W} \neq 0$ is then generated at one–loop via the renormalization group equations (RGEs) [123]. It is thus loop–suppressed and proportional to a product of $\mu|_{M_{\mathrm{GUT}}}$ and a small R–parity violating Yukawa coupling. This is naturally small and there is thus no new μ–problem.

Therefore P_6 models have a dark matter candidate, but must be extended to obtain massive neutrinos. B_3 models naturally have light neutrinos but lack a dark matter candidate. The purpose of this work is to solve the latter problem. We shall use the Ansatz by Rajagopal *et al.* to extend the axion [8, 9, 11, 10] introduced in the previous chapter to the supersymmetric case. We then embed this model in the B_3 mSUGRA model and consider the resulting axino as a dark matter candidate.

3.2 Supersymmetric DFSZ Axion Model with Broken R–Parity

In this section we briefly introduce the DFSZ axino. Furthermore we present the resulting axino interactions as well as the corresponding Feynman rules. With these rules we are able to calculate axino decays.

First we compute the supersymmetric version of the θ-term Eq. (2.24) where we restrict ourselves to the axino and its interactions. Afterwards we present the superpotential interactions and Feynman rules.

3.2.1 The Effective Axino Gauge Interactions from $\mathscr{L}_\theta$

In the last chapter we showed that the axion is directly related to the solution of the strong CP-problem in the SM. However, the strong CP problem persists when we extend the SM to include supersymmetry and thus still requires a solution. Supersymmetric

[1] Note that for a very light neutralino [130] even for standard Yukawa couplings the lifetimes can be very long.

versions of axion models were first presented in Refs. [139, 140, 136, 141]. The axion is then embedded in a chiral supermultiplet

$$\Phi_{\tilde{a}} = \varphi_{\tilde{a}} + \sqrt{2}\theta\psi_{\tilde{a}} + \theta\theta F_{\tilde{a}}\,, \tag{3.11}$$

where the phase of the complex scalar field $\varphi_{\tilde{a}}$ is the axion, and the other real component is called the saxion. $\psi_{\tilde{a}}$ denotes the 2-component fermionic axino field. $F_{\tilde{a}}$ is the associated auxiliary field. The complex scalar field $\varphi \in \Phi_{\tilde{a}}$ gets a large real vev $\langle\varphi\rangle = f_{\rm PQ}$ in the range of

$$10^9 \text{ GeV} \leq f_{\rm PQ} \leq 10^{12} \text{ GeV}\,, \tag{3.12}$$

cf. Fig. 2.4. The supersymmetric version of the QCD term of Eq. (2.22) is obtained from the F-term of the product

$$\mathscr{L}_{\rm eff}^{\rm SUSY} \supset (\Phi_{\tilde{a}} W^c W^c)\,|_F\,, \tag{3.13}$$

where W^c is the field strength chiral superfield of $SU(3)_C$ and the index $c = 1, \ldots, 8$ runs over the adjoint representation [25]. The relevant terms contributing to the axino–gluino–gluon interactions are computed from the term

$$\int \mathrm{d}^2\theta\, \frac{\alpha_s C_{agg}}{4\sqrt{2}\pi(f_{\rm PQ}/N)}\, \Phi_{\tilde{a}} W^c W^c + \text{h.c.}\,. \tag{3.14}$$

Beyond QCD world, there are further contributions to Eq. (3.13). For the complete calculation we start with the following operators *cf.* Ref. [25]:

$$\mathscr{L}_{\rm eff}^{\rm SUSY} \supset \frac{\alpha_Y C_{aYY}}{4\sqrt{2}\pi(f_{\rm PQ}/N)} (\Phi_{\tilde{a}} B_\alpha B^\alpha)\,|_F + \frac{\alpha_s C_{agg}}{4\sqrt{2}\pi(f_{\rm PQ}/N)} (\Phi_{\tilde{a}} W_c W^c)\,|_F\,. \tag{3.15}$$

Here the $SU(2)_L$ part is not included as it can be rotated away, see Ref. [142]. We calculate the non-abelian term and simplify the result to the $U(1)_Y$ case.

First we introduce the field strength superfield given by

$$\begin{aligned} W_\alpha^c &= \mathrm{i}\lambda_\alpha^c + \underbrace{[\delta_\alpha{}^\beta D^c + \frac{\mathrm{i}}{2}(\sigma^\eta\bar{\sigma}^\kappa)_\alpha{}^\beta V_{\eta\kappa}^c]}_{\equiv N_\alpha^\beta}\theta_\beta + \theta^2\sigma^\eta_{\alpha\dot{\alpha}} D_\eta \bar{\lambda}^{c\dot{\alpha}} && (3.16)\\ &= \mathrm{i}\lambda_\alpha^c + N_\alpha^\beta\theta_\beta + \theta^2\sigma^\eta_{\alpha\dot{\alpha}} D_\eta \bar{\lambda}^{c\dot{\alpha}}\,. && (3.17)\end{aligned}$$

Here λ^c is the spinor of the gauge superfield. The D_μ with the greek index represents derivatives whereas the D^c with a latin index are auxilliary fields. The $V_{\mu\nu}$ is the field strength tensor and σ^μ are the usual sigma matrices.

We first compute the product of the field strength superfields which reads

$$\begin{aligned} W^{c\,\alpha} W_\alpha^c &= \varepsilon^{\alpha\rho} W_\rho^c W_\alpha^c \\ &= \varepsilon^{\alpha\rho}(\mathrm{i}\lambda_\rho^c + N_\rho^\tau\theta_\tau + \theta^2\sigma^\mu_{\rho\dot{\rho}} D_\mu\bar{\lambda}^{c\dot{\rho}})(\mathrm{i}\lambda_\alpha^c + N_\alpha^\beta\theta_\beta + \theta^2\sigma^\eta_{\alpha\dot{\alpha}} D_\eta\bar{\lambda}^{c\dot{\alpha}}) \\ &= \varepsilon^{\alpha\rho}\big[-\lambda_\rho^c\lambda_\alpha^c + \mathrm{i}\lambda_\rho^c N_\alpha^\beta\theta_\beta + \mathrm{i}\lambda_\rho^c\theta^2\sigma^\eta_{\alpha\dot{\alpha}} D_\eta\bar{\lambda}^{c\dot{\alpha}} + \mathrm{i}N_\rho^\tau\theta_\tau\lambda_\alpha^c + N_\rho^\tau\theta_\tau N_\alpha^\beta\theta_\beta \\ &\quad + \mathrm{i}\theta^2\sigma^\mu_{\rho\dot{\rho}} D_\mu\bar{\lambda}^{c\dot{\rho}}\lambda_\alpha^c\big]\,. \end{aligned} \tag{3.18}$$

We have omitted all terms with more than two θ's. Now, consider the product of the latter result with the chiral axino supermultiplet introduced in Eq. (3.11) and keep only the F-terms

$$\begin{aligned}(\Phi W^{c\,\alpha} W^c_\alpha)_{|_{\theta\theta}} &= \varepsilon^{\alpha\rho}(\varphi_{\tilde{a}} + \sqrt{2}\,\theta\,\psi_{\tilde{a}} + \theta\theta F_{\tilde{a}})\Big[-\lambda^c_\rho\lambda^c_\alpha + \mathrm{i}\lambda^c_\rho N^\beta_\alpha\theta_\beta + \mathrm{i}\lambda^c_\rho\theta^2\sigma^\eta_{\alpha\dot{\alpha}} D_\eta\bar{\lambda}^{c\dot{\alpha}} \\ &\quad \mathrm{i}N^\tau_\rho\theta_\tau\lambda^c_\alpha + N^\tau_\rho\theta_\tau N^\beta_\alpha\theta_\beta + \mathrm{i}\theta^2\sigma^\mu_{\rho\dot{\rho}} D_\mu\bar{\lambda}^{c\dot{\rho}}\lambda^c_\alpha\Big]_{|_{\theta\theta}}\end{aligned} \tag{3.19}$$

The terms on the right hand side of Eq. (3.19) can be grouped according the their chiral axino supermultiplet origin:

$$\text{terms with } \varphi_{\tilde{a}} \;:\; \varepsilon^{\alpha\rho}\varphi_{\tilde{a}}\big(\mathrm{i}\lambda^c_\rho\theta^2\sigma^\eta_{\alpha\dot{\alpha}} D_\eta\bar{\lambda}^{c\dot{\alpha}} + N^\tau_\rho\theta_\tau N^\beta_\alpha\theta_\beta + \mathrm{i}\theta^2\sigma^\mu_{\rho\dot{\rho}} D_\mu\bar{\lambda}^{c\dot{\rho}}\lambda^c_\alpha\big) \tag{3.20}$$

$$\text{terms with } \psi_{\tilde{a}} \;:\; \varepsilon^{\alpha\rho}\sqrt{2}\,\theta\cdot\psi_{\tilde{a}}\big(\mathrm{i}\lambda^c_\rho N^\beta_\alpha\theta_\beta + \mathrm{i}N^\tau_\rho\theta_\tau\lambda^c_\alpha\big) \tag{3.21}$$

$$\text{terms with } F_{\tilde{a}} \;:\; -\varepsilon^{\alpha\rho}\theta\theta F_{\tilde{a}}\lambda^c_\rho\lambda^c_\alpha\,. \tag{3.22}$$

Note, that the third term in Eq. (3.20) is identical to the first one. Inserting the explicit expression for N^β_α from Eq. (3.17) into the second term of Eq. (3.20) we obtain

$$\begin{aligned}N^\tau_\rho\theta_\tau N^\beta_\alpha\theta_\beta &= \varepsilon^{\alpha\rho}\varphi_{\tilde{a}}\big(\delta_\rho{}^\tau D^c + \frac{\mathrm{i}}{2}(\sigma^\mu\bar{\sigma}^\nu)_\rho{}^\tau V^c_{\mu\nu}\big)\theta_\tau\big(\delta_\alpha{}^\beta D^c + \frac{\mathrm{i}}{2}(\sigma^\eta\bar{\sigma}^\kappa)_\alpha{}^\beta V^c_{\eta\kappa}\big)\theta_\beta \\ &= \theta\cdot\theta\varphi_{\tilde{a}} D^c D^c - \varepsilon^{\alpha\rho}\frac{1}{4}\varphi_{\tilde{a}}(\sigma^\mu\bar{\sigma}^\nu)_\rho{}^\tau\theta_\tau V^c_{\mu\nu}(\sigma^\eta\bar{\sigma}^\kappa)_\alpha{}^\beta\theta_\beta V^c_{\eta\kappa}\,.\end{aligned} \tag{3.23}$$

We have used Eq. (A.11) in Appendix A and the relation $\theta\sigma^{\mu\nu}\theta = 0$.

The second term in Eq. (3.23) can be rewritten with Eq. (A.13) as

$$\begin{aligned}-\varphi_{\tilde{a}}\varepsilon^{\alpha\rho}\frac{1}{4}(\sigma^\mu\bar{\sigma}^\nu)_\rho{}^\tau\theta_\tau V^c_{\mu\nu}(\sigma^\eta\bar{\sigma}^\kappa)_\alpha{}^\beta\theta_\beta V^c_{\eta\kappa} &= -\frac{1}{4}\varphi_{\tilde{a}}\varepsilon^{\alpha\rho}\theta_\tau\theta_\beta(\sigma^\mu\bar{\sigma}^\nu)_\rho{}^\tau(\sigma^\eta\bar{\sigma}^\kappa)_\alpha{}^\beta V^c_{\mu\nu}V^c_{\eta\kappa} \\ &= -\frac{1}{8}\varphi_{\tilde{a}}\,\theta\cdot\theta\,\varepsilon^{\alpha\rho}\varepsilon_{\tau\beta}\sigma^\mu_{\rho\dot{\rho}}\bar{\sigma}^{\nu\,\dot{\rho}\tau}\sigma^\eta_{\alpha\dot{\alpha}}\bar{\sigma}^{\kappa\,\dot{\alpha}\beta}V^c_{\mu\nu}V^c_{\eta\kappa}\,.\end{aligned} \tag{3.24}$$

Employing $\varepsilon_{\tau\beta}\varepsilon^{\alpha\rho} = -\delta_\tau{}^\alpha\delta_\beta{}^\rho + \delta_\tau{}^\rho\delta_\beta{}^\alpha$, Eq. (3.24) can be further simplified

$$\begin{aligned}(3.24) &= -\frac{1}{8}\,\theta\cdot\theta\varphi_{\tilde{a}}(-\delta_\tau{}^\alpha\delta_\beta{}^\rho + \delta_\tau{}^\rho\delta_\beta{}^\alpha)\sigma^\mu_{\rho\dot{\rho}}\bar{\sigma}^{\nu\,\dot{\rho}\tau}\sigma^\eta_{\alpha\dot{\alpha}}\bar{\sigma}^{\kappa\,\dot{\alpha}\beta}V^c_{\mu\nu}V^c_{\eta\kappa} \\ &= -\frac{1}{8}\,\theta\cdot\theta\varphi_{\tilde{a}}\Big(-\mathrm{tr}\big[\sigma^\mu\sigma^\nu\sigma^\eta\sigma^\kappa\big] + \mathrm{tr}\big[\sigma^\mu\sigma^\nu\big]\mathrm{tr}\big[\sigma^\eta\sigma^\kappa\big]\Big)V^c_{\mu\nu}V^c_{\eta\kappa} \\ &= -\frac{1}{8}\,\theta\cdot\theta\varphi_{\tilde{a}}\Big(-2(g^{\mu\nu}g^{\eta\kappa} - g^{\mu\eta}g^{\nu\kappa} + g^{\mu\kappa}g^{\nu\eta} + \mathrm{i}\varepsilon^{\mu\nu\eta\kappa}) + 2g^{\mu\nu}2g^{\eta\kappa}\Big)V^c_{\mu\nu}V^c_{\eta\kappa} \\ &= -\frac{1}{4}\,\theta\cdot\theta\varphi_{\tilde{a}}\Big(2V^c_{\mu\nu}V^{c\,\mu\nu} - \mathrm{i}\varepsilon^{\mu\nu\eta\kappa}V^c_{\mu\nu}V^c_{\eta\kappa}\Big)\,.\end{aligned} \tag{3.25}$$

Here we have used the trace relations shown in Appendix A. The symmetry of the $g^{\alpha\beta}$ tensors and the antisymmetry of the field strength tensor give a vanishing first- and last-term in the next to last line.

Collecting all results which are proportinal to the saxion and axion respectively we have

$$(3.20) \quad = \quad \theta\cdot\theta\,\varphi_{\tilde{a}}\big(D^aD^a-\frac{1}{2}V^c_{\mu\nu}V^{c\,\mu\nu}+\frac{1}{4}\mathrm{i}\varepsilon^{\mu\nu\eta\kappa}V^c_{\mu\nu}V^c_{\eta\kappa}\big) \tag{3.26}$$

For the axino we insert again the explicit expression for N^β_α and obtain

$$\begin{aligned}(3.21) \quad &= \varepsilon^{\alpha\rho}\sqrt{2}\,\theta\cdot\psi_{\tilde{a}}\Big[\mathrm{i}\lambda^c_\rho\big(\delta_\alpha{}^\beta D^c+\frac{\mathrm{i}}{2}(\sigma^\eta\bar\sigma^\kappa)_\alpha{}^\beta V^c_{\eta\kappa}\big)\theta_\beta+\mathrm{i}\big(\delta_\rho{}^\tau D^c+\frac{\mathrm{i}}{2}(\sigma^\mu\bar\sigma^\nu)_\rho{}^\tau V^c_{\mu\nu}\big)\theta_\tau\lambda^c_\alpha\Big]\\
&= \underbrace{\mathrm{i}\sqrt{2}\,\varepsilon^{\alpha\rho}\theta\cdot\psi_{\tilde{a}}\lambda^c_\rho\delta_\alpha{}^\beta D^c\theta_\beta}_{(a)}\underbrace{-\frac{\mathrm{i}}{2}\sqrt{2}\varepsilon^{\alpha\rho}\,\theta\cdot\psi_{\tilde{a}}\lambda^c_\rho(\sigma^\eta\bar\sigma^\kappa)_\alpha{}^\beta V^c_{\eta\kappa}\theta_\beta}_{(b)}\\
&\quad+\underbrace{\mathrm{i}\sqrt{2}\,\varepsilon^{\alpha\rho}\theta\cdot\psi_{\tilde{a}}\delta_\rho{}^\tau D^c\theta_\tau\lambda^c_\alpha}_{(c)}\underbrace{-\frac{\mathrm{i}}{2}\sqrt{2}\varepsilon^{\alpha\rho}\,\theta\cdot\psi_{\tilde{a}}(\sigma^\mu\bar\sigma^\nu)_\rho{}^\tau V^c_{\mu\nu}\theta_\tau\lambda^c_\alpha}_{(d)}\end{aligned} \tag{3.27}$$

Making use of the relation

$$(\theta\psi)(\chi\theta)=-\frac{1}{2}(\theta\theta)(\chi\psi)=(\theta\psi)(\theta\chi) \tag{3.28}$$

we get from the terms (a) and (c)

$$(a)+(c)=-\mathrm{i}\sqrt{2}(\theta\cdot\theta)(\psi_{\tilde{a}}\cdot\lambda^c)D^c \tag{3.29}$$

After a bit of manipulation the terms (b) and (d) can be grouped together

$$\begin{aligned}(b)+(d) \quad &= -\frac{\mathrm{i}}{2}\sqrt{2}\varepsilon^{\alpha\rho}\,\theta\cdot\psi_{\tilde{a}}\lambda^c_\rho(\sigma^\eta\bar\sigma^\kappa)_\alpha{}^\beta V^c_{\eta\kappa}\theta_\beta-\frac{\mathrm{i}}{2}\sqrt{2}\varepsilon^{\alpha\rho}\,\theta\cdot\psi_{\tilde{a}}(\sigma^\mu\bar\sigma^\nu)_\rho{}^\tau V^c_{\mu\nu}\theta_\tau\lambda^c_\alpha\\
&= -\frac{\mathrm{i}}{2}\sqrt{2}\left[\frac{1}{2}\theta\cdot\theta\delta^\gamma_\beta\psi_{\tilde{a}\gamma}\lambda^{c\,\alpha}(\sigma^\eta\bar\sigma^\kappa)_\alpha{}^\beta V^c_{\eta\kappa}+\frac{1}{2}\theta\cdot\theta\,\delta^\gamma_\tau\lambda^{c\,\rho}(\sigma^\mu\bar\sigma^\nu)_\rho{}^\tau\psi_{\tilde{a}\,\gamma}\right]\\
&= \frac{\mathrm{i}}{4}\sqrt{2}\,\theta\cdot\theta\left[\lambda^c\cdot(\sigma^\eta\bar\sigma^\kappa)\cdot\psi_{\tilde{a}}V^c_{\eta\kappa}+\lambda^c\cdot(\sigma^\mu\bar\sigma^\nu)\cdot\psi_{\tilde{a}}V^c_{\mu\nu}\right]\\
&= \sqrt{2}\,\theta\cdot\theta\left[\lambda^c\cdot\sigma^{\mu\nu}\cdot\psi_{\tilde{a}}V^c_{\mu\nu}\right],\end{aligned} \tag{3.30}$$

where in the second line the Grassmann variable has been interchanged with the axino spinor. In turn the axino spinor has been interchanged with the gauge spinor. Despite the anticommuting origin of all expressions we get no additional minus sign. After reordering these terms, Eq. (A.13) as applied aboved can be used to form the product $\theta\cdot\theta$. As a final step, the sigma matrices can be reexpressed with Eq. (A.11). An appropriate choice of the indices leads to two equal expression which can be summed to Eq. (3.30).

Hence the axino contribution reads then

$$(3.21) = \theta\cdot\theta\Big[-\mathrm{i}\sqrt{2}(\psi_{\tilde{a}}\cdot\lambda^c)D^c + \sqrt{2}\,\lambda^c\cdot\sigma^{\mu\nu}\cdot\psi_{\tilde{a}}V^c_{\mu\nu}\Big] \tag{3.31}$$

Thus collecting all terms and inserting them into Eq. (3.15), we have for the $SU(3)$ gauge group interactions

$$\begin{aligned}\frac{\alpha_s C_{agg}}{4\sqrt{2}\pi(f_{\mathrm{PQ}}/N)}\left(\Phi W^{c\,\alpha}W^c_\alpha\right)_{|\theta\theta} &= \frac{\alpha_s C_{agg}}{4\sqrt{2}\pi(f_{\mathrm{PQ}}/N)}\Bigg[2\,\mathrm{i}\,\varphi_{\tilde{a}}\lambda^c\cdot\sigma^\eta D_\eta\cdot\bar{\lambda}^c + \varphi_{\tilde{a}}D^cD^c \\ &\quad -\frac{1}{2}\,\varphi_{\tilde{a}}V^c_{\mu\nu}V^{c\,\mu\nu} + \frac{1}{4}\mathrm{i}\varepsilon^{\mu\nu\eta\kappa}\,\varphi_{\tilde{a}}V^c_{\mu\nu}V^c_{\eta\kappa} - \mathrm{i}\sqrt{2}(\psi_{\tilde{a}}\cdot\lambda^c)D^c \\ &\quad +\sqrt{2}\,\lambda^c\cdot\sigma^{\mu\nu}\cdot\psi_{\tilde{a}}V^c_{\mu\nu} - F_{\tilde{a}}\lambda^c\cdot\lambda^c\Bigg]\,. \end{aligned}\tag{3.32}$$

In addition there is the hermitean conjugate term. Eq. (3.32) contains two terms with an axino and several more terms with the axion and saxion respectively. Note, that the fourth term is the well known non-supersymmetric axion interaction. The other axion/saxion terms give rise to new interactions. This is beyond the scope of this work. We focus only on the axino part.

Hence we can conclude for the axino interaction in the $SU(3)$ case

$$\mathscr{L}_{\tilde{a}\tilde{g}g} = \frac{\alpha_s C_{agg}}{4\pi(f_{\mathrm{PQ}}/N)}\left[\lambda^c_{\tilde{g}}\sigma^{\mu\nu}\psi_{\tilde{a}}G^c_{\mu\nu} - \mathrm{i}(\psi_{\tilde{a}}\lambda^c_{\tilde{g}})D^c\right] + \mathrm{h.c.}\,, \tag{3.33}$$

where the D-terms are give explicitly by

$$D^c = g_s\sum_i \tilde{q}_i^{\dagger j}(T^c)_j{}^k\tilde{q}_{ki}\,. \tag{3.34}$$

Here i is summed over all the left– amd right–handed squark flavors and j,k are $SU(3)_C$ indices for the fundamental representation. Analogously the axino $U(1)_Y$ interactions are given by

$$\mathscr{L}_{\tilde{a}\tilde{Y}Y} = \frac{C_{aYY}\alpha_Y}{4\pi(f_{\mathrm{PQ}}/N)}\left[\lambda_{\tilde{B}}\sigma^{\mu\nu}\psi_{\tilde{a}}B_{\mu\nu} - \mathrm{i}(\psi_{\tilde{a}}\lambda_{\tilde{B}})D_Y\right] + \mathrm{h.c.} \tag{3.35}$$

Here $\alpha_Y = e^2/(4\pi\cos^2\theta_w)$. C_{aYY} is a model dependent parameter, see also Ref. [25]. For the simple DFSZ model which we employ, $C_{aYY} = 8/3$. D_Y denotes the D-term of the hypercharge boson vector superfield. It is given by

$$D_Y = g'\Big[\sum_{\tilde{f}}\frac{1}{2}\tilde{f}^\dagger Y_{\tilde{f}}\tilde{f} - \frac{1}{2}(v_d^2 - v_u^2)\Big]\,, \tag{3.36}$$

where we sum over all sfermions, *i.e.* the squarks and sleptons. $Y_{\tilde{f}}$ is the hypercharge: $Q - T^3 = Y_f/2$.

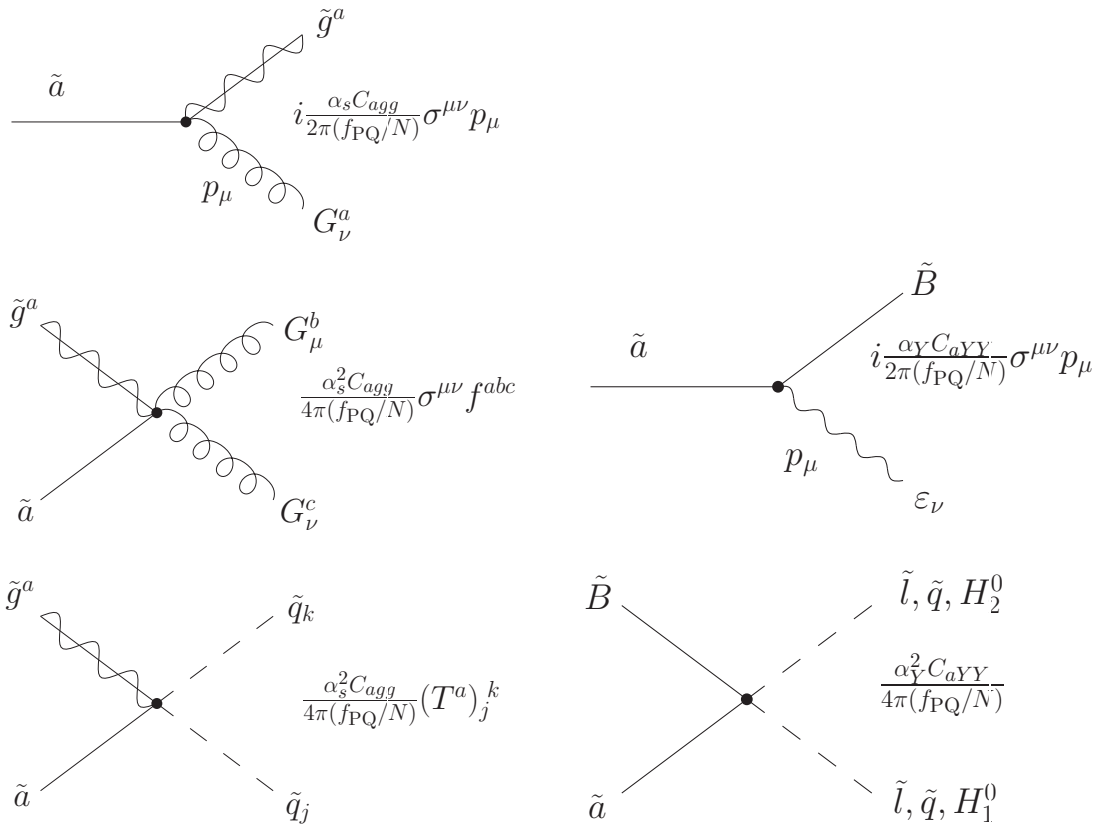

(a) Feynman rules from $\mathscr{L}_{\tilde{a}\tilde{g}g}$. Here j,k are the squark color indices. a,b,c are the gluon/gluino adjoint color indices.

(b) Feynman rules for the $\mathscr{L}_{\tilde{a}\tilde{Y}Y}$-term.

Figure 3.1: Axino Feynman rules from the supersymmetric θ-term Lagrangian, for details see the text.

From the first term in Eqs. (3.33) and (3.35), we obtain an effective axino–gaugino–gauge boson interaction, suppressed by $1/f_{\rm PQ}$. From the second term, via the D-term, we obtain an effective axino–gaugino–scalar fermion–scalar fermion interaction, which is also suppressed by $1/f_{\rm PQ}$. This term was recently employed in Ref. [88], when recalculating thermal production of axino dark matter. The corresponding Feynman rules are given in Fig. 3.1(a) for the QCD case and in Fig. 3.1(b) for the hypercharge case. In the figures, we have denoted the gluino by $\tilde{g}$ and the axino by $\tilde{a}$. Using these Feynman rules we can compute the axino decay rates in Sect. 5

3.2.2 Axino Superpotential Interactions

For the couplings of $\Phi_{\tilde{a}}$, we follow the ansatz of Rajagopal et. al. [145] and replace the μ–term in the superpotential, Eq. (3.4), by

$$W_{\tilde{a}} = c_1 \varepsilon_{ab} \Phi_{\tilde{a}} H_1^a H_2^b \,. \tag{3.37}$$

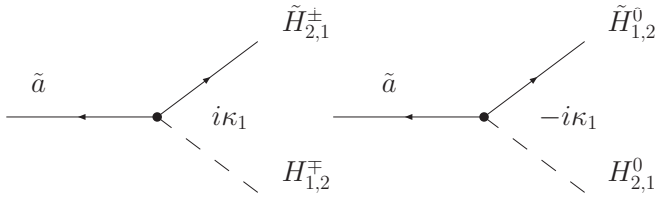

Figure 3.2: R–parity conserving axino Yukawa interactions from the $c_1\Phi_{\tilde{a}}H_1H_2$-term with the corresponding Feynman rules.

Here c_1 is a very small dimensionless parameter. With an appropriate choice of c_1 we get among other interactions the usual μ–term after PQ symmetry breaking, with

$$\mu = c_1 \cdot \langle\varphi\rangle\,. \tag{3.38}$$

We do not discuss the problem of fine–tuning here, but refer the reader to the solution in the supergravity context given in Refs. [136, 137].

Within B_3 models the lepton doublet chiral superfields, L_i, have the same gauge quantum numbers as the Higgs doublet chiral superfield H_1. It is thus natural to extend the bi–linear interaction in W_{B_3} to

$$\varepsilon_{ab}c_2^i\Phi_{\tilde{a}}L_i^aH_2^b, \quad \text{with } i=1,2,3\,. \tag{3.39}$$

This of course requires corresponding Peccei-Quinn charges. Here the c_2^i are a set of dimensionless coupling constants. Again, we retrieve the previous low–energy coupling after PQ symmetry breaking:

$$\kappa^i = c_2^i \cdot \langle\varphi\rangle\,. \tag{3.40}$$

With the shorthand notation of Ref. [35] we can define

$$\mathcal{L}^a_{\alpha=0,\ldots,3} \equiv (H_1^a,\, L^a_{i=1,2,3})\,, \tag{3.41}$$

and then combine Eqs. (3.37) and (3.39) to

$$W^{\tilde{a}}_{B_3} \equiv\ \varepsilon_{ab}c^\alpha\Phi_{\tilde{a}}\mathcal{L}^a_\alpha H_2^b\,, \qquad \text{with } \alpha=0,\ldots,3\,. \tag{3.42}$$

The terms in Eq. (3.42) lead to the following R–parity conserving axino Yukawa couplings with the Higgs bosons and Higgsinos

$$\mathscr{L}_{\rm Yuk} \;=\; c_1(H_1^-\psi_{\tilde{a}}\widetilde{H}_2^+ + H_2^+\psi_{\tilde{a}}\widetilde{H}_1^- - H_2^0\psi_{\tilde{a}}\widetilde{H}_1^0 - H_1^0\psi_{\tilde{a}}\widetilde{H}_2^0) + \text{h.c.}\,. \tag{3.43}$$

These interactions are depicted in Fig. 3.2 with the corresponding Feynman rules. We have denoted the axino $\psi_{\tilde{a}}$ as $\tilde{a}$ in the figure. After electroweak symmetry breaking, they lead to an axino–Higgsino mixing and thus to an extension of the neutralino sector. We shall return to this below. It is also worth mentioning, that these interactions are typical for DFSZ models and do not appear at tree–level in the KVSZ-model.

From Eq. (3.39) we get the relevant R–parity violating axino Yukawa interactions

$$\mathscr{L}_{B_3-\rm Yuk} \;=\; c_2^i(H_2^0\nu_i\psi_{\tilde{a}} + \tilde{\nu}_i\psi_{\tilde{a}}\tilde{H}_2^0 - H_2^+\psi_{\tilde{a}}e_i - \tilde{e}_i\psi_{\tilde{a}}\tilde{H}_2^+) + \text{h.c.}\,. \tag{3.44}$$

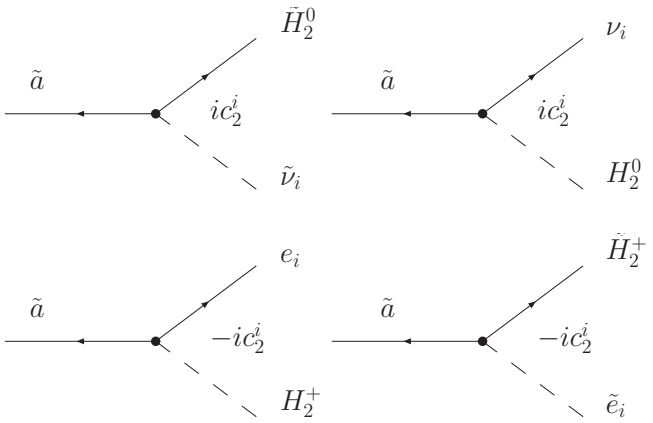

Figure 3.3: R–parity violating axino Yukawa interactions from the $c_2^i \Phi_{\tilde{a}} L_i H_2$-term with their Feynman rules. $i = 1, 2, 3$ is a generation index.

The resulting lepton–number violating interactions with their Feynman rules are shown in Fig. 3.3.

After electroweak symmetry breaking, we get an axino–neutrino mixing from these interactions. Since the neutrinos mix with the neutralinos in B_3 models, this extends the neutralino sector: it consists of the the original neutralinos, the neutrinos, and now the axinos. This results in a 8×8 neutralino mass matrix.

3.2.3 Soft Supersymmetry Breaking Interactions

After supersymmetry breaking there are purely scalar interactions corresponding to the above axino superpotential terms. They do not directly involve the axino, but we include them for completeness. In the theory without an axion we have the terms, *cf.* the notation in Ref. [35],

$$\mathscr{L}_{\text{soft}} \supset \varepsilon_{ab} b_\alpha \widetilde{\mathcal{L}}_\alpha^a H_2^b + \text{h.c.}, \tag{3.45}$$

with $b_\alpha = (\tilde{B}, \tilde{D}_i)$. Here $\widetilde{\mathcal{L}}_\alpha^a$ denotes the scalar component of $\mathcal{L}_\alpha^a$. Again as for the superpotential, we replace the bilinear by trilinear terms involving $\varphi_{\tilde{a}}$

$$\mathscr{L}_{\text{soft, }\tilde{a}\text{-case}} \supset \varepsilon_{ab} h_{\tilde{a},\alpha} \varphi_{\tilde{a}} \widetilde{\mathcal{L}}_\alpha^a H_2^b + \text{h.c.}, \quad \alpha = 0, \ldots, 3\,, \tag{3.46}$$

where $h_{\tilde{a},\alpha} \equiv (h_{\tilde{a},1}^{\varphi H_1 H_2}, h_{\tilde{a},i}^{\varphi L_i H_2}) \equiv (\tilde{B}_{\tilde{a}}, \tilde{D}_{\tilde{a},i})$. When the scalar part of the axion supermultiplet acquires a vev according to Eq. (3.12) the scalar Higgs and the sleptons mix. As for the superpotential, $h_{\tilde{a},\alpha}$ has to be chosen appropriately, so that Eq. (3.45) is reproduced from Eq. (3.46), after PQ symmetry breaking.

3.2.4 Axino Mass

In global softly broken supersymmetry the axino mass was first computed in Refs. [143, 144] in the context of a spontaneously broken global $U(1)$ symmetry. This was reconsid-

ered in Ref. [145]. It was found that the axino mass must be very light

$$m_{\tilde{a}} \sim \frac{M_{SUSY}^2}{f_{PQ}} = \mathcal{O}(1\,\mathrm{keV} - 1\mathrm{MeV})\,, \tag{3.47}$$

where we have set $M_{SUSY} \lesssim \mathcal{O}(1\,\mathrm{TeV})$ as the supersymmetry breaking scale (in the observable sector).

In spontaneously broken supergravity models, the mass of the axino must be reconsidered, Refs. [145, 146, 34, 60]. In such theories we have two mass scales. The Planck scale $M_{\mathrm{Pl}} = \mathcal{O}(10^{19}\,\mathrm{GeV})$ and $M_S = \mathcal{O}(10^{11}\,\mathrm{GeV})$, the supersymmetry breaking scale in the hidden–sector. This gives the additional small parameter

$$\eta = \frac{M_S}{M_{\mathrm{Pl}}} = \mathcal{O}(10^{-8})\,. \tag{3.48}$$

The gravitino mass can then be written as

$$m_{3/2} \sim \eta^2 M_{\mathrm{Pl}} \lesssim \mathcal{O}(1\,\mathrm{TeV})\,. \tag{3.49}$$

One might now expect that $m_{\tilde{a}} \sim m_{3/2}$, leading to a heavy axino. But in fact it was found that [34, 60]

$$m_{\tilde{a}} \sim \eta^k M_{\mathrm{Pl}}\,, \tag{3.50}$$

where k is a highly model dependent integer. We shall thus adopt the axino mass as a free parameter and let it vary in the range

$$\mathcal{O}(100\,\mathrm{keV}) < m_{\tilde{a}} < \mathcal{O}(500\,\mathrm{MeV})\,, \tag{3.51}$$

consistent with the models, which have been constructed [145, 146, 34, 60]. This mass range leads to axinos which are considered to be cold dark matter if we follow the approximate guideline of Ref. [28]. Furthermore, heavier axinos will have short lifetimes which are cosmologically not relevant. For the axino, we will assume a mass term of the general form of a neutral spin-1/2 Majorana fermion field

$$\mathscr{L}_{\tilde{a}\,\mathrm{mass\,term}} = -\frac{1}{2} m_{\tilde{a}} (\psi_{\tilde{a}} \psi_{\tilde{a}} + \mathrm{h.c.})\,, \tag{3.52}$$

see also Ref. [78]. This will contribute to the full 8×8 neutralino mass matrix.

3.2.5 Neutralino and Chargino Mixing

In this section, we derive the modified and extended neutralino and chargino mixing matrices. The corresponding matrices in the MSSM are given for example in Ref. [75]. We first consider the generalization of the 4x4 neutralino mass matrix and then briefly discuss the chargino case.

As we have seen in deriving the axino Lagrangian, the axino mixes with the Higgsinos, *cf.* Eq. (3.43), and thus with the neutralinos. The axino also mixes with the neutrinos, *cf.* Eq. (3.44), which in R–parity violation also mix with the neutralinos. Furthermore

the axino mixes directly with the bino, *cf.* Eq. (3.35), when the neutral Higgs or the sneutrinos get a vacuum expectation value. This is however suppressed by $1/f_{\rm PQ}$.

Furthermore, there is a new contribution to the original MSSM neutralino mass matrix. The F–term of the operator $\Phi_{\tilde{a}}WW$, *cf.* Eq. (3.13), which is computed in Appendix A, includes the expression

$$\xi \left(F_{\tilde{a}} \lambda_{\tilde{B}} \lambda_{\tilde{B}} \right), \tag{3.53}$$

where $\xi = \frac{\alpha_Y C_{aYY}}{4\sqrt{2}\pi(f_{\rm PQ}/N)}$. The vacuum expectation value of the axino F-term is given by:

$$F_{\tilde{a}} = c_1 v_u v_d - c_2^i v_i v_u. \tag{3.54}$$

Therefore Eq. (3.53) leads to a Bino mass term. This is of order $M_W^2/f_{\rm PQ}$ and thus highly suppressed. We neglect it in the following.

We thus have in total an 8×8 mass mixing matrix for the spin-1/2 neutral fermions. The matrix is given in the basis

$$\psi_j^{0\,T} = \left(-\mathrm{i}\widetilde{B},\, -\mathrm{i}\widetilde{W}^{(3)},\, \widetilde{H}_2^0,\, \nu_\alpha,\, \tilde{a} \right) \tag{3.55}$$

with $j = 1, \ldots, 8$. We follow the notation of Ref. [35], where

$$\nu_\alpha = (\tilde{H}_1^0, \nu_1, \nu_2, \nu_3), \qquad \alpha = 0, 1, 2, 3\,, \tag{3.56}$$

in accordance with Eq. (3.41). $\widetilde{B}$ denotes the bino field and $\widetilde{W}^3$ denotes the neutral wino field. $\nu_i,\ i = 1, 2, 3$ denote the sneutrino vev's. Explicitly, we then have for the mass terms in the Lagrangian

$$\mathscr{L}_{\chi^0} = -\frac{1}{2} \left(-\mathrm{i}\widetilde{B},\, -\mathrm{i}\widetilde{W}^{(3)},\, \widetilde{H}_2^0,\, \widetilde{H}_1^0,\, \nu_i,\, \tilde{a} \right) \mathcal{M}_{\rm N} \begin{pmatrix} -\mathrm{i}\widetilde{B} \\ -\mathrm{i}\widetilde{W}^{(3)} \\ \widetilde{h}_2^0 \\ \widetilde{h}_1^0 \\ \nu_j \\ \tilde{a} \end{pmatrix} \tag{3.57}$$

where the mass mixing matrix $\mathcal{M}_{\rm N}$ is given by

$$\mathcal{M}_{\rm N} = \begin{pmatrix} M_1 & 0 & M_Z s_W \frac{v_u}{\sqrt{v_\gamma^2}} & -M_Z s_W \frac{v_0}{\sqrt{v_\gamma^2}} & -M_Z s_W \frac{v_j}{\sqrt{v_\gamma^2}} & 0 \\ 0 & M_2 & -M_Z c_W \frac{v_u}{\sqrt{v_\gamma^2}} & M_Z c_W \frac{v_0}{\sqrt{v_\gamma^2}} & M_Z c_W \frac{v_j}{\sqrt{v_\gamma^2}} & 0 \\ M_Z s_W \frac{v_u}{\sqrt{v_\gamma^2}} & -M_Z c_W \frac{v_u}{\sqrt{v_\gamma^2}} & 0 & -\mu_0 & -\mu_j & c_1 v_d - c_2^j v_j \\ -M_Z s_W \frac{v_0}{\sqrt{v_\gamma^2}} & M_Z c_W \frac{v_0}{\sqrt{v_\gamma^2}} & -\mu_0 & 0 & 0 & -c_1 v_u \\ -M_Z s_W \frac{v_i}{\sqrt{v_\gamma^2}} & M_Z c_W \frac{v_i}{\sqrt{v_\gamma^2}} & -\mu_i & 0 & 0 & -c_2^j v_u \\ 0 & 0 & c_1 v_d - c_2^i v_i & -c_1 v_u & -c_2^i v_u & m_{\tilde{a}} \end{pmatrix} \tag{3.58}$$

Beyond the axino–neutrino–neutralino mixing, there is further mixing in the B_3 mSUGRA model. The details are presented in Ref. [35]. Here we mention only the mixing between the charged leptons and the charginos, since we use this below in determining the axino decays. The contribution to the Lagrangian is given by

$$\mathscr{L}_{\chi^\pm} = -(-i\widetilde{W}^-, e_{L_\alpha}^-)\mathcal{M}_{\rm C} \begin{pmatrix} -i\widetilde{W}^+ \\ \tilde{H}_2^+ \\ e_{R_k}^+ \end{pmatrix} + \text{h.c.}\,, \tag{3.59}$$

with $k = 1, 2, 3$. Here we define

$$e_{L_\alpha}^- \equiv (\widetilde{H}_1^-,\, e_L^-,\, \mu_L^-,\, \tau_L^-)\,, \tag{3.60}$$

with $\alpha = 0, \ldots, 3$. The 5×5 mass mixing matrix $\mathcal{M}_C$ is given by

$$\mathcal{M}_{\rm C} = \begin{pmatrix} M_2 & g_2 v_u & 0_k \\ g_2 v_\alpha & \mu_\alpha & \boldsymbol{\lambda}_{\beta\alpha k} v_\beta \end{pmatrix}\,. \tag{3.61}$$

We have also employed the 4–component notation for the combined $(\boldsymbol{\Lambda}_{E^k})_{ij} L_i L_j \bar{E}_k$ and $(\boldsymbol{Y}_E)_{ij} L_i H_1 \bar{E}_j$ operators

$$W_{LL\bar{E}+LH\bar{E}} \equiv \boldsymbol{\lambda}_{\alpha\beta k} L_\alpha L_\beta \bar{E}_k\,, \tag{3.62}$$

as well as for the vacuum expectation values

$$v_\alpha \equiv (v_d,\, v_1,\, v_2,\, v_3)\,, \quad \alpha = 0, \ldots, 3\,. \tag{3.63}$$

With this definition we can introduce the following sum

$$v_\gamma^2 \equiv \sum_\alpha v_\alpha^2. \tag{3.64}$$

3.2.6 Neutralino and Chargino Mass Eigenstate Notation

We have seen that the standard MSSM 4×4 neutralino mass matrix is enlarged to an 8×8 matrix. For the basis of the gauge or current eigenstates we introduced:

$$\psi_j^{0\,T} = (-\mathrm{i}\tilde{B},\, -\mathrm{i}\widetilde{W}^{(3)},\, \tilde{H}_2^0,\, \nu_\alpha,\, \tilde{a})\,, \tag{3.65}$$

with $j = 1, \ldots, 8$ and $\alpha = 0, \ldots, 3$. So we can rewrite Eq. (3.57) as

$$\mathscr{L}_{\chi^0} = -\frac{1}{2}(\psi^0)^T \mathcal{M}_{\mathrm{N}} \psi^0 + \mathrm{h.c.}, \tag{3.66}$$

where $\mathcal{M}_{\mathrm{N}}$ is the mass matrix, given in Eq. (3.58). For the mass eigenstates, we extend the standard notation of the 4×4 case to the eight–component vectors. They are defined via a unitary matrix N:

$$\widetilde{\xi}_i^0 \equiv N_{ij}\, \psi_j^0\,, \qquad i, j \in \{1, \ldots, 8\}\,, \tag{3.67}$$

where the matrix N satisfies the condition

$$N^* \mathcal{M}_{\mathrm{N}} N^{-1} = \mathcal{M}_{\mathrm{D}}\,, \tag{3.68}$$

and $\mathcal{M}_D$ is the diagonal mass matrix with real, non–negative entries[2]. We now have eight neutral-fermions. The mixing between the bino, wino and Higgsinos, on the one side, and the neutrinos and axinos, on the other side, is very weak. We therefore retain the standard notation for the individual eight mass eigenstates. We have in components

$$(\tilde{\xi}_i^0)^T = \left(\tilde{\chi}_1^0,\, \tilde{\chi}_2^0,\, \tilde{\chi}_3^0,\, \tilde{\chi}_4^0,\, \nu_1',\, \nu_2',\, \nu_3',\, \tilde{a}'\right)\,. \tag{3.69}$$

Just to be explicit: due to weak mixing the $\tilde{\chi}_{i=1,\ldots,4}^0$ are closely related to the standard MSSM neutralino mass eigenstates with only a very small neutrino and axino admixture. The lightest of these four we denote $\tilde{\chi}_1^0$, increasing in mass to $\tilde{\chi}_4^0$. The primed expressions are predominantly neutrino– or axino–like neutralino eigenstates, respectively. They also only have small admixtures of the other current eigenstates. We shall thus refer to these mass eigenstates as neutrinos and axinos in the following. We shall also drop the primes where it is clear that we are discussing mass eigenstates.

Given this notation, we can replace the gauge eigenstates used in the Lagragians in Eqs. (3.43), (3.44) and (3.35) by the mass eigenstates presented above. This then gives us the explicit axino mass eigenstate interactions, which we need in our computations below. This is presented in detail in Appendix B, including the relevant Feynman rules.

Analogously we can construct a notation for the chargino case, see *e.g.* Ref. [75, 35]. Using

$$\psi_j^+ = (-\mathrm{i}\tilde{W}^+,\, \widetilde{H}_2^+,\, e_{R_k}^+), \tag{3.70}$$

$$\psi_j^- = (-\mathrm{i}\tilde{W}^-,\, e_{L_\alpha}^-), \tag{3.71}$$

[2]See also the detailed discussion on fermion mass matrix decomposition in Appendix D of Ref. [78].

with $j = 1, \ldots, 5$, $k = 1, 2, 3$ and $\alpha = 1, \ldots, 4$, we can write the Lagrangian as:

$$\mathscr{L} = -\frac{1}{2}\left[\psi^{+T}\mathcal{M}_{\rm C}^{T}\psi^{-} + \psi^{-T}\mathcal{M}_{\rm C}\psi^{+}\right] + \text{h.c.}, \tag{3.72}$$

where $\mathcal{M}_{\rm C}$ is the non diagonal mass matrix. The mass eigenstates can be defined with unitary matrices V and U:

$$\widetilde{\eta}_i^{+} \equiv V_{ij}\,\psi_j^{+} \quad \text{and} \quad \widetilde{\eta}_i^{-} \equiv U_{ij}\,\psi_j^{-}\,, \quad i = 1\ldots 5, \tag{3.73}$$

where V and U satisfy

$$U^{*}\mathcal{M}_{\rm C}V^{-1} = \mathcal{M}_{\rm D} \tag{3.74}$$

and $\mathcal{M}_{\rm D}$ is the diagonal mass matrix. Here we again assume that the mixings of the leptons with the winos and higgsinos respectively are small. Thus we shall write

$$\widetilde{\eta}^{+} = (\widetilde{\chi}_\ell^{+}, e_{R_k}^{+})\,, \quad \widetilde{\eta}^{-} = (\widetilde{\chi}_\ell^{-}, e_{L_k}^{-})\,, \tag{3.75}$$

with $\ell = 1, 2$ and $k = 1, 2, 3$.

Finally the scalar higgs fields have to be rotated into the mass eigenstates. The details are described in the appendix of Ref. [78]. We just state the parametrization between the gauge- and mass eigenstate:

$$H_2^0 = v_u + \frac{1}{\sqrt{2}}\sum_{\phi^0} k_{u\phi^0}\phi^0\,, \quad H_2^{\pm} = \sum_{\phi^{\pm}} k_{u\phi^{\pm}}\phi^{\pm} \tag{3.76}$$

$$H_1^0 = v_d + \frac{1}{\sqrt{2}}\sum_{\phi^0} k_{d\phi^0}\phi^0\,, \quad H_1^{\pm} = \sum_{\phi^{\pm}} k_{d\phi^{\pm}}\phi^{\pm} \tag{3.77}$$

Finally the supersymmetrized version of the θ-term, cf. equation (3.35) reads

$$\mathscr{L}_{\tilde{a}\tilde{Y}Y} = \frac{C_{aYY}\alpha_Y}{4\pi(f_{\rm PQ}/N)}\left[(N_{i1}^{*}\widetilde{\xi}_i^0)\sigma^{\mu\nu}(N_{i8}^{*}\widetilde{\xi}_i^0)B_{\mu\nu}\right] + \text{h.c.}\,, \tag{3.78}$$

where we have restricted ourselves to the first term of Eq. (3.35).

3.2.7 Peccei–Quinn Charges

To complete our model we list here the required chiral superfield charges for the global Peccei-Quinn symmetry. We first define our notation in Tab. 3.1. In order to obtain the B_3 superpotential given in Eqs. (3.3), (3.4) and (3.6), we must satisfy the following relations between the Peccei-Quinn charges

$$Q_L + Q_{H_1} + Q_{E^c} = 0 \tag{3.79}$$

$$Q_Q + Q_{H_1} + Q_{D^c} = 0 \tag{3.80}$$

$$Q_Q + Q_{H_2} + Q_{U^c} = 0 \tag{3.81}$$

$$Q_{\tilde{a}} + Q_{H_1} + Q_{H_2} = 0 \tag{3.82}$$

$$Q_{\tilde{a}} + Q_L + Q_{H_2} = 0 \tag{3.83}$$

$$Q_L + Q_L - Q_{E^c} = 0 \quad \text{from } (\mathbf{\Lambda}_{E^k})_{ij} \tag{3.84}$$

$$Q_L + Q_Q - Q_{D^c} = 0 \quad \text{from } (\mathbf{\Lambda}_{D^k})_{ij} \tag{3.85}$$

	$\mathrm{SU}(3)_C$	$\mathrm{SU}(2)_L$	$\mathrm{U}(1)_Y$	$\mathrm{U}(1)_{\mathrm{PQ}}$
Q_i	3	2	1/3	Q_Q
U_i^c	$\bar{3}$	1	$-4/3$	Q_{U^c}
D_i^c	$\bar{3}$	1	2/3	Q_{D^c}
L_i	1	2	-1	Q_L
E_i^c	1	1	2	Q_{E^c}
H_2	1	2	1	Q_{H_2}
H_1	1	2	-1	Q_{H_1}
$\Phi_{\tilde{a}}$	1	1	0	Q_Φ

Table 3.1: Family universal charge assignments for the chiral superfields, including the field $\Phi_{\tilde{a}}$ which contains the axion, the saxion and the axino. $i = 1, 2, 3$ is the family index.

In this paper, we focus on the terms $(\mathbf{\Lambda}_{E^k})_{ij} L_i L_j \bar{E}_k$, leading to Eq. (3.84). We then have six equations [Eq. (3.79)–Eq. (3.84)] for the eight unknowns of Table 3.1. However not all of these are independent, as by our assumption $Q_L = Q_{H_1}$. We can thus express all charges in terms of three, which can for example be chosen as Q_{H_1}, Q_Q and $Q_{\tilde{a}}$.

$$
\begin{aligned}
Q_L &= Q_{H_1} && (3.86)\\
Q_{H_2} &= -Q_{\tilde{a}} - Q_{H_1} && (3.87)\\
-Q_{E^c} &= 2Q_{H_1} && (3.88)\\
-Q_{D^c} &= Q_Q + Q_{H_1} && (3.89)\\
-Q_{U^c} &= Q_Q - Q_{\tilde{a}} - Q_{H_1} && (3.90)
\end{aligned}
$$

The three independent charges should then be fixed in order to guarantee, that the SU(2) term does not contribute analogously to Eqs. (3.33) and (3.35).

4 The Renormalization Group Equations

4.1 New RGEs due to the DFSZ axino

In the following, we embed our B_3 model, including the axion, in mSUGRA [13]. We focus on the axion and axino couplings discussed above. Furthermore, we add one and only one of the lepton number violating operators

$$W_{LL\bar{E}} = \frac{1}{2}(\mathbf{\Lambda}_{E^k})_{ij}\epsilon_{ab}L_i^a L_j^b \bar{E}_k \tag{4.1}$$

at the unification scale. We defer the discussion of the effects of the $LQ\bar{D}$ operator after the quantitative analysis in the next section. The assumption of exactly one such operator is made mostly for simplicity. However, note that there is a similar hierarchy of Yukawa couplings in the SM. We thus just consider one R-parity violating coupling $\mathbf{\Lambda} \in \{(\mathbf{\Lambda}_{E^k})_{ij}\}$ at the unification scale at a time. As we shall see, the RGEs then generate further couplings at the weak scale. In our supersymmetric axion model, we have two further relevant parameters: the axino mass, $m_{\tilde{a}}$, as well as the PQ breaking scale f_{PQ}. We fix the latter at $f_{PQ} = 10^{11}\,\mathrm{GeV}$, *cf.* Eq. (3.12). We thus have the folllowing seven parameters at the unification scale

$$M_0,\, M_{1/2},\, A_0,\, \tan\beta,\, \mathrm{sgn}(\mu),\, \mathbf{\Lambda},\, m_{\tilde{a}}\,. \tag{4.2}$$

In order to obtain predictions at the weak scale we must employ the RGEs. We shall use the results and the notation of Ref. [37], which were applied to the R-parity violating case in Refs. [38, 35].

The general expression for the one-loop RGEs for the superpotential Yukawa couplings is given by

$$\frac{\mathrm{d}}{\mathrm{d}t}Y^{ijk} = Y^{ijp}\left[\frac{1}{16\pi^2}\gamma_p^k\right] + (k \leftrightarrow i) + (k \leftrightarrow j)\,, \tag{4.3}$$

with the anomalous dimensions

$$\gamma_i^j \equiv \frac{1}{2}Y_{ipq}Y^{jpq} - 2\delta_i^j \sum_a g_a^2 C_a(i). \tag{4.4}$$

Here $C_a(f)$ is the quadratic Casimir of the representation f of the gauge group G_a and the summation over repeated indices is implied. g_a is the corresponding gauge coupling. The anomalous dimensions for the MSSM chiral superfields including R-parity violation

are given upto 2-loop in Refs. [38, 35]. See also Refs. [147, 148, 149, 150]. We employ only the one-loop results. However, we must extend these results to the couplings c_1 of Eq. (3.37) and c_2^i of Eq. (3.39). For this we need the anomalous dimension of the $\Phi_{\tilde{a}}$ chiral superfield, given here at one-loop

$$\gamma_\Phi^\Phi = 2(c_1)^* c_1 + 2(c_2^i)^* c_2^i \,, \tag{4.5}$$

where we have introduced the notation:

$$Y^{H_1^a H_2^b \Phi} = \varepsilon^{ab} c_1, \tag{4.6}$$

$$Y^{L_i^a H_2^b \Phi} = \varepsilon^{ab} c_2^i \,. \tag{4.7}$$

c_1, c_2^i are trilinear couplings and thus enter in part of the anomalous dimensions of the other chiral superfields. This is in contrast to the former bilinear couplings μ and κ^i. We state here only the four changed one-loop anomalous dimensions. For completeness we present the entire set of expressions in Appendix C.

$$\gamma_{L_j}^{L_i} = \Big(\mathbf{Y}_E \mathbf{Y}_E^\dagger\Big)_{ij} + (\mathbf{\Lambda}_{E^q} \mathbf{\Lambda}_{E^q}^\dagger)_{ij} + 3(\mathbf{\Lambda}_{D^q} \mathbf{\Lambda}_{D^q}^\dagger)_{ij} - \delta_j^i \Big[\frac{3}{10} g_1^2 + \frac{3}{2} g_2^2\Big] + (c_2^j)^* c_2^i, \tag{4.8}$$

$$\gamma_{H_1}^{H_1} = -\mathrm{Tr}\left(3\mathbf{Y}_D \mathbf{Y}_D^\dagger + \mathbf{Y}_E \mathbf{Y}_E^\dagger\right) - \left(\frac{3}{10} g_1^2 + \frac{3}{2} g_2^2\right) + (c_1)^* c_1 \,, \tag{4.9}$$

$$\gamma_{H_2}^{H_2} = -3\mathrm{Tr}\left(\mathbf{Y}_U \mathbf{Y}_U^\dagger\right) - \left(\frac{3}{10} g_1^2 + \frac{3}{2} g_2^2\right) + (c_1)^* c_1 + (c_2^i)^* c_2^i \,, \tag{4.10}$$

$$\gamma_{L_i}^{H_1} = (\gamma_1)_{H_1}^{L_i\ *} = -3(\mathbf{\Lambda}_{D^q}^* \mathbf{Y}_{D^q})_{iq} - (\mathbf{\Lambda}_{E^q}^* \mathbf{Y}_E)_{iq} + (c_2^i)^* c_1 \,. \tag{4.11}$$

Now, we have all the tools for the RGE derivation of the Yukawa couplings c^α of Eq. (3.42). We start with the version in explicit components:

$$W_{\mathrm{B}_3}^{\tilde{a}} = \varepsilon^{ab}\big(c_1 \Phi_{\tilde{a}} H_1^a H_2^b + c_2^i \Phi_{\tilde{a}} L_i^a H_2^b\big) \tag{4.12}$$

Thus we obtain:

$$16\pi^2 \frac{\mathrm{d}}{\mathrm{d}t} c_1 = c_1\big(\gamma_{H_2}^{H_2} + \gamma_\Phi^\Phi + \gamma_{H_1}^{H_1}\big) + c_2^i \gamma_{L_i}^{H_1} \tag{4.13}$$

with the γ's listed above. For the second trilinear term we get:

$$16\pi^2 \frac{\mathrm{d}}{\mathrm{d}t} c_2^i = c_2^i\big(\gamma_\Phi^\Phi + \gamma_{H_2}^{H_2}\big) + c_1 \gamma_{H_1}^{L_i} + c_2^p \gamma_{L_p}^{L_i}. \tag{4.14}$$

We use the analogous procedure for the derivation of the soft-supersymmetry breaking Yukawa couplings, starting with

$$\mathscr{L}_{\tilde{a},\mathrm{soft}} \supset \varepsilon_{ab}\big(\tilde{B}_{\tilde{a}} \varphi_{\tilde{a}} \widetilde{\mathcal{L}}^a H_2^b + \tilde{D}_{\tilde{a},i} \varphi_{\tilde{a}} \widetilde{\mathcal{L}}_i^a H_2^b\big) + \mathrm{h.c.} \tag{4.15}$$

In Ref. [151], Jack, Jones and Pickering present a very elegant method to calculate the soft symmetry breaking RGEs

$$16\pi^2 \frac{\mathrm{d}\boldsymbol{h}^{ijk}}{\mathrm{d}t} = \gamma_l^i \boldsymbol{h}^{jkl} + \gamma_l^j \boldsymbol{h}^{ikl} + \gamma_l^k \boldsymbol{h}^{jil} - 2(\gamma_1)_l^i \mathbf{Y}^{jkl} - 2(\gamma_1)_l^j \mathbf{Y}^{ikl} - 2(\gamma_1)_l^k \mathbf{Y}^{jil}, \tag{4.16}$$

with

$$(\gamma_1)^i_j \equiv O\gamma^i_j, \tag{4.17}$$

and O is an operator given by

$$O \equiv \left(M_a g_a^2 \frac{\partial}{\partial g_a^2} - \boldsymbol{h}^{lmn} \frac{\partial}{\partial \boldsymbol{Y}^{lmn}} \right) . \tag{4.18}$$

So with Eq. (4.16) we obtain:

$$\begin{aligned} 16\pi^2 \frac{\mathrm{d}\tilde{B}_{\tilde{a}}}{\mathrm{d}t} &= \gamma^\Phi_\Phi \tilde{B}_{\tilde{a}} + \gamma^{H_1}_{H_1} \tilde{B}_{\tilde{a}} + \gamma^{H_1}_{L_i} \tilde{D}_{\tilde{a},i} + \gamma^{H_2}_{H_2} \tilde{B}_{\tilde{a}} - 2(\gamma_1)^\Phi_\Phi c_1 - 2(\gamma_1)^{H_1}_{H_1} c_1 \\ &\quad -2(\gamma_1)^{H_1}_{L_i} c_2^i - 2(\gamma_1)^{H_2}_{H_2} c_1 \, . \end{aligned} \tag{4.19}$$

For the second trilinear term we get

$$\begin{aligned} 16\pi^2 \frac{\mathrm{d}\tilde{D}_{\tilde{a},i}}{\mathrm{d}t} &= \gamma^\Phi_\Phi \tilde{D}_{\tilde{a},\,i} + \gamma^{L_i}_{H_1} \tilde{B}_{\tilde{a}} + \gamma^{H_2}_{H_2} \tilde{D}_{\tilde{a},\,i} + \gamma^{L_i}_{L_j} \tilde{D}_{\tilde{a},\,j} - 2(\gamma_1)^\Phi_\Phi c_2^i - 2(\gamma_1)^{L_i}_{H_1} c_1 - 2(\gamma_1)^{H_2}_{H_2} c_2^i \\ &\quad -2(\gamma_1)^{L_i}_{L_j} c_2^j. \end{aligned} \tag{4.20}$$

In addition, you can find the explicit result in the notation of Ref. [37] in Appendix C. We have compared the explicit expression of both calculations and they agree. In the next section we numerically compare the new RGEs with the old ones.

4.2 Quantitative analysis of c^α

The additional new Yukawa couplings play a crucial role for the axino interactions and enter the axino-higgsino-neutrino matrix respectively. This is our motivation to study them in more detail. In particular, we would like to investigate, whether the inclusion of the axion chiral superfield and the resultant shift from the bi–linear interactions Eq. (3.38), (3.40) to the tri–linear interactions Eq. (3.42), has any effect on the low–energy spectrum and couplings.

For an explicit numerical evaluation, we see from the expression for the RGE of c^α in Appendix C, that the couplings $\mathbf{Y}_F$ as well as $\mathbf{\Lambda}_{F^k}$, $F = E, U, D$ are involved. For the Higgs Yukawa matrices, $\mathbf{Y}_F$, we shall assume only the third generation terms contribute [4]

$$(\mathbf{Y}_E)_{33} = y_\tau, \quad (\mathbf{Y}_U)_{33} = y_t, \quad (\mathbf{Y}_D)_{33} = y_b. \tag{4.21}$$

In this first analysis, we ignore the mixing in the quark sector, for simplicity. In general it has to be included [35, 152].

For the $\mathbf{\Lambda}$ couplings upper bounds are given for example in Ref. [35, 122]. The $\mathbf{\Lambda}_{E^k}$ or $\mathbf{\Lambda}_{D^k}$ trilinear couplings are at the most of $\mathcal{O}(0.1)$ at M_{GUT}. So as a first approximation we can neglect quadratic terms in the $\mathbf{\Lambda}$'s. Introducing these simplifications the one-loop

anomalous dimensions read:

$$\begin{aligned}
\gamma_{L_3}^{L_3} &= (\mathbf{Y}_E)_{33}^2 - \Big[\frac{3}{10}g_1^2 + \frac{3}{2}g_2^2\Big] + (c_2^3)^2, \\
\gamma_{E_3}^{E_3} &= 2\left(\mathbf{Y}_E^\dagger \mathbf{Y}_E\right)_{33} - \frac{6}{5}g_1^2 \\
\gamma_{Q_3}^{Q_3} &= (\mathbf{Y}_D)_{33}^2 + (\mathbf{Y}_U)_{33}^2 - \big[\frac{1}{30}g_1^2 + \frac{3}{2}g_2^2 + \frac{8}{3}g_3^2\Big], \\
\gamma_{D_3}^{D_3} &= 2\,(\mathbf{Y}_D)_{33}^2 - \Big[\frac{2}{15}g_1^2 + \frac{8}{3}g_3^2\Big], \\
\gamma_{U_3}^{U_3} &= 2\,(\mathbf{Y}_U)_{33}^2 - \Big[\frac{8}{15}g_1^2 + \frac{8}{3}g_3^2\Big], \\
\gamma_{H_1}^{H_1} &= -\left(3\mathbf{Y}_D^2 + \mathbf{Y}_E^2\right)_{33} - \left(\frac{3}{10}g_1^2 + \frac{3}{2}g_2^2\right) + (c_1)^* c_1 \\
\gamma_{H_2}^{H_2} &= -3\,(\mathbf{Y}_U)_{33}^2 - \left(\frac{3}{10}g_1^2 + \frac{3}{2}g_2^2\right) + (c_1)^* c_1 + (c_2^i)^* c_2^i\,, \\
\gamma_{L_i}^{H_1} &= (\gamma_1)_{H_1}^{L_i\,*} = -3(\mathbf{\Lambda}_{D^q}^* \mathbf{Y}_D)_{iq} - (\mathbf{\Lambda}_{E^q}^* \mathbf{Y}_E)_{iq} + (c_2^i)^* c_1, \qquad (4.22)
\end{aligned}$$

Eq. (4.22) shows in comparison with Eq. (C.9) of Appendix C, that we have to specify our choice of $\mathbf{\Lambda}$ to proceed further. As an example we choose

$$(\mathbf{\Lambda}_{E^3})_{13} \neq 0, \qquad (4.23)$$

at the GUT scale. This implies that we can neglect the remaining down-quark coupling. It is a few orders of magnitude smaller than $(\mathbf{\Lambda}_{E^3})_{13}$. Collecting all these conditions we get for the RGE for c_1

$$\begin{aligned}
16\pi^2 \frac{\mathrm{d}}{\mathrm{d}t} c_1 &= c_1\Big[3\,(\mathbf{Y}_U)_{33}^2 + 3\,(\mathbf{Y}_D)_{33}^2 + (\mathbf{Y}_E)_{33}^2 - \left(\frac{3}{5}g_1^2 + 3g_2^2\right) + 4c_1^* c_1 + 3(c_2^j)^* c_2^j\Big] \\
&\quad + c_2^1\Big[-(\mathbf{\Lambda}_{E^3}^* \mathbf{Y}_E)_{13} + (c_2^1)^* c_1\Big]. \qquad (4.24)
\end{aligned}$$

This RGE is coupled to c_2^1. All the introduced simplifications give for the corresponding RGE involving c_2^1:

$$\begin{aligned}
16\pi^2 \frac{\mathrm{d}}{\mathrm{d}t} c_2^1 &= c_2^1\Big[3\,(\mathbf{Y}_U)_{33}^2 - \left(\frac{3}{10}g_1^2 + \frac{3}{2}g_2^2\right) + 3c_1^* c_1 + 3(c_2^j)^* c_2^j\Big] \qquad (4.25) \\
&\quad + c_1\Big[-(\mathbf{\Lambda}_{E^3}^* \mathbf{Y}_E)_{13} + (c_2^1)^* c_1\Big] + c_2^j\Big[-\delta_j^1\left(\frac{3}{10}g_1^2 + \frac{3}{2}g_2^2\right) + (c_2^j)^* c_2^1\Big].
\end{aligned}$$

We see that both equations are also coupled to the remaining c_2^i, as we have not evaluated sum over j. But we will not consider c_2^2 and c_2^3. The reason is that we have seen that the c_2^i have to match at M_Z with the former bilinear couplings. For the chosen trilinear Yukawa coupling $(\mathbf{\Lambda}_{E^3})_{13}$ and the later stated parameter space point for our analysis, we anticipate that c_2^2 and c_2^3 are equal to zero at all scales. Of course, this changes in

dependence of the choices of the couplings, parameter space or SUSY benchmark points, respectively. So we can set $j = 1$ and continue with the MSSM Yukawa coupling RGE:

$$16\pi^2 \frac{\mathrm{d}}{\mathrm{d}t}(\mathbf{Y}_E)_{33} = (\mathbf{Y}_E)_{33}\Big[4(\mathbf{Y}_E)^2_{33} + 3(\mathbf{Y}_D)^2_{33} - \frac{9}{5}g_1^2 - 3g_2^2\Big], \tag{4.26}$$

$$16\pi^2 \frac{\mathrm{d}}{\mathrm{d}t}(\mathbf{Y}_D)_{33} = (\mathbf{Y}_D)_{33}\Big[6(\mathbf{Y}_D)^2_{33} + (\mathbf{Y}_E)^2_{33} + (\mathbf{Y}_U)^2_{33} - \frac{7}{15}g_1^2 - 3g_2^2 - \frac{16}{3}g_3^2\Big], \tag{4.27}$$

$$16\pi^2 \frac{\mathrm{d}}{\mathrm{d}t}(\mathbf{Y}_U)_{33} = (\mathbf{Y}_U)_{33}\Big[6(\mathbf{Y}_U)^2_{33} + (\mathbf{Y}_U)^2_{33} - \frac{13}{15}g_1^2 - 3g_2^2 - \frac{16}{3}g_3^2\Big]. \tag{4.28}$$

For the three gauge couplings g_i we have within the MSSM in one-loop order, see Ref. [37]

$$16\pi^2 \frac{\mathrm{d}}{\mathrm{d}t} g_i^2 = b_i g_i^3, \tag{4.29}$$

with $b_i = \{33/5, 1, -3\}$ for $i = 1, 2, 3$. The RGE for the trilinear $\not{R}_p$ Yukawa couplings are given by

$$16\pi^2 \frac{\mathrm{d}}{\mathrm{d}t}(\mathbf{\Lambda}_{E^3})_{13} = (\mathbf{\Lambda}_{E^3})_{13}\Big[4(\mathbf{Y}_E)^2_{33} - \frac{9}{5}g_1^2 - 3g_2^2\Big]. \tag{4.30}$$

In total we have nine coupled differential equations which we want to evaluate numerically. For this purpose we need initial values to start with. To get these we will use the program `SOFTSUSY3.0` that calculates the superparticle spectrum in the MSSM [39]. `SOFTSUSY3.0` needs as input the MSSM scenario and the according input parameters - in our case it is mSUGRA.

As mentioned above, mSUGRA has five free parameters. We will focus on the widely studied benchmark point SPS1a [36] with $M_0 = 100$ GeV, $M_{1/2} = 250$ GeV, $A_0 = -100$ GeV, $\tan\beta = 10$ and $\mathrm{sgn}(\mu) = +1$. Using these parameters we computed the initial values for the differential equation at M_Z. The last needed parameter is $(\mathbf{\Lambda}_{E^3})_{13}$ which has an upper bound of 2.6×10^{-5} see Ref. [35].

Table 4.1: Comparison of our results from Eqs. (4.26)-(4.28) with SOFTSUSY3.0 for two RG scales

	$Q = 1 \times 10^5$ GeV		$Q = 1 \times 10^8$ GeV	
	Eq.[4.26-4.28]	`SOFTSUSY`	Eq.[4.26-4.28]	`SOFTSUSY`
$(\mathbf{Y}_E)_{33}$	$9.55 \cdot 10^{-2}$	$9.56 \cdot 10^{-2}$	$8.86 \cdot 10^{-2}$	$8.87 \cdot 10^{-2}$
$(\mathbf{Y}_D)_{33}$	$1.11 \cdot 10^{-2}$	$1.10 \cdot 10^{-1}$	$8.72 \cdot 10^{-2}$	$8.69 \cdot 10^{-2}$
$(\mathbf{Y}_U)_{33}$	$7.80 \cdot 10^{-1}$	$7.81 \cdot 10^{-1}$	$6.87 \cdot 10^{-1}$	$6.88 \cdot 10^{-1}$
$(\mathbf{\Lambda}_{E^3})_{13}$	$3.61 \cdot 10^{-5}$	$3.61 \cdot 10^{-5}$	$3.34 \cdot 10^{-5}$	$3.34 \cdot 10^{-5}$

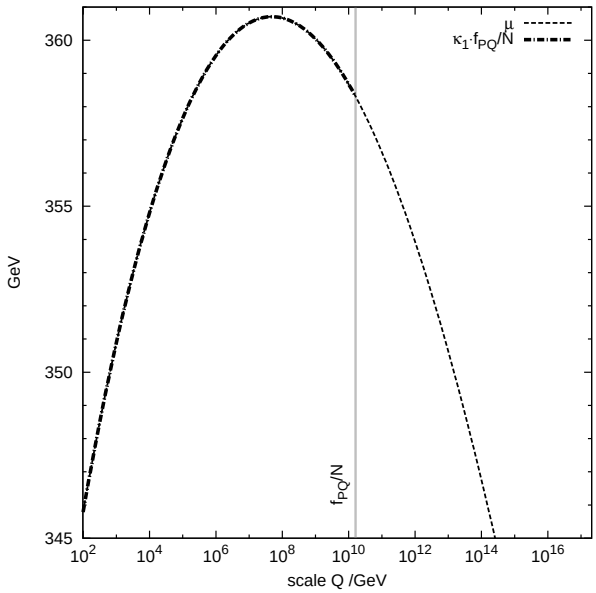

Figure 4.1: Bilinear coupling μ compared to axino trilinear c_1. The gray line indicates the Peccei-Quinn breaking scale which was chosen in this example $f_{\rm PQ} = 10^{11}$ GeV. Beyond this line we have not evaluated the c_1 coupling as there takes a phase transition place which is not part of this work.

With these values we have solved independently the RGEs of `SOFTSUSY3.0` by using our approximate RGEs equation (4.24)-(4.30). We now compare both solutions. But of course the solutions of c_1 and c_2^1 cannot be compared directly with μ and κ^i as they have a priori a different order of magnitude due to $f_{\rm PQ}$.

However, considering our solutions of the 'usual' Yukawa couplings from Eqs. (4.26)-(4.30) and the computation of `SOFTSUSY3.0` we can conlcude that they are in total agreement. In table 4.1 we have summarized two sets of values estimated with `SOFTSUSY3.0` and with our program. Without loss of generality we have chosen for the comparison the RGE scale values $Q = 10^5, 10^8$ GeV and we see that both sets agree[1]. However keeping this agreement in mind we focus now on the c_1 and c_2^1.

We have solved the RGE for both couplings. Now, we want to compare c_1 and μ see Fig. 4.1 and c_2^1 with κ as a function of Q the RG scale, see Fig. 4.2. For a better comparability we have multiplied the trilinear axino coupling c_1 with PQ breaking scale, see also Eq. (3.38). We see that both values match. The reason is the smallness of the c_1 coupling on the right hand side of Eq. (4.24) which is suppressed by $f_{\rm PQ}$. So we can neglect higher orders of c_1 in the RGE. If we do so Eq. (4.24) simplifies and reduces to:

$$16\pi^2 \frac{\mathrm{d}}{\mathrm{d}t} c_1 \;=\; c_1 \Big[3\left(\mathbf{Y}_U\right)^2_{33} + 3\left(\mathbf{Y}_D\right)^2_{33} + \left(\mathbf{Y}_E\right)^2_{33} - \left(\frac{3}{5} g_1^2 + 3 g_2^2\right) \Big] - c_2^1 (\mathbf{\Lambda}^*_{E^3} \mathbf{Y}_E)_{13}. \tag{4.31}$$

This equation has basically the identical structure like the μ RGE [153] except for the

[1] We have checked the values at further scales and they agree to the same precision.

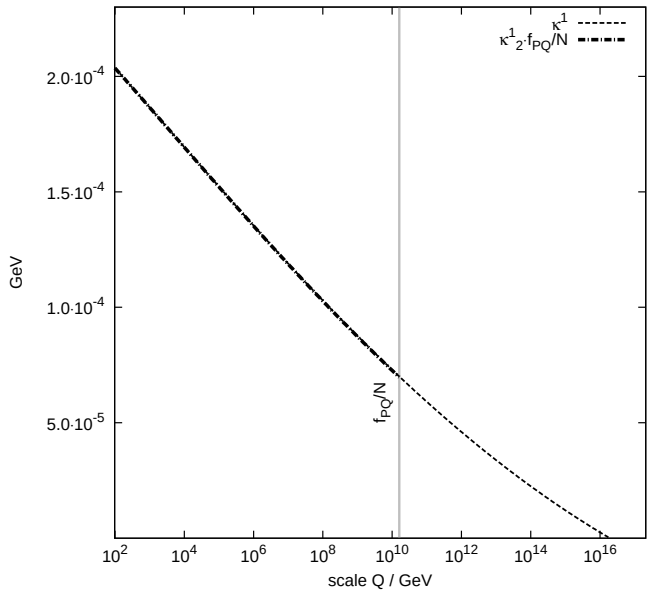

Figure 4.2: Bilinear coupling κ compared to axino trilinear c_2^1. The gray line indicates the Peccei-Quinn breaking scale which was chosen in this example $f_{\mathrm{PQ}} = 10^{11}$ GeV. Beyond this line we have not evaluated the c_1 coupling as there takes a phase transition place which is not part of this work.

constant factor f_{PQ}.

We get a similar result for c_2^1 - see Fig. 4.2. Here the same argumentation holds like in the previous case. Simplifying Eq. (4.25) we get again the same structure for the RGE as for κ, see Ref. [153].

A consequence of these considerations is that we can in general neglect higher orders of c_1 and c_2^i in the RGE. Obtaining the same RGE structure as in the non-axino case we can use `SOFTSUSY3.0` for detailed analysis of the MSSM mSUGRA parameter space with the focus on the axino. Of course, the analysis holds up to a value of $M = f_{\mathrm{PQ}}$ as mentioned above for higher values a phase transition takes place and thereby the framework changes. Note that in the case of the $LQ\bar{D}$ operator we have a similar structure of the RGE. Thus a analogous procedure would return the same results from which can conclude that `SOFTSUSY3.0` can be used here as well.

5 Axino–LSP Decays

As discussed in Sect. 3.2.4, the axino mass can range from a few keV up to several GeV. Even at the upper end it is lighter than the other supersymmetric particles[1]. And we explicitly check this, in our numerical computations of the supersymmetric spectrum, below. We assume the gravitino mass is of order 100 GeV. Thus the axino is the LSP in our models. In B_3 mSUGRA models the LSP is not stable, and thus the axino decays. These decays have previously been studied in Refs. [29, 87, 86, 26]. There the DFSZ axino and its lifetime have been considered in the context of cosmological [29] or observational bounds [87, 86]. The authors focused on specific decay modes, depending on the physical problem they were addressing. In Ref. [29, 87] the authors have given estimates of the axino lifetime in $\not{R}_p$ breaking models with $\mathbf{\Lambda}_{\rm E} \neq 0$ and by a specific $\not{R}_p$ bilinear term, respectively. Ref. [86] concentrates on the 511 keV line from the galactic bulge, and looks for an appropriate axino decay mode. In contrast to these works, we provide a systematic analysis of all the leading axino decays, having embedded our supersymmetric axion sector in the general B_3 mSUGRA model. We thus consider all two- and three-body decay modes that arise from the operators introduced in Sect. 3.2. We compute the branching ratios as a function of the $\not{R}_p$ and axino input parameters. For definiteness we fix the other supersymmetric parameters to the benchmark point SPS1a [36].

For a light axino, $m_{\tilde{a}} \lesssim 500\,\mathrm{MeV}$, we discuss in detail the following decay modes, some of which result from more than one operator

$$\begin{aligned}
\tilde{a} &\to \nu + \gamma\,, && (5.1)\\
\tilde{a} &\to M^0 + \nu\,, \quad \text{with } M^0 = \pi^0, K^0\,, && (5.2)\\
\tilde{a} &\to M^\pm + \ell^\mp\,, \quad \text{with } M^0 = \pi^\pm, K^\pm\,, && (5.3)\\
\tilde{a} &\to \nu + \ell^+ + \ell^-\,, && (5.4)\\
\tilde{a} &\to \nu + \nu + \bar{\nu}\,. && (5.5)
\end{aligned}$$

Here $\nu = \nu_e$, ν_μ, ν_τ indicates the three possible neutrino flavours. We then comment on additional modes, which open for larger axino masses. In the following calculations of the decay amplitudes we apply the two component notation and rules presented in Ref. [78], as well as the additional axino couplings discussed in Sect. 3.2. Furthermore we neglect the mass of the electron. However, due to the mass restriction on the axino the tau is excluded as a final state lepton.

Note that decays which have identical final states in general interfere. However, we will calculate all amplitudes as well as decay widths individually. The reason is that as already

[1] We do not consider a possibly very light neutralino [130], since the experimental constraints were determined for at most very weak R-parity violation.

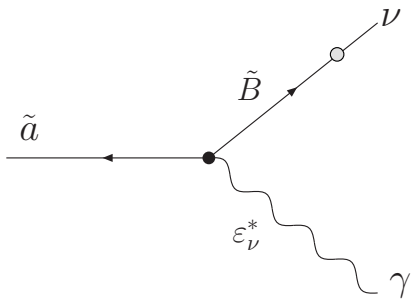

Figure 5.1: Axino decay to a photon and a neutrino. The gray dot indicates the Bino-neutrino mixing. Here $\nu = \nu_e$, ν_μ, ν_τ is possible.

pointed out authors of previous works were focussing on very specific decay channels, *cf.* Refs [26, 29, 86, 87]. Using our approach and computing the BR in the next chapter we will be able to conclude which specific decay channel is the dominant one and which one can be neglected. In cases of non-negligible contributions of two decays with the same final states we will comment on interference in the text.

5.1 Axino Decay $\tilde{a} \to \nu + \gamma$

The radiative axino decay mode, Eq. (5.1), follows from the supersymmetrized version of the axion interaction Eq. (3.35), see also Fig. 5.1. As discussed in Sect. 3.2.5, the neutralino mixes with the three neutrinos, leading to a mixing matrix element N^*_{i1} with $i = 5, 6, 7$. This we compute using the program `SOFTSUSY`. Furthermore the hypercharge gauge boson, B_μ, has a photon component, slightly suppressed by $\cos\theta_W$,

$$B_\mu = \cos\theta_\mathrm{w} A_\mu - \sin\theta_\mathrm{w} Z_\mu \,. \tag{5.6}$$

Using $a_Y = g'^2/4\pi$ and $g' = e/\cos\theta_\mathrm{w}$ as well as the Feynman rules presented in section 3.2.2 we obtain for the amplitude

$$\mathrm{i}\mathcal{M} \;=\; \frac{\alpha\, C_{aYY} N_{i1}}{4\pi\cos\theta_W (f_\mathrm{PQ}/N)} x(p_{\tilde{a}}) k_\mu \sigma^{\mu\nu} y(p_\nu) \varepsilon^*_\nu \,. \tag{5.7}$$

The momenta were denoted according to the particle letters in the subscript. To avoid confusion with the Lorentz index we introduced k_μ for the photon momentum. Here α is the fine structure constant. Squaring the matrix element and averaging over the incoming- and summing over the outgoing spins we get

$$\frac{1}{2}\sum_\mathrm{spins} |\mathcal{M}_1|^2 \;=\; \frac{\alpha^2\, C^2_{aYY} |N_{i1}|^2}{2\pi^2 \cos^2\theta_W (f_\mathrm{PQ}/N)^2} (p_{\tilde{a}} \cdot k)(p_\nu \cdot k) \,. \tag{5.8}$$

Evaluating the momenta in the rest frame of the axino and using the known formula for the two body decay, see Eq. (A.14) and Ref. [48] we get for the decay width

$$\Gamma_1 = \frac{\alpha^2 C^2_{aYY} |N_{i1}|^2}{128 \cos^2\theta_\mathrm{w} \pi^3 (f_\mathrm{PQ}/N)^2} m^3_{\tilde{a}} \,, \tag{5.9}$$

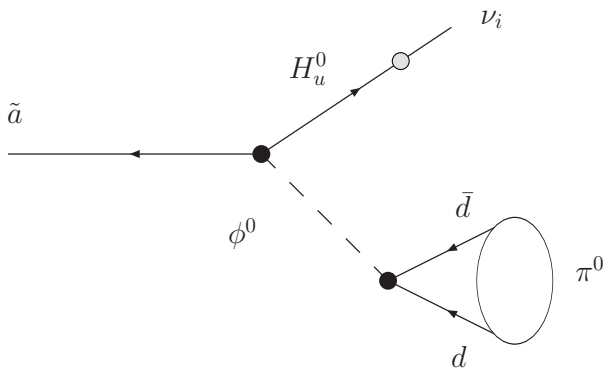

Figure 5.2: Axino decay via a neutral pion and a neutrino. The small gray dot indicates the Higgsino-neutrino mixing with $i = e, \mu, \tau$. The white dot indicates the bound state of the pion. The Higgs represents both mass eigentstates $\phi^0 = (h^0, H^0)$. For the decay width see Γ_2.

with $i = 5, 6, 7$. Note that the Bino mixes with all neutrino families and therefore the diagram in Fig. 5.1 represents in total three decay modes depending on the neutrino flavor.

Note, by coupling the photon to an e^+e^--pair, we can get a contribution to the purely leptonic axino decay mode, Eq. (5.4). However, this is suppressed by α^2 and we thus neglect it.

5.2 The Decay $\tilde{a} \to M^0 \nu_i$

The mesonic decay channel can be realized in different ways. As indicated in Eqs. (5.2) and (5.3), we can have a neutral or charged pion in the final state. Of course, other scalar mesons can be formed as well. But with axino masses below 500 MeV only the pion and the kaon are present.

In Fig. 5.2 we present the first diagram with a neutral pion. The axino couples to an uncharged up type higgsino and a down type higgs. The Higgs itself couples to a $d-\bar{d}$-pair which then form a neutral pion. For the derivation of the pseudoscalar matrix element see, *e.g.* Ref. [154]. This diagram has its origin in the $\Phi_{\tilde{a}} H_2 H_1$ operator.

The diagram in Fig. 5.2 is not unique as we can reverse the arrows independently for each vertex. However, the ϕ^0 denotes one of the two CP even eigenstate – $\phi^0 = (h^0, H^0)$. If we consider both eigenstates and the reversibility of the arrows we get in total eight diagrams which interfere. The higgs-quark vertex factor can be found in Ref. [78]. The connected quarks can form a bound states to a neutral pion – π^0.

The corresponding amplitudes are given by

$$\mathcal{M}_a = \mathrm{i} x^\dagger(p_\nu)(-\mathrm{i}c_1) y^\dagger(p_{\tilde{a}}) \frac{N_{i3}}{M^2_{\phi^0}} \left(-\frac{\mathrm{i}}{\sqrt{2}} Y_d k_{d\phi^0}\right) \frac{1}{\sqrt{2}} \left(\frac{m_\pi^2 f_\pi}{2 m_d}\right) \tag{5.10}$$

$$\mathcal{M}_b = \mathrm{i} x^\dagger(p_\nu)(-\mathrm{i}c_1) y^\dagger(p_{\tilde{a}}) \frac{N_{i3}}{M^2_{\phi^0}} \left(-\frac{\mathrm{i}}{\sqrt{2}} Y_d k_{d\phi^0}\right) \frac{1}{\sqrt{2}} \left(\frac{m_\pi^2 f_\pi}{2 m_d}\right) \tag{5.11}$$

$$\mathcal{M}_c = \mathrm{i}y(p_\nu)(\mathrm{i}c_1)x(p_{\tilde{a}})\frac{N_{i3}}{M^2_{\phi^0}}\left(-\frac{\mathrm{i}}{\sqrt{2}}Y_d k_{d\phi^0}\right)\frac{1}{\sqrt{2}}\left(\frac{m_\pi^2 f_\pi}{2m_d}\right) \tag{5.12}$$

$$\mathcal{M}_d = \mathrm{i}y(p_\nu)(\mathrm{i}c_1)x(p_{\tilde{a}})\frac{N_{i3}}{M^2_{\phi^0}}\left(-\frac{\mathrm{i}}{\sqrt{2}}Y_d k_{d\phi^0}\right)\frac{1}{\sqrt{2}}\left(\frac{m_\pi^2 f_\pi}{2m_d}\right), \tag{5.13}$$

where a, b, c and d imply the matrix elements of the four different Feynman diagrams. The differences between a and b (c and d) are that the arrows are reversed for the quarks (axino and neutrino). Furthermore N_{i3} denotes the mixing angle of the higgsino and one of the three neutrino flavors. $k_{d\phi^0_{h^0,H^0}}$ are the mixing angles between the Higgs gauge- and mass eigenstate, see Ref. [78], and $M_{\phi^0_{h^0,H^0}}$ are the corresponding masses. Y_d is the Yukawa coupling. The pion decay constant and the down quark mass m_d is due to the fact that we have integrated out the pseudoscalar pion state, see Ref. [154, 155]. This leads to the fact that the first and second as well as the third and fourth matrix elements are identical. Sorting and summing the terms we conclude for the squared amplitude:

$$|\mathcal{M}_{2,\mathrm{tot}}|^2 = (2\mathcal{M}_a + 2\mathcal{M}_c)(2\mathcal{M}_a^* + 2\mathcal{M}_c^*) = 4(|\mathcal{M}_a|^2 + 2\mathrm{Re}\mathcal{M}_a\mathcal{M}_c^* + |\mathcal{M}_c|^2), \tag{5.14}$$

where we have considered that the two mixed terms are identical. However, we can drop the mixed terms as they are proportional to the mass of the neutrino, which we assume to be zero. The remaining two terms are proportional to the momentum relation $(p_{\tilde{a}} \cdot p_\nu)$ and hence also identical. Thus we have:

$$\Rightarrow |\mathcal{M}_{2,\mathrm{tot}}|^2 = 8|\mathcal{M}_a|^2. \tag{5.15}$$

But, this would be the result if we have only one Higgs mass eigenstate. For the second eigenstate we obtain a similar result. We denote the second set of matrix elements by a prime. Finally we obtain:

$$|\mathcal{M}_{2,\mathrm{tot,all}}|^2 = 8(|\mathcal{M}_a|^2 + |\mathcal{M}_a^{'}|^2 + 2\mathrm{Re}\mathcal{M}_a\mathcal{M}_a^{*'}). \tag{5.16}$$

Note that the difference of the primed and unprimed amplitude is the different the mixing angle of the Higgs eigenstate k_{d,ϕ^0} and the corresponding mass in the propagator M_{ϕ^0}. A short calculation shows that the amplitude squared $|\mathcal{M}_a|^2$ reads:

$$\frac{1}{2}\sum_{\mathrm{spins}}|\mathcal{M}_a|^2 = 8\frac{|N_{i3}|^2\,|c_1|^2\,|Y_d|^2\,|k_{d\phi^0}|^2}{32M^2_{\phi^0_{h^0}}}\left(\frac{m_\pi^2 f_\pi}{m_d}\right)^2(m_{\tilde{a}}^2 - m_\pi^2). \tag{5.17}$$

Hence from this result we can easily deduce the total decay width

$$\Gamma_2 = \left[\frac{k_{d\phi^0_{h^0}}}{M^2_{\phi^0_{h^0}}} + \frac{k_{d\phi^0_{H^0}}}{M^2_{\phi^0_{H^0}}}\right]^2 \frac{|N_{i3}|^2\,|c_1|^2\,|Y_d|^2}{64\,\pi\,m_{\tilde{a}}^3}\left(\frac{m_\pi^2 f_\pi}{m_d}\right)^2(m_{\tilde{a}}^2 - m_\pi^2)^2. \tag{5.18}$$

Here we used the fact that we have a two body decay, where Eq. (A.14) can be applied, *cf.* Appendix A.2.

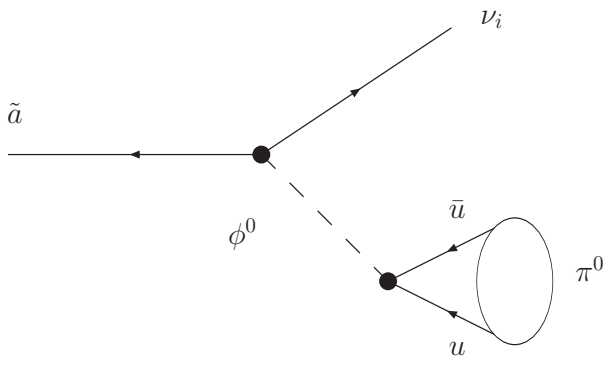

Figure 5.3: Axino decay via a neutral pion and a neutrino. The small gray dot indicates the axino-neutrino mixing with $i = e, \mu, \tau$. The white circle indicates the bound state of the pion. For further explanations see text below. The decay width is given by Γ_3.

Our next decay has identical final states but its origin is the $\Phi L_i H_2$ operator, *cf.* Eq. (3.39). The consequential Yukawa interaction allows a direct coupling of the axino to the neutrino and to an up-like higgs. In Fig. 5.3 we have drawn the related Feynman diagram. The Higgs is one of the CP even mass eigenstates h^0, H^0. Due to the up-type nature of the Higgs it couples to an up quark pair which form a π^0 bound state. However, the diagram shown in Fig. 5.3 represents three processes, as the axino couples to each neutrino family.

Similarly to the decay channel shown before, the Feynman diagram in Fig. 5.3 is not unique. For each CP-even Higgs mass eigenstate we have four diagrams, thus leading to in total eight diagrams which interfere. In an analogous procedure we find for the amplitudes

$$\mathrm{i}\mathcal{M}_{a/b} = x^\dagger(p_\nu)(\mathrm{i}c_2^i)y^\dagger(p_{\tilde{a}})\frac{1}{M^2_{\phi_0}}\left(\frac{-\mathrm{i}}{\sqrt{2}}Y_u k_{u\phi^0}\right)\frac{1}{\sqrt{2}}\left(\frac{m_\pi^2 f_\pi}{2m_u}\right), \tag{5.19}$$

$$\mathrm{i}\mathcal{M}_{c/d} = \mathrm{i}y(p_\nu)(\mathrm{i}c_2^i)x(p_{\tilde{a}})\frac{1}{M^2_{\phi_0}}\left(\frac{-\mathrm{i}}{\sqrt{2}}Y_u k_{u\phi^0}\right)\frac{1}{\sqrt{2}}\left(\frac{m_\pi^2 f_\pi}{2m_u}\right), \tag{5.20}$$

where we have integrated out the mesonic states and grouped the matrix elements. As the Higgs is of up-like charcater the mixing angles are given by $k_{u\phi^0}$ as well as the Yukawa couplings are Y_u, see *e.g.* Ref [78]. Now, following the steps of Eq. (5.14)-(5.16) the amplitude squared reads

$$\frac{1}{2}\sum_{\text{spins}}|\mathcal{M}_{3,\text{tot}}|^2 = \left[\frac{k_{u\phi^0_{h^0}}}{M^2_{\phi^0_{h^0}}} + \frac{k_{u\phi^0_{H^0}}}{M^2_{\phi^0_{H^0}}}\right]^2 \frac{|c_2^i|^2\,|Y_u|^2}{4}\left(\frac{m_\pi^2 f_\pi}{m_u}\right)^2 (m_{\tilde{a}}^2 - m_\pi^2)\,. \tag{5.21}$$

The decay width has the same structure as in the previous case and can be evaluated in the same way to

$$\Gamma_3 = \left[\frac{k_{u\phi^0_{h^0}}}{M^2_{\phi^0_{h^0}}} + \frac{k_{u\phi^0_{H^0}}}{M^2_{\phi^0_{H^0}}}\right]^2 \frac{|c_2^i|^2\,|Y_u|^2}{64\,\pi\,m_{\tilde{a}}^3}\left(\frac{m_\pi^2 f_\pi}{m_u}\right)^2 (m_{\tilde{a}}^2 - m_\pi^2)^2\,. \tag{5.22}$$

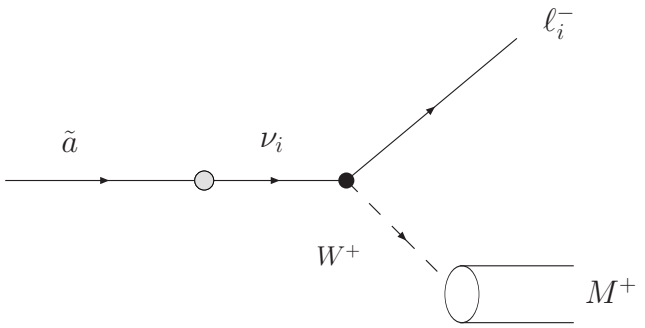

Figure 5.4: Axino decay via a meson and a lepton. The gray dot indicates the axino-neutrino mixing with $i = e, \mu, \tau$. Except of this mixing all other couplings are SM like.

This closes the section of axino decays into neutral mesons. In the next paragraph we will present decays to charged mesons.

5.3 The Decay $\tilde{a} \to \ell_i^{\pm} M^{\mp}$

5.3.1 Decay via W^+.

As seen in Sect. 3.2.2, the axino mixes with the three neutrino flavours via the operators $\Phi_{\tilde{a}} L_i H_2$. This opens up new decay channels, *e.g.* the semi-leptonic decay $\tilde{a} \to M^{\pm} + \ell^{\mp}$, where $M^{\pm} = \pi^{\pm}, K^{\pm}$, *cf.* Fig. 5.4. Modulo the axino–neutrino mixing this decay only involves SM couplings. The amplitude in two component notation is given by

$$\mathrm{i}\mathcal{M}_4 \;=\; G_F N_{i8} K_{ud} \sqrt{2} f_{M^+} p_{\mu\, M^+} y(p_\ell) \sigma^\mu y^\dagger(p_{\tilde{a}})\,. \tag{5.23}$$

Here K_{ud} denotes the CKM matrix element, N_{i8} is the relevant axino–neutrino mixing angle and G_F is the Fermi constant. The corresponding amplitude squared can be immediately computed

$$\frac{1}{2}\sum_{\text{spins}} |\mathcal{M}_4|^2 \;=\; G_F^2 f_{M^+}^2 |N_{i8}|^2 |K_{ud}|^2 \Big[(m_{\tilde{a}}^2 - m_\ell^2)^2 - m_{M^+}^2 (m_{\tilde{a}}^2 + m_\ell^2)\Big] \tag{5.24}$$

Making use of the two body decay width Eq. (A.14) presented in Appendix A.2 we obtain

$$\Gamma_4 \;=\; \frac{G_F^2 f_{M^+}^2 |N_{i8}|^2 \, |K_{ud}|^2 \, |\mathbf{p}|^2}{16\pi m_{\tilde{a}}^3} \Big[(m_{\tilde{a}}^2 - m_\ell^2)^2 - m_{M^+}^2 (m_{\tilde{a}}^2 + m_\ell^2)\Big]\,, \tag{5.25}$$

where we have introduced the momentum parameter

$$|\mathbf{p}|^2 = \sqrt{m_{\tilde{a}}^4 + m_{M^+}^4 + m_\ell^4 - 2m_{\tilde{a}}^2 m_{M^+}^2 - 2m_{\tilde{a}}^2 m_\ell^2 - 2m_\ell^2 m_{M^+}^2}\,. \tag{5.26}$$

If we consider that the lepton is an electron we can assume $m_e \ll m_{M^+} < m_{\tilde{a}}$. The decay width simplifies then to

$$\Gamma_{4e} = \frac{G_F^2 f_{M^+}^2 |N_{i8}|^2 \, |K_{ud}|^2}{16\pi m_{\tilde{a}}} (m_{\tilde{a}}^2 - m_{M^+}^2)^2\,. \tag{5.27}$$

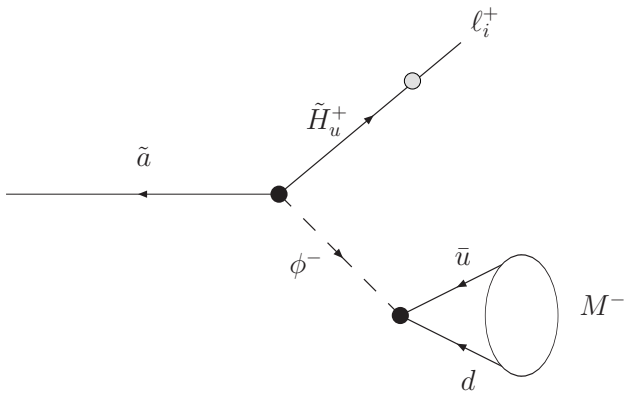

Figure 5.5: Axino decay to $M^- + \ell^+$ with $M^- = \pi^-, K^-$. The gray dot indicates the higgsino-lepton mixing with $i = e, \mu, \tau$. But $i = \tau$ is kinematically forbidden, see text. The white circle indicates the bound state of the charged meson.

Note the axino can mix with all neutrino flavors. But as the axino is assumed to be much lighter than the tau a coupling to the third lepton family in this decay channel is not present. Consequently we then have two final state possibilities per meson.

5.3.2 Decay via Charged Higgs.

We pointed out that the axino has a coupling to both Higgs doublets, *cf.* sec. 3.2.2. The Yukawa interaction in Eq. (3.43) shows an existing coupling of an axino to a charged up-like higgsino and a down-like higgs, respectively. Of course, a vice versa Higgs coupling is also possible and will be discussed as the next scenario. However, a quark pair coupling to the Higgs can form a negatively charged meson, namely a π^- or K^-. In a $\not{R}_p$ theory the positive higgsino mixes with the charged leptons, *cf.* sec. 3.2.5. In Fig. 5.5 you will find the related Feynman diagram. The corresponding amplitude is

$$\mathrm{i}\mathcal{M}_5 = \mathrm{i}\, V_{i2}\, y^\dagger(p_{\tilde{a}})(\mathrm{i}c_1)x^\dagger(p_\ell)\frac{1}{M^2_{\phi^-}}\Big(\mathrm{i}\, Y_d\, K_{ud}\, k_{d\phi^-}\Big)\frac{1}{\sqrt{2}}\frac{m^2_{M^-} f_{M^-}}{m_u + m_d}\,. \tag{5.28}$$

After squaring and averaging over incoming- and summing over outgoing spins we obtain

$$\frac{1}{2}\sum_{\text{spins}}|\mathcal{M}_5|^2 \;=\; \left(\frac{m^2_{M^-} f_{M^-}}{m_u + m_d}\right)^2 \frac{|c_1|^2\,|V_{i2}|^2\,|Y_d|^2\,|K_{ud}|^2\,|k_{d\phi^-}|^2}{4\,M^4_{\phi^-}}\left(m^2_{\tilde{a}} + m^2_\ell - m^2_{M^-}\right)\,. \tag{5.29}$$

As in the foregoing case we can compute the decay width

$$\Gamma_5 \;=\; \frac{1}{64\pi}\frac{|\mathbf{p}|^2}{m^3_{\tilde{a}}}\frac{|c_1|^2\,|V_{i2}|^2\,|Y_d|^2\,|K_{ud}|^2\,|k_{d\phi^-}|^2}{M^4_{\phi^-}}\left(\frac{m^2_{M^-} f_{M^-}}{m_u + m_d}\right)^2 (m^2_{\tilde{a}} + m^2_\ell - m^2_{M^-}) \tag{5.30}$$

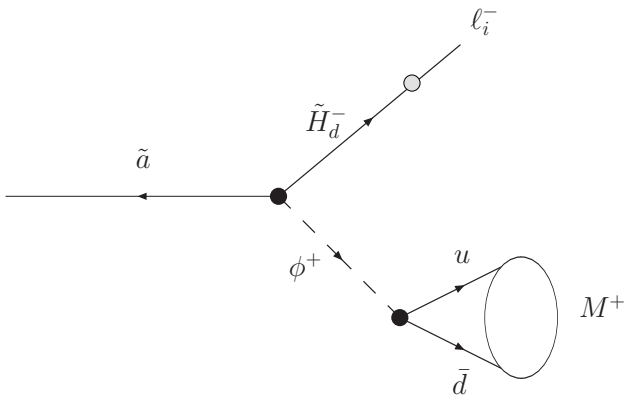

Figure 5.6: The decay is due to the $\Phi_{\tilde{a}} H_2 H_1$ operator and includes a meson $M^+ = \pi^+, K^+$. The higgssino is down-like and the Higgs is up-like, where the ϕ^+ denotes here the Higgs mass eigenstate. The grey dot indicates the higgsino-lepton mixing with $i = e, \mu, \tau$. The tauon case in kinematically forbidden, see text. The decay width is given by Γ_6.

with $|\mathbf{p}|$ defined above. Y_d is the down quark Yukawa coupling, V_{i2} is the chargino mixing angle, K_{ud} is the CKM matrix element, $k_{d\phi^-}$ is the mixing angle between the gauge- and mass eigenstate of the Higgs and M_{ϕ^-} is the related mass. This process has four different final state combinations - two per meson state. In the case of an electron in the final state this expression simplifies as we can neglect the electron mass. We obtain an expression similar to Eq. (5.27)

$$\Gamma_{5e} = \frac{1}{64\pi m_{\tilde{a}}^3} \frac{|c_1|^2 |V_{32}|^2 |Y_d|^2 |K_{ud}|^2 |k_{d\phi^-}|^2}{M_{\phi^-}^4} \left(\frac{m_{M^-}^2 f_{M^-}}{m_u + m_d} \right)^2 (m_{\tilde{a}}^2 - m_\pi^2)^2 \,. \quad (5.31)$$

We explained above that we can interchange the type of the Higgs at the axino vertex, see Fig. 5.6. Note, the positively charged pion couples to an up-like higgs. The decay width can easily be read off of Eq. (5.30)

$$\Gamma_6 = \frac{1}{64\pi} \frac{|\mathbf{p}|^2}{m_{\tilde{a}}^3} \frac{|c_1|^2 |U_{i2}|^2 |Y_u|^2 |K_{ud}|^2 |k_{u\phi^+}|^2}{M_{\phi^+}^4} \left(\frac{m_{M^+}^2 f_{M^+}}{m_u + m_d} \right)^2 (m_{\tilde{a}}^2 + m_\ell^2 - m_{M^+}^2) \,. \quad (5.32)$$

The momentum $|\mathbf{p}|$ is given above. We have introduced the appropriate up quark mixing angles as well as the couplings. For this process we can have either an electron or a muon in the final state in addition to the pion and kaon. Of course, a simplfication of Eq. (5.32) in case of an electron holds, *cf.* Eq. (5.27).

$$\Gamma_{6e} = \frac{1}{64\pi\, m_{\tilde{a}}^3} \frac{|c_1|^2 |U_{42}|^2 |Y_u|^2 |K_{ud}|^2 |k_{u\phi^+}|^2}{M_{\phi^+}^4} \left(\frac{m_{M^+}^2 f_{M^+}}{m_u + m_d} \right)^2 (m_{\tilde{a}}^2 - m_{M^+}^2)^2 \,. \quad (5.33)$$

We can find a last pseudoscalar mesonic decay which is constructed via a c_2^i vertex. This kind of interaction derived in Eq. (3.44) from the operator $\Phi_{\tilde{a}} L_i H_2$ give rise to a

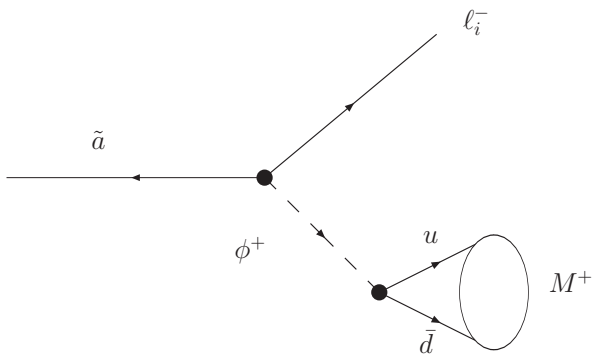

Figure 5.7: The first vertex of this interaction has a c_2^i coupling. The Higgs is of up-like character, where ϕ^+ denote the mass eigenstate. The meson can be $M^+ = \pi^+, K^+$. Depending on the chosen c_2^i we get a specific lepton in the final state. Obviously, a tauon can not be part of the decay. Γ_7 is the related decay width, see text.

direct axino lepton coupling. For $i = 1$ the axino couples to an electron and with $i = 2$ to a muon. The involved Higgs doublet is of the up-type and mediates this axino decay. Obviously, the u-$\bar{d}$ quarks have a Yukawa coupling with the Higgs in common. This quark pair form a π^+ or K^+. This decay channel shares a comparable structure to the process already discussed. Thus, we only state the decay width

$$\Gamma_7 = \frac{1}{64\pi} \frac{|\mathbf{p}|}{m_{\tilde{a}}^3} \frac{|c_2^i|^2 \, |Y_u|^2 \, |K_{ud}|^2 \, |k_{u\phi^+}|^2}{M_{\phi^+}^4} \left(\frac{m_{M^+}^2 f_{M^+}}{m_u + m_d} \right)^2 (m_{\tilde{a}}^2 + m_\ell^2 - m_{M^+}^2) \,. \quad (5.34)$$

The related diagram can be found in Fig. 5.7.

5.4 The Decay $\tilde{a} \longrightarrow \ell_i^- \ell_j^+ \nu_j$

5.4.1 Decay via $W^\pm, Z^0$ Bosons.

Now, we consider the purely leptonic decay $\tilde{a} \to \ell^+ + \ell^- + \nu$. This process can be realised in different ways. Of course, when we include $\not{R}_p$ we get additional possibilities which we will discuss below. We will briefly explain how the diagrams are constructed. We start with a process where the axino mixes with a neutrino and couples again like in the SM to a W-Boson. The connected lepton is of the same family. The resulting diagram can be seen in Fig. 5.8. The second lepton pair can have an flavor independent of the first pair. We conlcude that there exists four combinations, namely:

1. $i = e$ and $j = e$,
2. $i = \mu$ and $j = e$,
3. $i = e$ and $j = \mu$,
4. $i = \mu$ and $j = \mu$,

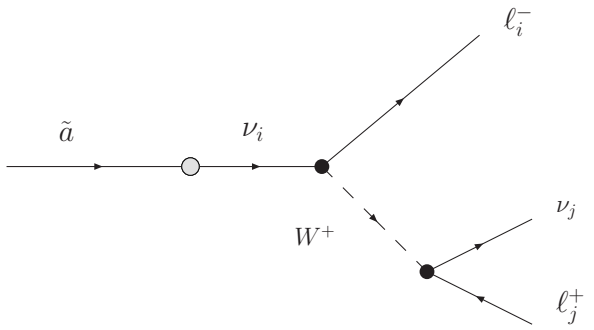

Figure 5.8: The gray dot indicates the axino-neutrino mixing. The neutrino itself couples like in the SM to a W^+ boson. In principle the coupling of the axino to all neutrino flavours is possible. The decay width is Γ_8. For all final state combinations see text.

where we have used the labels according to Fig. 5.8. The related amplitude in two component notation is given through

$$\mathrm{i}\mathcal{M}_8 = x^\dagger(p_{\ell_i}) \left(-\frac{\mathrm{i}g}{\sqrt{2}}\bar{\sigma}_\mu\right) x(p_{\tilde{a}}) \frac{\mathrm{i}g^{\mu\nu}}{M_{W^+}^2} x^\dagger(p_{\nu_j}) \left(-\frac{\mathrm{i}g}{\sqrt{2}}\bar{\sigma}_\nu\right) y(p_{\ell_j}) \tag{5.35}$$

In the cases where a muon is involved we cannot neglect the masses. The computation of the decay width is non trivial due to the non-trivial phases space integration. As we have several such scenarios it is convenient to state only the amplitude squared. We have

$$\frac{1}{2}\sum_{\text{spins}} |\mathcal{M}_8|^2 = 64\, G_F^2\, |N_{i8}|^2\, [p_{\tilde{a}} \cdot p_{\ell_j}][p_{\ell_i} \cdot p_{\nu_j}]\,, \tag{5.36}$$

where we have denoted the momenta of the particle by a letter in the subscript, *cf.* also Fig. 5.8. The amplitude was averaged over incoming- and summed over outgoing spins, as indicated.

For the first case with the electron family the calculations are rather simple and we find

$$\Gamma_{8e} = \frac{G_F^2 |N_{i8}|^2}{192\pi^3}\, m_{\tilde{a}}^5\,. \tag{5.37}$$

Let us now focus on a process with the inclusion of a Z^0-boson. Instead of coupling a neutrino to a W^+-boson the neutrino can couple to a Z^0 boson as well. This process is depicted in Fig. 5.9. This diagram interferes with three more diagrams where the arrows are reversed. The amplitudes for all four Feynman diagrams are

$$\mathrm{i}\mathcal{M}_a = \mathrm{i}\left(\frac{g a_\nu}{c_\mathrm{w}}\right) N_{i8}\, y^\dagger(p_{\tilde{a}}) \bar{\sigma}_\mu y(p_\nu) \frac{1}{M_Z^2}\, x^\dagger(p_{l^+}) \left(-\frac{g b_f}{c_\mathrm{w}}\right) \bar{\sigma}^\mu y(p_{\ell^-}) \tag{5.38}$$

$$\mathrm{i}\mathcal{M}_b = -\mathrm{i}\left(\frac{g a_\nu}{c_\mathrm{w}}\right) N_{i8}\, y^\dagger(p_{\tilde{a}}) \bar{\sigma}_\rho y(p_\nu) \frac{1}{M_Z^2}\, x^\dagger(p_{l^-}) \left(-\frac{g a_f}{c_\mathrm{w}}\right) \bar{\sigma}^\rho y(p_{\ell^+}) \tag{5.39}$$

$$\mathrm{i}\mathcal{M}_c = \mathrm{i}\left(\frac{g a_\nu}{c_\mathrm{w}}\right) N_{i8}\, x^\dagger(p_\nu) \bar{\sigma}_\lambda x(p_{\tilde{a}}) \frac{1}{M_Z^2}\, x^\dagger(p_{l^+}) \left(-\frac{g b_f}{c_\mathrm{w}}\right) \bar{\sigma}^\lambda y(p_{\ell^+}) \tag{5.40}$$

$$\mathrm{i}\mathcal{M}_d = -\mathrm{i}\left(\frac{g a_\nu}{c_\mathrm{w}}\right) N_{i8}\, x^\dagger(p_\nu) \bar{\sigma}_\alpha x(p_{\tilde{a}}) \frac{1}{M_Z^2}\, x^\dagger(p_{l^-}) \left(-\frac{g a_f}{c_\mathrm{w}}\right) \bar{\sigma}^\alpha y(p_{\ell^+})\,, \tag{5.41}$$

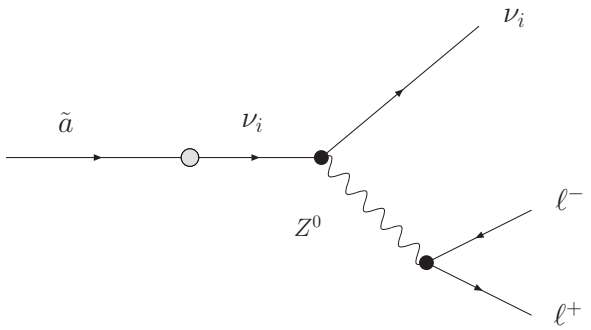

Figure 5.9: Axino decay via the axino-neutrino mixing. In principle the coupling to all neutrino flavours is possible. The two vertices are SM like. This diagram interfers with three more diagrams. The according decay width is given by Γ_9.

with $a_f = T_3^\ell - Q_\ell \sin^2\theta_\mathrm{w}$, $b_f = Q_\ell \sin^2\theta_\mathrm{w}$ and $c_\mathrm{w} = \cos\theta_\mathrm{w}$. We find for the spin summed and averaged amplitude squared:

$$\frac{1}{2}\sum_{\text{spins}} |\mathcal{M}_9|^2 \;=\; 128\, G_F^2\, |N_{i8}|^2 \Big[(a_f^2 + b_f^2)(p_{\tilde{a}} \cdot p_{\ell^+})(p_{\ell^-} \cdot p_{\nu_i}) - 2 a_f b_f (p_{\tilde{a}} \cdot p_{\nu_i}) m_\ell^2 \Big] . \tag{5.42}$$

This amplitude can take a simpler form depending on the final state particles. For this decay we have in general three different final state classes. On the one hand we have decays into electrons as well as muons. On the other hand the Z^0 couples to a neutrino anti-neutrino pair. Hence in total we have nine decay chains: 3 neutrino flavors times the lepton combinations $e + \bar{e}$, $\mu + \bar{\mu}$ and $\nu + \bar{\nu}$. If the lepton is purely electron like we get

$$\Gamma_{9e} = \frac{|N_{i8}|^2 G_F^2 (a_f^2 + b_f^2)}{96\pi^3} m_{\tilde{a}}^5 . \tag{5.43}$$

For the neutrino case we know that $b_f \equiv 0$ which leads to

$$\Gamma_{9\nu} = \frac{|N_{i8}|^2\, G_F^2\, a_f^2}{96\pi^3} m_{\tilde{a}}^5 \,, \tag{5.44}$$

with $a_f = 1/2$.

5.4.2 Decay via Neutral Higgs

In subsection 5.2 we already presented the axino couplings to the neutral higgsino and higgs, *cf.* also Eq. (3.43). Furthermore we saw that such a vertex lead to a meson in the final state. Now, instead of a neutral meson, the Higgs can couple to a free fermion-antifermion pair. Like in the mesonic case the higgsino mixes with the neutrinos. In Fig. 5.10 we show the related Feynman diagram. There exist four diagrams per Higgs mass eigenstate $\phi^0 = (h^0, H^0)$, where in the other diagrams the arrows are reversed. Hence

in total we have eight diagrams. Exemplarily we present only four amplitudes where the mass eigenstate of the Higgs is implicit

$$\begin{aligned}
\mathrm{i}\mathcal{M}_a &= \mathrm{i}x^\dagger(p_\nu)(-\mathrm{i}c_1 N_{i3})y^\dagger(p_{\tilde{a}})\frac{1}{M^2_{\phi_0}}y(p_{\ell^-})\Big(\frac{-\mathrm{i}}{\sqrt{2}}Y_\ell k_{d\phi^0}\Big)y(p_{\ell^+}) && (5.45)\\
\mathrm{i}\mathcal{M}_b &= \mathrm{i}x^\dagger(p_\nu)(-\mathrm{i}c_1 N_{i3})y^\dagger(p_{\tilde{a}})\frac{1}{M^2_{\phi_0}}x^\dagger(p_{\ell^-})\Big(\frac{-\mathrm{i}}{\sqrt{2}}Y_\ell k_{d\phi^0}\Big)x^\dagger(p_{\ell^+}) && (5.46)\\
\mathrm{i}\mathcal{M}_c &= \mathrm{i}y(p_\nu)(-\mathrm{i}c_1 N_{i3})x(p_{\tilde{a}})\frac{1}{M^2_{\phi_0}}y(p_{\ell^-})\Big(\frac{-\mathrm{i}}{\sqrt{2}}Y_\ell k_{d\phi^0}\Big)y(p_{\ell^+}) && (5.47)\\
\mathrm{i}\mathcal{M}_d &= \mathrm{i}y(p_\nu)(-\mathrm{i}c_1 N_{i3})x(p_{\tilde{a}})\frac{1}{M^2_{\phi_0}}x^\dagger(p_{\ell^-})\Big(\frac{-\mathrm{i}}{\sqrt{2}}Y_\ell k_{d\phi^0}\Big)x^\dagger(p_{\ell^+})\,, && (5.48)
\end{aligned}$$

where Y_ℓ are the diagonlised Yukawa couplings and the Higgs mixing parameters $k_{d\phi^0}$ are given for example in Ref. [78]. N_{i3} where $i = 5, 6, 7$ denotes the mixing of the neutrino with the Higgsino. Thus squaring all eight matrix element we would get altogether 64 terms. But half of these terms are proportional to the neutrino mass which can be neglected. Furthermore note that the difference between the 4+4 sets of matrix elements is only the mass propagator and the according Higgs mixing angle. The spinor structure is identical leading to a further simplification. Hence, after a little bit of algebra the amplitudes squared reads

$$|\mathcal{M}_{10}|^2 = \left[\frac{k_{d\phi^0_{h^0}}}{M^2_{\phi^0_{h^0}}} + \frac{k_{d\phi^0_{H^0}}}{M^2_{\phi^0_{H^0}}}\right]^2 |N_{i3}|^2|c_1|^2|Y_\ell|^2\Big[4(p_{\tilde{a}}\cdot p_\nu)(p_{\ell^+}\cdot p_{\ell^-}) - 2\,(p_{\tilde{a}}\cdot p_\nu)m^2_\ell\Big]\,. \tag{5.49}$$

Note, in the case of electrons in the final state we get for the decay width

$$\Gamma_{10e} = \left[\frac{k_{d\phi^0_{h^0}}}{M^2_{\phi^0_{h^0}}} + \frac{k_{d\phi^0_{H^0}}}{M^2_{\phi^0_{H^0}}}\right]^2 \frac{|N_{i3}|^2|Y_\ell|^2|c_1|^2}{6(8\pi)^3} m^5_{\tilde{a}}\,, \tag{5.50}$$

as the mass of the electron can be neglected. For this decay channel we have all in all six modes. The axino decay can be accomplished by three neutrino flavors in addition to the electron- and muon pair combination. The tau is kinematically not accessible.

5.4.3 Decay via Charged Higgs.

The axino can couple to the charged higgsinos, which in turn mix with the electrons, *cf.* Sect. 3.2.5. We thus obtain again purely leptonic final states, *cf.* Fig. 5.11. Similar to the decays mediated by the W^+ boson here the charged Higgs couples to a lepton pair. Hence we have the same final state combinations as seen in section 5.4.1:

1. $i = e$ and $j = e$,
2. $i = \mu$ and $j = e$,

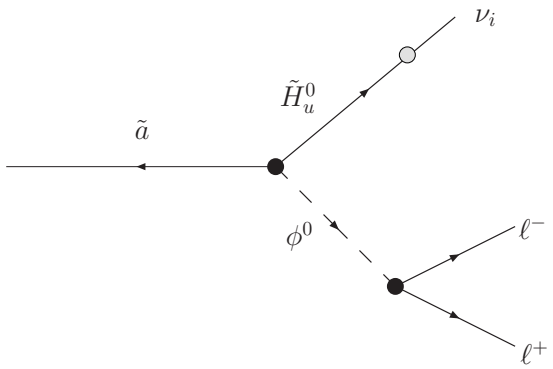

Figure 5.10: One of the Feynman graphs for the axino decay $\tilde{a} \to \nu + \ell^+ + \ell^-$ via neutral Higgs bosons. The grey dot indicates higgsino–neutrino mixing with $i = e, \mu, \tau$. Γ_{10} is the related decay width.

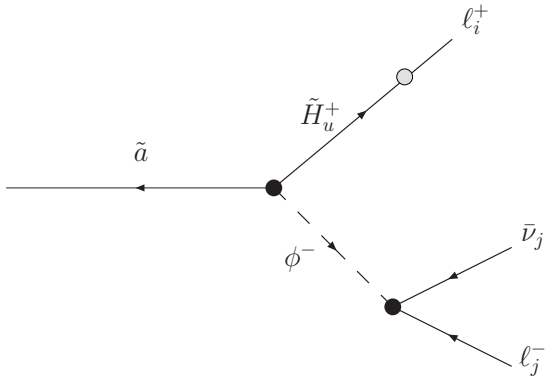

Figure 5.11: One of the diagrams for axino decay via $\Phi_{\tilde{a}} H_1 H_2$. The gray dot indicates the mixing of the chargino with the lepton with $i = e, \mu, \tau$. The tau case is kinematically forbidden.

3. $i = e$ and $j = \mu$,

4. $i = \mu$ and $j = \mu$,

where the choice of the indices are according to the labels in Fig. 5.11. The Higgs–lepton vertex factor can be found in Ref. [78]. Note, this diagram is unique

$$\mathrm{i}\mathcal{M}_{11} = \mathrm{i}\, V_{i2}\, x^\dagger(p_{\ell^+})(\mathrm{i}c_1) y^\dagger(p_{\tilde{a}}) \frac{1}{M^2_{\phi^-}} y(p_\nu)(\mathrm{i}Y_\ell k_{d\phi^-}) y(p_{\ell^-})\,, \tag{5.51}$$

and the amplitude squared reads

$$\frac{1}{2}\sum_{\text{spins}} |\mathcal{M}_{11}|^2 = \frac{2\,|c_1|^2 |Y_\ell|^2\, |k_{d\phi^-}|^2\, |V_{i2}|^2}{M^4_{\phi^-}} (p_{\tilde{a}} \cdot p_{\ell^+})(p_\nu \cdot p_{\ell^-}) \tag{5.52}$$

Here $M_{\phi^+} = M_{\phi^-}$ denotes the mass of the charged Higgs boson. Furthermore for the

first of the four final state scenarios we obtain the simplified decay width:

$$\Gamma_{11e} = \frac{|c_1|^2 |Y_\ell|^2 \, |k_{d\phi^-}|^2 \, |V_{32}|^2}{12(8\pi)^3 M_{\phi^-}^4} \, m_{\tilde{a}}^5 \,, \tag{5.53}$$

where only the electron flavor participates.

5.5 Decay via the $\not{R}_p \; LL\bar{E}$ operator.

5.5.1 The decay $\tilde{a} \to \ell_i^- \ell_j^+ \nu_j$

In this section we contruct decays which explicitly include a $\not{R}_p$ vertex. Here we use blockwise the Feynman diagrams of Appendix L of Ref. [78]. For such a first diagram we assume that an axino mixes with a neutrino. Now, we are able to contruct a three body decay where two leptonic $\not{R}_p$ vertices are included. Considering this we get the diagram in Fig. 5.12. We have to clarify what kind of leptons we have in the final state. To give a concrete answer to this problem we have to assume a specific nonzero $\not{R}_p$ Yukawa coupling. We choose $(\mathbf{\Lambda}_{E^1})_{21} \neq 0$. Note that the Yukawa matrix of the corresponding $\not{R}_p$ operator is antisymmetric.

For our concrete example this means, that we have in total four final state lepton combinations, where in any scenario the slepton propagator is a selectron. This becomes more obvious when we take a closer look at the Yukawa couplings. In the labels of Fig. 5.12 the first Yukawa vertex reads $(\mathbf{\Lambda}_{E^k})_{ij}$ and the second $(\mathbf{\Lambda}_{E^k})_{mn}$. The index $k = 1$ is identical in both vertices resulting in a selectron. Keeping in mind that $\{i, j\}$ and $\{m, n\} \in \{1, 2\}$ and the anti symmetry of the Yukawa matrix we get the mentioned four cases:

1. ν_e, μ^+ with ν_e, μ^-
2. ν_μ, e^+ with ν_e, μ^-
3. ν_e, μ^+ with ν_μ, e^-
4. ν_μ, e^+ with ν_μ, e^- .

In each case the first pair of leptons represents the leptons involved in the first vertex and the second pair in the second vertex. As mentioned this discussion of the final states due to $(\mathbf{\Lambda}_{E^1})_{12}$ is an example. We can perform such a consideration for all $LL\bar{E}\,\not{R}_p$ operators. In Table 5.1 we have summarized the results. Note that we excluded the tau lepton as a final state particle. From Fig. 5.12 we deduce

$$\mathrm{i}\mathcal{M}_{12} \;=\; \mathrm{i}N_{i8}\, y(p_{\ell^+})(-\mathrm{i}(\mathbf{\Lambda}_{E^k})_{ij}) x(p_{\tilde{a}}) \frac{1}{M_{\tilde{\ell}_R^2}} x^\dagger(p_\nu)(-\mathrm{i}(\mathbf{\Lambda}_{E^k})_{mn}) x^\dagger(p_{\ell^-}) \tag{5.54}$$

The corresponding amplitude squared is given by

$$\frac{1}{2}\sum_{\text{spins}} |\mathcal{M}_{12}|^2 \;=\; \frac{2|N_{i8}|^2}{M_{\tilde{\ell}_R}^4} |(\mathbf{\Lambda}_{E^k})_{ij}|^4 (p_{\tilde{a}} \cdot p_{\ell^+})(p_\nu \cdot p_{\ell^-}) \,, \tag{5.55}$$

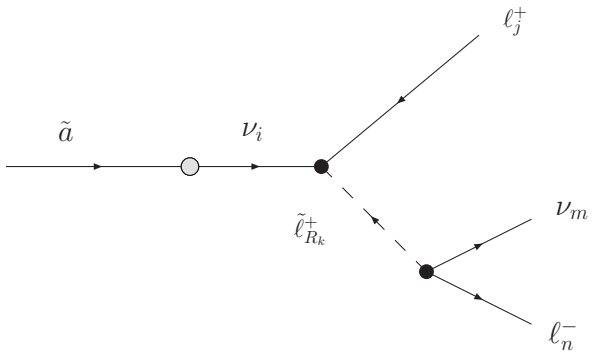

Figure 5.12: The first considered $\not{R}_p$ decay, where both vertices are $\not{R}_p$-like due to the $LL\bar{E}$ operator. The gray dot indicates the mixing of the axino with the neutrino with $i = e, \mu, \tau$. Not all neutrino flavors are accessible since the mixing depends crucially on the $\not{R}_p$ coupling. For details see text. The decay width is given by Γ_{12}.

where we have combined the $\not{R}_p$ couplings of both vertices. For the electron-positron final state combinations, *cf.* Table 5.1 the decay width reads

$$\Gamma_{12e} = \frac{|(\mathbf{\Lambda}_{E^k})_{ij}|^4 |N_{i8}|^2}{12(8\pi)^3 M^4_{\tilde{\ell}_R}}\, m^5_{\tilde{a}}\,. \tag{5.56}$$

The latter process includes a slepton propagator which is originally a SU(2) singlet superfield. This singlet can provide as well a fermionic final state. Consequently one of the two remaining doublets has to mediate a possible three body decay. This point of view alters the structure of the $\not{R}_p$ vertex and leads to an interaction like in Fig 5.13. Assuming again as an example $(\mathbf{\Lambda}_{E^1})_{12}$ we have only two decay channels:

1. ν_e, e^- and ν_e, e^+ with $\tilde{\mu}_L$

2. ν_μ, e^- and ν_μ, e^+ with $\tilde{e}_L$.

We explained above the of each case the first lepton pair is related to the first vertex etc. This structure can be easily obtained. Consider that the first vertex has a coupling of the form $(\mathbf{\Lambda}_{E^k})_{ij}$ and the second vertex accordingly $(\mathbf{\Lambda}_{E^n})_{mj}$. Assuming that $(\mathbf{\Lambda}_{E^1})_{12} \neq 0$ and the anti symmetry of the $LL\bar{E}$ operator we can conclude immediately that $k = n$ and $i = m$. The j's are equal anyway. Now, it becomes apparent why we have only two sets of final states. Both Yukawa coupling are identical and cannot be chosen independently from each other. Hence this identity in addition with the symmetry of the operator gives us in total the two cases stated above. A listing of all decay modes for the remaining $\not{R}_p$ operators can be found in Table 5.2. Comparing the processes in Fig. 5.13 and Fig. 5.12 we can directly conclude

$$\mathrm{i}\mathcal{M}_{13} \;=\; \mathrm{i}N_{i8}\, y(p_{\ell^-})(-\mathrm{i}(\mathbf{\Lambda}_{E^k})_{ij})x(p_{\tilde{a}})\frac{1}{M^2_{\tilde{\ell}_L}}x^\dagger(p_\nu)(-\mathrm{i}(\mathbf{\Lambda}_{E^k})_{mn})x^\dagger(p_{\ell^+}) \tag{5.57}$$

$\not{R}_p$ Coupling	1st vertex	2nd vertex	propagator
$(\mathbf{\Lambda}_{E^1})_{12}$	ν_e, μ^+	ν_e, μ^-	$\tilde{e}_R$
	ν_μ, e^+	ν_e, μ^-	
	ν_e, μ^+	ν_μ, e^-	
	ν_μ, e^+	ν_μ, e^-	
$(\mathbf{\Lambda}_{E^1})_{13}$	ν_τ, e^+	ν_τ, e^-	$\tilde{e}_R$
$(\mathbf{\Lambda}_{E^2})_{12}$	ν_e, μ^+	ν_e, μ^-	$\tilde{\mu}_R$
	ν_μ, e^+	ν_e, μ^-	
	ν_e, μ^+	ν_μ, e^-	
	ν_μ, e^+	ν_μ, e^-	
$(\mathbf{\Lambda}_{E^2})_{23}$	ν_τ, μ^+	ν_τ, μ^-	$\tilde{\mu}_R$
$(\mathbf{\Lambda}_{E^3})_{13}$	ν_τ, e^+	ν_τ, e^-	$\tilde{\tau}_R$
$(\mathbf{\Lambda}_{E^3})_{23}$	ν_τ, μ^+	ν_τ, μ^-	$\tilde{\tau}_R$

Table 5.1: Depending on the choice of the $\not{R}_p$ operator the possible final states are predetermined, *cf.* Fig. 5.12. The first column shows only six of in general nine $LL\bar{E}$ operators. The reason is that in the case of the omitted operators the results in vanishing axino Yukawa couplings. We will go into details in a later chapter. The second (third) column show the particle combinations at the first (second) vertex of the axino decay. The fourth column shows the related propagator.

Squaring the latter expression, averaging over incoming- and summing over outgoing spins results in

$$\frac{1}{2}\sum_{\text{spins}}|\mathcal{M}_{13}|^2 = \frac{2|N_{i8}|^2}{M^4_{\tilde{\ell}_L}}|(\mathbf{\Lambda}_{E^k})_{ij}|^4(p_{\tilde{a}}\cdot p_{\ell^-})(p_\nu \cdot p_{\ell^+})\,. \tag{5.58}$$

The decay width can be obtained easily for massless electrons in the final state

$$\Gamma_{13e} = \frac{|(\mathbf{\Lambda}_{E^k})_{ij}|^4|N_{i8}|^2}{12(8\pi)^3 M^4_{\tilde{\ell}_L}}\, m^5_{\tilde{a}}\,. \tag{5.59}$$

In Fig. 5.14 we show another diagram where a $\not{R}_p$ vertex is involved. The first vertex is due to the $\Phi_{\tilde{a}}L_iH_2$ and the second to the $LL\bar{E}$ operator. The family of the sparticle propagator is chosen by the according c_2^i coupling of the first vertex. In general all three couplings are possible. But this choice is restricted by the $\not{R}_p$ coupling at the second vertex. For example, if we have $(\mathbf{\Lambda}_{E^k})_{ij} : |(\mathbf{\Lambda}_{E^1})_{12}| = |(\mathbf{\Lambda}_{E^1})_{21}| \neq 0$ this would mean that at any scenario the negatively charged fermion is an electron, as $k = 1$.

For the propagator we can have either a c_2^1 coupling leading to a selectron propagator and a muon neutrino or for c_2^2 we have the opposite way around. You can find all possible

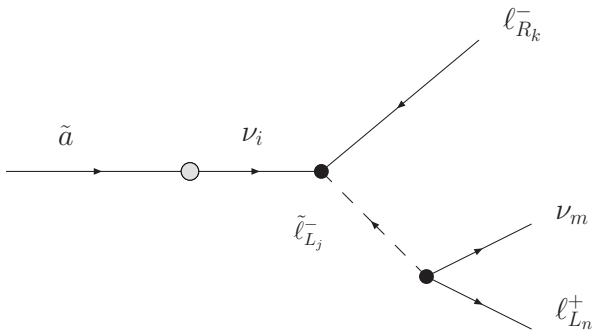

Figure 5.13: The second considered $\not{R}_p$ decay, where both vertices are $\not{R}_p$-like. The gray dot indicates the mixing of the axino with the neutrino with $i = e, \mu, \tau$. Not all neutrino flavors are accessible since the mixing depends crucially on the $\not{R}_p$ coupling. For details see text. The decay width is given by Γ_{13}.

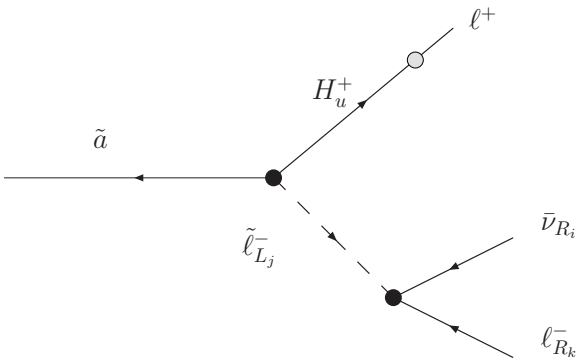

Figure 5.14: A decay via the c_2^j vertex, where the gray dot indicate a higgsino-positron mixing. Depending on the chosen $LL\bar{E}$ operator we can have diffrent final state constellations. For a complete list see Table 5.3. The decay width is given by Γ_{14}.

states in Table 5.3. Thus using Fig. 5.14 we obtain

$$\mathrm{i}\mathcal{M}_{14} \;=\; \mathrm{i}V_{i2}x^\dagger(p_{\ell^+})(-\mathrm{i}c_2^j)y^\dagger(p_{\tilde{a}})\frac{1}{M^2_{\tilde{\ell}_j}}y(p_{\nu_i})(-\mathrm{i}(\mathbf{\Lambda}_{E^k})_{ij})y(p_{\ell^-})\,, \tag{5.60}$$

and for the amplitude squared

$$\frac{1}{2}\sum_{\text{spins}}|\mathcal{M}_{14}|^2 \;=\; \frac{2|V_{i2}|^2|c_2^j|^2|(\mathbf{\Lambda}_{E^k})_{ij}|^2}{M^4_{\tilde{\ell}_j}}\,(p_{l^+}\cdot p_{\tilde{a}})\,(p_{\nu_i}\cdot p_{\ell^-})\,. \tag{5.61}$$

For the electron like scenarios in Table 5.3 we obtain the simplified expression

$$\Gamma_{14e} = \frac{|V_{32}|^2|c_2^j|^2|(\mathbf{\Lambda}_{E^k})_{ij}|^2}{12(8\pi)^3 M^4_{\tilde{\ell}_j}}\,m^5_{\tilde{a}}\,. \tag{5.62}$$

We left over one last possible $\not{R}_p$ like decay. From the $\Phi L_i H_2$ operator we can have an

$\not{R}_p$ Coupling	1st vertex	2nd vertex	propagator
$(\mathbf{\Lambda}_{E^1})_{12}$	ν_e, e^-	ν_e, e^+	$\tilde{\mu}_L$
	ν_μ, e^-	ν_μ, e^+	$\tilde{e}_L$
$(\mathbf{\Lambda}_{E^1})_{13}$	ν_e, e^-	ν_e, e^+	$\tilde{\tau}_L$
	ν_τ, e^-	ν_τ, e^+	$\tilde{e}_L$
$(\mathbf{\Lambda}_{E^2})_{12}$	ν_e, μ^-	ν_e, μ^+	$\tilde{\mu}_L$
	ν_μ, μ^-	ν_μ, μ^+	$\tilde{e}_L$
$(\mathbf{\Lambda}_{E^2})_{23}$	ν_μ, μ^-	ν_μ, μ^+	$\tilde{\tau}_L$
	ν_τ, μ^-	ν_τ, μ^+	$\tilde{\mu}_L$
$(\mathbf{\Lambda}_{E^3})_{13}$	–	–	–
$(\mathbf{\Lambda}_{E^3})_{23}$	–	–	–

Table 5.2: Depending on the choice of the $\not{R}_p$ operator the possible final states are predetermined, *cf.* Fig. 5.13. The first column shows only six of in general nine $LL\bar{E}$ operators. The reason is that in the case of the omitted operators the RGEs return vanishing axino Yukawa couplings. We will go into details in a later chapter. The second (third) column show the particle combinations at the first (second) vertex of the axino decay. The fourth column shows the associated propagator. The last two rows contain in general tau leptons in the final state which is kinematically not allowed. Thus we left the fields empty.

axino-sneutrino-higgsino vertex. The flavour of the sneutrino propagator is determined by the choice of the c_2^i coupling. Again, it is restricted by the choice of the $\not{R}_p$ coupling. We can only have a electron- or muon-like flavor combinations with $(\mathbf{\Lambda}_{E^1})_{21}$. In total we have six final state combinations with this operator. Of course, similar results can be derived for the remaining $LL\bar{E}$ couplings, *cf.* Table 5.4.

Hence with the labels of Fig. 5.15 the amplitude yields to

$$\mathrm{i}\mathcal{M}_{15} \;=\; N_{i4}x^\dagger(p_\nu)(\mathrm{i}c_2^i)y^\dagger(p_{\tilde{a}})\frac{1}{M^2_{\tilde{\nu}_i}}y(p_{\ell^+})(-\mathrm{i}(\mathbf{\Lambda}_{E^k})_{ij})y(p_{\ell^-})\,. \tag{5.63}$$

After squaring the amplitude, summing over the final state fermion spins as well as averaging over the incoming axino spin the result reads

$$\frac{1}{2}\sum_{\text{spins}}|\mathcal{M}_{15}|^2 \;=\; \frac{2|N_{i4}|^2|c_2^i|^2|(\mathbf{\Lambda}_{E^k})_{ij}|^2}{M^4_{\tilde{\nu}_i}}(p_{\tilde{a}}\cdot p_\nu)(p_{\ell^+}\cdot p_{\ell^-}) \tag{5.64}$$

Neglecting the electron mass we obtain the same simplified structure as in the cases before:

$$\Gamma_{15e} = \frac{|N_{i4}|^2|c_2^2|^2|(\mathbf{\Lambda}_{E^k})_{ij}|^2}{12(8\pi)^3M^4_{\tilde{\nu}_i}}m^5_{\tilde{a}} \tag{5.65}$$

This last example concludes the section with axino decays which are due to the $LL\bar{E}$ operator. As indicated before the $LQ\bar{D}$ operator provides a second possibility for the

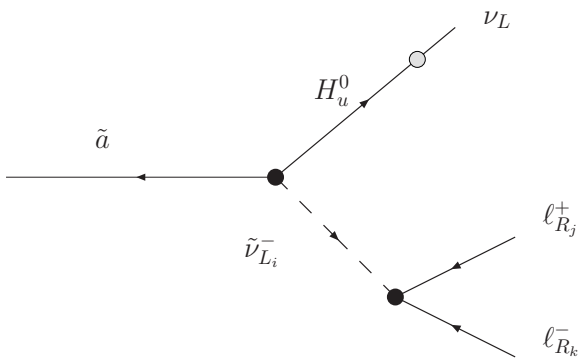

Figure 5.15: Through the c_2^i vertex the axino couples to the neutral higgsinos and a sneutrino. The gray dot indicates the higgsino neutrino mixing. The second vertex is a $\not{R}_p$-vertex. See table 5.4 for all final state combinations. The decay width is given by Γ_{15}.

$\not{R}_p$ Coupling	1st vertex		2nd vertex	propagator
$(\mathbf{\Lambda}_{E^1})_{12}$	c_2^1	e^+	$\bar{\nu}_\mu, e^-$	$\tilde{e}_L$
	c_2^1	μ^+	$\bar{\nu}_\mu, e^-$	$\tilde{e}_L$
	c_2^2	e^+	$\bar{\nu}_e, e^-$	$\tilde{\mu}_L$
	c_2^2	μ^+	$\bar{\nu}_e, e^-$	$\tilde{\mu}_L$
$(\mathbf{\Lambda}_{E^1})_{13}$	c_2^1	e^+	$\bar{\nu}_\tau, e^-$	$\tilde{e}_L$
	c_2^1	μ^+	$\bar{\nu}_\tau, e^-$	$\tilde{e}_L$
	c_2^3	e^+	$\bar{\nu}_e, e^-$	$\tilde{\tau}_L$
	c_2^3	μ^+	$\bar{\nu}_e, e^-$	$\tilde{\tau}_L$
$(\mathbf{\Lambda}_{E^2})_{12}$	c_2^1	e^+	$\bar{\nu}_\mu, \mu^-$	$\tilde{e}_L$
	c_2^1	μ^+	$\bar{\nu}_\mu, \mu^-$	$\tilde{e}_L$
	c_2^2	e^+	$\bar{\nu}_e, \mu^-$	$\tilde{\mu}_L$
	c_2^2	μ^+	$\bar{\nu}_e, \mu^-$	$\tilde{\mu}_L$
$(\mathbf{\Lambda}_{E^2})_{32}$	c_2^2	e^+	$\bar{\nu}_\tau, \mu^-$	$\tilde{\mu}_L$
	c_2^2	μ^+	$\bar{\nu}_\tau, \mu^-$	$\tilde{\mu}_L$
	c_2^3	e^+	$\bar{\nu}_\mu, \mu^-$	$\tilde{\tau}_L$
	c_2^3	μ^+	$\bar{\nu}_\mu, \mu^-$	$\tilde{\tau}_L$
$(\mathbf{\Lambda}_{E^3})_{13}$		–	–	–
$(\mathbf{\Lambda}_{E^3})_{23}$		–	–	–

Table 5.3: Depending on the choice of the $\not{R}_p$ operator the possible final states are predetermined. The first column shows only six of in general nine $LL\bar{E}$ operators. The reason is that in the case of the omitted operators the results in vanishing axino Yukawa couplings. We will go into details in a later chapter. The second (third) column show the particle combinations at the first (second) vertex of the axino decay. The mostright part show the associated propagator. The last two rows contain in general tau leptons in the final state which is kinematically not allowed. Thus we left the fields empty. This particle list belongs to the decay in Fig. 5.14.

$\not{R}_p$ Coupling	1st vertex		2nd vertex	propagator
$(\mathbf{\Lambda}_{E^1})_{12}$	c_2^1	ν_e ν_μ ν_τ	μ^+, e^-	$\tilde{\nu}_e$
	c_2^2	ν_e ν_μ ν_τ	e^+, e^-	$\tilde{\nu}_\mu$
$(\mathbf{\Lambda}_{E^1})_{13}$	c_2^3	ν_e ν_μ ν_τ	e^+, e^-	$\tilde{\nu}_\mu$
$(\mathbf{\Lambda}_{E^2})_{12}$	c_2^1	ν_e ν_μ ν_τ	μ^+, μ^-	$\tilde{\nu}_e$
	c_2^2	ν_e ν_μ ν_τ	e^+, μ^-	$\tilde{\nu}_\mu$
$(\mathbf{\Lambda}_{E^2})_{23}$	c_2^3	ν_e ν_μ ν_τ	μ^+, μ^-	$\tilde{\nu}_\tau$
$(\mathbf{\Lambda}_{E^3})_{13}$		–	–	–
$(\mathbf{\Lambda}_{E^3})_{23}$		–	–	–

Table 5.4: Depending on the choice of the $\not{R}_p$ operator the final states a predetermined. The first column show only six of in general nine $LL\bar{E}$ operators. Since in the case of the omitted operators the results in vanishing axino Yukawa couplings. We will go into details in a later chapter. The second (third) column show the particle combinations at the first (second) vertex of the axino decay. The mostright part show the associated propagator. The last two rows contain in general tau leptons in the final state which is kinematically not allowed. Thus we left the fields empty. This particle list belongs to the decay presented in Fig. 5.15.

lepton number violation. The decays which could be obtain from this sector are presented in the next section.

However, assuming that the lepton number violation comes from the $LL\bar{E}$ operator the branching ratios (BR) can be computed. This will be our task in the next chapter.

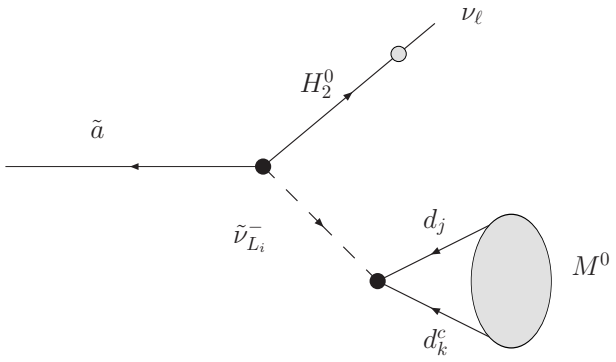

Figure 5.16: The first axino decay via the $LQ\bar{D}$ operator. The neutral Higgsino can mix with the neutrino and represent the first part of the final state. On the other hand the second vertex is realized through the $LQ\bar{D}$ operator giving a quark-anti quark pair. This pair can form a neutral meson, denoted by M^0. This meson can be rather a π^0 or a K^0 depending on the rest mass of the decaying axino. The decay width is given by Γ_{16}, see text.

5.6 Decay via the $\not{R}_p\ LQ\bar{D}$ operator

In the previous section we have presented axino decays which are mediated by the $\not{R}_p$ operator $LL\bar{E}$. We saw that for different non-zero operators we can have different final states.

However, from section 3.1 and Eq. (3.6) we know that the lepton number violating superpotential contains as well the $LQ\bar{D}$-term. Having one of the operators non-zero it leads to axino decays in a similar way as in the scenario of non-zero $LL\bar{E}$ operators. Analogously, this term can explicitly be involved in axino decay vertices.

In this section we briefly explain possible axino decays via a non-zero $LQ\bar{D}$-operator. Note, that depending on the mixing in the quark sector even initially zero couplings can be generated dynamically via the RGE couplings. But, such effects are expected to be suppressed in comparison to decays which contain a direct coupling of non-zero $LQ\bar{D}$ operators.

5.6.1 The decay $\tilde{a} \to M^0 \nu_i$

In this section we show axino decays into a neutral meson and a neutrino which contain explicitly a $LQ\bar{D}$ vertex. One such decay is shown in Fig. 5.16 and is comparable to the decays presented in section 5.2. The first vertex in Fig. 5.16 is due to the $\Phi_{\tilde{a}} L_i H_2$ operator. As already discussed in models with R-parity violation the neutrino mixes with the neutralinos. Hence the up-like Higgsino mixes with a neutrino which is denoted by the gray dot in Fig. 5.16.

The decay is mediated by sneutrinos and thus via the $LQ\bar{D}$ operator the quark pair can couple at the second vertex. This quark pair form a neutral meson M^0 in the final

Coupling	ν_f	$\tilde{\nu}_L$	π^0	K^0
c_2^1	ν_e ν_μ ν_τ	$\tilde{\nu}_e$	$(\mathbf{\Lambda}_{D^1})_{11}$	$(\mathbf{\Lambda}_{D^1})_{12}$
c_2^2	ν_e ν_μ ν_τ	$\tilde{\nu}_\mu$	$(\mathbf{\Lambda}_{D^2})_{11}$	$(\mathbf{\Lambda}_{D^2})_{12}$
c_2^3	ν_e ν_μ ν_τ	$\tilde{\nu}_\tau$	$(\mathbf{\Lambda}_{D^3})_{11}$	$(\mathbf{\Lambda}_{D^3})_{12}$

Table 5.5: Possible final state combinations of the decay presented in Fig. 5.16. The last two columns show the $LQ\bar{D}$ operators which, if non-zero, creates the listed meson in the first row. Of course, even if the couplings are zero, in a scenario with quark mixing we will have contributions due to dynamical effects. The sneutrino denotes the propagator, see text.

state, with $M^0 = \pi^0, K^0$. In the two component notation the according amplitude reads

$$\mathrm{i}\mathcal{M}_{16} \;=\; \frac{N_{\ell 3}}{M^2_{\tilde{\nu}_i}}\, x^\dagger(p_\nu)(\mathrm{i}c_2^i)y^\dagger(p_{\tilde{a}})(-\mathrm{i}\mathbf{\Lambda}_{D^k})_{ij}\frac{1}{\sqrt{2}}\left(\frac{m^2_{M^0} f_{M^0}}{m_{d_j}+m_{d_k}}\right), \tag{5.66}$$

where $N_{\ell 3}$ is the mixing angle of the Higgsino and the neutrino, with $\ell = 5, 6, 7$ depending on the neutrino family. $M_{\tilde{\nu}_i}$ and $m_{d_{j,k}}$ are the masses of the sneutrino propagator and the down quarks respectively.

As mentioned above we can have a pion or a kaon as a final state meson. A pion consists of the down-antidown quark pair. This leads directly to the conclusion that $j = k = 1$. In an analogous way we have for the kaon $j = 1$ and $k = 2$. The remaining free index i is correlated to the first vertex and its coupling, where it defines the flavor of the propagating sneutrino. Note that in addition to this we have three different neutrinos as possible final states which can be chosen independently. Thus in total we have nine final state combinations for each neutral meson. We have summarized them in Table 5.5. However, for the amplitude squared we have

$$\frac{1}{2}\sum_{\text{spins}}|\mathcal{M}_{16}|^2 \;=\; \frac{|N_{\ell 3}|^2|c_2^i|^2|(\mathbf{\Lambda}_{D^k})_{ij}|^2}{4M^4_{\tilde{\nu}_i}}\left(\frac{m^2_{M^0} f_{M^0}}{m_{d_j}+m_{d_k}}\right)^2 (m^2_{\tilde{a}} - m^2_{M^0})\,. \tag{5.67}$$

If we neglect the mass of the neutrino and if we use the known relation for the two body decay width, *cf.* Eq. (A.14) we obtain for the total decay width

$$\Gamma_{16} = \frac{1}{64\pi}\frac{|N_{\ell 3}|^2|c_2^i|^2|(\mathbf{\Lambda}_{D^k})_{ij}|^2}{M^4_{\tilde{\nu}_i}}\left(\frac{m^2_{M^0} f_{M^0}}{m_{d_j}+m_{d_k}}\right)^2 \frac{1}{m^3_{\tilde{a}}}\,(m^2_{\tilde{a}} - m^2_{M^0})^2\,. \tag{5.68}$$

The next process is shown in Fig. 5.17 which differs compared to the previous one. The

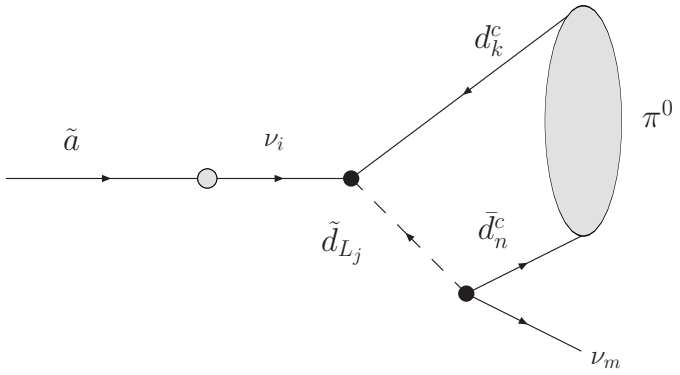

Figure 5.17: The second axino decay via the $LQ\bar{D}$ operator. Of course, usually if kinematically allowed the pion could be replaced through another neutral meson. But as only the pion consist of down quarks we can not have a decay into other neutral mesons, see text for details. The decay width is given by Γ_{17}.

axino as part of the neutralinos can mix with the neutrinos. This fact is used in this decay where the axino becomes a neutrino. This neutrino on his part can interact with a quark-squark via the $LQ\bar{D}$ operator. The second vertex can be as well realized through this operator leading to a neutrino in the final state. Hence, we have to construct an effective vertex, where the two quarks form a mesonic bound state. This can be easily performed after writing down the amplitude and applying a Fierz reordering

$$\mathrm{i}\mathcal{M}_{17} \;=\; \mathrm{i}N_{i8}\, y(d_k^c)[-\mathrm{i}(\mathbf{\Lambda}_{D^k})_{ij}]x(p_{\tilde{a}})\,\frac{1}{M^2_{\tilde{d}_{L_j}}}\,x^\dagger(p_\nu)[-\mathrm{i}(\mathbf{\Lambda}_{D^n})_{mj}]x^\dagger(d_n^c)\,. \tag{5.69}$$

Now, we can apply the following Fierz reordering in two component notation for the spinors z_i, see Ref. [78]

$$2(z_3^\dagger z_4^\dagger)(z_2 z_1) = (z_3^\dagger \bar{\sigma}^\mu z_1)(z_4^\dagger \bar{\sigma}_\mu z_2)\,. \tag{5.70}$$

With this equation the amplitude reads now:

$$\mathrm{i}\mathcal{M}_{17} \;=\; \frac{-\mathrm{i}N_{i8}}{2M^2_{\tilde{d}_{L_j}}}(\mathbf{\Lambda}_{D^k})_{ij}(\mathbf{\Lambda}_{D^n})_{mj}[x^\dagger(p_\nu)\bar{\sigma}_\mu x(p_{\tilde{a}})]\,[x^\dagger(d_n^c)\bar{\sigma}^\mu y(d_k^c)]\,. \tag{5.71}$$

The second term in the matrix element can be integrated out and we obtain the pseudoscalar decay constant of a meson [155]. Hence we have

$$\mathrm{i}\mathcal{M}_{17} = \frac{-\mathrm{i}N_{i8}}{2M^2_{\tilde{d}_{L_j}}}(\mathbf{\Lambda}_{D^k})_{ij}(\mathbf{\Lambda}_{D^n})_{mj}[x^\dagger(p_\nu)\bar{\sigma}_\mu x(p_{\tilde{a}})]\,\frac{1}{\sqrt{2}}f_\pi q_\pi^\mu\,. \tag{5.72}$$

Here we have used the fact that only the pion can be the neutral final state meson. This can be explained by the index structure of the two Yukawa couplings from the $LQ\bar{D}$ operator. These two couplings are correlated. Usually only one $\not{R}_p$ coupling is chosen to be non-zero which can be directly translated to the condition that $i = m$ and $n = k$. The

$\tilde{a} \to \nu_i$	ν_m	$\tilde{d}_j$	π^0
ν_e	ν_e		$(\mathbf{\Lambda}_{D^1})_{11}$
ν_μ	ν_μ	$\tilde{d}_L$	$(\mathbf{\Lambda}_{D^1})_{21}$
ν_τ	ν_τ		$(\mathbf{\Lambda}_{D^1})_{31}$
ν_e	ν_e		$(\mathbf{\Lambda}_{D^1})_{21}$
ν_μ	ν_μ	$\tilde{s}_L$	$(\mathbf{\Lambda}_{D^1})_{22}$
ν_τ	ν_τ		$(\mathbf{\Lambda}_{D^1})_{32}$
ν_e	ν_e		$(\mathbf{\Lambda}_{D^1})_{13}$
ν_μ	ν_μ	$\tilde{b}_L$	$(\mathbf{\Lambda}_{D^1})_{23}$
ν_τ	ν_τ		$(\mathbf{\Lambda}_{D^1})_{33}$

Table 5.6: Possible final state combinations of the decay presented in Fig. 5.17. The last column shows the $LQ\bar{D}$ operators which, if non-zero, creates the listed meson in the first row. Of course, even if the couplings are zero, in a scenario with quark mixing we will have contributions due to dynamical effects. The down squark denotes the propagator of this decay, see text.

neutral kaon is made up of $(d\bar{s})$ which would require $n \neq k$. This is not possible and yielding instead to a pion $(d\bar{d})$ as the final state. Hence in total we have nine final state combinations which are summarized in Table 5.6

Squaring the latter equation, averaging over the axino- and summing over the neutrino-spin we get for the amplitude squared

$$\frac{1}{2}\sum_{\text{spins}}|\mathcal{M}_{17}|^2 \;=\; \frac{|N_{i8}|^2}{16M^4_{\tilde{d}_{Lj}}}|(\mathbf{\Lambda}_{D^k})_{ij}|^2|(\mathbf{\Lambda}_{D^n})_{mj}|^2 f_\pi^2\, m_{\tilde{a}}^2(m_{\tilde{a}}^2 - m_\pi^2)\,. \tag{5.73}$$

As in the previous case we can insert this expression in Eq. (A.14) leading to the decay width

$$\Gamma_{17} = \frac{|N_{i8}|^2\,|(\mathbf{\Lambda}_{D^k})_{ij}|^2|(\mathbf{\Lambda}_{D^n})_{mj}|^2 f_\pi^2}{256\pi\, M^4_{\tilde{d}_{L_i}}\, m_{\tilde{a}}}(m_{\tilde{a}}^2 - m_\pi^2)^2\,. \tag{5.74}$$

The third decay, see Fig. 5.18, is comparable to the foregoing decay. The difference is that here the propagator has its origin in the singlet quark superfield. This results in a different diagram and employs a different Feynman rule, see Appendix of Ref. [78]. Thus in a similar way to Eq. (5.69) we find for the amplitude

$$\mathrm{i}\mathcal{M}_{18} \;=\; \mathrm{i}N_{i8}\, y(d_j)(-\mathrm{i}(\mathbf{\Lambda}_{D^k})_{ij})x(p_{\tilde{a}})\,\frac{1}{M^2_{\tilde{d}_{Rk}}}\,x^\dagger(p_\nu)(-\mathrm{i}(\mathbf{\Lambda}_{D^k})_{mn})x^\dagger(d_n)\,. \tag{5.75}$$

In an analogous calculation to Eq. (5.73) we find for the amplitude squared

$$\frac{1}{2}\sum_{\text{spins}}|\mathcal{M}_{18}|^2 \;=\; \frac{|N_{i8}|^2}{16M^4_{\tilde{d}_{Rk}}}|(\mathbf{\Lambda}_{D^k})_{ij}|^2|(\mathbf{\Lambda}_{D^k})_{mn}|^2 f_\pi^2\, m_{\tilde{a}}^2(m_{\tilde{a}}^2 - m_\pi^2)\,. \tag{5.76}$$

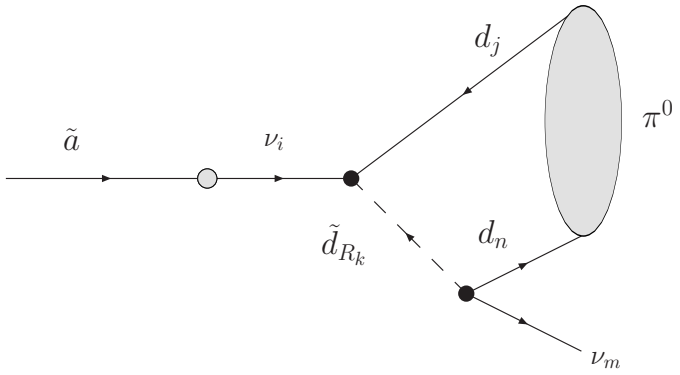

Figure 5.18: The third axino decay via the $LQ\bar{D}$ operator. Of course, usually if kinematically allowed the pion could be replaced through another neutral meson. But as only the pion consist of down-like quarks we can not have a decay into other neutral mesons. The decay width is given by Γ_{18}.

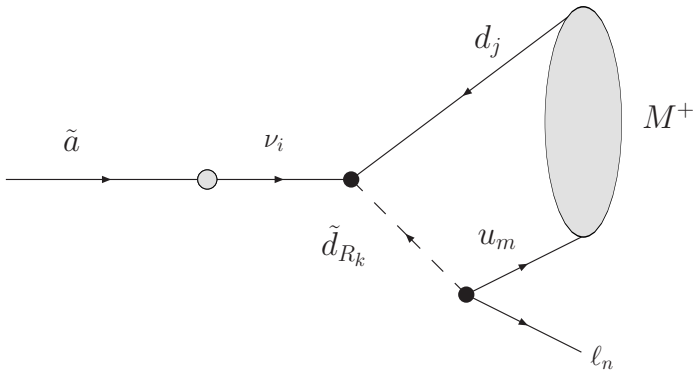

Figure 5.19: The fifth axino decay via the $LQ\bar{D}$ operator. Of course, usually if kinematically allowed the pion could be replaced through another charged meson. In this scenario here with a $u\bar{d}$ combination we can have *e.g.* K^+, D^+, or B^+ etc.

The latter equation only differs in the structure of the $\mathbf{\Lambda}_D$ couplings.

The decay width reads then

$$\Gamma_{18} = \frac{|N_{i8}|^2\,|(\mathbf{\Lambda}_{D^k})_{ij}|^2|(\mathbf{\Lambda}_{D^k})_{mn}|^2 f_\pi^2}{256\pi\, M^4_{\tilde{d}_{Rk}}\, m_{\tilde{a}}}(m_{\tilde{a}}^2 - m_\pi^2)^2\,. \tag{5.77}$$

Likewise as before both vertices in Fig. 5.18 are of $\mathbf{\Lambda}_D$ nature and thus correlated. This means that the indices are restricted that only a Pion can be formed in the final state. In total we have nine final state combinations which are listed in Table 5.7.

$\tilde{a} \to \nu_i$	ν_m	$\tilde{d}_{R_k}$	π^0
ν_e	ν_e		$(\mathbf{\Lambda}_{D^1})_{11}$
ν_μ	ν_μ	$\tilde{d}_R$	$(\mathbf{\Lambda}_{D^1})_{21}$
ν_τ	ν_τ		$(\mathbf{\Lambda}_{D^1})_{31}$
ν_e	ν_e		$(\mathbf{\Lambda}_{D^1})_{21}$
ν_μ	ν_μ	$\tilde{s}_R$	$(\mathbf{\Lambda}_{D^1})_{22}$
ν_τ	ν_τ		$(\mathbf{\Lambda}_{D^1})_{32}$
ν_e	ν_e		$(\mathbf{\Lambda}_{D^1})_{13}$
ν_μ	ν_μ	$\tilde{b}_R$	$(\mathbf{\Lambda}_{D^1})_{23}$
ν_τ	ν_τ		$(\mathbf{\Lambda}_{D^1})_{33}$

Table 5.7: Possible final state combinations of the decay presented in Fig. 5.18. The last column shows the $LQ\bar{D}$ operators which, if non-zero, creates the listed meson in the first row. Of course, even if the couplings are zero, in a scenario with quark mixing we will have contributions due to dynamical effects. The down squark denotes the propagator of this decay, see text.

5.6.2 The decay $\tilde{a} \to M^\pm \ell_i^\mp$

The last two decays contain a charged meson as well as a charged lepton. In the decay in Fig. 5.19 the axino mixes with the neutrino. This neutrino interacts with a quark-squark pair. Both vertices are due to the $LQ\bar{D}$ operator and correlated. This means that the $\mathbf{\Lambda}_D$ vertex factors are restricted.

These restriction become more obvious if we take a closer look at the amplitude given by

$$\mathrm{i}\mathcal{M}_{19} = \frac{\mathrm{i}N_{i8}}{M^2_{\tilde{d}_{Rk}}} y(d_j)(-\mathrm{i}(\mathbf{\Lambda}_{D^k})_{ij}) x(p_{\tilde{a}})\, x^\dagger(p_{\ell_m})(-\mathrm{i}(\mathbf{\Lambda}_{D^k})_{mn}) x^\dagger(u_n)\,. \tag{5.78}$$

It is obvious that we have for the indices of the $\mathbf{\Lambda}_D$ couplings $j = n$ and $i = m$. We can deduce that the neutrino and the up quark are related. On the other hand the charged final state lepton and the down quark have an identical family index. Keeping this in mind we can have a π^+ and a K^+ in the final state. In Table 5.8 you find all possible final states for this decay process.

After applying the Fierz reordering and integrating over the meson states we obtain for the amplitude squared

$$\frac{1}{2}\sum_{\text{spins}} |\mathcal{M}_{19}|^2 = \frac{|N_{i8}|^2}{16 M^4_{\tilde{d}_{R_k}}} |(\mathbf{\Lambda}_{D^k})_{ij}|^2 |(\mathbf{\Lambda}_{D^k})_{mj}|^2 f^2_{M^+} \left[(m^2_{\tilde{a}} + m^2_{M^+} - m^2_\ell)(m^2_{\tilde{a}} - m^2_\ell - m^2_{M^+}) - m^2_{M^+}(m^2_{\tilde{a}} - m^2_{M^+} + m^2_\ell)\right]. \tag{5.79}$$

The mass of the final state lepton can not be neglected which explains the lengthy latter equation. Furthermore for the decay width we use Eq. (A.14) where the according

M^+	$\tilde{a} \to \nu_i$	ℓ_m	$\tilde{d}_{R_k}$	$\mathbf{\Lambda_D}$
π^+	ν_e	e^-	$\tilde{d}_R$	$(\mathbf{\Lambda}_{D^1})_{11}$
			$\tilde{s}_R$	$(\mathbf{\Lambda}_{D^2})_{11}$
			$\tilde{b}_R$	$(\mathbf{\Lambda}_{D^3})_{11}$
K^+	ν_e	μ^-	$\tilde{d}_R$	$(\mathbf{\Lambda}_{D^1})_{12}$
			$\tilde{s}_R$	$(\mathbf{\Lambda}_{D^2})_{12}$
			$\tilde{b}_R$	$(\mathbf{\Lambda}_{D^3})_{12}$

Table 5.8: Possible final state combinations of the decay presented in Fig. 5.19. The last column shows the $LQ\bar{D}$ operators which, if non-zero, creates the listed meson in the first column. Of course, even if the couplings are zero, in a scenario with quark mixing we will have contributions due to dynamical effects. The down squark denotes the propagator, see text.

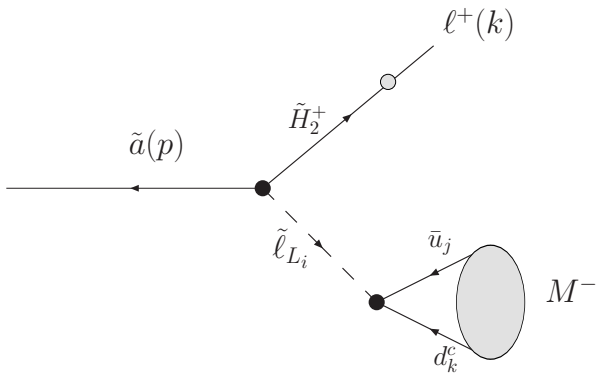

Figure 5.20: The second axino decay via the $LQ\bar{D}$ operator. Of course, usually if kinematically allowed the charged meson M^- could be replaced by π^- or K^-.

momentum parameter is given by

$$|p_2| = \frac{1}{2m_{\tilde{a}}}\sqrt{m_{\tilde{a}}^4 + m_{M^+}^4 + m_\ell^4 - 2m_{\tilde{a}}^2 m_{M^+}^2 - 2m_{\tilde{a}}^2 m_\ell^2 - 2m_{M^+}^2 m_\ell^2}\,. \tag{5.80}$$

Hence, finally we obtain for the decay width

$$\begin{aligned}\Gamma_{19} \;=\; & \frac{|N_{i8}|^2|(\mathbf{\Lambda}_{D^k})_{ij}|^2|(\mathbf{\Lambda}_{D^k})_{mj}|^2 f_{M^+}^2}{256 M_{\tilde{d}_{Rk}}^4\, m_{\tilde{a}}^3}\sqrt{m_{\tilde{a}}^4 + m_{M^+}^4 + m_\ell^4 - 2m_{\tilde{a}}^2 m_{M^+}^2 - 2m_{\tilde{a}}^2 m_\ell^2 - 2m_{M^+}^2 m_\ell^2} \\ & \times\Big[(m_{\tilde{a}}^2 + m_{M^+}^2 - m_\ell^2)(m_{\tilde{a}}^2 - m_\ell^2 - m_{M^+}^2) - \, m_{M^+}^2(m_{\tilde{a}}^2 - m_{M^+}^2 + m_\ell^2)\Big]\end{aligned} \tag{5.81}$$

The last decay is shown in Fig. 5.20. This decay is pretty similar to the fifth decay presented in section 5.3.2. There we had as well an axino decay to a charged meson-lepton pair mediated by a charged Higgs. Thus, the structure is identical, but we have

Coupling	ℓ^+	$\tilde{\ell}_{L_i}$	π^-	K^-
c_2^1	e^+ μ^+	$\tilde{e}_L$	$(\mathbf{\Lambda}_{D^1})_{11}$	$(\mathbf{\Lambda}_{D^2})_{11}$
c_2^2	e^+ μ^+	$\tilde{\mu}_L$	$(\mathbf{\Lambda}_{D^2})_{11}$	$(\mathbf{\Lambda}_{D^2})_{21}$
c_2^3	e^+ μ^+	$\tilde{\tau}_L$	$(\mathbf{\Lambda}_{D^3})_{11}$	$(\mathbf{\Lambda}_{D^2})_{31}$

Table 5.9: Possible final state combinations of the decay presented in Fig. 5.20. The last two columns show the Yukawa couplings of the $LQ\bar{D}$ operator where the pion or the kaon respectively are realized. The listed slepton denotes the propagator of the decay, see text.

a different propagator and a $(\mathbf{\Lambda}_{D^k})_{ij}$ Yukawa coupling at the second vertex. Considering these changes the amplitude reads

$$\mathrm{i}\mathcal{M}_{20} = \frac{\mathrm{i}\,V_{i2}}{M^2_{\tilde{\ell}_{L_i}}}\, y^\dagger(p_{\tilde{a}})(\mathrm{i}c_2^i)x^\dagger(k_l)(\mathbf{\Lambda}_{D^k})_{ij}\frac{1}{\sqrt{2}}\frac{m^2_{M^-}f_{M^-}}{m_{u_j}+m_{d_k}}\,. \tag{5.82}$$

Here we have only one $\mathbf{\Lambda}_D$ coupling which gives a free choice of the coupling itself. But, the first vertex and the family index of the propagator are correlated. Hence, the choice of c_2^i predefines the slepton family. However, we can have a pion or a kaon in the final state, see Table 5.9.

$$\frac{1}{2}\sum_{\text{spins}}|\mathcal{M}_{20}|^2 \;=\; \frac{|c_2^i|^2\,|V_{i2}|^2\,|(\mathbf{\Lambda}_{D^k})_{ij}|^2}{4\,M^4_{\tilde{\ell}_{L_i}}}\left(\frac{m^2_{M^-}f_{M^-}}{m_{u_j}+m_{d_k}}\right)^2(m^2_{\tilde{a}}+m^2_\ell-m^2_{M^-})\,. \tag{5.83}$$

Comparing this amplitude squared with Eq. (5.79) the decay width can be easily read of to

$$\begin{aligned}\Gamma_{20} \;=\; &\frac{|c_2^i|^2|V_{i2}|^2|(\mathbf{\Lambda}_{D^k})_{ij}|^2}{64M^4_{\tilde{\ell}_{L_i}}\,m^3_{\tilde{a}}}\left(\frac{m^2_{M^-}f_{M^-}}{m_{u_j}+m_{d_k}}\right)^2(m^2_{\tilde{a}}+m^2_\ell-m^2_M)\\ &\times\sqrt{m^4_{\tilde{a}}+m^4_{M^-}+m^4_\ell-2m^2_{\tilde{a}}m^2_{M^-}-2m^2_{\tilde{a}}m^2_\ell-2m^2_\ell m^2_{M^-}}\,.\end{aligned} \tag{5.84}$$

With the setting that the lepton number violation is due to the $LQ\bar{D}$ operator we saw that the additional axino decays are solely of mesonic nature. Furthermore it was shown that even in the case of higher axino masses not every meson state can be generated. These restrictions are an intrinsic result of the vertex- and thus Yukawa-coupling structure of the decay processes. Note that these restrictions and the resulting decrease of final state combinations were only present in cases where we had two vertices with two $LQ\bar{D}$ Yukawa couplings. Keeping these decays in mind we can now go on to compute the branching ratios and to find the preferred processes of the axino decay.

6 The Branching Ratios

In the last chapter we have presented all possible axino decays coming from the θ-term and the DFSZ supersymmetric axion model. Furthermore we split this analysis due to the origin of R-Parity violation. We have on the one hand decays from the $LL\bar{E}$ operator and on the other hand from the $LQ\bar{D}$ operator.

In this chapter we specify the corresponding branching ratios (BR) depending on the chosen $\not{R}_p$ coupling. Of course, going through every $\not{R}_p$ coupling from the $LL\bar{E}$- and $LQ\bar{D}$-operator is tedious. We have 9 $LL\bar{E}$ operators, 27 $LQ\bar{D}$ operators and the latter with various mixing scenarios to be analysed.

Taking a closer look at the RGEs we can deduce which axino Yukawa coupling is the largest in each scenario. We will restrict our analysis to representative cases which then can be generalized to other $\not{R}_p$ coupling. Nevertheless for completeness, we show the omitted branching ratios in Appendix D.

This chapter is devided into two parts. Similar, to the previous chapter we first present the results coming from the $LL\bar{E}$ operator. In the second part we focus on the couplings coming from the $LQ\bar{D}$ operator. Both analyses will be performed, as in section 4.2, for the benchmark point SPS1a. The parameters of SPS1a are

$$M_0 = 100 \text{ GeV},\ M_{1/2} = 250 \text{ GeV},\ A_0 = -100 \text{ GeV},\ \tan\beta = 10\ \ \text{sgn}(\mu) = +1\,. \qquad (6.1)$$

The BRs were computed with our own program where the particle masses, mixing angles etc. were obtained from the program `Softsusy3.0`, see Ref. [39]. We already pointed out in chapter 4 that the RGE of `Softsusy3.0` can be used as well in our case. The changes in the RGEs due to the axino are of minor importance. Hence, we have implemented the axino as a new additional neutralino together with all the decay processes introduced in the previous chapter.

6.1 The BR with the $\not{R}_p\, LL\bar{E}$ operator

Before we present the results of the BRs we estimate of the dominant $\not{R}_p\, LL\bar{E}$ couplings. In section 3.1 it was pointed out that at M_{GUT} the c_2^i can be rotated to zero. But we have $c_2^i|_{M_{\text{W}}} \neq 0$ which means that the couplings are generated dynamically via the RGEs.

Hence we take a closer look at the RGEs at the M_{GUT} scale. From Eq. (C.10) we have

$$16\pi^2 \frac{\mathrm{d}}{\mathrm{d}t} c_2^i \approx c_1 \Big[-3(\mathbf{\Lambda}^*_{D^q} \mathbf{Y}_{D^q})_{iq} - (\mathbf{\Lambda}^*_{E^q} \mathbf{Y}_E)_{iq} \Big]\,, \qquad (6.2)$$

where this part is the only non-zero contribution of the RGE. All other terms include explicitly a c_2^i which is zero at M_{GUT}. Now, depending on the choice of the $\not{R}_p$ operator

$(\mathbf{\Lambda}_{E^k})_{ij}$	c_2^i	Upper bound
$(\mathbf{\Lambda}_{E^1})_{21}$	c_2^2	0.1
$(\mathbf{\Lambda}_{E^1})_{31}$	c_2^3	0.1
$(\mathbf{\Lambda}_{E^1})_{23}$	none	not considered
$(\mathbf{\Lambda}_{E^2})_{12}$	c_2^1	$6 \cdot 10^{-4}$
$(\mathbf{\Lambda}_{E^2})_{13}$	none	not considered
$(\mathbf{\Lambda}_{E^2})_{32}$	c_2^3	$6 \cdot 10^{-4}$
$(\mathbf{\Lambda}_{E^3})_{12}$	none	not considered
$(\mathbf{\Lambda}_{E^3})_{13}$	c_2^1	$3.5 \cdot 10^{-5}$
$(\mathbf{\Lambda}_{E^3})_{23}$	c_2^2	$3.5 \cdot 10^{-5}$

Table 6.1: Dominant c_2^i coupling depending on the chosen $LL\bar{E}$ operator at $M_{\rm GUT}$. In the rightmost column you find the upper bound for the $\not{R}_p$ couplings, *cf.* also Ref. [35]. The values differ a slightly in comparison to Ref. [35], see Ref. [156].

we can directly deduce the non-zero c_2^i Yukawa coupling or the largest one, respectively. Taking as an example $(\mathbf{\Lambda}_{E^3})_{13}$ it is obvious that the first term in Eq. (6.2) vanishes. Keeping in mind that $\mathbf{\Lambda}_E$ is antisymmetric we have

$$16\pi^2 \frac{\mathrm{d}}{\mathrm{d}t} c_2^{i=1} \approx -(\mathbf{\Lambda}^*_{E^3})_{13}(\mathbf{Y}_E)_{33} \quad \text{or} \quad 16\pi^2 \frac{\mathrm{d}}{\mathrm{d}t} c_2^{i=3} \approx +(\mathbf{\Lambda}^*_{E^3})_{31}(\mathbf{Y}_E)_{13}\,, \tag{6.3}$$

where we have decomposed the matrix product. It is apparent that the first option with $i = 1$ will be prefered and dominant because the $\not{R}_p$ operator is multiplied with a diagonal part of the SM Yukawa coupling. We performed such a check with all $\not{R}_p\, LL\bar{E}$ operators and summarize the results in Table 6.1. From this table we see that due to the symmetries and anti-symmetries the number of non-zero couplings has been reduced to six. Among these six it is resonable to analyse the BR only of three different $(\mathbf{\Lambda}_{E^k})_{ij}$ operators which have three different dominant c_2^i. The BR for the remaining operators can then be deduced easily. Another point is the discussion of the c_1 Yukawa coupling which we will perform below.

In Fig. 6.1 we show the BR as a function of the axino mass, employing the decays presented in the last chapter. Here we have chosen the $\not{R}_p$ coupling $(\mathbf{\Lambda}_{E^2})_{12} = 6 \times 10^{-4}$. From the previous considerations we know that c_2^1 is the strongest axino coupling, *cf.* Table 6.1. As a consequence, all couplings to the electron lepton family are preferred, i.e. vertices/mixings with the electron neutrino or the electron itself. This conclusion is confirmed by Fig. 6.1. Obviously the chosen $\not{R}_p$ coupling has a direct impact on the final state combinations. One important point is that all decay channels which include a c_1 vertex do not play a role. Recalling the related decay width expressions from the last chapter we see that denominator is rather large and the nominator small when we insert all couplings and masses. Hence we can neglect all such decays.

Furthermore in Fig. 6.1 it can be seen that several mass regimes exist. These regimes

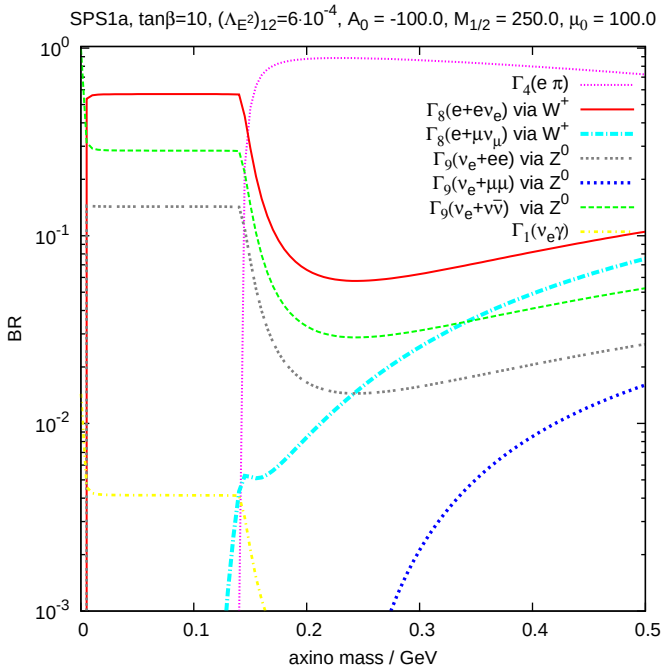

Figure 6.1: The BR of the axino decays at the benchmark point SPS1a with the $\not{R}_p$ coupling $(\mathbf{\Lambda}_{E^2})_{12} = 6 \times 10^{-4}$. With the chosen $\not{R}_p$ operator c_2^1 is the relevant Yukawa coupling where the axino couples preferred to the electron family. Due to kinematical thresholds of the decay channels several mass regimes are formed with different behaviour. For details see text.

are due to the sum of the rest masses of the different final state particles. *A priori* there exist seven mass region, which are summarized in Table 6.2. We will go through each mass domain and explain the origin of the dominant decay process.

First, assuming a massless neutrino at the lowest energies, the first- as well as the neutrino channel of the ninth decay are kinematically possible. But the latter process $\tilde{a} \to \nu_e\nu\nu$ is preferred as can be seen in Fig. 6.1. This dominance changes at a energy of about 1 MeV, which corresponds to the rest mass energy of an electron-positron pair. At such masses two more decays are kinematically accessible play and compete against each other. Note all three processes are SM-like where the gauge bosons are mediating the decays. In the case of Γ_8 it is the W^+ boson and for Γ_9 it is the Z^0 boson.

An interesting issue within this window is that we observe for the ratios $\Gamma_{8e}/\Gamma_{9e} \approx 4$ and $\Gamma_{9,3\nu}/\Gamma_{9e} \approx 2$. This behaviour can be easily understood by considering the explicit decay widths given in section 5.4.1. For the first case we have, *cf.* Eqs. (5.37) and (5.43),

$$\begin{aligned} \frac{\Gamma_{8e}}{\Gamma_{9e}} &= \frac{G_F^2 |N_{i8}|^2}{192\pi^3}\, m_{\tilde{a}}^5 \Big/ \frac{|N_{i8}|^2 G_F^2 (a_f^2 + b_f^2)}{96\pi^3} m_{\tilde{a}}^5 \\ &= \frac{1}{2(a_f^2 + b_f^2)} \approx 4\,. \end{aligned} \tag{6.4}$$

Recall that $a_f = \sin^2\theta_{\mathrm{W}} - \frac{1}{2}$ and $b_f = \sin^2\theta_{\mathrm{W}}$. A similar calculations holds for the other case.

	Mass regions
1	$2m_e \geqslant m_{\tilde{a}}$
2	$m_\mu + m_e \geqslant m_{\tilde{a}} > 2m_e$
3	$m_\pi \geqslant m_{\tilde{a}} > m_\mu + m_e$
4	$2m_\mu \geqslant m_{\tilde{a}} > m_\pi$
5	$m_\pi + m_\mu > m_{\tilde{a}} > 2m_\mu$
6	$m_K \geqslant m_{\tilde{a}} \geqslant m_\pi + m_\mu$
7	$m_{\tilde{a}} > m_K$

Table 6.2: In this table the different kinematical mass regions are summarized. Depending on the mass of the axino we can have several possibilities for the axino decay.

Note that the decay widths Γ_{8e} and Γ_{9e} employ the same final states. As shown, both decay channels are of the same order and thus we have to consider the interference. If we neglect the mass of the electron we obtain for the continued decay width

$$\Gamma_{W,Z,e} = \frac{7}{4}\frac{G_F^2|N_{i8}|^2}{192\pi^3}m_{\tilde{a}}^5\,. \tag{6.5}$$

Using the latter expression and Eq. (5.44) we have

$$\Gamma_{\text{tot}} = \Gamma_{W,Z,e} + \Gamma_{9\nu} \Longleftrightarrow \frac{7}{2}\Gamma_{9\nu} + \Gamma_{9\nu} = \frac{9}{2}\Gamma_{9\nu}\,. \tag{6.6}$$

Hence the three neutrino channel has a BR of ~ 22 % which means a decrease of ~ 8 % or in turn an increase to $\Gamma_{W,Z,e}$ in comparison to the scenario without interference. Note that this only holds in scenarios with c_2^1 where this Yukawa coupling leads to a preference of an electron positron pair in the final state for $\Gamma_{8,9}$. In scenarios with c_2^2 (c_2^3) the axino mixes dominantly with the muon (tau) flavor. The decay $\tilde{a} \to e^+e^-\nu$ via the W boson then becomes negligible. In general, adding only the BR contributions of Γ_{8e} and Γ_{9e} is a good approximation.

This mass regime persists up to the muon mass. At this threshold the muon channel of Γ_8. But all three processes, $\Gamma_{8_{e,\mu}}$ and $\Gamma_{9_{e,\nu}}$, drop off at the pion mass, where Γ_4 including a pion has the significantly the largest BR.

Going over to higher energies the order mentioned above is not changed. The BR of the pionic decay remains the largest even when the axino mass is larger than the kaon mass. The decay into the kaon mediated by the W boson is smaller as the according CKM matrix element is smaller. Hence, we can conclude that decays into the kaon do not play a role and that no further interferences have to be taken into account.

Another conclusion is that no decay with an explicit $\not{R}_p\, LL\bar{E}$ vertex comes into play. All decays of this kind are suppressed by a few orders of magnitude. We know that the corresponding matrix elements are proportional to the quadratic $\not{R}_p$ coupling. Hence,

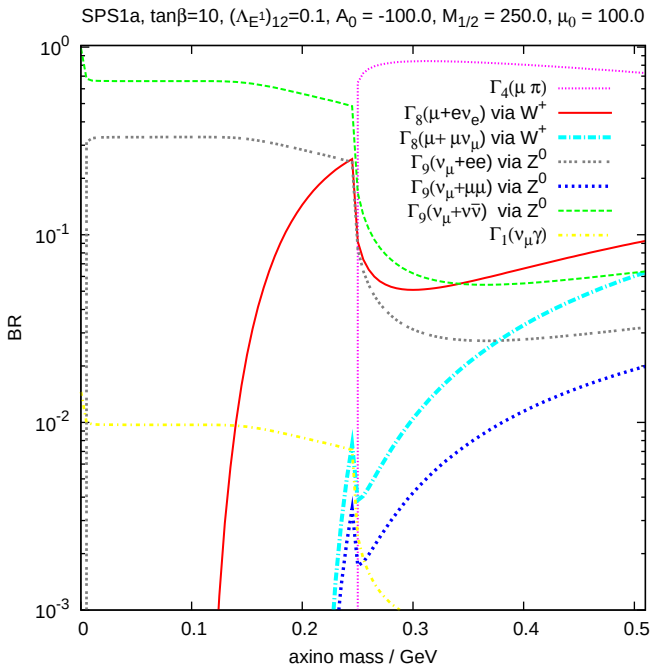

Figure 6.2: The BR of the axino decays at the benchmark point SPS1a with the $\not{R}_p$ coupling $(\mathbf{\Lambda}_{E^1})_{12} = 0.1$. With the chosen $\not{R}_p$ operator c_2^2 is the relevant Yukawa coupling where the axino couples preferred to the muon family. Due to kinematical thresholds of the decay channels several mass regimes are formed with different behaviour. For details see text.

at first glance one would assume that we have to choose a possibly larger value for the $\not{R}_p$ coupling that decays due to $LL\bar{E}$ become dominant. This can lead then to larger decay widths and therefore to a dominance of a decay due to the $LL\bar{E}$ operator. But we have seen in the previous sections that all couplings are connected by the RGE, see *e.g.* Eq. (6.2). Changing $\mathbf{\Lambda}_{E^i}$ has a direct impact on the RGE and, thus on the c^α. These play a crucial role for the predominant part of the considered decay processes. However, we know that the c^α are related to the sneutrino *vevs* through the minimization conditions of the scalar potential in the MSSM, see Ref. [35]. On the other hand the sneutrino vevs describe the strength of the neutralino- and chargino-mixing respectively. Thus changing the value of the $\not{R}_p$ coupling changes accordingly all other decay relevant couplings. In conclusion the order of the decays remains and any decay channel including an $LL\bar{E}$ vertex is negligible.

As a next example, we choose $(\mathbf{\Lambda}_{E^1})_{12} = 0.1$ which means that c_2^2 is the preferred axino Yukawa coupling. The corresponding BRs as a function of the axino mass can be found in Fig. 6.2. Similarly to the discussion above, all decays into muon flavour are the largest. This includes as well the mixing of the axino with the neutrinos.

Again, we see here different mass regions, *cf.* Table 6.2. Analogously, we go through the mass domains.

Obviously, for low axino masses only the radiative and the three neutrino decay are possible, where the latter is dominant. Nevertheless, we observe a higher BR of the

radiative mode in comparison to the previous example. The crucial factors for the ratio of the BRs of these two decays are the relevant mixing angles. Despite the fact that the mSUGRA parameter space point is the same, the different $\not{R}_p$ couplings lead to a different ratio of the mixing angles and thus of the BRs. If we increase the mass above the threshold for electron-positron pair production the ninth decay which is mediated by Z^0 comes into play. At this second mass region[1], we have no other SM like decay. Apparently an inclusion of the W^+ based decay, as previously seen, would require a mixing $\tilde{a} \leftrightsquigarrow \nu_e$, which is not possible with the chosen $\not{R}_p$ operator. Hence, the BR is dominated by $\Gamma_9(\tilde{a} \to \nu_\mu \nu\nu)$ by a factor of two, as explained above.

With the beginning of the third mass region, muons can be produced. Only process eight via the charged gauge boson, challenges with Γ_9 taking 30 % of the BR. This value is reached at the edge of the fifth and sixth mass region. At this level, decays into muon+pion become kinematically accessible and thus Γ_4 is dominant. All other decay modes drop off. This leads to the visible kinks in Fig. 6.2. In general, we would have to consider the interference of the decays into two muons coming from the eighth and ninth decay. But, the full amplitude squared reads

$$\frac{1}{2}\sum_{\text{spins}} |\mathcal{M}_8 + \mathcal{M}_9|^2 \;=\; 128\, G_F^2\, |N_{i8}|^2 \left[\left(\frac{1}{2} + a_f^2 + b_f^2\right)(p_{\tilde{a}} \cdot p_{\ell^+})(p_{\ell^-} \cdot p_{\nu_i}) - 2\left(a_f b_f + \frac{b_f}{16}\right)(p_{\tilde{a}} \cdot p_{\nu_i}) m_\ell^2 \right], \tag{6.7}$$

where the expression proportional to $b_f/16$ in the second term denotes the contribution from the interference of $\mathcal{M}_8$ and $\mathcal{M}_9$. In this case the interference contribution is small and thus we drop it. We also do not have any impact of the kaonic decays where the same argument holds as in the scenario before.

As a last example of the $LL\bar{E}$ operator we have $(\mathbf{\Lambda}_{E^1})_{31} = 0.1$, see Fig. 6.3, where c_2^3 is the strongest axino coupling. As consequence, in this scenario interactions with the tau lepton family are favored. Obviously Fig. 6.3 has a clear structure. The simple reason is that we are not considering axinos with masses comparable to the tau mass. As a matter of fact no taus can be produced which reduces the number of decays. Escpecially, no interactions with the W-boson are possible. This excludes the up to now always present pionic fourth decay mode.

Hence, we observe only three processes which play a role. At all scales the three neutrino decay channel of the nineth process is dominant. Of course, depending on the axino mass we can have slightly changed BRs. Increasing the mass of the axino the other channels of Γ_9 come into play. Obviously, next to the purely neutrino decay we have the decay to the electron positron pair followed by the two muon final state. However, it is apparent from Fig. 6.3 that we have again a ratio of two in the BR between the electron and neutrino final states. The upcoming muonic channel causes a small decrease of the first two cases but without changing the overall order.

We mentioned at the beginning of this section that the figures presented here are

[1]This label is according to the definition in Table 6.2

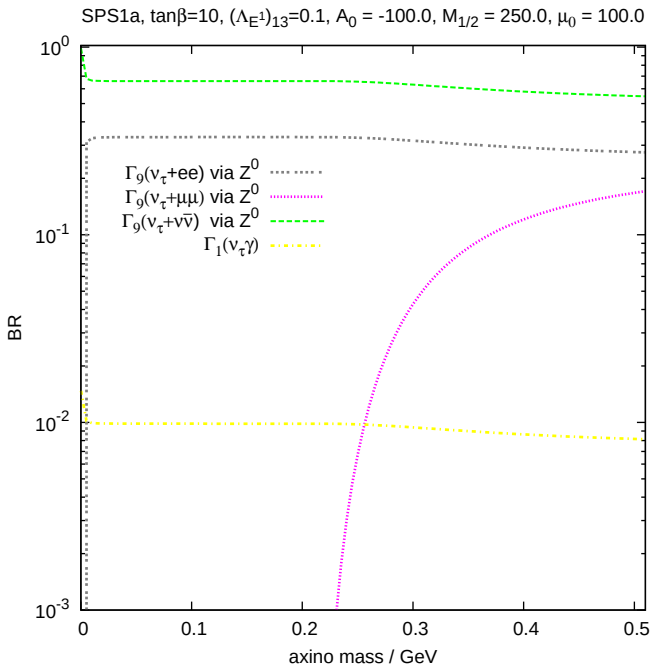

Figure 6.3: The BR of the axino decays at the benchmark point SPS1a with the $\not{R}_p$ coupling $(\mathbf{\Lambda}_{E^1})_{31} = 0.1$. With the chosen $\not{R}_p$ operator c_2^3 is the relevant Yukawa coupling where the axino couples preferred to the tau family. Due to kinematical thresholds of the decay channels several mass regimes are formed with different behaviour. For details see text.

reprensentative. In Appendix D.1 you will find the three remaining BRs. The arguments listed here can be transfered without loss of generality.

6.2 The BRs with the $LQ\bar{D}$ operator

In comparison to the previous section the scenario with non-zero $LQ\bar{D}$ coupling is more complicated. At first, the different quark flavors mix among one another, which is described by the CKM matrix [35, 157]. This mixing leads to a coupling of the corresponding RGEs. As a consequence one non-zero $(\mathbf{\Lambda}_{D^k})_{ij}$ operator at the GUT scale affects a dynamical generation of many other B_3 couplings at lower energy scales.

However, due to these new effects the following analysis can be split into three categories of quark mixing [35]:

- no mixing,
- up-mixing,
- down-mixing.

Here up- (down-) mixing refers to the sector where we have predominantly the mixing in the quark sector. This will also be the order in which we present the results in the following

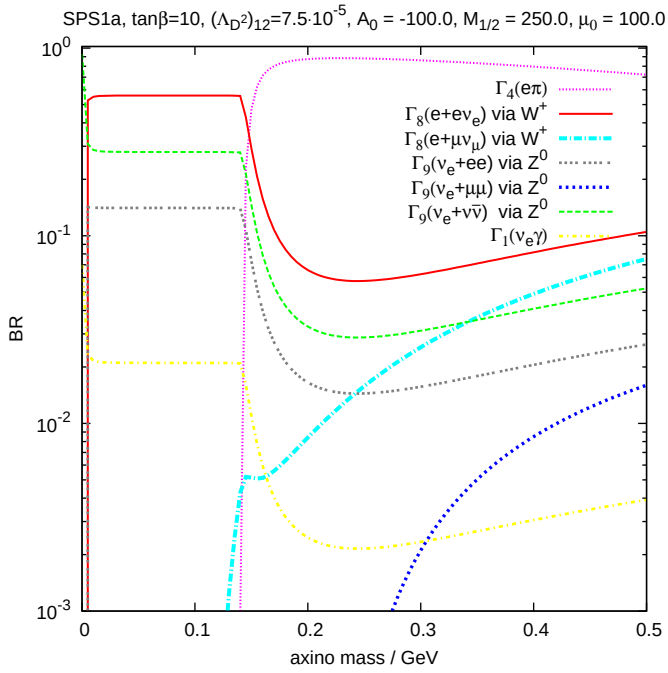

Figure 6.4: The BR of the axino decays at the benchmark point SPS1a with the $\not{R}_p$ coupling $(\mathbf{\Lambda}_{D^2})_{12} = 7.5 \times 10^{-5}$, no-mixing assumption. With the chosen $\not{R}_p$ operator c_2^1 is the relevant Yukawa coupling where the axino couples preferred to the electron family. Due to kinematical thresholds of the decay channels several mass regimes are formed with different behaviour.

sections. Of course, the condition that no mixing is present is a strong simplification which we cite for a better comparability with the mixing cases.

6.2.1 No mixing scenario

In section 6.1 we argued that at M_{GUT} the axino couplings c_2^i can be rotated away to zero. Furthermore the considerations of Eq. (6.2) showed that a single non-zero $\not{R}_p$ coupling generates non-zero c_2^i dynmically, due to the RGE. Furthermore with the same arguments as in the section before all decays with a c_1 are of no significance.

In our previous example of the $LL\bar{E}$ operator other B_3 coupling have been zero in Eq. (6.2). Now, we have the opposite where the lepton number violation is due to $LQ\bar{D}$ operator yielding

$$16\pi^2 \frac{\mathrm{d}}{\mathrm{d}t} c_2^i \supset c_1 \Big[-3(\mathbf{\Lambda}^*_{D^q} \mathbf{Y}_D)_{iq} \Big] . \tag{6.8}$$

Hence, having a $\mathbf{\Lambda}_{D^i} \neq 0$, we have again a preference of axino couplings in dependence on the chosen operator. Thus we can conclude as in the section before that for a given operator we are able to read off the strongest axino coupling generated by the RGE. Except of the absolute value which the RGE returns at lower energy scales the phenomenology of the BR will be the same in the leading cases. Note that the $\mathbf{\Lambda}_D$ matrices are not anti-symmetric which results in 27 possible couplings. Inserting these couplings into Eq. (6.8) we obtain only from 9 couplings a non-zero contribution. Of course, this reduction is due

to the no-mixing assumption as the SM Yukawa coupling matrices are diagonal. Having some kind of mixing these matrices are not diagonal any longer and additional terms will contribute dynamically to the c_2^i RGEs. In the following examples we assume the upper bounds for the $\not{R}_p\, LQ\bar{D}$ trilinear couplings presented in Ref. [35] and summarized in Table 6.3.

As a first example we show in Fig. 6.4 the axino BRs for the coupling $(\mathbf{\Lambda}_{D^2})_{12} \neq 0$. Comparing Fig. 6.4 and Fig. 6.1 with a $LL\bar{E}$ coupling, we observe no major difference in the BRs of the leading decay channels. Similarly, in the second mass window the electron channel of $\Gamma_{8e,9e}$ interfere, as explained above. Note that here the radiative decay mode has a higher BR fraction. This depends on the ratio of the related mixing angles of the decay widths which in turn depends on the chosen $\not{R}_p$ operator.

However, we do not expect to see any changes in the order of the BRs. The reason is that for a chosen $\not{R}_p$ coupling, we can directly deduce the preferred axino coupling c_2^i and the relevant decay channels. Furthermore the coupling strength of the c_2^i does not play a role as it is canceled in the BR. Thus in general the procedure is the same in both scenarios independently whether we have a non zero $LL\bar{E}$ or $LQ\bar{D}$ operator.

In conclusion the BR remain in the same order and dominance as seen in the previous section. We expect a similar behaviour for the other $\not{R}_p$ operators.

To confirm this conclucion we show a second example in Fig. 6.5(a). In this graph $(\mathbf{\Lambda}_{D^1})_{21} = 1.3 \cdot 10^{-3}$ is chosen at the GUT scale with c_2^2 as the preferred axino coupling. As stated in the $(\mathbf{\Lambda}_{D^2})_{12}$ case, the order of all BRs remains. For the lowest energies we have again $\Gamma_9(\tilde{a} \to \nu_\mu \nu\nu)$ as the dominant decay channel where $\Gamma_1(\tilde{a} \to \nu\gamma)$ contributes with a few percent to the BR. But nevertheless up to the axino masses of the rest mass of the muon+pion, $\Gamma_{9,3\nu}$ remains the dominant channel where it competes with Γ_{9_e} and Γ_8. All BRs suffer from a kink at the sixth mass region where $\Gamma_4(\tilde{a} \to \mu\pi)$ is kinematically allowed. This latter channel is the strongest for the higher axino masses. This behaviour has been observed as well in Fig. 6.2 for the $LL\bar{E}$ operator.

As a last example, we have chosen the $\not{R}_p$ coupling $(\mathbf{\Lambda}_{D^1})_{31} = 1.3 \cdot 10^{-3}$ at M_{GUT}. The according BRs are shown in Fig. 6.5(b). Again, the same arguments hold as in the previous section. We have no $\not{R}_p$ like decay and the neutrino channel of the ninth decay is overall dominant. As mentioned in the previous section we have only a few decays due to the fact that the axino mass is much smaller than the tau mass. This restricts the possible final state combinations.

This closes the section of examples with no-mixing among the quarks. For completness- and comparableness-reason of $\not{R}_p$ with the $LL\bar{E}$ and the $LQ\bar{D}$ operators respectively we show three more couplings in Appendix D.2.

6.2.2 Mixing scenarios

In our previous considerations we assumed that simplified condition the we have no mixing among the quark flavors. This section is dedicted to the two remaining scenarios where quark mixing is possible and described by the CKM matrix. We have extreme case where the mixing is mainly due to the up- or down-quark sector respectively. We will treat both cases together because the foregoing analysis suggests that the BR of the

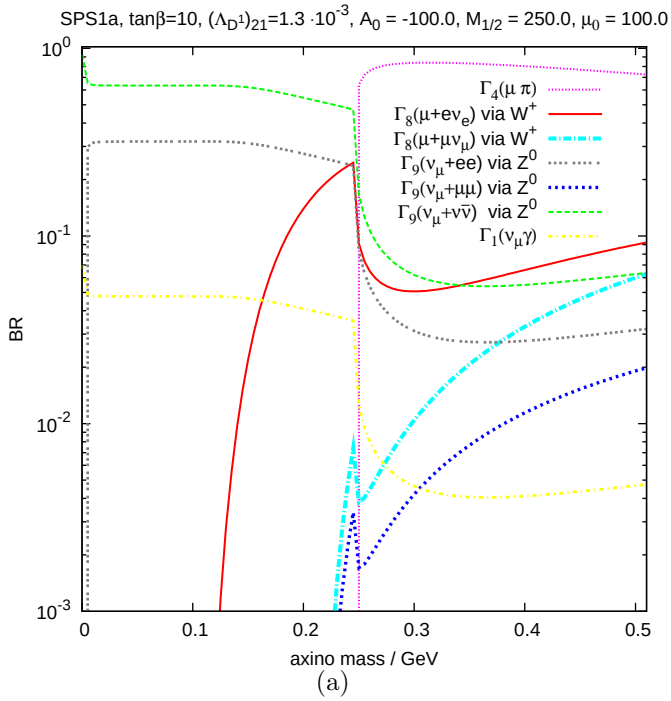

(a)

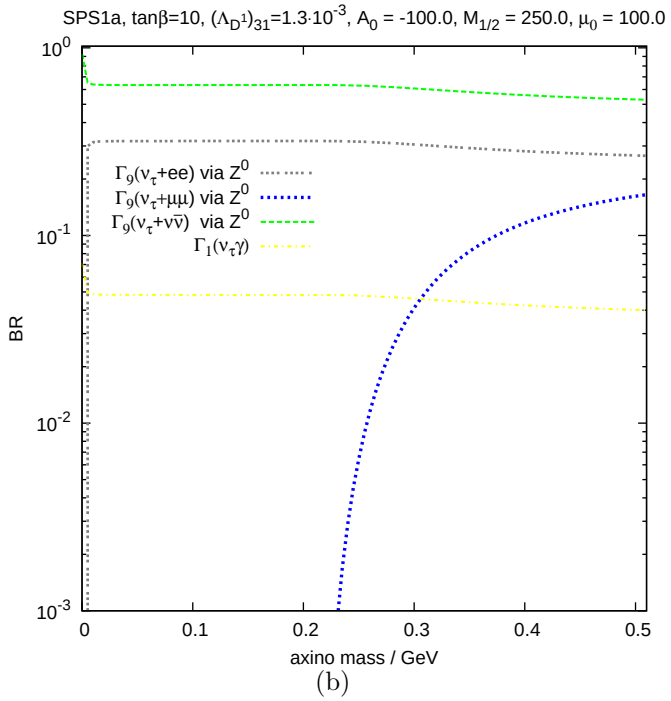

(b)

Figure 6.5: The BR of the axino decays at the benchmark point SPS1a with the $\not{R}_p$ couplings $(\mathbf{\Lambda}_{D^1})_{21} = 1.3 \times 10^{-3}$ (upper figure) and $(\mathbf{\Lambda}_{D^1})_{31} = 1.3 \times 10^{-3}$ (lower figure), (no-mixing). With the chosen $\not{R}_p$ operator c_2^2 and c_2^3 are the relevant Yukawa couplings where the axino couples preferred to the muon or tau family respectively. Due to kinematical thresholds of the decay channels several mass regimes are formed with different behaviour.

different couplings can be categorized according to their preferred axino coupling c_2^i. This suggestion will be confirmed in this section.

However, the mixing of the quark flavors leads to non-diagonal SM Yukawa coupling matrices. A consequence is that all 27 trilinear $(\mathbf{\Lambda}_{D^i})_{jk}$ couplings, with $i,j,k = 1,2,3$ have non-zero RGE. As example we consider a previously the nonexistant RGE of c_2^i with $(\mathbf{\Lambda}_{D^1})_{12} \neq 0$. Inserting this assumption into Eq. (6.8) we get

$$16\pi^2 \frac{\mathrm{d}}{\mathrm{d}t} c_2^{i=1} \supset c_1 \Big[-3(\mathbf{\Lambda}^*_{D^1})_{12}(\mathbf{Y}_{D^1})_{21} \Big] . \tag{6.9}$$

Here we have used the decomposed version of Eq. (6.8). It is apparent that for a contribution to the RGE of this $\not{R}_p$ operator we need $(\mathbf{Y}_{D^1})_{21} \neq 0$ which realized in the mixing cases. As in our previous sections we can directly read of the the preferred axino Yukawa coupling. Again, according to these couplings the BR follow the characterisic behaviour which we have observed before. Thus for a better overview you find in Table 6.3 a list of the trilinear $(\mathbf{\Lambda}_{D^i})_{jk}$ with its preferred axino coupling according Eq. (6.9).

Obviously for the two remaining scenarios we have in total 54 BR which is tedious to present all of them. Thus, we restrict ourselves without loss of generality on a few examples. These examples will make clear changes that are connected with the assumption of quark mixing in comparison to no-mixing.

In general we have concluded in the foregoing section that we have three different behaviours of the BR. Each of them is correlated with one of the three axino Yukawa couplings c_2^i. We will see that these arguments can be applied here as well.

At first we see in Table 6.3 that the nine couplings without quark mixing have almost the same coupling strength in each scenario. Inserting these values in Eq. (6.8) these $\not{R}_p$ couplings are multiplied with the diagonal SM Yukawa couplings. However, the diagonal ones are the strongest and thus assuming any kind of quark mixing does not affect the RGE remarkably. The differences are marginal and thus negligible. Hence, the BRs remain the same and can be compared to those presented in section 6.2.1 and in Appendix D.2. For this reason we exclude these couplings from the further considerations in this section. However, we have a similar behaviour for the BR of all couplings if down quark mixing is assumed.

The situation is different if the CKM mixing is assumed to be in the up-quark sector. Nevertheless the BR can be categorized according to the preferred c_2^i. We discern a difference of the BR in the cases where the $LQ\bar{D}$ coupling bounds are due to the absence of tachyons, *cf.* Table 6.3. Choosing one of these couplings, *e.g.* with c_2^1 largest, the radiative axino mode Γ_1 competes significantly with the other modes. A representative diagram is shown in Fig. 6.6(a) where the chosen $LQ\bar{D}$ operator indicates a preference for c_2^1. We observe that Γ_1 and $\Gamma_{9,3\nu}$ have the same BR. The explanation is that the chosen scenario, taking into account the restriction due to tachyons, has a direct impact on the minimization condition of the scalar potential. This solution returns a considerably different ratio of the mixing angles of Γ_1 and $\Gamma_{9,3\nu}$ than before.

A similar result is obtained for the $LQ\bar{D}$ couplings with c_2^2 and c_2^3 as the largest axino Yukawa couplings, *cf.* Appendix D.2.2 see Fig. D.5(a) and Fig. D.5(b), respectively.

Some of the couplings of the $LQ\bar{D}$ operator are restricted in the no-mixing case due to

the absence of tachyons. But in the up-mixing scenario they obey the neutrino mass limit. Fig. 6.6(b) shows such an example with $(\mathbf{\Lambda}_{D^3})_{22} = 4.6 \cdot 10^{-4}$ with up-mixing. Here the first decay channel does not have the same BR as $\Gamma_{9,3\nu}$ but gives a higher contribution than observed previously. A complete list for the other c_2^i Yukawa coupling can be found in Appendix D.2.2, see Fig. D.6(a) and Fig. D.6(b). There we notice a comparable behaviour.

In conclusion despite what kind of lepton number violation $\not{R}_p$ operator is chosen we obtain a preference for one of the axino Yukawa couplings c_2^i. Each of the couplings has a specific type of dominant BR. Furthmore we saw, that if the bound on the $LQ\bar{D}$ operator comes from the absence of tachyons the underlying RGEs do not generate non-zero values for the c_2^i if the quarks are not mixing. In contrast to this in cases with quark mixing described by the CKM matrix all $LQ\bar{D}$ operators give contributions. One exception in the general behaviour of the BRs is given by the mixing in the up-quark sector. Here the coupling whose bounds come from the absence of tachyons lead to a significant contribution to the radiative axino decay $\Gamma(\tilde{a} \to \nu\gamma)$. Assuming down quark mixing returns unspectacular results which fit into our categorization as presented with the $LL\bar{E}$ operator and the no-mixing case.

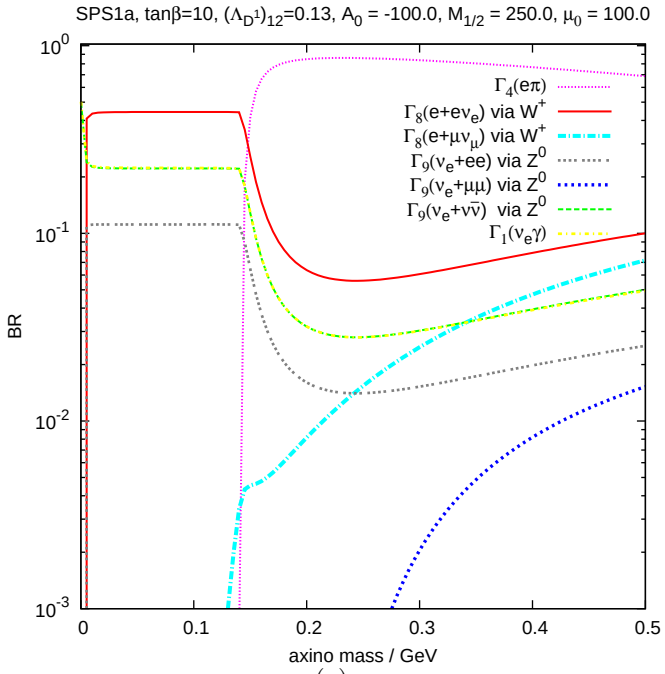

(a)

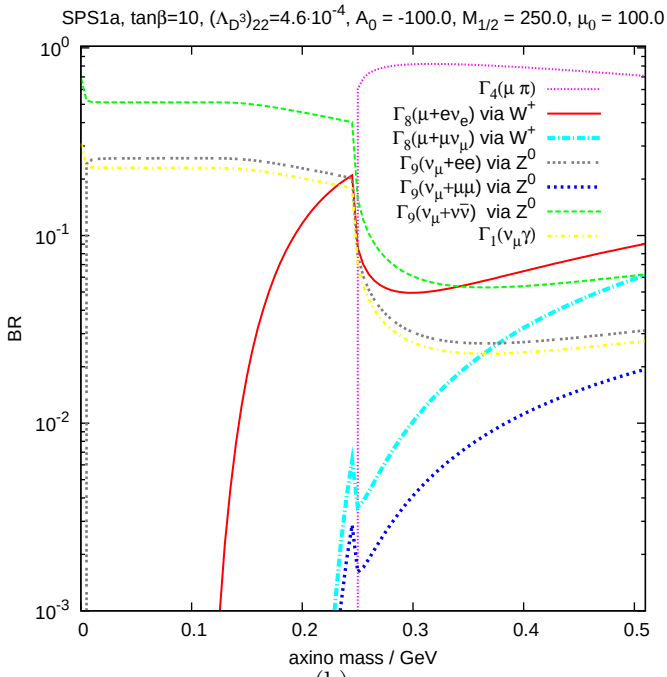

(b)

Figure 6.6: The BR of the axino decays at the benchmark point SPS1a with the $\not{R}_p$ couplings $(\mathbf{\Lambda}_{D^1})_{12} = 0.13$ (upper figure) and $(\mathbf{\Lambda}_{D^3})_{22} = 4.6 \cdot 10^{-4}$ (lower figure) (both up-mixing). With the chosen $\not{R}_p$ operator c_2^1 and c_2^2 are the relevant Yukawa couplings where the axino couples preferred to the muon family. Due to kinematical thresholds of the decay channels several mass regimes are formed with different behaviour.

	No mixing		Up mixing		Down mixing	
	$M_{\rm GUT}$	c_2^i	$M_{\rm GUT}$	c_2^i	$M_{\rm GUT}$	c_2^i
$(\mathbf{\Lambda}_{D^1})_{11}$	1.3×10^{-3}	c_2^1	1.3×10^{-3}	c_2^1	7.2×10^{-4}	c_2^1
$(\mathbf{\Lambda}_{D^1})_{21}$	1.3×10^{-3}	c_2^2	1.3×10^{-3}	c_2^2	7.2×10^{-4}	c_2^2
$(\mathbf{\Lambda}_{D^1})_{31}$	1.3×10^{-3}	c_2^3	1.3×10^{-3}	c_2^3	7.1×10^{-4}	c_2^3
$(\mathbf{\Lambda}_{D^1})_{12}$	0.13^t	–	0.13^t	c_2^1	3.6×10^{-4}	c_2^1
$(\mathbf{\Lambda}_{D^1})_{22}$	0.13^t	–	0.13^t	c_2^2	3.6×10^{-4}	c_2^2
$(\mathbf{\Lambda}_{D^1})_{32}$	0.13^t	–	0.13^t	c_2^3	3.5×10^{-4}	c_2^3
$(\mathbf{\Lambda}_{D^1})_{13}$	0.15^t	–	0.15^t	c_2^1	6.4×10^{-4}	c_2^1
$(\mathbf{\Lambda}_{D^1})_{23}$	0.15^t	–	0.15^t	c_2^2	6.4×10^{-4}	c_2^2
$(\mathbf{\Lambda}_{D^1})_{33}$	0.15^t	–	0.15^t	c_2^3	6.4×10^{-4}	c_2^3
$(\mathbf{\Lambda}_{D^2})_{11}$	0.13^t	–	0.13^t	c_2^1	3.6×10^{-4}	c_2^1
$(\mathbf{\Lambda}_{D^2})_{21}$	0.13^t	–	0.13^t	c_2^2	3.6×10^{-4}	c_2^2
$(\mathbf{\Lambda}_{D^2})_{31}$	0.13^t	–	0.13^t	c_2^3	3.5×10^{-4}	c_2^3
$(\mathbf{\Lambda}_{D^2})_{12}$	7.5×10^{-5}	c_2^1	7.2×10^{-5}	c_2^1	7.4×10^{-4}	c_2^1
$(\mathbf{\Lambda}_{D^2})_{22}$	7.5×10^{-5}	c_2^2	7.5×10^{-5}	c_2^2	7.4×10^{-5}	c_2^2
$(\mathbf{\Lambda}_{D^2})_{32}$	7.5×10^{-5}	c_2^3	7.5×10^{-5}	c_2^3	7.3×10^{-5}	c_2^3
$(\mathbf{\Lambda}_{D^2})_{13}$	0.15^t	–	1.7×10^{-2}	c_2^1	5.4×10^{-5}	c_2^1
$(\mathbf{\Lambda}_{D^2})_{23}$	0.15^t	–	1.7×10^{-2}	c_2^2	5.4×10^{-5}	c_2^2
$(\mathbf{\Lambda}_{D^2})_{33}$	0.15^t	–	1.7×10^{-2}	c_2^3	5.3×10^{-5}	c_2^3
$(\mathbf{\Lambda}_{D^3})_{11}$	0.13^t	–	3.3×10^{-3}	c_2^1	5.7×10^{-4}	c_2^1
$(\mathbf{\Lambda}_{D^3})_{21}$	0.13^t	–	3.3×10^{-3}	c_2^2	5.7×10^{-4}	c_2^2
$(\mathbf{\Lambda}_{D^3})_{31}$	0.13^t	–	3.2×10^{-3}	c_2^3	5.7×10^{-4}	c_2^3
$(\mathbf{\Lambda}_{D^3})_{12}$	0.13^t	–	4.6×10^{-4}	c_2^1	4.8×10^{-5}	c_2^1
$(\mathbf{\Lambda}_{D^3})_{22}$	0.13^t	–	4.6×10^{-4}	c_2^2	4.8×10^{-5}	c_2^2
$(\mathbf{\Lambda}_{D^3})_{32}$	0.13^t	–	4.5×10^{-4}	c_2^3	4.8×10^{-5}	c_2^3
$(\mathbf{\Lambda}_{D^3})_{13}$	2.2×10^{-6}	c_2^1	2.6×10^{-5}	c_2^1	2.2×10^{-6}	c_2^1
$(\mathbf{\Lambda}_{D^3})_{23}$	2.2×10^{-6}	c_2^2	2.2×10^{-6}	c_2^2	2.2×10^{-6}	c_2^2
$(\mathbf{\Lambda}_{D^3})_{33}$	2.1×10^{-6}	c_2^3	2.1×10^{-6}	c_2^3	6.2×10^{-6}	c_2^3

Table 6.3: In the mostleft column the trilinear $\mathbf{\Lambda}_D$ are listed. According to the three quark mixing cases the upper bound for the couplings are given. The values are taken from Ref. [35]. Couplings denoted with t show that the strongest bounds come from the absence of tachyons. The remaining ones use the neutrino mass constraint. For each case the preferred axino couplings are shown. Under the assumption that the quarks are not mixing several couplings do not contribute to the RGE and have no preference, for details see text.

7 Axino as Dark Matter

7.1 Axino energy density

We saw in one of the previous sections that the axino is a weakly interacting particle which is electrically neutral. Thus it is a promising dark matter candidate, possibly even a *cold* DM candidate, depending on the mass. Within this work we assume the same axino mass range for hot-, warm- and cold-dark mater as it is often found in the literature [25, 24, 27, 28]. However, as the axino can decay in the $\not{R}_p$ framework the question araises whether the axino abundance as well as the axino energy density is sufficiently large to be CDM.

The question of an axino as a DM candidate has been discussed in Refs. [25, 24, 27, 28] as well as in recent works see Refs. [30, 26, 88]. Except for Ref. [26] most of the works focus on the KVSZ axino and perform the DM analysis within this framework. The thermal production of axinos in the early universe through 2+2 scattering processes via the axion-gluon-gluino interaction was performed in Ref. [28] from a generel viewpoint, and thus the DFSZ model is also included. This underlying interaction has its origin in the $SU(3)$ part of Eq. (3.33). We already pointed out that in the derivation of Eq. (3.33) the according D-term is involved, which was only considered in Ref [88].

As a first step for the calculation of the axino energy density $\Omega_{\tilde{a}}$, we consider the axino yield $Y_{\tilde{a}}$ which is a function of the reheating temperature, see Ref [28]. We have to keep in mind that for temperatures higher than the decoupling temperature $T_{\rm D}$ the equilibrium number density for Majorana particles hold, for details see Ref [28]. Thus evaluating $Y_{\tilde{a}}$ we can determine an upper value for $T_{\rm R}$ which is also an important parameter for the analysis of the axino energy density. We comment on this fact more extensively below.

With the results of Ref [88], we can evaluate the axino yield to

$$Y_{\tilde{a}}(T_0) \;\approx\; 9\times 10^{-8}\, g_s^6\, \ln\left(\frac{3}{g_s}\right)\left(\frac{10^{11}\ \text{GeV}}{f_{\rm PQ}/N}\right)^2\left(\frac{T_{\rm R}}{10^4\ \text{GeV}}\right), \tag{7.1}$$

where $g_s = g_s(T_{\rm R})$ is the running strong coupling as function of the reheating temperature $T_{\rm R}$. For more details about calculations of the axino density in the early universe we refer the reader to Ref. [25, 24, 27] and especially to Ref. [28, 88]. Inserting for the coupling the expression (see also Ref. [28])

$$g_s(T_{\rm R}) = \left(\frac{1}{g_s^2(M_Z)} + \frac{3}{8\pi^2}\ln\left[\frac{T_{\rm R}}{M_Z}\right]\right), \tag{7.2}$$

with the initial value of the coupling at the Z-Boson mass $g_s^2(M_Z)/(4\pi) = 0.118$ [28] we can estimate the axino yield. The graphical result for different Peccei-Quinn breaking scales is given in Fig. 7.1.

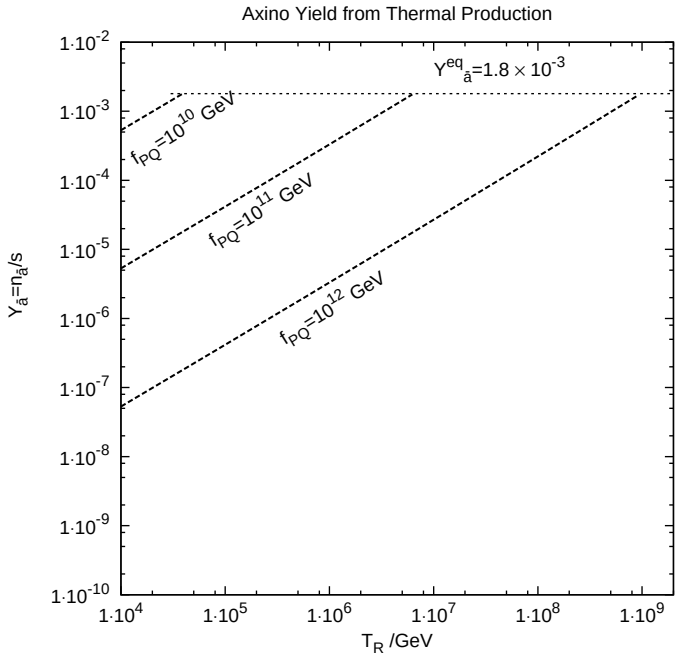

Figure 7.1: The axino yield $Y_{\tilde{a}}$ as a function of the reheating temperature $T_{\rm R}$ for different Peccei-Quinn breaking scales $f_{\rm PQ}$. The upper bound is the equilibrium yield of the axino before the decoupling which is independent of $T_{\rm R}$.

In Fig. 7.1 you see as well an upper bound for $Y_{\tilde{a}}$. This upper bound is governed by the equilibrium number density of the axinos. As mentioned above, in this case the reheating temperature is higher than $T_{\rm D}$ the decoupling temperature: $T_{\rm R} \gtrsim T_{\rm D}$. The equilibrium yield $Y^{\rm eq}_{\tilde{a}}$ is independent of $T_{\rm R}$

$$Y^{\rm eq}_{\tilde{a}} = \frac{135\zeta(3)}{(2\pi^2)^2 g_{*s}(T_{\rm D})} = 1.8 \cdot 10^{-3}\,, \tag{7.3}$$

where $g_{*s}(T_{\rm D}) = 228.75$ is the effective number of degrees of freedom at the axino decoupling temperature in the MSSM [15, 28]. The value of $Y^{\rm eq}_{\tilde{a}}$ is indicated in Fig. 7.1 by the horizontal line. However, in comparison with Ref. [28] our diagram differs in two points. In the first place we have considered the recent results of Ref. [88] which modify the production cross section. Secondly as we consider the DFSZ model the Peccei-Quinn breaking scale is divided by $N = 6$.

These two aspects give us in addition a non-negligible change for the decoupling temperature. In Ref. [145, 28] we find *e.g.* $T_{\rm D} = 10^9$ GeV for $f_{\rm PQ} = 10^{11}$ GeV in the KVSZ model. In contrast to this we have in the DFSZ model a two orders of magnitude smaller temperature, namely $T_{\rm D} \sim 10^7$ GeV at the same $f_{\rm PQ}$ breaking scale. This is in agreement with Ref. [145].

Keeping these results in mind we can focus on the energy density of the axino, see *e.g.*

Ref. [88]

$$\Omega_{\tilde{a}} h^2 \;=\; 2.48\, g^6 \ln\left(\frac{3}{g}\right)\left(\frac{m_{\tilde{a}}}{0.1\mathrm{GeV}}\right)\left(\frac{10^{11}\ \mathrm{GeV}}{f_{\mathrm{PQ}}/N}\right)^2\left(\frac{T_{\mathrm{R}}}{10^4\ \mathrm{GeV}}\right), \tag{7.4}$$

where $m_{\tilde{a}}$ is the mass of the axino. Of course, this expression is only valid for a stable axino. For the scenario of a decaying axino with the lifetime compareble with the age of the universe we have to modify $\Omega_{\tilde{a}}$ with the exponential decay law. The energy density for a decaying axino reads:

$$\Omega_{\tilde{a}} h^2 \;=\; 2.48\, g^6 \ln\left(\frac{3}{g}\right)\left(\frac{m_{\tilde{a}}}{0.1\mathrm{GeV}}\right)\left(\frac{10^{11}\ \mathrm{GeV}}{f_{\mathrm{PQ}}/N}\right)^2\left(\frac{T_{\mathrm{R}}}{10^4\ \mathrm{GeV}}\right)\cdot\exp\left(-\frac{\tau}{t_{\tilde{a}}}\right), \tag{7.5}$$

where $t_{\tilde{a}}$ is the lifetime of the axino and τ is the age of the universe.

Using Eq. (7.5), we can evaluate the axino energy density for each $\not{R}_p$ scenario. As before the axino mass will be kept as a free parameter. Hence, for every axino mass and $\not{R}_p$ coupling we will have a different lifetime which has a direct impact on Eq. (7.5). Finally the reheating temperature is variable whose value also influences the strong coupling g_s. Hence the evaluation of $\Omega_{\tilde{a}}$ is non-trivial and can only be performed numerically.

In the following sections, we show different examples of $\Omega_{\tilde{a}}$ for the lepton number violating scenarios due to the $LL\bar{E}$- and $LQ\bar{D}$-operators. Again, the behaviour of the energy density can be categorized, as seen in the previous chapter, according to the dominant BR.

7.2 Axino as Dark Matter with the $\not{R}_p\, LL\bar{E}$ operator

In the foregoing paragraph we presented the axino energy density $\Omega_{\tilde{a}}$. Obviously the expression (7.5) has three free parameters: $m_{\tilde{a}}, T_{\mathrm{R}}, t_{\tilde{a}}$. Furthermore the axino lifetime depends implicitly on the chosen lepton number violating operator leading to in total 3+1 parameters.

We will perform our analysis as follows. As our main focus lays on the $\not{R}_p$ operators and the according axino parameters. We will not discuss implications coming from the reheating temperature T_{R} in particular, for further details see Refs. [160, 161, 162]. Hence in the diagrams shown later on we keep T_{R} implicit. That means that we conduct a scan by

- varying a concrete $LL\bar{E}$ coupling, upper bounds given in Tab. 6.1,
- varying the axino mass within the discussed limits,
- varying the reheating temperature within the discussed limits.

The results will be presented in a diagram $\mathbf{\Lambda}_E$ vs $m_{\tilde{a}}$. As first example we present the result for $(\mathbf{\Lambda}_{E^2})_{12} \neq 0$ in Fig. 7.2. This diagram is a contour plot where we have on the xy-plane the $(\mathbf{\Lambda}_{E^2})_{12}$ coupling and $m_{\tilde{a}}$ the axino mass. As mentioned earlier T_{R} the

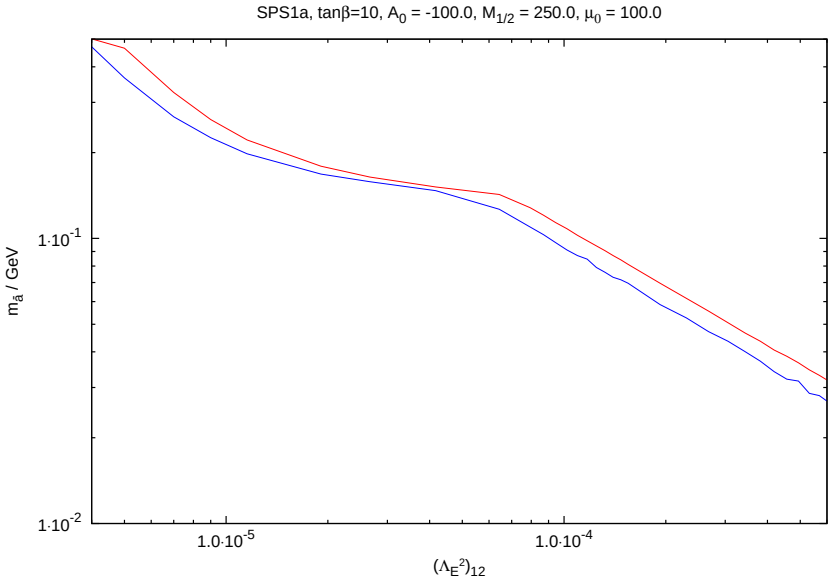

Figure 7.2: A contour plot of the axino mass as a function of $\not{R}_p$ coupling $(\mathbf{\Lambda}_{E^2})_{12}$ and $T_{\rm R}$ - implcit on the z-axis. The analysis is performed at the benchmark point SPS1a with the parameter space values as shown on the top of the figure. The red (blue) line indicates the upper (lower) axino mass for a given $(\mathbf{\Lambda}_{E^2})_{12}$ value where the condition $\Omega_{\tilde{a}} = \Omega_{\rm DM}$ is satisfied. The behaviour of the lines is due to different boundary conditions of the reheating temperature as well as the BR, see text for details. This results are obtained for a PQ breaking scale of $f_{\rm PQ} = 10^{11}$ GeV.

reheating temperature is implicit and thus on the $z-$axis. Obviously there exist regions where the axino provides the CDM in the chosen $\not{R}_p$ framework.

In the projection of Fig. 7.2 you find a red (blue) line which denotes the upper (lower) axino mass limit where the condition $\Omega_{\tilde{a}} = \Omega_{\rm DM}$ is satisfied by varying $T_{\rm R}$. The upper (lower) limit is due to the limited reheating temperatures which can take values of 10^4 GeV$\leq T_{\rm R} \lesssim 10^7$ GeV. The upper temperature represents the decoupling temperature where the axino number density is in equilibrium, see section 7.1. The behaviour of the red (blue) line is restricted because of the suppression of the exponential decay law. This suppression does not allow a larger mass window as heavier axinos decay faster, leading to a shorter lifetime in comparison to the age of the universe. Thus we would obtain to small axino energy densities.

Besides these restrictions, we observe three different regimes in Fig. 7.2. For small $(\mathbf{\Lambda}_{E^2})_{12}$ couplings both lines in the xy-plane show an exponential like behaviour. At an axino mass of $\sim 140 - 150$ MeV both lines are approaching. For lower axino masses they both fall off. This characteristics can be easily explained with a closer look at the corresponding BR in Fig. 6.1.

At first note that the BRs are independent of the coupling strength itself. Hence the BR order shown in the previous chapter remains the same for all possible values of the $\not{R}_p$ coupling as well as reheating temperatures. As pointed out the BRs are characterized by the dominant axino Yukawa coupling due to the associated $\not{R}_p$ operators.

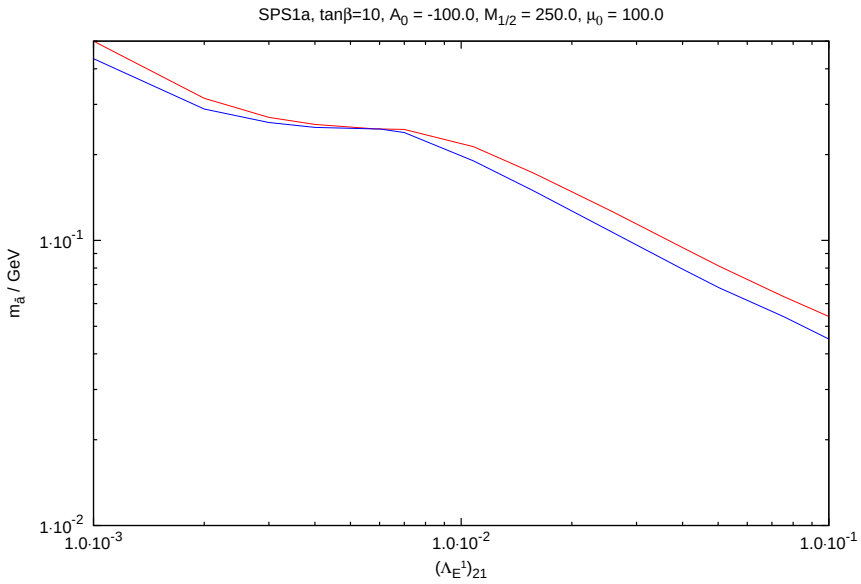

Figure 7.3: A contour plot of the axino mass as a function of $\not{R}_p$ coupling $(\mathbf{\Lambda}_{E^1})_{21}$ and T_{R} - implcit on the z-axis. The analysis is performed at the benchmark point SPS1a with the parameter space values as shown on the top of the figure. The red (blue) line indicates the upper (lower) axino mass for a given $(\mathbf{\Lambda}_{E^1})_{21}$ value where the condition $\Omega_{\tilde{a}} = \Omega_{\mathrm{DM}}$ is satisfied. The behaviour of the lines is due to different boundary conditions of the reheating temperature as well as the BR, see text for details. This results are obtained for a PQ breaking scale of $f_{\mathrm{PQ}} = 10^{11}$ GeV.

For the result in Fig. 7.2 and axino masses up to the pion mass the BR is constant. Obviously in this regime the corresponding energy density is governed by the exponential decay law in Eq. (7.5). As we use a logarithmic scale on the $y-$axis in Fig. 7.2 the red (blue) line show a linear drop off.

Around the pion mass the order of the BRs is changed and thus a transition takes place. This transition region of the decays is the reason for the proximity of the red and blue lines. Note that the inverse decay width is proportional to the lifetime of the axino. From a mathematical point of view regions with transitions are accompanied by a transition of the according inverse decay width functions with different slopes. Thus a step in the BR results in a step in the axino lifetime. A consequence is that for a slight change in mass we obtain a much larger change in lifetime. Furthermore this explains as well the change of slope of the lines which are not constant any longer, *cf.* the BR in Fig. 6.1.

In the end we can sum up, for every $(\mathbf{\Lambda}_{E^2})_{12}$ value the axino can constitute the DM for a wide range of the assumed axino mass. Even larger masses would not be a problem as the $\not{R}_p$ coupling could be lowered yielding longer axino lifetimes comparable to the age of the universe. Note that the lowest possible axino mass is around 30 MeV whereas the upper mass limit is due to our restrictions and considerations, *cf.* chapter 5.

Similarly to our considerations of the BR also the analysis of $\Omega_{\tilde{a}}$ can be categorized. On the one hand we have for each $\not{R}_p$ operator a preferred axino coupling which determines the order of the BR. This BR directly leads to specific characteristics of the energy density.

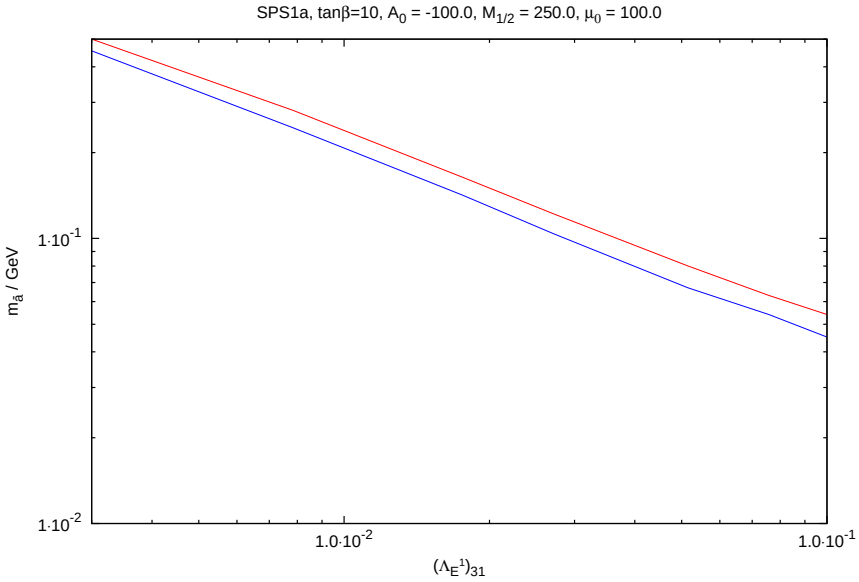

Figure 7.4: A contour plot of the axino mass as a function of $\not{R}_p$ coupling $(\mathbf{\Lambda}_{E^1})_{31}$ and T_{R} - implcit on the z-axis. The analysis is performed at the benchmark point SPS1a with the parameter space values as shown on the top of the figure. The red (blue) line indicates the upper (lower) axino mass for a given $(\mathbf{\Lambda}_{E^1})_{31}$ value where the condition $\Omega_{\tilde{a}} = \Omega_{\mathrm{DM}}$ is satisfied. The behaviour of the lines is due to different boundary conditions of the reheating temperature as well as the BR, see text for details. This results are obtained for a PQ breaking scale of $f_{\mathrm{PQ}} = 10^{11}$ GeV. Note that the small kinks at the blue line are due to numerical artefacts and have no significance.

Note, despite of some similarities amoung the BRs of the $\mathbf{\Lambda}_F$ operators with $F = E, D$ all effects take place for different values and orders of the according couplings.

To support these conclusion we show in Fig. 7.3 a second example. Here we have $(\mathbf{\Lambda}_{E^1})_{21} \neq 0$ where c_2^2 is the largest axino Yukawa coupling. Again, the upper (lower) bound of the possible axino masses which can constitute DM is marked with a red (blue) line. We see a similar behaviour as in the case before, *i.e.* both lines approach each other. At a mass of ~ 250 MeV they coincide. Comparing this point with the according BR in Fig. 6.2 it is obvious that at such a mass a transition in the BR takes place. Remember, that the fourth decay mode with a muon and a pion in the final state becomes accessible and has the largest BR. Here again the upper limit for axino masses is reached. But the lowest possible axino masses to be DM is of order 50 MeV which is slightly larger than in the foregoing example.

As a last example in Fig. 7.4 we have $(\mathbf{\Lambda}_{E^1})_{31} \neq 0$. In this scenario it is a c_2^3 characteristical BR which means that one decay is overall dominant. In turn we have no transitions as described above. Hence the energy density follow the exponential decay law which is reflected by the linear behaviour of $\Omega_{\tilde{a}}$ in Fig. 7.4. Here the possible axino masses for DM start at 50 MeV.

We have presented the axino energy density of three different $\not{R}_p$ operators. All of them show another behaviour which can be traced back to the preferred axino coupling,

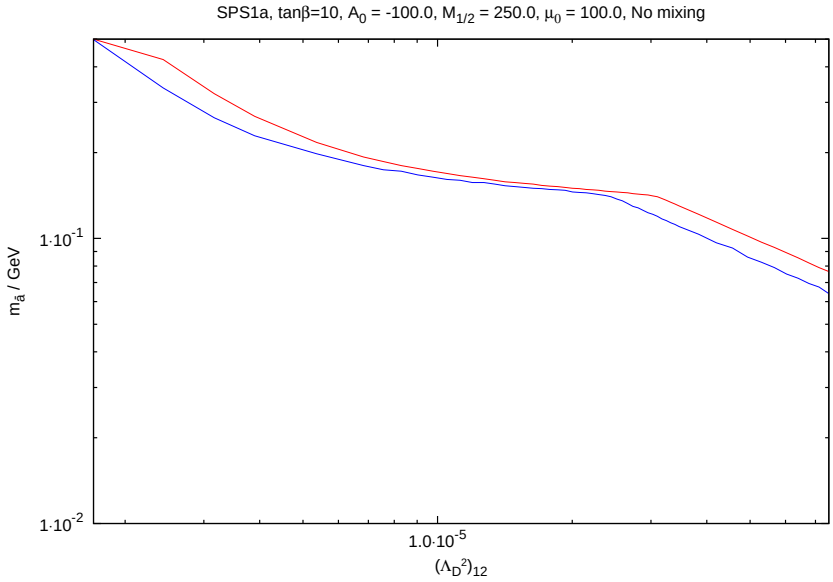

Figure 7.5: A contour plot of the axino mass as a function of $\not{R}_p$ coupling $(\mathbf{\Lambda}_{D^2})_{12}$ with no-mixing assumption and T_{R} - implcit on the z-axis. The analysis is performed at the benchmark point SPS1a with the parameter space values as shown on the top of the figure. The red (blue) line indicates the upper (lower) axino mass for a given $(\mathbf{\Lambda}_{D^2})_{12}$ value where the condition $\Omega_{\tilde{a}} = \Omega_{\mathrm{DM}}$ is satisfied. The behaviour of the lines is due to different boundary conditions of the reheating temperature as well as the BR, see text for details. This results are obtained for a PQ breaking scale of $f_{\mathrm{PQ}} = 10^{11}$ GeV. Note that the small kinks at the blue line are due to numerical artefacts and have no significance.

similarl to the BR discussion in the foregoing chapter. Nevertheless in all cases the axino can provide the DM. Depending on the preferred axino mass for the possible dark matter model we can choose the appropiate $\not{R}_p$ coupling and strength.

In Appendix E.1 we show three more examples of the $LL\bar{E}$ operator where the same behaviour as discussed here is observed.

7.3 Axino as Dark Matter with the $\not{R}_p\, LQ\bar{D}$ operator

Our discussion about the axino BRs as well as the axino energy density $\Omega_{\tilde{a}}$ up to now showed that we can categorize them according to their preference of the c_2^i coupling. This allows us to draw the conclusion that it is analogous in a lepton number violating scenario due to the $LQ\bar{D}$ operator. Hence, we treat all quark mixing scenarios in the following section.

As a first example, we have the operator $(\mathbf{\Lambda}_{D^2})_{12}$ which means a c_2^1 dominance and where the BRs suffer from a transition around the pion mass as the fourth decay mode becomes accessible. In Fig. 7.5 we observe exactly the same structure as expected and already seen in the scenario of $(\mathbf{\Lambda}_{E^2})_{12}$, *cf.* Fig. 7.2. The red- and the blue line approach each other for larger couplings. Finally the kink indicates the transition to the fourth

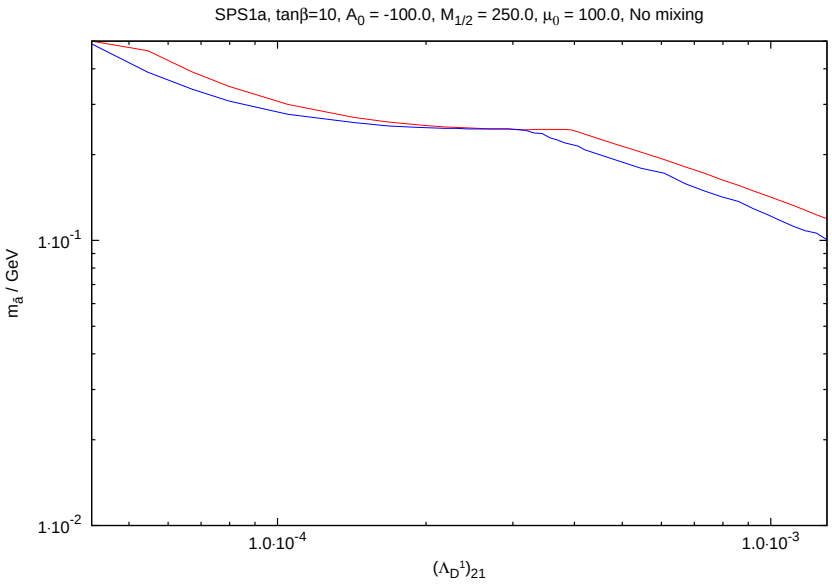

Figure 7.6: A contour plot of the axino mass as a function of $\not{R}_p$ coupling $(\mathbf{\Lambda}_{D^1})_{21}$ with no-mixing assumption and T_R - implcit on the z-axis. The analysis is performed at the benchmark point SPS1a with the parameter space values as shown on the top of the figure. The red (blue) line indicates the upper (lower) axino mass for a given $(\mathbf{\Lambda}_{D^1})_{21}$ value where the condition $\Omega_{\tilde{a}} = \Omega_\mathrm{DM}$ is satisfied. The behaviour of the lines is due to different boundary conditions of the reheating temperature as well as the BR, see text for details. This results are obtained for a PQ breaking scale of $f_\mathrm{PQ} = 10^{11}$ GeV. Note that the small kinks at the blue line are due to numerical artefacts and have no significance.

decay leading mode in the BRs, which results as well in a different slope of the $m_{\tilde{a}}$ to $\mathbf{\Lambda}_D$ ratio. The only difference is that here the lowest possible axino masses which can provide DM are between 70-100 MeV. In the $LL\bar{E}$ case we had masses of $\sim$ 30 MeV. The reason is that Table 6.3 contains upper bounds on the $LQ\bar{D}$ operator from Ref. [35]. These bounds were obtained with an older version of the program `Softsusy`. Our more recent version includes some updates and corrections which in turn applying the neutrino mass or tachyon restriction lead to larger possible upper bounds of the $LQ\bar{D}$ couplings. Using these even smaller axino masses would be reached for the DM analysis. But for reasons of a better comparability we kept the values from Table 6.3. Assuming quark mixing in the up- or down-sector would not change Fig. 7.5 significantly as the differences of the coupling strength are negligible, *cf.* section 6.2.2.

Considering $(\mathbf{\Lambda}_{D^1})_{21}$ we have a c_2^2 case where a transition of the leading decay mode in the BRs occurs at a mass of $\sim$ 250 MeV. At such a mass an axino decay to a pion and a muon in the final states becomes possible. Again, we see the same pattern as discussed in the $LL\bar{E}$ scenario. As explained above the two diagrams differ in the values for the lowest axino masses based on the smaller possible couplings of Table 6.3. Note that even with this $\not{R}_p$ operator we have no change for the mixing cases as the couplings do not vary.

The remaining dominant axino Yukawa coupling is c_2^3. A representative choice is the assumption of a non-zero $(\mathbf{\Lambda}_{D^1})_{31}$, see also Fig. 7.7. This picture would also remain

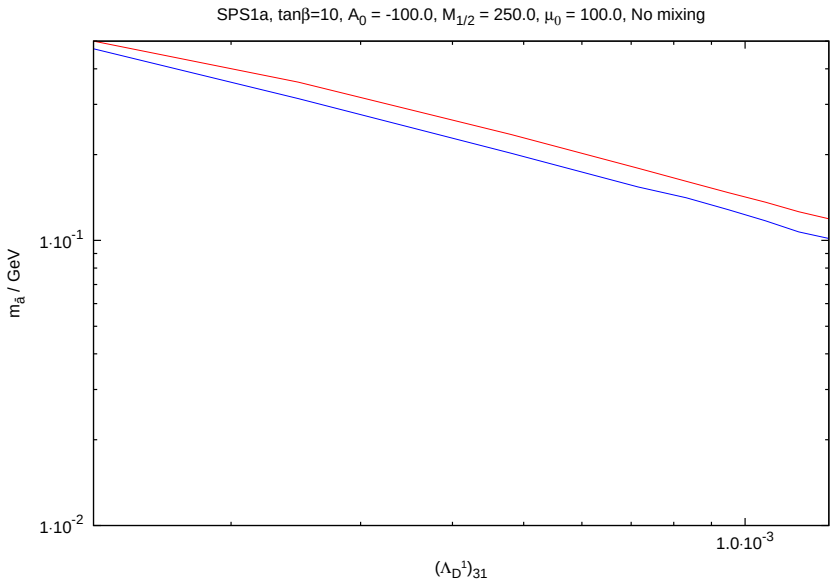

Figure 7.7: A contour plot of the axino mass as a function of $/\!\!R_p$ coupling $(\mathbf{\Lambda}_{D^1})_{31}$ with no-mixing assumption and T_{R} - implcit on the z-axis. The analysis is performed at the benchmark point SPS1a with the parameter space values as shown on the top of the figure. The red (blue) line indicates the upper (lower) axino mass for a given $(\mathbf{\Lambda}_{D^1})_{31}$ value where the condition $\Omega_{\tilde{a}} = \Omega_{\mathrm{DM}}$ is satisfied. The behaviour of the lines is due to different boundary conditions of the reheating temperature as well as the BR, see text for details. This results are obtained for a PQ breaking scale of $f_{\mathrm{PQ}} = 10^{11}$ GeV. Note that the small kinks at the blue line are due to numerical artefacts and have no significance.

unchanged under the assumption of quark mixing.

However, up to now we get the expected structure due to the preferred c_2^i. But first note that in scenarios with no mixing all couplings which are bound by the absence of tachyons do not return a viable model where the axino can provide the DM. Furthermore even switching on the mixing in the up quark sector in the tachyonic cases (*cf.* Table 6.3), we do not get a valid result for the axino as the DM. This is in contrast to our considerations of the BRs. The reason for this discrepancy is that the computed axino Yukawa couplings are so small that the axino lifetime becomes very large. This in turn means that exponential decay term in $\Omega_{\tilde{a}}$, *cf.* Eq. (7.5), is equal to one. Hence, this is identical to the R-parity conserving case. As a matter of fact we need very low masses $\mathcal{O}$(keV) to get axino energy densities of order of Ω_{DM}. Nevertheless we get a result for such low $m_{\tilde{a}}$ but it is ruled out because this would mean that the axino is warm DM, *cf.* Ref. [28]. As mentioned above this statement is only valid if the quark mixing is mainly in the up-sector and if the upper bounds of the $/\!\!R_p$ operator coupling are due to the absence of tachyons. Hence for the remaining 18 coupling in this sector we get analogous result and diagrams as shown before.

Going to the down quark mixing scenario we do no longer have any couplings which are restricted by the absence of tachyons. Hence all 27 $/\!\!R_p$ operators, *cf.* Table 6.3, result in models where the axino can provide the DM. Of course, as seen before lower values for

the $LQ\bar{D}$ operators are needed so that high axino masses become accessible for DM.

For completeness we again show 3+3 more examples in the Appendix E.2. As we presented in this section only scenarios without quark mixing the first set in Appendix E.2 is due to the assumption of the quark mixing mainly in the up quark sector. The second set shows examples with the mixing in the down sector.

8 Prospects for other Benchmark Points

The analysis presented so far was only performed at the benchmark point SPS1a [36]. We saw that independently of the chosen lepton number violating operator the behaviour of the BRs as well as from the axino energy density could be categorized. In general we had three different types of scenarios which were due to the largest axino Yukawa coupling c_2^i. Thus it was possible to predict the properties of the BRs or $\Omega_{\tilde{a}}$ only with deriving the preferred axino coupling from the $\not{R}_p$ operator.

However, such kind of prediction was valid and correct for the benchmark point SPS1a. In this section we show exemplary a BR and $\Omega_{\tilde{a}}$ for a different benchmark point so that we can conclude that this also holds for other scenarios. For this purpose we chose without loss of generality the mSUGRA benchmark points SPS2 and SPS4. These points are characterized by the parameters

$$M_0 = 1450 \text{ GeV},\ M_{1/2} = 300 \text{ GeV},\ A_0 = 0 \text{ GeV},\ \tan\beta = 10\ \ \text{sgn}(\mu) = +1\,, \tag{8.1}$$

for SPS2 and for SPS4 we have

$$M_0 = 400 \text{ GeV},\ M_{1/2} = 300 \text{ GeV},\ A_0 = 0 \text{ GeV},\ \tan\beta = 50\ \ \text{sgn}(\mu) = +1\,, \tag{8.2}$$

see Ref. [36]. In contrast to SPS1a we have at these points large differences in the soft breaking scalar mass M_0, $\tan\beta$ and the soft breaking trilinear parameter A_0. The scenario SPS2 features heavy scalars and SPS4 has a large value of $\tan\beta$ which has an impact on the Higgs sector, for details see Ref. [36]. These points represent a spread of the parameter space. Likewise to the SPS1a scenario we use the program `Softsusy3.0` for the analysis.

8.1 The BRs at SPS2 and SPS4

In the previous chapter we saw that among all possible lepton number violating operators we have similar behaviour of the BRs. Depending on the largest c_2^i coupling we were able to deduce the order of the BR. Hence in this section we present two examples of $\not{R}_p$ operators as a crosscheck to see whether the conclusions made earlier hold for other regions of the parameter space.

As mentioned above we consider the benchmark points SPS2 and SPS4. Furthermore we perform the analysis for the $\not{R}_p$ couplings $(\mathbf{\Lambda}_{D^2})_{12}$ at SPS2 and $(\mathbf{\Lambda}_{E^1})_{21}$ at SPS4. For the first coupling we assume that quark mixing is mainly in the up-quark sector.

Before we show the BRs we have to point out that we must employ a specific value for the couplings. For this we searched for an upper limit of $(\mathbf{\Lambda}_{E^1})_{21}$ and $(\mathbf{\Lambda}_{D^2})_{12}$ with the

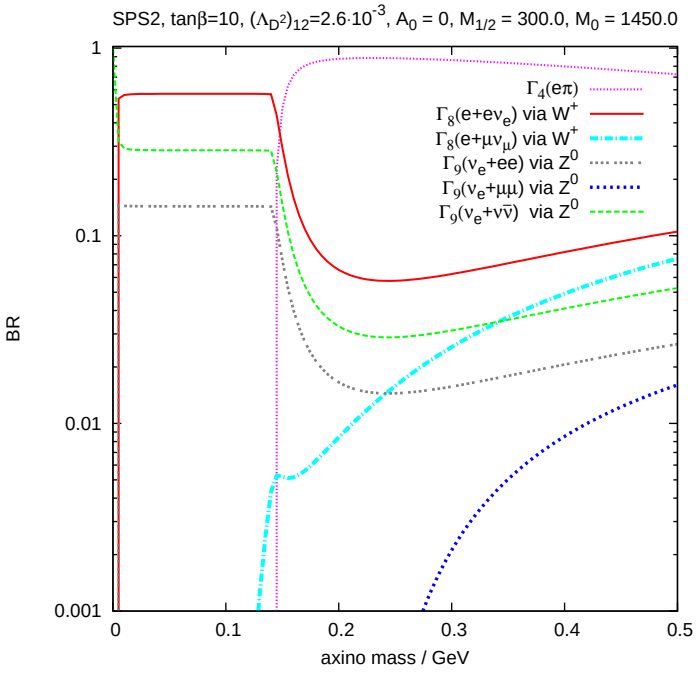

Figure 8.1: The BR of the axino decays at the benchmark point SPS2 with the $\not{R}_p$ couplings $(\mathbf{\Lambda}_{D^2})_{12} = 2.6 \times 10^{-3}$ (up mixing). With the chosen $\not{R}_p$ operator c_2^1 is the relevant Yukawa coupling where the axino couples preferred to the electron family respectively. Due to kinematical thresholds of the decay channels several mass regimes are formed with different behaviour.

program `Softsusy3.0` [39]. On both couplings we employed that the limits are due to the sum of the neutrino masses [35]. The values found due to this restriction were

$$(\mathbf{\Lambda}_{E^1})_{21} = 0.3\,, \qquad (\mathbf{\Lambda}_{D^2})_{12} = 2.6 \times 10^{-3}\,. \tag{8.3}$$

Keeping this bound in mind you can see in Fig. 8.1 the branching ratios of the axino decays for $(\mathbf{\Lambda}_{D^1})_{11}$. Despite the fact that the BRs are computed from another parameter space point the characteristical behaviour of a c_2^1 axino coupling remains. This was exactly our expectation. In comparison to the BRs, *e.g.* in Fig. 6.1 or Fig. 6.4, we have here a total drop off of the first decay. But we already pointed out that this issue is due to the sensitive minimalization conditions of the scalar potential especially at this new parameter point, see section 6.2.1.

Our second example at the SPS4 benchmark point with the $(\mathbf{\Lambda}_{E^1})_{21}$ operator is shown in Fig. 8.2. In this case, we expect a c_2^2-like form of the BRs. This is exactly what we observe. Again the only small difference to Fig. 6.2 or Fig. 6.5(a) comes from the fact that Γ_1 is not contributing to the BRs at masses above $2m_e$. This is similar to the observation at SPS2 in Fig. 8.1.

Recalling our analysis of Chapter 6 at the benchmark point SPS1a and in addition the results of the benchmark points SPS2 and SPS4 shown here we can draw the strong conclusion that the characteristic behaviour of the BRs is predefined by the largest axino Yukawa coupling c_2^i. Only small deviations originating in the minimization conditions

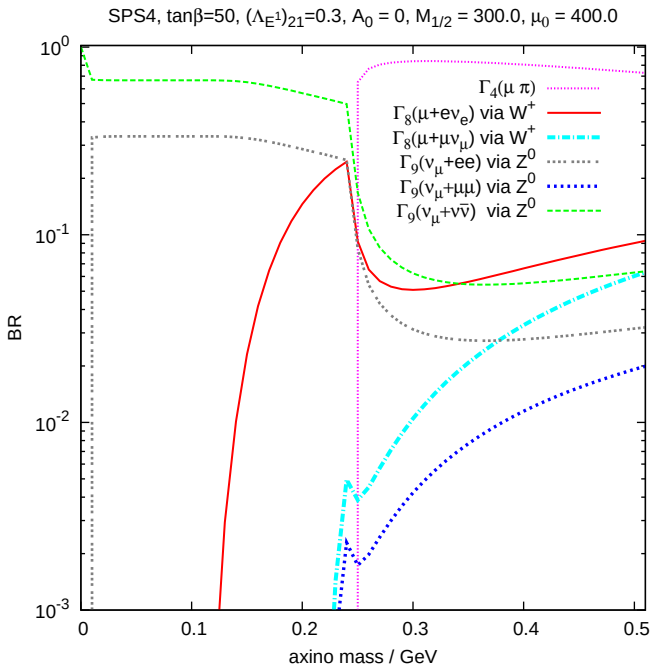

Figure 8.2: The BR of the axino decays at the benchmark point SPS4 with the $\not{R}_p$ couplings $(\mathbf{\Lambda}_{E^1})_{21} = 0.3$. With the chosen $\not{R}_p$ operator c_2^2 is the relevant Yukawa coupling where the axino couples preferred to the electron family respectively. Due to kinematical thresholds of the decay channels several mass regimes are formed with different behaviour.

of the scalar potential are present. Of course, as indicated before couplings with strong bounds due to the absence of tachyons have to be treated separately.

8.2 Axino as Dark Matter at SPS2 and SPS4

In the foregoing paragraph we have shown the BRs of $\not{R}_p$ couplings $(\mathbf{\Lambda}_{D^2})_{12}$ at SPS2 and $(\mathbf{\Lambda}_{E^1})_{21}$ at SPS4. In this section we extend this to the axino energy densities. We saw that the BRs showed no extraordinary exceptions in behaviour. Thus it supports the assumption that the axino energy density will have the same properties as seen in chapter 7. This means that $\Omega_{\tilde{a}}$ can also be characterized by the c_2^i.

Fig. 8.3 shows the contour plot $m_{\tilde{a}}$ vs. $\mathbf{\Lambda}_D$ vs. T_{R} where the latter parameter is kept implicit as already discussed. The red (blue) line shows the upper (lower) limit on the axino mass where the condition $\Omega_{\tilde{a}} = \Omega_{\mathrm{DM}}$ is satisfied. The chosen $\not{R}_p$ coupling induces a dominant c_2^1 and thus leads to its characteristic result for the energy density. In the previous chapter we pointed out that the function shows a kink at an energy close to the pion mass. The reason is that the pionic decay mode opens up and has the largest BR. The accompaning transition which is related to this change in the order of the BRs explains the kink, the approach of the two lines as well as the different slopes, *cf.* section 7.3. Furthermore we note that in this scenarios axino masses of (10-500) MeV can provide the DM. This mass range is larger than in the cases shown for the benchmark point SPS1a in

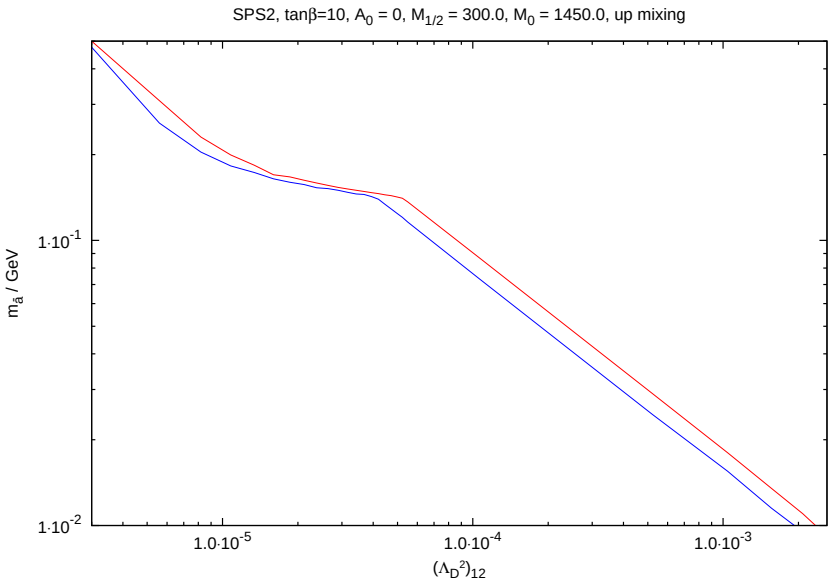

Figure 8.3: A contour plot of the axino mass as a function of $\not{R}_p$ coupling $(\mathbf{\Lambda}_{D^2})_{12}$ with up-mixing assumption and T_{R} - implcit on the z-axis. The analysis is performed at the benchmark point SPS2 with the parameter space values as shown on the top of the figure. The red (blue) line indicates the upper (lower) axino mass for a given $(\mathbf{\Lambda}_{D^2})_{12}$ value where the condition $\Omega_{\tilde{a}} = \Omega_{\mathrm{DM}}$ is satisfied. The behaviour of the lines is due to different boundary conditions of the reheating temperature as well as the BR, see text for details. This results are obtained for a PQ breaking scale of $f_{\mathrm{PQ}} = 10^{11}$ GeV. Note that the small kinks at the blue line are due to numerical artefacts and have no significance.

section 7.3. The reason is that we have evaluated the upper bound on $(\mathbf{\Lambda}_{D^2})_{12}$ operator ourselves wheras for the point SPS1a we used the bounds in Table 6.3 from Ref. [35]. We already argued that these values are not up-to-date and could be chosen more loosely.

In Fig. 8.4 the second $\not{R}_p$ coupling at benchmark point SPS4 is shown. Note that in this case we have a dominant c_2^2 case. From the BRs, we know that a transition takes place at a mass of ~ 250 MeV, where the $\tilde{a} \to \mu + \pi$ decay channel becomes accessible. As this change in the order of the BRs is not smooth, the red and blue line coincide at this mass. Again this property leads to a modification in the slope of the curve. Here we have the possibility of smaller masses for the axino as DM. The same arguments hold as for the $(\mathbf{\Lambda}_{D^2})_{12}$ case.

In conclusion we can state that indeed depending on the $\not{R}_p$ operator we can deduce the largest axino Yukawa coupling. The form of the function describing areas of $\Omega_{\tilde{a}} \equiv \Omega_{\mathrm{DM}}$ can then be predicted. This argumentat holds for any point in SUSY parameter space and thus the axino represents a strong and viable DM candidate in the discussed framework with $\not{R}_p$.

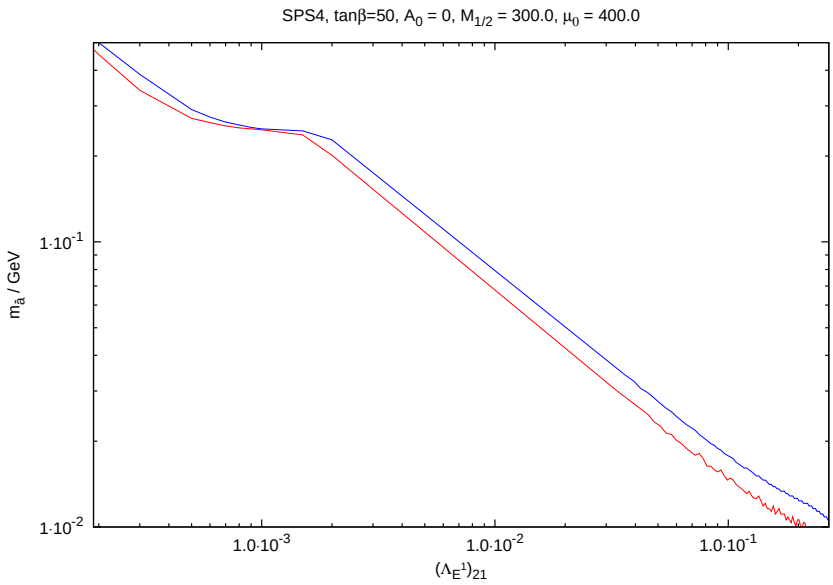

Figure 8.4: A contour plot of the axino mass as a function of $\not{R}_p$ coupling $(\mathbf{\Lambda}_{E^1})_{21}$ with up-mixing assumption and T_{R} - implcit on the z-axis. The analysis is performed at the benchmark point SPS4 with the parameter space values as shown on the top of the figure. The red (blue) line indicates the upper (lower) axino mass for a given $(\mathbf{\Lambda}_{E^1})_{21}$ value where the condition $\Omega_{\tilde{a}} = \Omega_{\mathrm{DM}}$ is satisfied. The behaviour of the lines is due to different boundary conditions of the reheating temperature as well as the BR, see text for details. This results are obtained for a PQ breaking scale of $f_{\mathrm{PQ}} = 10^{11}$ GeV. Note that the small kinks at the blue line are due to numerical artefacts and have no significance.

9 Summary and Conclusion

The introduction and spontaneous breaking of the additional $U(1)_{\mathrm{PQ}}$ symmetry solves the strong CP-problem of the Standard Model (SM) of particle physics. The associated pseude Goldstone boson is the yet unobserved axion which enlarges the particle content of the SM. One way to implement the axion is the DFSZ model. Nevertheless the SM faces several unsolved problems where Supersymmetry (SUSY) represents a very promising extension. In this thesis we studied the supersymmmetrized version of the DFSZ model with the axino as the fermonic SUSY partner of the axion.

For this purpose we pointed out that imposing baryon-triality B_3 within the most general superpotential keeps the proton stable. Furthermore it enlarges the SSM parameter space and naturally includes neutrino masses. Here we consider a possible solution of the DM problem within B_3 mSUGRA.

Focusing on the B_3 mSUGRA model we as first step investigated the supersymmetrised version of the θ-term. We have seen that the axino couples to the bino-photon, the gluino-gluon as well as to two gluons and a gluino. The last mentioned interaction is the main axino production channel in the early universe.

We continued our analysis following the Ansatz of Rajagopal et. al. by introducing the axino superfield into the μ-term of the superpotential. After the PQ symmetry breaking the scalar part of the newly introduced superfield acquires a vev and the usual μ-term is restored in a natural way. As shown this term leads through the coupling to the Higgs doublets to the mixing of the axino and the higgsino. We thus have one additional neutralino, which is axino-like.

Keeping in mind that we work in the B_3 mSUGRA model this treatment of the axino is not complete. The lepton- and the first Higgs-doublet have the same quantum numbers. We thus introduced the axino superfield in the lepton number violating bilinear term of the superpotential. This modification led to the coupling of the axino again with the Higgs but now also with the neutrinos. In total this model has eight neutralinos which mix.

Of course, in this axino B_3 mSUGRA model the soft-supersymmetry breaking terms as well as the RGE are modified due to the new Yukawa couplings. We computed the new one-loop anomalous dimensions. The newly introduced Yukawa coupling are quite small thus the changes in the RGEs do not have a large effect on the spectrum. We have checked this issue by performing a representative analysis of the RGEs at the SUSY benchmark point SPS1a.

Neglecting the small RGE corrections, we were able to use `SOFTSUSY` [39] to calculate the superparticle spectrum. We implemented the axino interactions to get the mixing angles of the axino with bino, higgsino and neutrinos.

In our scenario the axino is the LSP and it can decay. The decay via the SUSY

$U(1)_Y$ θ-term, $\tilde{a} \to \nu\gamma$ is kinematically always always open. We considered all possible combiantions of the decay $\tilde{a} \to \ell_i^+ \ell_j^- \nu_k$ as well as $\tilde{a} \to M^\pm + \ell_i^\mp$ and $\tilde{a} \to M^0 + \nu$ with $M = \pi, K$. We calculated the corresponding decay widths and evaluted the lifetime at SPS1a with non-zero $\not{R}_p$ operators $(\mathbf{\Lambda}_{E^i})_{jk}$ and $(\mathbf{\Lambda}_{D^i})_{jk}$ for different axino masses. Due to the intrinsic structure of the RGEs, we get a preference for specific axino Yukawa couplings c_2^i for a chosen $\not{R}_p$ operator. From this we were able to categorize the behaviour of the BRs for each operator. We discerned that several regions were formed where different decay channels are dominant. In general the decays $\tilde{a} \to 3\nu, e^+e^-\nu, e\pi, \mu\pi$ are preferred. Small deviations from these cases according to the preferred c_2^i were obtained in scenarios with $(\mathbf{\Lambda}_{D^i})_{jk}$ couplings where quark mixing and restrictions on the bounds from the absence of tachyons come into play.

We further pointed out that due the weakly interacting nature of the axino it could provide cold dark matter (CDM). A requirement is that the axino has a long life time comparable to the age of the universe.

An important parameter for the determination of the the axino energy density, $\Omega_{\tilde{a}}$, is the reheating temperature T_R. For this purpose we modified existing results to the scenario of a decaying axino with an exponential decay. The modification of the axino yield gave us the possibility to determine the reheating temperature T_R for different f_PQ. We got *e.g.* for $f_\mathrm{PQ} = 10^{11}$ GeV a $T_\mathrm{R} \sim 10^7$ GeV. For temperatures above this value the yield is governed by the equilibrium number density of a Majorana particle which is temperature independent and thus a constant.

In the next part of our work, we applied the limits on the reheating temperature to an analysis of the axino energy density. The results show that the axino indeed can provide DM in our studied $\not{R}_p$ models and that the functional behaviour of $\Omega_{\tilde{a}}$ can be traced back to the underlying BRs. The masses of the axino turned out to be in the region of $\sim (30 - 500)$ MeV depending on the value of the $\not{R}_p$ coupling. This holds independently of whether the $\not{R}_p$ is due to the $LL\bar{E}$- or the $LQ\bar{D}$ operator.

We conclude that the categorization of the BRs as well as the axino energy density can be applied in general to the SUSY parameter space. We veryfied this by perfoming exemplary analyses for two $\not{R}_p$ couplings at the benchmark points SPS2 and SPS4. Hence the axino represents a strong and viable DM candidate in the DFSZ model embedded in the R-Parity violating mSUGRA model. Furthermore the final state combinations which consist of only SM particles give rise to a potential discovery of the axino and thus possible evidence as CDM.

A Useful Relations

A.1 Metric, sigma matrix conventions and relations

Throughout this thesis we use for the four dimensional Minkowski space the following metric:

$$g^{\mu\nu} = g_{\mu\nu} = \mathrm{diag}(+1, -1, -1, -1)\,, \tag{A.1}$$

where $\mu, \nu = 0, 1, 2, 3$. Furthermore the sigma matrices are defined by

$$\sigma^\mu = (\mathbb{1}_2, \vec{\boldsymbol{\sigma}}), \qquad \bar{\sigma}^\mu = (\mathbb{1}_2, -\vec{\boldsymbol{\sigma}})\,. \tag{A.2}$$

Note that the bar shuld not be confused with the bar used for spinors. For the computation of the decay width as well as the lifetimes the trace of a product of sigma matrices has to be evaluated. These products include alternating combinations of the sigma matrices in Eq. (A.2). In a similar way to the four component gamma matrices we have for the traces of the sigma matrix combinations

$$\begin{aligned}
\mathrm{tr}[\sigma^\mu\bar{\sigma}^\nu] = \mathrm{tr}[\bar{\sigma}^\nu\sigma^\mu] &= 2g^{\mu\nu}\,, && \text{(A.3)}\\
\mathrm{tr}[\sigma^\mu\bar{\sigma}^\nu\sigma^\rho\bar{\sigma}^\lambda] &= 2(g^{\mu\nu}g^{\rho\lambda} - g^{\mu\rho}g^{\nu\lambda} + g^{\mu\lambda}g^{\nu\rho} + \mathrm{i}\varepsilon^{\mu\mu\rho\lambda})\,, && \text{(A.4)}\\
\mathrm{tr}[\bar{\sigma}^\mu\sigma^\nu\bar{\sigma}^\rho\sigma^\lambda] &= 2(g^{\mu\nu}g^{\rho\lambda} - g^{\mu\rho}g^{\nu\lambda} + g^{\mu\lambda}g^{\nu\rho} + \mathrm{i}\varepsilon^{\mu\mu\rho\lambda})\,, && \text{(A.5)}
\end{aligned}$$

where the totaly antisymmetric tensor obeys the relation

$$\varepsilon^{0123} = -\varepsilon_{0123} = +1\,. \tag{A.6}$$

In some of the calculations a product of two traces occurs involving four sigma matrices and momenta in each case. Of course, all Lorentz indices are contracted. Next we present such an example. Starting with the first trace we have

$$\begin{aligned}
\mathrm{tr}[\bar{\sigma}_\mu p^\nu \sigma_\nu \bar{\sigma}_\rho k^\lambda \sigma_\lambda] &= p^\nu k^\lambda \mathrm{tr}[\bar{\sigma}_\mu \sigma_\nu \bar{\sigma}_\rho \sigma_\lambda]\\
&= p^\nu k^\lambda 2(g_{\mu\nu}g_{\rho\lambda} - g_{\mu\rho}g_{\nu\lambda} + g_{\mu\lambda}g_{\nu\lambda} - \mathrm{i}\varepsilon_{\mu\nu\rho\lambda})\\
&= 2(p_\mu k_\rho - g_{\mu\rho}(p\cdot k) + p_\rho k_\mu - \mathrm{i}p^\nu k^\lambda \varepsilon_{\mu\nu\rho\lambda}) && \text{(A.7)}
\end{aligned}$$

$$\begin{aligned}
\mathrm{tr}[\bar{\sigma}^\mu s_\kappa \sigma^\kappa \bar{\sigma}^\rho r_\alpha \sigma^\alpha] &= s_\kappa r_\alpha \mathrm{tr}[\bar{\sigma}^\mu \sigma^\kappa \bar{\sigma}^\rho \sigma^\alpha]\\
&= 2(s^\mu r^\rho - g^{\mu\rho}(r\cdot s) + s^\rho r^\mu - \mathrm{i}s_\kappa r_\alpha \varepsilon^{\mu\kappa\rho\alpha})\,. && \text{(A.8)}
\end{aligned}$$

Here p, k, r and s are four momenta. Multiplying both results of the traces we get:

$$\mathrm{tr}[\bar{\sigma}_\mu p^\nu \sigma_\nu \bar{\sigma}_\rho k^\lambda \sigma_\lambda] \cdot \mathrm{tr}[\bar{\sigma}^\mu s_\kappa \sigma^\kappa \bar{\sigma}^\rho r_\alpha \sigma^\alpha] = 16(p\cdot s)(k\cdot r)\,. \tag{A.9}$$

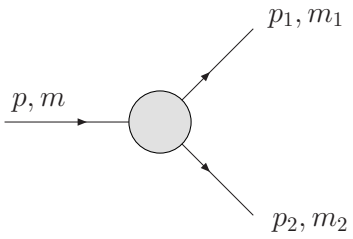

Figure A.1: Labels for the two body decay width discussed in the text, *cf.* also Ref. [48]

Note, that all products with the ε-tensor vanish except for the quadratic term. This can be evaluated with the relation:

$$\varepsilon_{\alpha\beta\rho\delta}\varepsilon^{\alpha\beta\mu\nu} = -2(\delta^{\mu}_{\ \rho}\delta^{\nu}_{\ \sigma} - \delta^{\mu}_{\ \sigma}\delta^{\nu}_{\ \rho}) \tag{A.10}$$

In the computation of the supersymmetrized version of the θ-term we used the relation

$$\sigma^{\mu}\bar{\sigma}^{\nu}V_{\mu\nu} - 2\mathrm{i}\sigma^{\mu\nu}V_{\mu\nu}\,, \tag{A.11}$$

where $\sigma^{\mu\nu}$ is the antisymmetrized product of the sigma matrices. It is given by

$$\sigma^{\mu\nu} \equiv \frac{\mathrm{i}}{4}(\sigma^{\mu}\bar{\sigma}^{\nu} - \sigma^{\nu}\bar{\sigma}^{\mu})\,. \tag{A.12}$$

Furthermore we made use of the following relation for the Grassmann numbers

$$\theta_{\tau}\theta_{\beta} = \frac{1}{2}\varepsilon_{\tau\beta}\theta^{\beta}\theta_{\beta} = \frac{1}{2}\varepsilon_{\tau\beta}\theta\theta\ . \tag{A.13}$$

For further details and relations we refer the reader to Ref. [78, 158].

A.2 Two Body decay width

In chapter 5 we have presented axino decays. Some of them are two body decays $\tilde{a} \to b_1 b_2$ and hence it is convinient to use the widely known two body decay width, *cf. e.g.* Ref. [48]

$$\Gamma = \frac{1}{8\pi}|\mathcal{M}|^2\frac{|p_1|}{m^2_{\tilde{a}}}\,, \tag{A.14}$$

where the labels are according to Fig. A.1. The momentum of the outgoing particle is given by

$$|p_1| = \frac{1}{2m_{\tilde{a}}}\sqrt{m^4_{\tilde{a}} + m^4_1 + m^4_2 - 2m^2_{\tilde{a}}m^2_1 - 2m^2_{\tilde{a}}m^2_2 - 2m^2_1m^2_2}\,, \tag{A.15}$$

and $\mathcal{M}$ is the corresponding amplitude.

B Axino Mass Eigenstate Interactions

B.1 SM Neutrino Interactions

First consider the SM interactions of the neutrinos to the W and Z bosons. These are given in Eq. (J.1.2) of Ref. [78]

$$\mathscr{L} = -\frac{g}{\sqrt{2}}\left[\hat{\nu}^{\dagger i}\bar{\sigma}^{\mu}\hat{\ell}_i W_{\mu}^{+} + \hat{\ell}^{\dagger i}\bar{\sigma}^{\mu}\hat{\nu}_i W_{\mu}^{-}\right] - \frac{g}{2c_W}\hat{\nu}^{\dagger i}\bar{\sigma}^{\mu}\hat{\nu}_i Z_{\mu}\,. \tag{B.1}$$

Here i runs over the three lepton flavors and the hat denotes the interaction states. Inserting the neutralino and chargino mass eigenstates, we obtain

$$\mathscr{L} \;=\; -\frac{g}{\sqrt{2}}\left[(N_{ci}^{*}\widetilde{\xi}_c^{0})^{\dagger}\bar{\sigma}^{\mu}U_{mi}^{*}\,\widetilde{\eta}_m^{-}W_{\mu}^{+} + (U_{mi}^{*}\,\widetilde{\eta}_m^{-})^{\dagger}\bar{\sigma}^{\mu}N_{ci}^{*}\widetilde{\xi}_c^{0}W_{\mu}^{-}\right] - \frac{g}{2c_W}(N_{ci}^{*}\widetilde{\xi}_c^{0})^{\dagger}\bar{\sigma}^{\mu}N_{di}^{*}\widetilde{\xi}_d^{0}Z_{\mu}\,. \tag{B.2}$$

As before, $i = 5,6,7$ runs over the neutrino flavors, whereas $c,d = 1,\ldots,8$ and $m = 1,\ldots,5$. We thus have explicitly for the axinos

$$\begin{aligned}\mathscr{L}_{\tilde{a}} \;=\; & -\frac{g}{\sqrt{2}}\left[N_{i8}U_{mi}^{*}\tilde{a}^{\dagger}\bar{\sigma}^{\mu}\widetilde{\eta}_m^{-}W_{\mu}^{+} + U_{im}N_{8i}^{*}(\widetilde{\eta}_m^{-})^{\dagger}\bar{\sigma}^{\mu}\tilde{a}W_{\mu}^{-}\right] \\ & -\frac{g}{2c_W}\left[N_{i8}N_{ci}^{*}\tilde{a}^{\dagger}\bar{\sigma}^{\mu}\widetilde{\xi}_c^{0} + \text{h.c.}\right]Z_{\mu}\,.\end{aligned} \tag{B.3}$$

Here we used the fact that the neutralino is a Majorana particle. In Fig. B.1 you find the Feynman diagram which describes the axino interaction with the charginos $\eta^{\pm}$ and the $W^{\pm}, Z^0$ gauge bosons.

Note that Eq. (B.3) is not the only contribution for the axino, neutralino and Z^0 interaction, see also Eq. (B.6).

Finally the Yukawa interaction between the axino, chargino and the W^{-} boson has also a term in Eq. (B.10).

B.2 Bino, Wino and Higgsino Interactions

The Z^0–Higgsino–Higgsino interaction is given by

$$\mathscr{L} = \frac{g}{2c_W}\left[-\tilde{H}_1^{\dagger}\bar{\sigma}^{\mu}\tilde{H}_1 + \tilde{H}_2^{\dagger}\bar{\sigma}^{\mu}\tilde{H}_2\right]Z_{\mu} \tag{B.4}$$

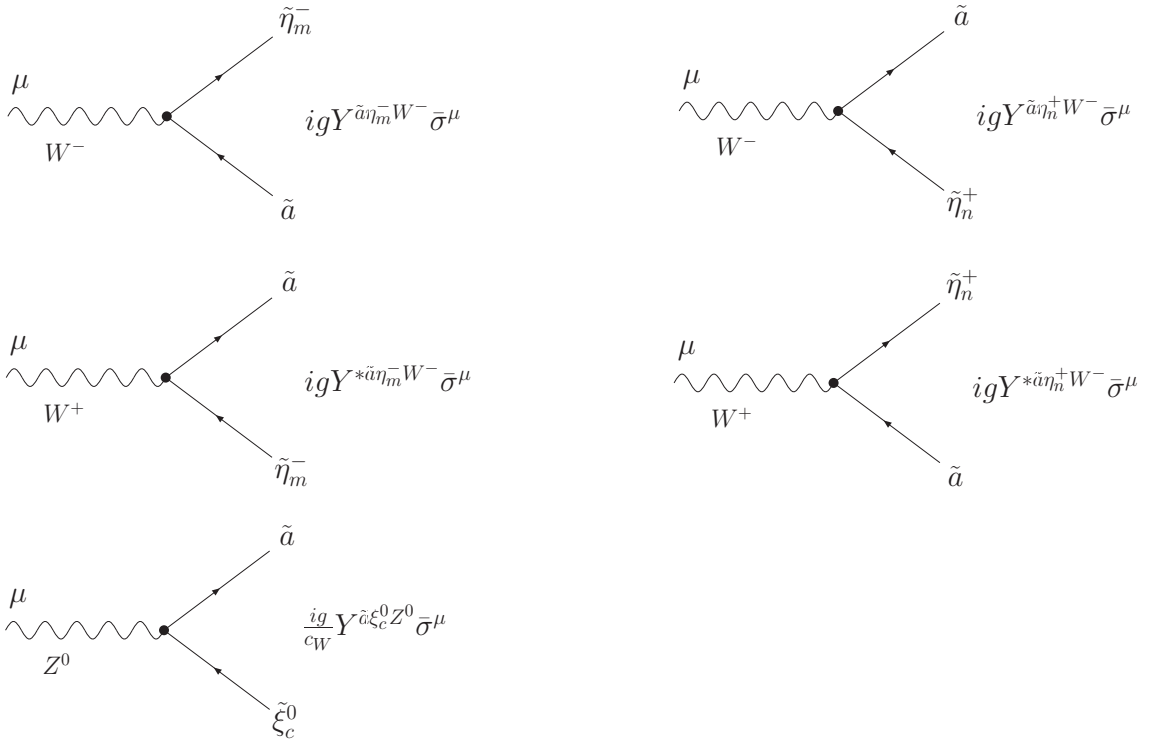

Figure B.1: Feynman rules for axino interaction with charginos $\eta^\pm$ and the gauge bosons $W^\pm, Z^0$. The vertex factors $Y^{\tilde{a}\tilde{\xi}_c^0 Z^0}$ and $Y^{\tilde{a}\tilde{\eta}^\pm W^-}$ are given by Eq. (B.7), Eq. (B.11) and Eq. (B.12).

Here $\tilde{H}$ refers to a neutral Higgsino, *cf.* Fig. K.2.1 in Ref. [78]. Inserting the mass eigenstates we have

$$\mathscr{L} = \frac{g}{2c_W}\left[-(N_{c4}^*\widetilde{\xi}_c^0)^\dagger\bar{\sigma}^\mu(N_{d4}^*\widetilde{\xi}_d^0) + (N_{c3}^*\widetilde{\xi}_c^0)^\dagger\bar{\sigma}^\mu N_{d3}^*\widetilde{\xi}_d^0\right] Z_\mu\,, \tag{B.5}$$

where $i,j = 1,\ldots,8$. The resulting axino interaction Lagrangian reads

$$\mathscr{L}_{\tilde{a}} = \frac{g}{2c_W}\left[(-N_{48}N_{c4}^* + N_{38}N_{c3}^*)\tilde{a}^\dagger\bar{\sigma}^\mu\tilde{\xi}_c^0 + \text{h.c.}\right] Z_\mu\,. \tag{B.6}$$

Collecting all contributions of the axino, neutralino and Z^0 interaction we define:

$$Y^{\tilde{a}\tilde{\xi}_c^0 Z^0} = \frac{1}{2}\left[N_{38}N_{c3}^* - N_{48}N_{c4}^* - N_{i8}N_{ci}^*\right]\,. \tag{B.7}$$

A further Higgsino contribution reads [78]:

$$\mathscr{L} = g\left[-\frac{1}{\sqrt{2}}\tilde{H}_2^\dagger\bar{\sigma}^\mu\tilde{H}_2^+ + \tilde{W}^{0\dagger}\bar{\sigma}^\mu\tilde{W}^+ + \frac{1}{\sqrt{2}}\tilde{H}_1^+\bar{\sigma}^\mu\tilde{H}_1 - \tilde{W}^{-\dagger}\bar{\sigma}^\mu\tilde{W}^0\right] W_\mu^- + \text{h.c.} \tag{B.8}$$

which in terms of mass eigenstates reads

$$\begin{aligned}\mathscr{L} &= g\left[-\frac{1}{\sqrt{2}}(N^*_{c3}\widetilde{\xi}^0_c)^\dagger\bar{\sigma}^\mu(V^*_{n2}\,\widetilde{\eta}^+_n) + (N^*_{c2}\widetilde{\xi}^0_c)^\dagger\bar{\sigma}^\mu(V^*_{n1}\,\widetilde{\eta}^+_n) + \frac{1}{\sqrt{2}}(U^*_{m2}\,\widetilde{\eta}^-_m)^\dagger\bar{\sigma}^\mu(N^*_{c4}\widetilde{\xi}^0_c)\right.\\ &\quad \left.-(U^*_{m1}\,\widetilde{\eta}^-_m)^\dagger\bar{\sigma}^\mu(N^*_{c2}\widetilde{\xi}^0_c)\right]W^-_\mu + \text{h.c.}\,, \qquad \text{(B.9)}\end{aligned}$$

here we have $c = 1,\ldots,8$ and $m,n = 1,\ldots,5$. The axino part of the latter equation is given by

$$\begin{aligned}\mathscr{L}_{\tilde{a}} &= g\left[\left(-\frac{1}{\sqrt{2}}N_{38}V^*_{n2} + N_{28}V^*_{n1}\right)\tilde{a}\,\bar{\sigma}^\mu\widetilde{\eta}^+_n + \left(\frac{1}{\sqrt{2}}N^*_{84}U_{2m} - N^*_{82}U_{1m}\right)(\widetilde{\eta}^-_m)^\dagger\,\bar{\sigma}^\mu\tilde{a}\right]W^-_\mu\\ &\quad +\text{h.c.} \qquad \text{(B.10)}\end{aligned}$$

Summarizing all terms of the axino, chargino and W^- interaction it is convenient to define

$$Y^{\tilde{a}\tilde{\eta}^+_n W^-} = -\frac{1}{\sqrt{2}}N_{38}V^*_{n2} + N_{28}V^*_{n1}\,, \qquad \text{(B.11)}$$

$$Y^{\tilde{a}\tilde{\eta}^-_m W^-} = \frac{1}{\sqrt{2}}N^*_{84}U_{2m} - N^*_{82}U_{1m} - \frac{1}{\sqrt{2}}N^*_{8i}U_{im}\,. \qquad \text{(B.12)}$$

The hermitian conjugate returns the coupling for the axino interaction with the W^+ boson. The Feynman rules are given in Fig. B.1.

B.3 Higgs-Chargino-Neutralino interaction

This Lagrangian corresponding to Fig. K.3.1 in Ref. [78] can also be found in Ref. [159]

$$\begin{aligned}\mathscr{L} &= ig(H^+_1\widetilde{W}^-\widetilde{H}_1 + H^-_2\widetilde{W}^+\widetilde{H}_2) + \frac{i}{\sqrt{2}}(g\widetilde{W}^0 - g'\widetilde{B})(H^{0\dagger}_1\widetilde{H}_1 - H^{0\dagger}_2\widetilde{H}_2)\\ &\quad +\frac{i}{\sqrt{2}}(g\widetilde{W}^0 + g'\widetilde{B})(H^-_2\widetilde{H}^+_2 - H^+_1\widetilde{H}^-_1)\,. \qquad \text{(B.13)}\end{aligned}$$

Translating this to the mass eigenstate basis we get

$$\begin{aligned}\mathscr{L} &= -g\Big[U^*_{m1}N^*_{c4}\sin\beta_\pm\,H^+\,\widetilde{\eta}^-_m\widetilde{\xi}^0_c + V^*_{n1}N^*_{c3}\cos\beta_\pm\,H^-\,\widetilde{\eta}^+_n\widetilde{\xi}^0_c\Big]\\ &\quad -\frac{1}{\sqrt{2}}\Big[g(N^*_{c2}\widetilde{\xi}^0_c) - g'(N^*_{c1}\widetilde{\xi}^0_c)\Big]\frac{1}{\sqrt{2}}\sum_{\phi^0}\Big[(k_{d\phi^0}\phi^0)^\dagger(N^*_{c4}\widetilde{\xi}^0_c) - (k_{u\phi^0}\phi^0)^\dagger(N^*_{c3}\widetilde{\xi}^0_c)\Big]\\ &\quad -\frac{1}{\sqrt{2}}\Big[g(N^*_{c2}\widetilde{\xi}^0_c) + g'(N^*_{c1}\widetilde{\xi}^0_c)\Big]\Big[(\cos\beta_\pm\,H^-(V^*_{n2}\,\widetilde{\eta}^+_n) - \sin\beta_\pm\,H^+(U^*_{m2}\,\widetilde{\eta}^-_m)\Big]\,, \qquad \text{(B.14)}\end{aligned}$$

where again $c = 1, \ldots, 8$ and $m, n = 1, \ldots, 5$. For the axino we then have explicitly

$$\begin{aligned}
\mathscr{L}_{\tilde{a}} &= -g\Big[\sin\beta_\pm\, N^*_{84} U^*_{m1} H^+ \widetilde{\eta}^-_m + \cos\beta_\pm\, N^*_{83} V^*_{n1} H^- \widetilde{\eta}^+_n\Big]\tilde{a} \\
&\quad -\frac{1}{2}\Big[gN^*_{82} - g'N^*_{81}\Big] \times \sum_{\phi^0}\Big[k_{d\phi^0} N^*_{c4} - k_{u\phi^0} N^*_{c3}\Big]\tilde{a}\phi^0\widetilde{\xi}^0_c \\
&\quad -\frac{1}{2}\Big[gN^*_{c2} - g'N^*_{c1}\Big] \times \sum_{\phi^0}\Big[k_{d\phi^0} N^*_{84} - k_{u\phi^0} N^*_{83}\Big]\tilde{a}\phi^0\widetilde{\xi}^0_c \\
&\quad -\frac{1}{\sqrt{2}}\Big[gN^*_{82} + g'N^*_{81}\Big] \times \Big[\cos\beta_\pm\, V^*_{n2}\, H^-\, \widetilde{\eta}^+_n - \sin\beta_\pm\, U^*_{m2}\, H^+\, \widetilde{\eta}^-_m\Big]\tilde{a}\,. \quad \text{(B.15)}
\end{aligned}$$

Obviously the first and the last line of Eq. (B.15) describe axino, Higgs and chargino interactions. Considering as well Eq. (B.28) we have

$$Y^{\tilde{a}\tilde{\eta}^+_n H^-} = -g\cos\beta_\pm\, N^*_{83} V^*_{n1} - \frac{1}{\sqrt{2}}\Big[gN^*_{82} + g'N^*_{81}\Big]\cos\beta_\pm\, V^*_{n2} + (\mathbf{Y}_\ell)^i{}_j \sin\beta_\pm N^*_{8i} U_{jn}\,, \quad \text{(B.16)}$$

where the last term is an additional contribution of Eq. (B.28). Furthermore we get for the other axino, Higgs and chargino combination

$$Y^{\tilde{a}\tilde{\eta}^-_m H^+} = -g\sin\beta_\pm\, N^*_{84} U^*_{m1} + \frac{1}{\sqrt{2}}\Big[gN^*_{82} + g'N^*_{81}\Big]\sin\beta_\pm\, U^*_{m2}\,. \quad \text{(B.17)}$$

In the neutral case we can define

$$Y^{\tilde{a}\phi^0\tilde{\xi}^0_c} = -\frac{1}{2}\sum_{\phi^0}\Big[(gN^*_{82} - g'N^*_{81})(k_{d\phi^0} N^*_{c4} - k_{u\phi^0} N^*_{c3}) + (gN^*_{c2} - g'N^*_{c1})(k_{d\phi^0} N^*_{84} - k_{u\phi^0} N^*_{83})\Big] \quad \text{(B.18)}$$

The corresponding Feynman diagrams can be found in Fig. B.2.

B.4 Quark-squark-neutralino interactions

Using Eq. (C72) from Ref. [75], we have in our notation according to Ref. [78]

$$\mathscr{L} = \frac{i}{\sqrt{2}} g'(Y_u \hat{u}\tilde{u}^*_R + Y_d \hat{d}_L \tilde{d}^*_R)\widetilde{B} + \frac{i}{\sqrt{2}}(g\tau^3_{ij}\widetilde{W}^0 + Y_Q g'\delta_{ij}\widetilde{B}) Q^i \tilde{Q}^*_j\,, \quad \text{(B.19)}$$

where Y_Q, Y_u, Y_d are the according hypercharges. Inserting the hypercharges and restricting ourselves to one quark generation we obtain:

$$\begin{aligned}
\mathscr{L} &= \frac{i}{\sqrt{2}} g'\Big[-\frac{4}{3}\widetilde{B}\hat{u}\tilde{u}^*_R + \frac{2}{3}\widetilde{B}\hat{d}\tilde{d}^*_R\Big] + \frac{i}{\sqrt{2}}\Big[g\widetilde{W}^0 + \frac{1}{3}g'\widetilde{B}\Big]\hat{u}\tilde{u}^*_L \\
&\quad + \frac{i}{\sqrt{2}}\Big[-g\widetilde{W}^0 + \frac{1}{3}g'\widetilde{B}\Big]\hat{d}\tilde{d}^*_L + \text{h.c.} \quad \text{(B.20)}
\end{aligned}$$

Rotating into the mass eigenbasis we get

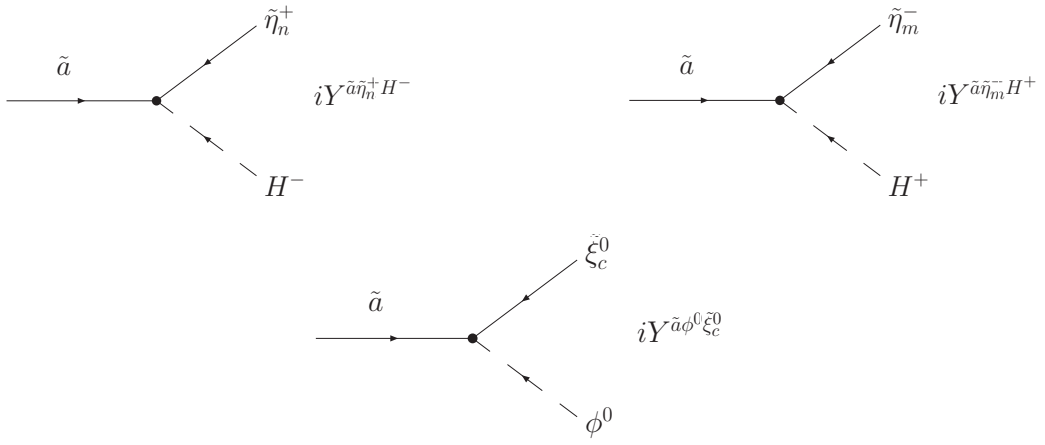

Figure B.2: Feynman rules which desribe the axino interaction with charginos and Higgs. The according Yukawa couplings are given in the text, cf. Eq. (B.16)-(B.18).

$$\begin{aligned}\mathscr{L} &= +\frac{1}{\sqrt{2}}g'\Big[\frac{4}{3}N_{c1}^*\widetilde{\xi}_c^0\hat{u}\tilde{u}_R^* - \frac{2}{3}N_{c1}^*\widetilde{\xi}_c^0\hat{d}\tilde{d}_R^*\Big] - \frac{1}{\sqrt{2}}\Big[gN_{c2}^*\widetilde{\xi}_c^0 + \frac{1}{3}g'N_{c1}^*\widetilde{\xi}_c^0\Big]\hat{u}\tilde{u}_L^* \\ &\quad +\frac{1}{\sqrt{2}}\Big[gN_{c2}^*\widetilde{\xi}_c^0 - \frac{1}{3}g'N_{c1}^*\widetilde{\xi}_c^0\Big]\hat{d}\tilde{d}_L^* + \text{h.c.}\,, \end{aligned} \tag{B.21}$$

with a sum over $c = 1, \cdots, 8$. Selecting only the axino mass eigenstate and rotating the quark (squark) fields to their mass eigenbases the Lagrangian reads

$$\begin{aligned}\mathscr{L}_{\tilde{a}} &= \frac{1}{\sqrt{2}}g'N_{81}^*\Big[\frac{4}{3}\,u\tilde{u}_R^* - \frac{2}{3}\,d\tilde{d}_R^*\Big]\tilde{a} - \frac{1}{\sqrt{2}}\Big[gN_{82}^* + \frac{1}{3}g'N_{81}^*\Big]\tilde{a}u\tilde{u}_L^* \\ &\quad +\frac{1}{\sqrt{2}}\Big[gN_{82}^* - \frac{1}{3}g'N_{81}^*\Big]\tilde{a}d\tilde{d}_L^* + \text{h.c.}\,. \end{aligned} \tag{B.22}$$

Fig. B.3 shows the corresponding Feynman rules.

B.5 Lepton-slepton-neutralino interactions

The according Lagrangian can directly be obtained from the latter quark squark case, by replacing $(u, d) \to (\nu, \ell)$ and analogously the corresponding charges. Hence,

$$\mathscr{L} = \frac{i}{\sqrt{2}}\Big[-g\widetilde{W}^0 + \frac{1}{3}g'\widetilde{B}\Big]\ell^i\tilde{\ell}_{L_i}^* - \frac{i}{\sqrt{2}}g'\tilde{B}\nu\tilde{\nu}_R^* - \frac{i}{\sqrt{2}}g'\widetilde{B}\ell\tilde{\ell}_R^* + \text{h.c.}\,, \tag{B.23}$$

where we have omitted the first term as we have no $\bar{\nu}_L$ and thus no $\tilde{\nu}_L^*$. The mass eigenstates read

$$\begin{aligned}\mathscr{L} &= +\frac{1}{\sqrt{2}}\Big[gN_{c2}^*\widetilde{\xi}_c^0 - \frac{1}{3}g'N_{c1}^*\widetilde{\xi}_c^0\Big](U_{mi}^*\,\widetilde{\eta}_m^-)\tilde{\ell}_{L_i}^* + \frac{1}{\sqrt{2}}g'(N_{c1}^*\widetilde{\xi}_c^0)(N_{ci}^*\widetilde{\xi}_c^0)\tilde{\nu}_R^* \\ &\quad +\frac{1}{\sqrt{2}}g'(N_{c1}^*\widetilde{\xi}_c^0)(U_{mi}^*\,\widetilde{\eta}_m^-)\tilde{\ell}_R^* + \text{h.c.}\,. \end{aligned} \tag{B.24}$$

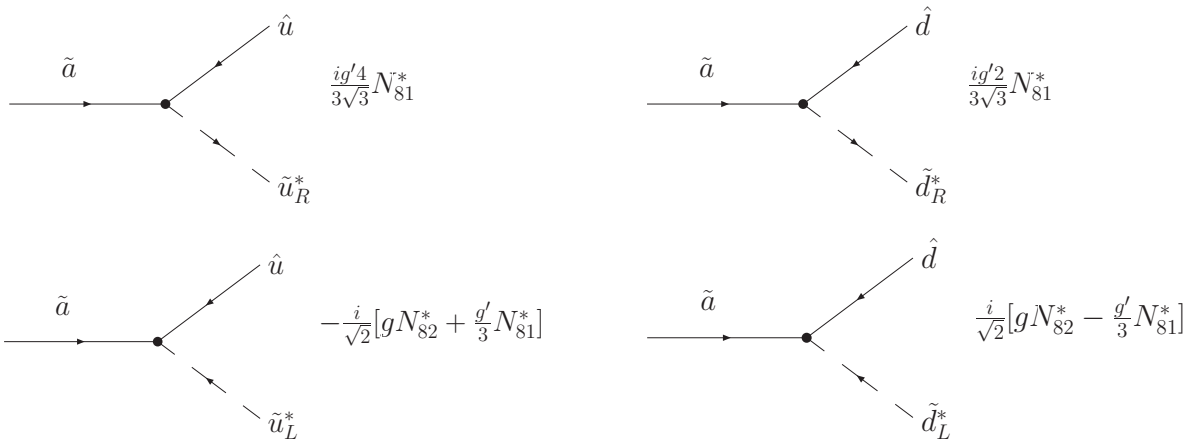

Figure B.3: Feynman rules which originate in the Lagrangian given by Eq. (B.22).

Here we have the same index structure as in the quark case before. Furthermore for the axino the Lagrangian reads

$$\begin{aligned}\mathscr{L}_{\tilde{a}} &= +\frac{1}{\sqrt{2}}\Big[gN_{82}^* - \frac{1}{3}g'N_{81}^*\Big]U_{mi}^*\,\tilde{a}\,\widetilde{\eta}_m^-\tilde{\ell}_{L_i}^* + \frac{1}{\sqrt{2}}g'\Big[N_{81}^*N_{ci}^* + N_{c1}^*N_{8i}^*\Big]\widetilde{\xi}_c^0\tilde{a}\tilde{\nu}_R^* \\ &\quad +\frac{1}{\sqrt{2}}\,g'N_{81}^*U_{mi}^*\,\tilde{a}\,\widetilde{\eta}_m^-\tilde{\ell}_R^* + \text{h.c.}\,. \end{aligned} \tag{B.25}$$

The related Feynman diagrams are shown in Fig. B.4.

B.6 Yukawa interactions from the MSSM superpotential

$$\begin{aligned}\mathscr{L}_{\text{MSSM}} &= (\mathbf{Y}_\ell)^i{}_j\Big[H_1^-\hat{\nu}_i\hat{\tilde{\ell}}^j + \tilde{\ell}_R^{*j}\tilde{H}_1^-\hat{\nu}_i - \tilde{\ell}_R^{*j}\tilde{H}_1\hat{\ell}_i - \tilde{\ell}_{L_i}\tilde{H}_1\hat{\tilde{\ell}}^j\Big] - (\mathbf{Y}_D)^i{}_j\Big[\tilde{d}_R^{*j}\hat{d}_i\tilde{H}_1 + \tilde{d}_i\tilde{H}_1\hat{\tilde{d}}_j\Big] \\ &\quad +(\mathbf{Y}_U)^i{}_j\Big[\tilde{u}_R^{*j}\hat{u}_i\tilde{H}_2 + \tilde{u}_i\hat{\tilde{u}}^j\tilde{H}_2\Big] + \text{h.c.}\end{aligned} \tag{B.26}$$

with a sum over $i,j = 1,2,3$. In terms fo the mass eigenstates

$$\begin{aligned}\mathscr{L}_{\text{MSSM}} &= (\mathbf{Y}_\ell)^i{}_j\Big[\sin\beta_\pm\, H^-(N_{ci}^*\widetilde{\xi}_c^0)(U_{mj}^*\,\widetilde{\eta}_m^-)^\dagger + \tilde{\ell}_R^{*j}(U_{m2}^*\,\widetilde{\eta}_m^-)(N_{ci}^*\widetilde{\xi}_c^0) - \tilde{\ell}_R^{*j}(N_{c4}^*\widetilde{\xi}_c^0)(U_{mi}^*\,\widetilde{\eta}_m^-) \\ &\quad -\tilde{\ell}_{L_i}(N_{c4}^*\widetilde{\xi}_c^0)(U_{mj}^*\,\widetilde{\eta}_m^-)^\dagger\Big] - (\mathbf{Y}_D)^i{}_j\Big[\tilde{d}_R^{*j}\hat{d}_i(N_{c4}^*\widetilde{\xi}_c^0) + \tilde{d}_{L_i}(N_{c4}^*\widetilde{\xi}_c^0)\hat{\tilde{d}}^j\Big] \\ &\quad +(\mathbf{Y}_U)^i{}_j\Big[\tilde{u}_R^{*j}\hat{u}_i(N_{c3}^*\widetilde{\xi}_c^0) + \tilde{u}_{L_i}\hat{\tilde{u}}_j(N_{c3}^*\widetilde{\xi}_c^0)\Big] + \text{h.c.}\end{aligned} \tag{B.27}$$

Here $c = 1,\ldots,8$ runs over the neutralino indices and $m = 1,\ldots,5$ runs over the chargino indices.

$$\begin{aligned}\mathscr{L}_{\text{MSSM},\tilde{\text{a}}} &= (\mathbf{Y}_\ell)^i{}_j\Big[\sin\beta_\pm\, N_{8i}^*\,U_{jn}\,\tilde{a}H^-\widetilde{\eta}_n^+ + (N_{8i}^*U_{m2}^* - N_{84}^*U_{mi}^*)\,\widetilde{\eta}_m^-\tilde{a}\,\tilde{\ell}_R^{*j} - N_{84}^*U_{jn}\,\widetilde{\eta}_n^+\tilde{a}\,\tilde{\ell}_{L_i}\Big] \\ &\quad -(\mathbf{Y}_D)^i{}_j\Big[\tilde{d}_R^{*j}\hat{d}_i + \tilde{d}_{L_i}\hat{\tilde{d}}^j\Big]N_{84}^*\tilde{a} + (\mathbf{Y}_U)^i{}_j\Big[\tilde{u}_R^{*j}\hat{u}_i + \tilde{u}_{L_i}\hat{\tilde{u}}_j\Big]N_{83}^*\,\tilde{a} + \text{h.c.}\end{aligned} \tag{B.28}$$

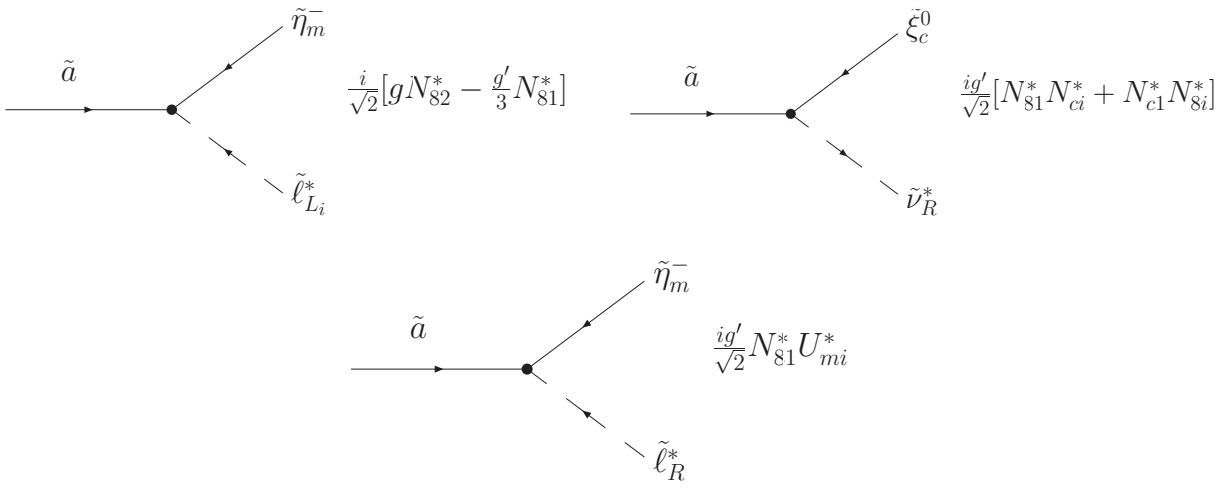

Figure B.4: Feynman rules for the axino interaction with charginos, neutralinos and sleptons, for details see text.

The Feynman rules corresponding to the latter equation are depicted in Fig. B.5. Note that the first term in Eq. (B.28) has already been considered in Eq. (B.16) and Fig. B.2. The terms containing quark fields have been rotated into the mass eigenbasis. The squarks are the superpartners of these fields.

However, from the $\not{R}_p$ superpotential we obtain further contributions to the lepton and down quark terms, *cf.* Eq. (B.35). For clarity we introduce the following vertex factors

$$Y^{\tilde{a}\tilde{\eta}_m^-\tilde{\ell}_R^{*j}} = (\mathbf{Y}_\ell)^i{}_j(N_{8i}^* U_{m2}^* - N_{84}^* U_{mi}^*) - \frac{1}{2}(\mathbf{\Lambda}_{E^j})_{ik}(N_{8i}^* U_{mk}^* - N_{8k}^* U_{mi}^*) \quad \text{(B.29)}$$

$$Y^{\tilde{a}\tilde{\eta}_n^+\tilde{\ell}_{L_i}} = -(\mathbf{Y}_\ell)^i{}_j N_{84}^+ - \frac{1}{2}(\mathbf{\Lambda}_{E^k})_{ij}(N_{8i}^* U_{kn} - N_{8j}^* U_{kn}) \quad \text{(B.30)}$$

$$Y^{\tilde{a}\tilde{d}_{R_j}^* d_i} = -Y_{Dj}\,\delta_j^i N_{84}^* - (\mathbf{\Lambda}_{D^j})_{ki} N_{8k}^* \quad \text{(B.31)}$$

$$Y^{\tilde{a}\tilde{d}_{L_i}\bar{d}_j} = -Y_{Dj}\,\delta_j^i N_{84}^* - (\mathbf{\Lambda}_{D^j})_{ki} N_{8k}^* \quad \text{(B.32)}$$

B.7 RPV Interactions

The relevant R–parity violating interactions involving a neutrino, *cf.* Ref. [78] are

$$\begin{aligned}\mathscr{L}_{\rm RPV} = & -\frac{1}{2}(\mathbf{\Lambda}_{E^k})_{ij}\left[\tilde{\ell}_{R_k}^*\nu_i\ell_j + \tilde{\ell}_{L_j}\bar{\ell}_k\nu_i - \tilde{\ell}_{R_k}^*\ell_i\nu_j - \tilde{\ell}_{L_i}\nu_j\bar{\ell}_k\right] \\ & -(\mathbf{\Lambda}_{D^k})^i{}_j\left[\tilde{d}_{R_k}^*\nu_i d_j + \tilde{d}_{L_j}\nu_i\bar{d}_k\right], \end{aligned} \quad \text{(B.33)}$$

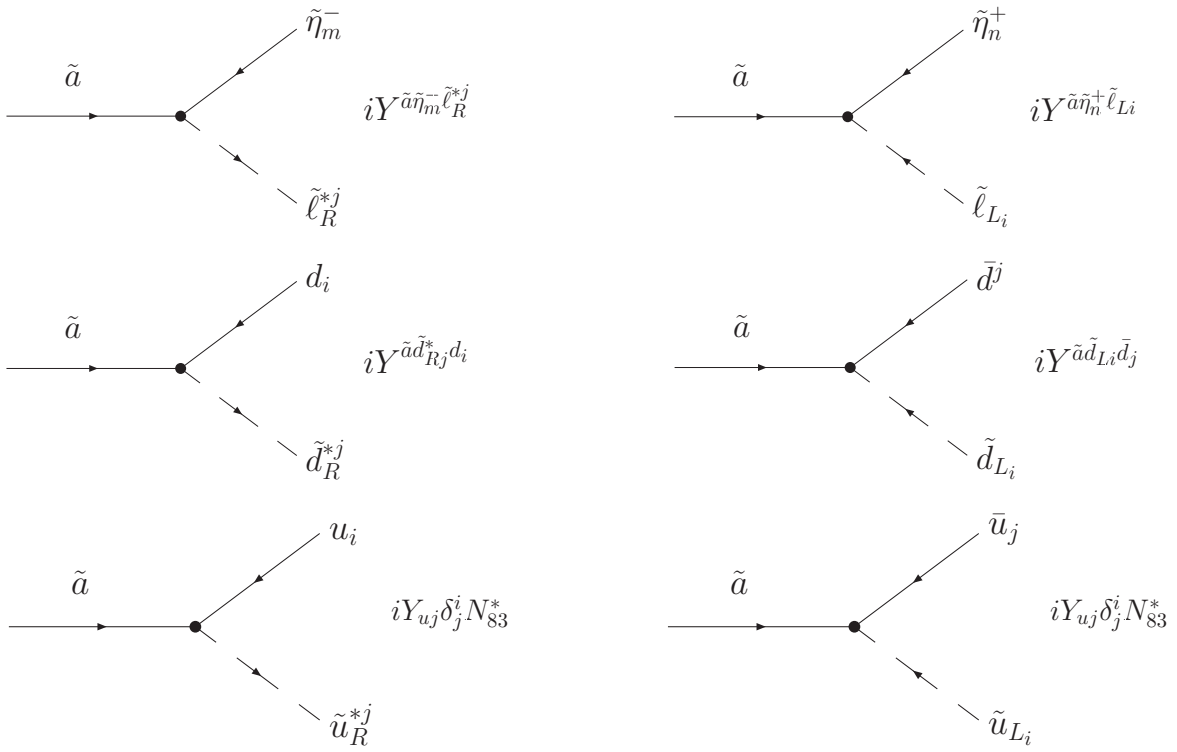

Figure B.5: Feynman diagrams given by the Eq. (B.28).

with a sum over $i, j, k = 1, 2, 3$. Inserting the neutralino and chargino mass eigenstates, we have

$$\begin{aligned}\mathscr{L}_{\rm RPV} &= -\frac{1}{2}(\mathbf{\Lambda}_{E^k})^i{}_j\Big[\tilde{\ell}^*_{R_k}(N^*_{ci}\widetilde{\xi}^0_c)(U^*_{mj}\,\widetilde{\eta}^-_m) + \tilde{\ell}_{L_j}(U^*_{mk}\,\tilde{\eta}^-_m)^\dagger(N^*_{ci}\widetilde{\xi}^0_c) - \tilde{\ell}^*_{R_k}(U^*_{mi}\,\widetilde{\eta}^-_m)(N^*_{cj}\widetilde{\xi}^0_c)\\ &\quad -\tilde{\ell}_{L_i}(N^*_{cj}\widetilde{\xi}^0_c)(U^*_{mk}\,\tilde{\eta}^-_m)^\dagger\Big] - (\mathbf{\Lambda}_{D^k})^i{}_j\Big[\tilde{d}^*_{R_k}(N^*_{ci}\widetilde{\xi}^0_c)d_j + \tilde{d}_{L_j}(N^*_{ci}\widetilde{\xi}^0_c)\bar{d}_k\Big]\,. \qquad \text{(B.34)}\end{aligned}$$

Focusing on the axino we obtain

$$\begin{aligned}\mathscr{L}_{\rm RPV,\tilde{a}} &= -\frac{1}{2}(\mathbf{\Lambda}_{E^k})^i{}_j\Big[N^*_{8i}U^*_{mj}\,\tilde{\ell}^*_{R_k}\,\tilde{a}\,\widetilde{\eta}^-_m + N^*_{8i}U_{km}\,\tilde{\ell}_{L_j}\tilde{\eta}^+_m\,\tilde{a} - N^*_{8j}U^*_{mi}\,\tilde{\ell}^*_{R_k}\,\widetilde{\eta}^-_m\tilde{a} - N^*_{8j}U_{km}\,\tilde{\ell}_{L_i}\tilde{a}\,\tilde{\eta}^+_m\Big]\\ &\quad -(\mathbf{\Lambda}_{D^k})^i{}_j\Big[N^*_{8i}\,\tilde{d}^*_{R_k}\,\tilde{a}\,d_j + N^*_{8i}\,\tilde{d}_{L_j}\tilde{a}\,\bar{d}_k\Big]\\ &= -\frac{1}{2}(\mathbf{\Lambda}_{E^k})^i{}_j\Big[(N^*_{8i}U^*_{mj} - N^*_{8j}U^*_{mi})\,\tilde{\ell}^*_{R_k}\,\widetilde{\eta}^-_m\tilde{a} + (N^*_{8i}U_{km} - N^*_{8j}U_{km})\,\tilde{\ell}_{L_i}\tilde{a}\,\tilde{\eta}^+_m\Big]\\ &\quad -(\mathbf{\Lambda}_{D^k})^i{}_j\Big[N^*_{8i}\,\tilde{d}^*_{R_k}\,\tilde{a}\,d_j + N^*_{8i}\,\tilde{d}_{L_j}\tilde{a}\,\bar{d}_k\Big]\,. \qquad \text{(B.35)}\end{aligned}$$

The related Feynman rules are shown in Fig. B.5. Note that all terms derived from the $\not{R}_p$ superpotential are included in Eqs. (B.29)-(B.32).

C Explicit RGE expressions

C.1 One-loop anomalous dimensions

In this section we give the full RGEs of the c^α parameters and of the soft breaking term $h_{\tilde{a},\alpha}$. We employ the notation of Martin and Vaughn, *cf.* Ref. [37]. Furthermore we have calculated the RGEs with the method given in Ref. [151], as a cross check. We have obtained the same results.

But at first we state the full set of one-loop anomalous dimensions which are needed for the derivation of the RGEs.

$$\gamma^{L_i}_{L_j} = \left(\mathbf{Y}_E\mathbf{Y}_E^\dagger\right)_{ij} + (\mathbf{\Lambda}_{E^q}\mathbf{\Lambda}^\dagger_{E^q})_{ij} + 3(\mathbf{\Lambda}_{D^q}\mathbf{\Lambda}^\dagger_{D^q})_{ij} - \delta^i_j\Big[\frac{3}{10}g_1^2 + \frac{3}{2}g_2^2\Big] + (c_2^j)^* c_2^i, \tag{C.1}$$

$$\gamma^{E_i}_{E_j} = 2\left(\mathbf{Y}_E^\dagger\mathbf{Y}_E\right)_{ji} + \mathrm{Tr}(\mathbf{\Lambda}_{E^i}\mathbf{\Lambda}^\dagger_{E^j}) - \delta^i_j\Big[\frac{6}{5}g_1^2\Big] \tag{C.2}$$

$$\gamma^{Q_i}_{Q_j} = \left(\mathbf{Y}_D\mathbf{Y}_D^\dagger\right)_{ij} + \left(\mathbf{Y}_U\mathbf{Y}_U^\dagger\right)_{ij} + (\mathbf{\Lambda}^\dagger_{D^q}\mathbf{\Lambda}_{D^q})_{ji} - \delta^i_j\big[\frac{1}{30}g_1^2 + \frac{3}{2}g_2^2 + \frac{8}{3}g_3^2\Big], \tag{C.3}$$

$$\gamma^{D_i}_{D_j} = 2\left(\mathbf{Y}_D^\dagger\mathbf{Y}_D\right)_{ji} + 2\mathrm{Tr}(\mathbf{\Lambda}^\dagger_{D^j}\mathbf{\Lambda}_{D^i}) + 2(\mathbf{\Lambda}_{U^q}\mathbf{\Lambda}^\dagger_{U^q})_{ij} - \delta^i_j\Big[\frac{2}{15}g_1^2 + \frac{8}{3}g_3^2\Big], \tag{C.4}$$

$$\gamma^{U_i}_{U_j} = 2\left(\mathbf{Y}_U^\dagger\mathbf{Y}_U\right)_{ji} + \mathrm{Tr}(\mathbf{\Lambda}_{U^i}\mathbf{\Lambda}^\dagger_{U^j}) - \delta^i_j\Big[\frac{8}{15}g_1^2 + \frac{8}{3}g_3^2\Big], \tag{C.5}$$

$$\gamma^{H_1}_{H_1} = -\mathrm{Tr}\left(3\mathbf{Y}_D\mathbf{Y}_D^\dagger + \mathbf{Y}_E\mathbf{Y}_E^\dagger\right) - \left(\frac{3}{10}g_1^2 + \frac{3}{2}g_2^2\right) + (c_1)^* c_1, \tag{C.6}$$

$$\gamma^{H_2}_{H_2} = -3\mathrm{Tr}\left(\mathbf{Y}_U\mathbf{Y}_U^\dagger\right) - \left(\frac{3}{10}g_1^2 + \frac{3}{2}g_2^2\right) + (c_1)^* c_1 + (c_2^i)^* c_2^i, \tag{C.7}$$

$$\gamma^{H_1}_{L_i} = (\gamma_1)^{L_i}_{H_1}{}^* = -3(\mathbf{\Lambda}^*_{D^q}\mathbf{Y}_{D^q})_{iq} - (\mathbf{\Lambda}^*_{E^q}\mathbf{Y}_E)_{iq} + (c_2^i)^* c_1,$$

$$\gamma^{\Phi}_{\Phi} = 2(c_1)^* c_1 + 2(c_2^i)^* c_2^i. \tag{C.8}$$

C.2 RGEs for the axino trilinear terms and the axino soft trilinear terms

Thus for the RGEs we have:

$$\begin{aligned}
16\pi^2\frac{\mathrm{d}}{\mathrm{d}t}c_1 &= c_1\big[\gamma_{H_2}^{H_2}+\gamma_{\Phi}^{\Phi}+\gamma_{H_1}^{H_1}\big]+c_2^i\gamma_{L_i}^{H_1}\\
&= c_1\Big[3\mathrm{Tr}\left(\mathbf{Y}_U\mathbf{Y}_U^\dagger\right)+\mathrm{Tr}\left(3\mathbf{Y}_D\mathbf{Y}_D^\dagger+\mathbf{Y}_E\mathbf{Y}_E^\dagger\right)-\left(\frac{3}{5}g_1^2+3g_2^2\right)+4c_1^*c_1+3(c_2^m)^*c_2^m\Big]\\
&\quad +c_2^i\Big(-3(\mathbf{\Lambda}_{D^q}^*\mathbf{Y}_{D^q})_{iq}-(\mathbf{\Lambda}_{E^q}^*\mathbf{Y}_E)_{iq}+(c_2^i)^*c_1\Big)\,. \qquad \text{(C.9)}
\end{aligned}$$

$$\begin{aligned}
16\pi^2\frac{\mathrm{d}}{\mathrm{d}t}c_2^i &= c_2^i\big(\gamma_{\Phi}^{\Phi}+\gamma_{H_2}^{H_2}\big)+c_1\gamma_{H_1}^{L_i}+c_2^p\gamma_{L_j}^{L_i}\\
&= c_2^i\Big[3\mathrm{Tr}\left(\mathbf{Y}_U\mathbf{Y}_U^\dagger\right)-\left(\frac{3}{10}g_1^2+\frac{3}{2}g_2^2\right)+3c_1^*c_1+3(c_2^m)^*c_2^m\Big]\\
&\quad +c_1\Big[-3(\mathbf{\Lambda}_{D^q}^*\mathbf{Y}_{D^q})_{iq}-(\mathbf{\Lambda}_{E^q}^*\mathbf{Y}_E)_{iq}+(c_2^i)^*c_1\Big]\\
&\quad +c_2^p\left[\left(\mathbf{Y}_E\mathbf{Y}_E^\dagger\right)_{ij}+(\mathbf{\Lambda}_{E^q}\mathbf{\Lambda}_{E^q}^\dagger)_{ij}+3(\mathbf{\Lambda}_{D^q}\mathbf{\Lambda}_{D^q}^\dagger)_{ij}-\delta_j^i\Big[\frac{3}{10}g_1^2+\frac{3}{2}g_2^2\Big]+(c_2^j)^*c_2^i\right]. \qquad \text{(C.10)}
\end{aligned}$$

$$\begin{aligned}
16\pi^2\frac{\mathrm{d}\tilde{B}_{\tilde{a}}}{\mathrm{d}t} &= \tilde{B}_{\tilde{a}}\Big[3\mathrm{Tr}(\mathbf{Y}_D\mathbf{Y}_D^\dagger)-3\mathrm{Tr}(\mathbf{Y}_U\mathbf{Y}_U^\dagger)+\mathrm{Tr}(\mathbf{Y}_E\mathbf{Y}_E^\dagger)+12\kappa_1^*\kappa_1+5(\kappa_2^m)^*\kappa_2^m\Big]\\
&\quad +\tilde{D}_{\tilde{a},\,m}\Big[7c_1(c_2^m)^*-3(\mathbf{\Lambda}_{D^n}^*\mathbf{Y}_D)_{ln}-(\mathbf{\Lambda}_{E^n}^*\mathbf{Y}_E)_{ln}\Big]+c_1\Big[6\mathrm{Tr}(\mathbf{h}_U\mathbf{Y}_U^\dagger)+2\mathrm{Tr}(\mathbf{Y}_E^\dagger\mathbf{h}_E)\\
&\quad +6\mathrm{Tr}(\mathbf{Y}_D^\dagger\mathbf{h}_D)\Big]-2\big(\tilde{B}_{\tilde{a}}-2Mc_1\big)\sum_a g_a^2\Big[C_a(H_2)+C_a(H_1)\Big]\\
&\quad +2c_2^l\Big[-(\mathbf{\Lambda}_{E^n}^*\mathbf{h}_E)_{ln}-3(\mathbf{\Lambda}_{D^n}^*\mathbf{h}_D)_{ln}\Big]\,. \qquad \text{(C.11)}
\end{aligned}$$

$$\begin{aligned}
16\pi^2\frac{\mathrm{d}\tilde{D}_{\tilde{a},j}}{\mathrm{d}t} &= \tilde{D}_{\tilde{a},\,j}\Big[5c_2^n(c_2^n)^*+3c_1^*c_1+3\mathrm{Tr}(\mathbf{Y}_U^\dagger\mathbf{Y}_U)\Big]+\tilde{B}_{\tilde{a}}\Big[-(\mathbf{\Lambda}_{E^n}\mathbf{Y}_E^*)_{jn}-3(\mathbf{\Lambda}_{D^n}\mathbf{Y}_D^*)_{jn}\\
&+ 7c_1^*c_2^j\Big]+\tilde{D}_{\tilde{a},l}\Big[(\mathbf{\Lambda}_{E^n}\mathbf{\Lambda}_{E^n}^\dagger)_{jl}-3(\mathbf{\Lambda}_{D^n}\mathbf{\Lambda}_{D^n}^\dagger)_{jl}+(\mathbf{Y}_E\mathbf{Y}_E^\dagger)_{jl}+7(c_2^l)^*c_2^j\Big]\\
&+ 2c_1\Big[-(\mathbf{Y}_E^*\mathbf{h}_{E^n})_{jn}-3(\mathbf{h}_{D^n}\mathbf{Y}_D^*)_{jn}+c_1^*c_2^j\Big]\\
&+ 2c_2^l\Big[(\mathbf{h}_{E^n}\mathbf{\Lambda}_{E^n}^\dagger)_{jl}+3(\mathbf{h}_{D^n}\mathbf{\Lambda}_{D^n}^\dagger)_{jl}+(\mathbf{h}_E\mathbf{Y}_E^\dagger)_{jl}\Big]\\
&+ 6c_2^j\mathrm{Tr}(\mathbf{Y}_U^\dagger\mathbf{h}_U)-2(\tilde{D}_{\tilde{a},\,j}-2Mc_2^j)\sum_a g_a^2C_a(H_2)\,. \qquad \text{(C.12)}
\end{aligned}$$

D The complete Branching ratios

D.1 The BR with the $\not{R}_p\, LL\bar{E}$ operator

In section 6.1 we only presented the BRs of three couplings due to the $LL\bar{E}$ operator. From the in general nine couplings only six are relevant, for details see section 6.1. In this appendix we discuss the three remaining couplings. The structure of the presented diagrams is as in section 6.1. As before, the diagrams are shown in the order c_2^1, c_2^2 and c_2^3, for the benchmark point SPS1a.

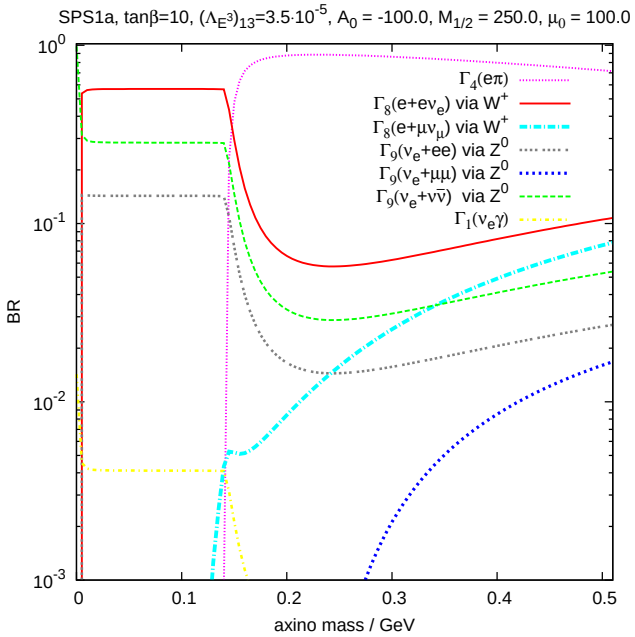

Figure D.1: The BR of the axino decays at the benchmark point SPS1a with the $\not{R}_p$ coupling $(\mathbf{\Lambda}_{E^3})_{13} = 3.5 \times 10^{-5}$. Here c_2^1 is the relevant Yukawa coupling for which the axino couples preferentially to the electron family. Due to kinematical thresholds of the decay channels several mass regimes are formed with different behaviour. For details see the text.

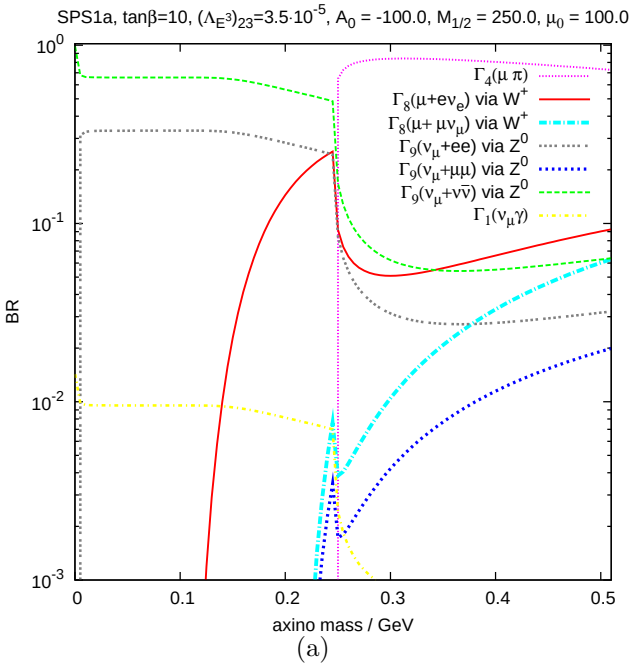

(a)

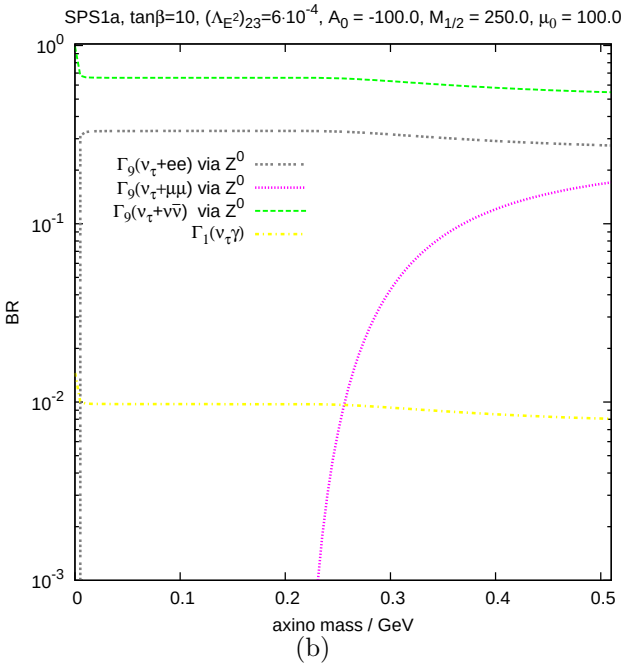

(b)

Figure D.2: The BRs of the axino decays at the benchmark point SPS1a with the $\not{R}_p$ coupling $(\mathbf{\Lambda}_{E^3})_{23} = 3.5\times10^{-5}$ (upper figure) and $(\mathbf{\Lambda}_{E^2})_{23} = 6\times10^{-4}$ (lower figure). For these $\not{R}_p$ operators c_2^2 and c_2^3 are the relevant Yukawa couplings for which the axino couples preferentially to the muon and tau family, respectively. Due to kinematical thresholds of the decay channels several mass regimes are formed with different behaviour. For details see the text.

D.2 The BR with the $\not{R}_p\, LQ\bar{D}$ operator

In section 6.2 we presented the BRs for non-zero $(\mathbf{\Lambda}_{D^i})_{jk}$ operators. We pointed out that in general there exists then three scenarios. Thus we can in turn assume that the quarks do not mix, and that the mixing is mainly in the up- or down-sector. In total we would have 27 couplings per case but where this number for the no-mixing assumption is reduced due to restrictions coming from the RGEs, see section 6.2 for details.

We already explained that according to the preferred axino Yukawa coupling c_2^i we obtain a specific structure for the BRs. In section 6.2 we showed a set of examples where we claimed that one can directly deduce from the c_2^i the behaviour of the BR.

In the following two sections we present further examples of BR which prove our statement. The first part is dedicated to the case of no-mixing among the quarks. The second part shows further examples of the BR for the up-mixing case. Here we focus on the interesting scenario where the bounds on the $\not{R}_p$ coupling are due to the absence of tachyons but we also complete the set of figures of section 6.2. For further explanations see text in section 6.2.

D.2.1 No mixing

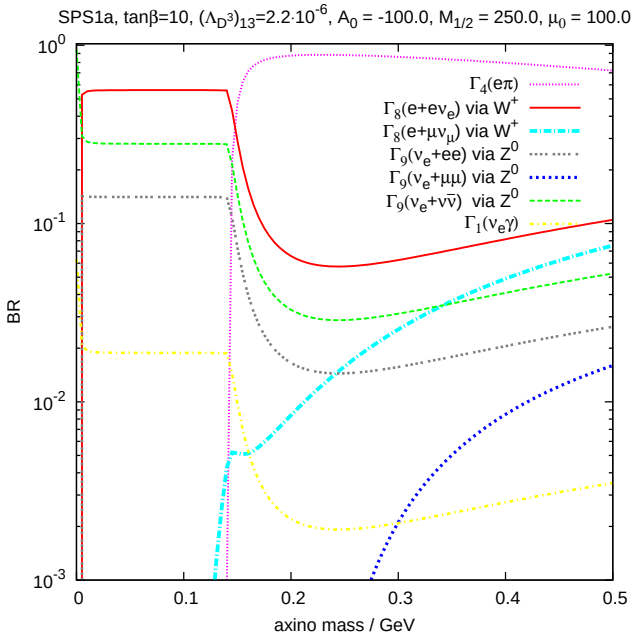

Figure D.3: The axino BRs at the benchmark point SPS1a with the $\not{R}_p$ coupling $(\mathbf{\Lambda}_{D^3})_{13} = 2.2 \times 10^{-6}$, (no-mixing). For the chosen $\not{R}_p$ operator, c_2^1 is the relevant Yukawa coupling. The axino couples preferentially to the electron family. Due to kinematical thresholds of the decay channels several mass regimes are formed with different behaviour.

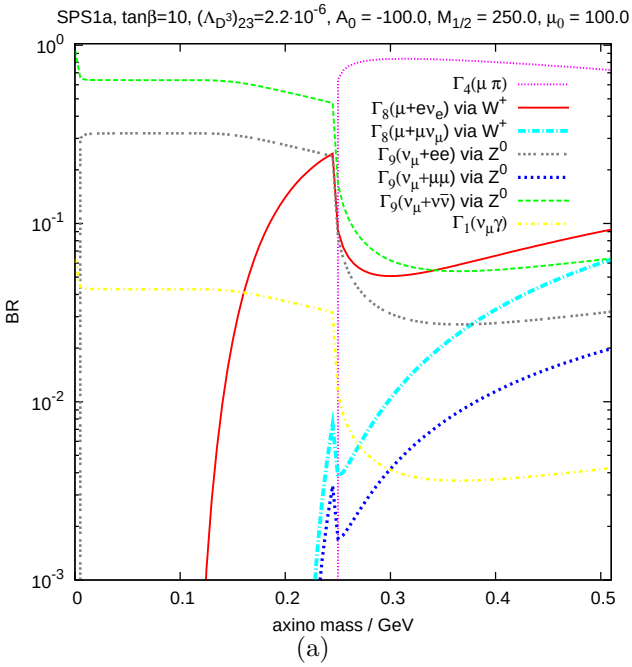

(a)

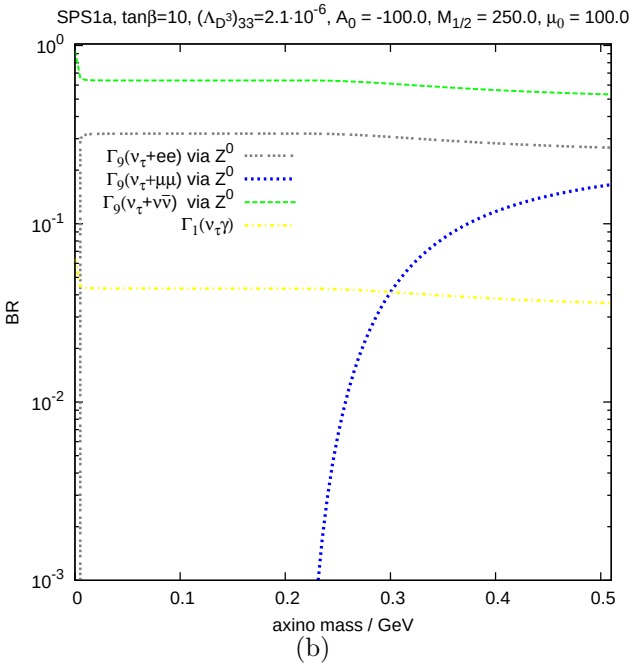

(b)

Figure D.4: The axino BRs at the benchmark point SPS1a with the $\not{R}_p$ couplings $(\mathbf{\Lambda}_{D^3})_{23} = 2.2 \times 10^{-6}$ (upper figure) and $(\mathbf{\Lambda}_{D^3})_{33} = 2.1 \times 10^{-6}$ (lower figure), (no-mixing). For the chosen $\not{R}_p$ operators c_2^2 and c_2^3 are the relevant Yukawa couplings. The axino couples preferentially to the muon and tau family, respectively. Due to kinematical thresholds of the decay channels several mass regimes are formed with different behaviour.

D.2.2 Mixing scenarios

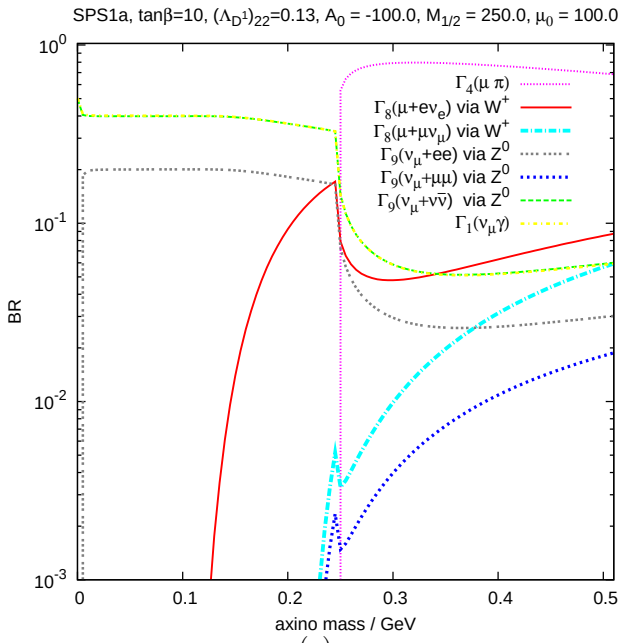

(a)

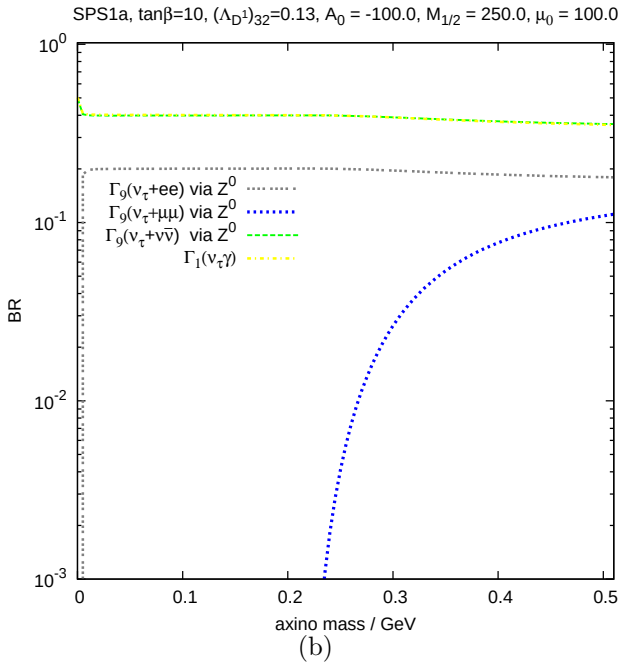

(b)

Figure D.5: The axino BRs at the benchmark point SPS1a with the $\not{R}_p$ couplings $(\mathbf{\Lambda}_{D^1})_{22} = 0.13$ (upper figure) and $(\mathbf{\Lambda}_{D^1})_{32} = 0.13$ (lower figure), (up-mixing). For the chosen $\not{R}_p$ operators c_2^2 and c_2^3 are the relevant Yukawa couplings. The axino couples preferentially to the muon and tau family, respectively. Due to kinematical thresholds of the decay channels several mass regimes are formed with different behaviour.

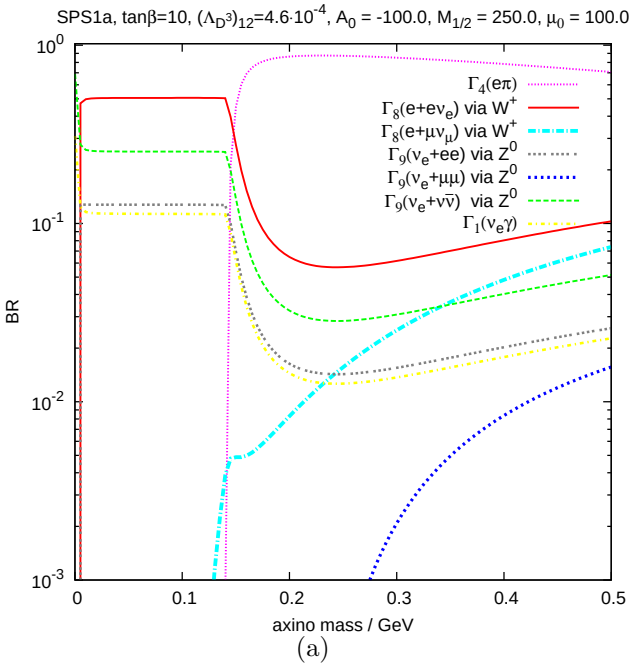

(a)

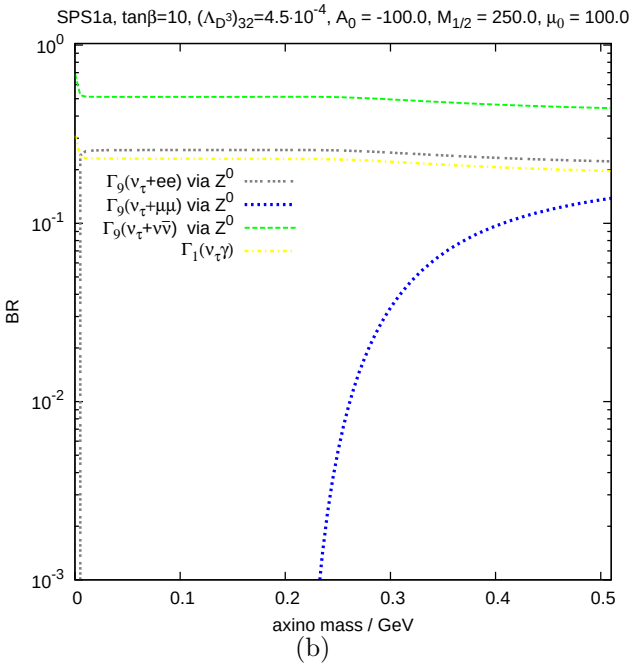

(b)

Figure D.6: The axino BRs at the benchmark point SPS1a with the $\not{R}_p$ couplings $(\mathbf{\Lambda}_{D^3})_{12} = 4.6 \times 10^{-4}$ (upper figure) and $(\mathbf{\Lambda}_{D^3})_{32} = 4.5 \times 10^{-4}$ (lower figure), (up-mixing). For the chosen $\not{R}_p$ operator c_2^1 and c_2^3 are the relevant Yukawa couplings. The axino couples preferentially to the electron and tau family, respectively. Due to kinematical thresholds of the decay channels several mass regimes are formed with different behaviour.

E Further axino energy density analysis

In section 7.2-7.3 we discussed the axino as dark matter candidate with non-zero $LL\bar{E}$ and $LQ\bar{D}$ operators. It was shown that similarly to the BR analysis the couplings could be categorized. Depending on the chosen $\not{R}_p$ operator a preferred axino Yukawa coupling c_2^i is obtained which determines the behaviour of the BR as well as the axino energy density function.

However, we made clear that the axino can provide DM in a wide mass- and coupling range. Of course, cases with c_2^1 and c_2^2 as dominant axino coupling have a kink in their energy density distribution as function of $m_{\tilde{a}}, t_{\tilde{a}}$ and $T_{\rm R}$. This is explained by the according BR presented in section 6.1-6.2 and *cf.* section 7.2-7.3. See also these sections for the constant c_2^3 case.

In this Appendix we show further examples for $\Omega_{\tilde{a}}$ in models with non-zero $LL\bar{E}$ as well as $LQ\bar{D}$ operator. These examples confirm the conclusion of the three categories of behaviour for $\Omega_{\tilde{a}}$ depending on the correlated c_2^i.

E.1 The $\Omega_{\tilde{a}}$ with the $\not{R}_p\, LL\bar{E}$ operator

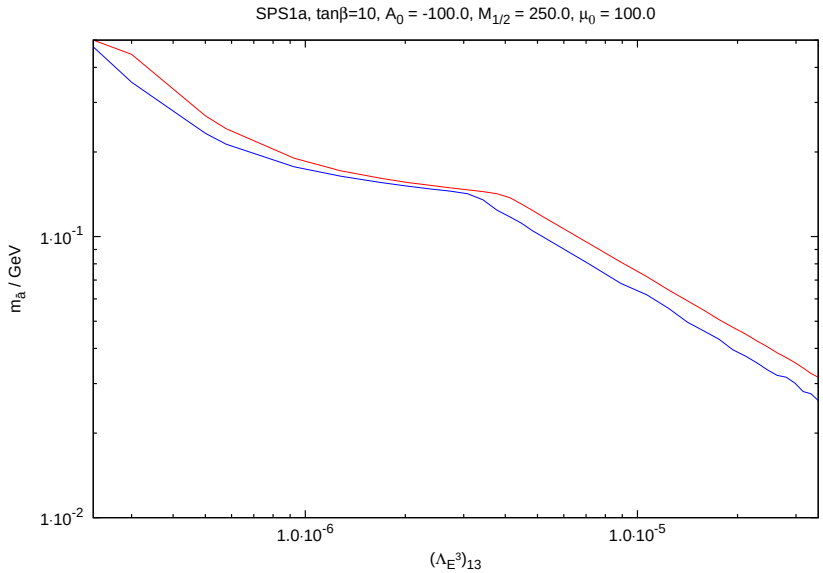

Figure E.1: A contour plot of the axino mass as a function of $\not{R}_p$ coupling $(\mathbf{\Lambda}_{E^3})_{13}$ and $T_{\rm R}$ - implcit on the z-axis. The analysis is performed at the benchmark point SPS1a with the parameter space values as shown on the top of the figure. The red (blue) line indicates the upper (lower) axino mass for a given $(\mathbf{\Lambda}_{E^3})_{13}$ value where the condition $\Omega_{\tilde{a}} = \Omega_{\rm DM}$ is satisfied. The behaviour of the lines is due to different boundary conditions of the reheating temperature as well as the BRs, see the text for details. This results are obtained for a PQ breaking scale of $f_{\rm PQ} = 10^{11}$ GeV. Note that the small kinks at the blue line are due to numerical artefacts and have no significance.

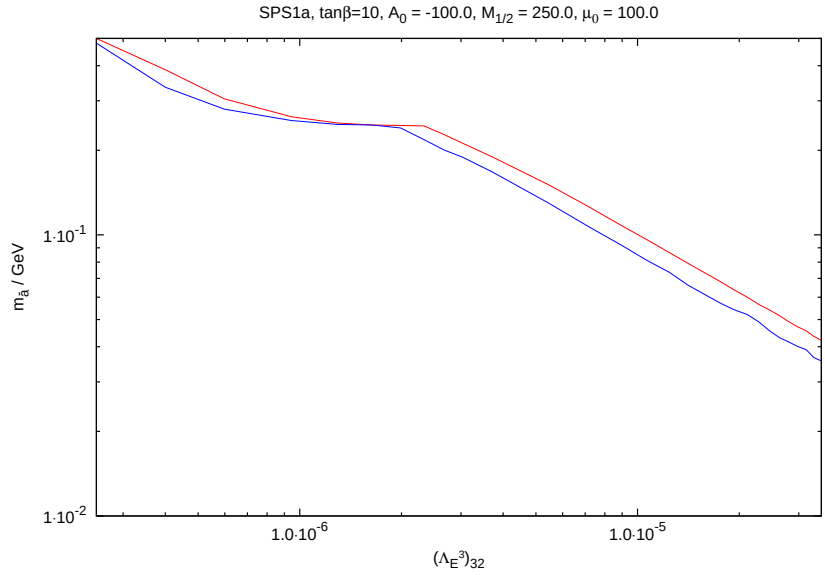

(a)

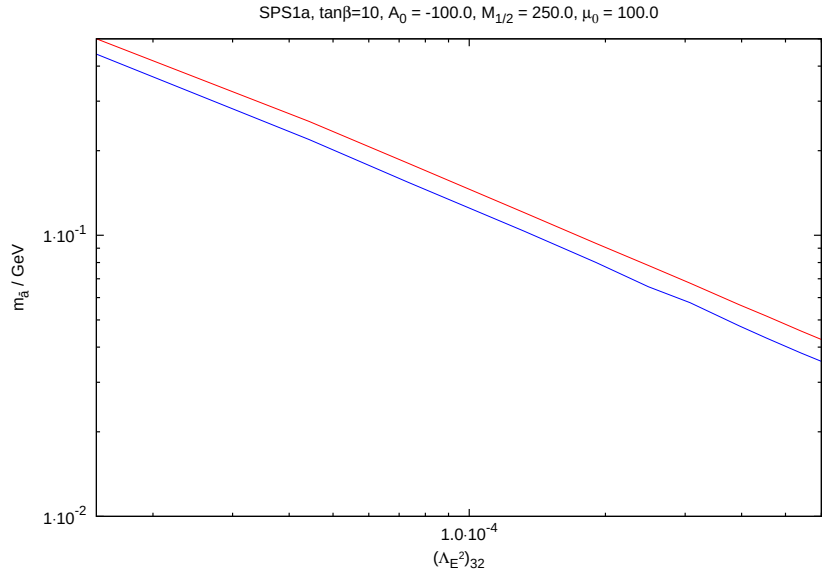

(b)

Figure E.2: A contour plot of the axino mass as a function of $\not{R}_p$ coupling $(\mathbf{\Lambda}_{E^3})_{23}$ (upper figure) $[(\mathbf{\Lambda}_{E^2})_{23}$ lower figure] and T_{R} - implcit on the z-axis. The analysis is performed at the benchmark point SPS1a with the parameter space values as shown on the top of the figure. The red (blue) line indicates the upper (lower) axino mass for a given $(\mathbf{\Lambda}_{E^3})_{23}$ $[(\mathbf{\Lambda}_{E^2})_{23}]$ value where the condition $\Omega_{\tilde{a}} = \Omega_{\mathrm{DM}}$ is satisfied. The behaviour of the lines is due to different boundary conditions of the reheating temperature as well as the BRs, see the text for details. This results are obtained for a PQ breaking scale of $f_{\mathrm{PQ}} = 10^{11}$ GeV. Note that the small kinks at the blue line are due to numerical artefacts and have no significance.

E.2 The $\Omega_{\tilde{a}}$ with the $\not{R}_p\, LQ\bar{D}$ operator

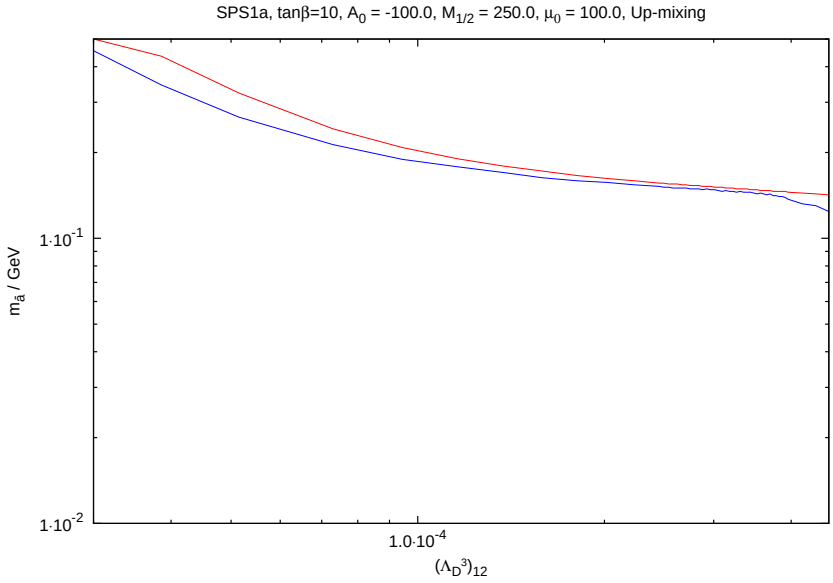

(a)

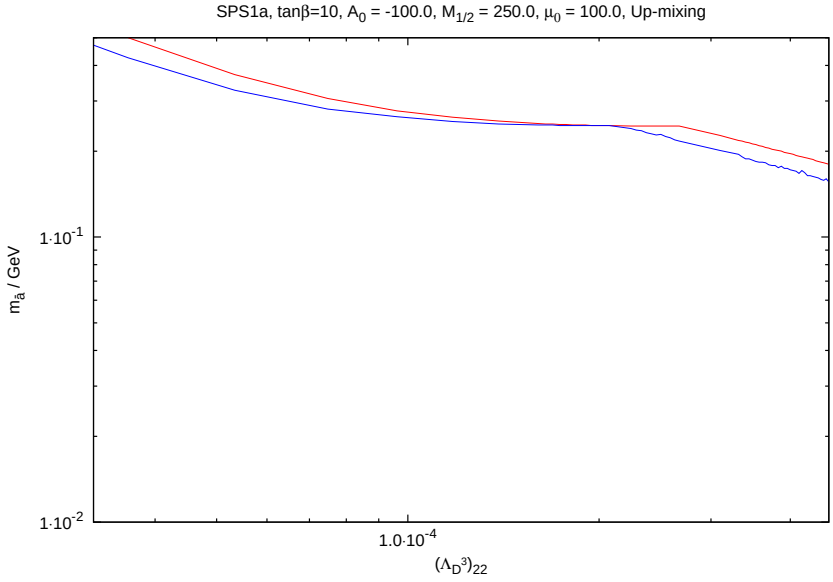

(b)

Figure E.3: A contour plot of the axino mass as a function of $\not{R}_p$ coupling $(\mathbf{\Lambda}_{D^3})_{12}$ (upper figure) $[(\mathbf{\Lambda}_{D^3})_{22}$ lower figure] and $T_{\rm R}$ - implcit on the z-axis. The analysis is performed at the benchmark point SPS1a with the parameter space values as shown on the top of the figure. The red (blue) line indicates the upper (lower) axino mass for a given $(\mathbf{\Lambda}_{D^3})_{12}$ $[(\mathbf{\Lambda}_{D^3})_{22}]$ value where the condition $\Omega_{\tilde{a}} = \Omega_{\rm DM}$ is satisfied. The behaviour of the lines is due to different boundary conditions of the reheating temperature as well as the BRs, see the text for details. This results are obtained for a PQ breaking scale of $f_{\rm PQ} = 10^{11}$ GeV. Note that the small kinks at the blue line are due to numerical artefacts and have no significance.

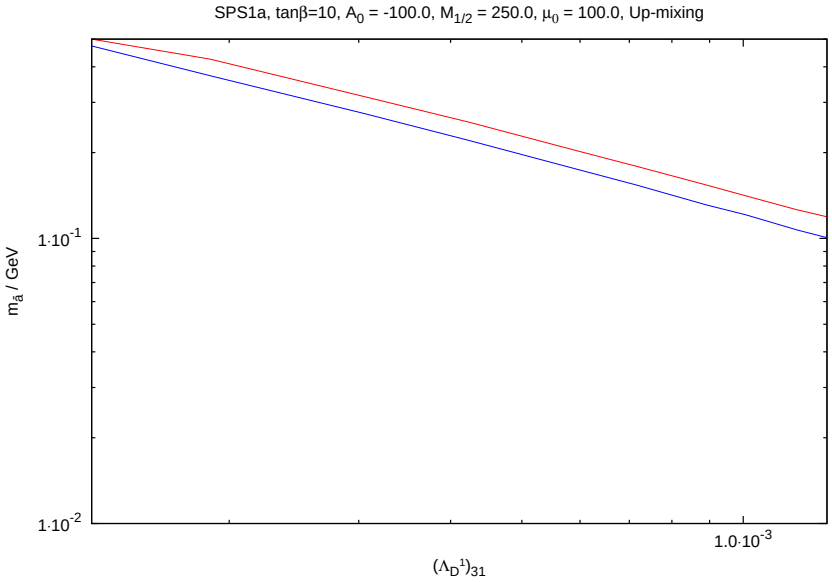

(a)

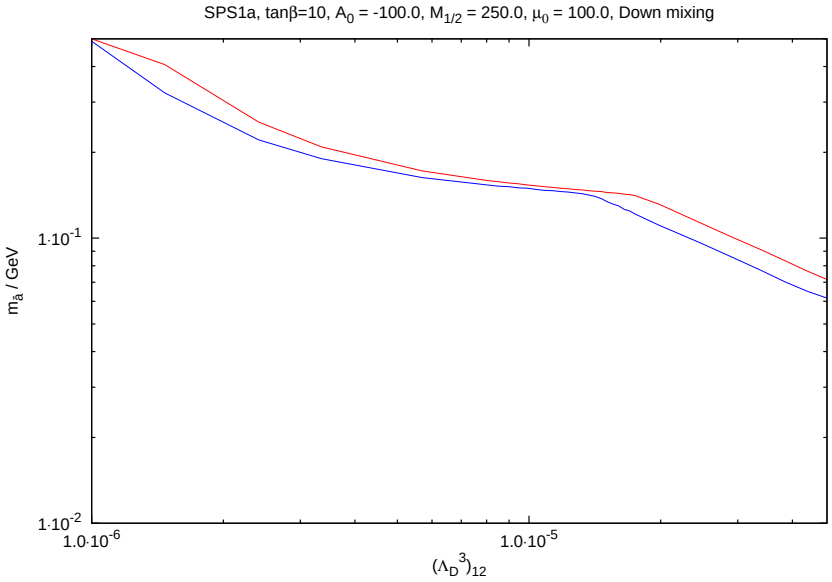

(b)

Figure E.4: A contour plot of the axino mass as a function of $\not{R}_p$ coupling $(\mathbf{\Lambda}_{D^1})_{31}$ (upper figure) $[(\mathbf{\Lambda}_{D^3})_{12}$ lower figure] and T_{R} - implcit on the z-axis. The analysis is performed at the benchmark point SPS1a with the parameter space values as shown on the top of the figure. The red (blue) line indicates the upper (lower) axino mass for a given $(\mathbf{\Lambda}_{D^1})_{31}$ $[(\mathbf{\Lambda}_{D^3})_{12}]$ value where the condition $\Omega_{\tilde{a}} = \Omega_{\mathrm{DM}}$ is satisfied. The behaviour of the lines is due to different boundary conditions of the reheating temperature as well as the BRs, see the text for details. This results are obtained for a PQ breaking scale of $f_{\mathrm{PQ}} = 10^{11}$ GeV. Note that the small kinks at the blue line are due to numerical artefacts and have no significance.

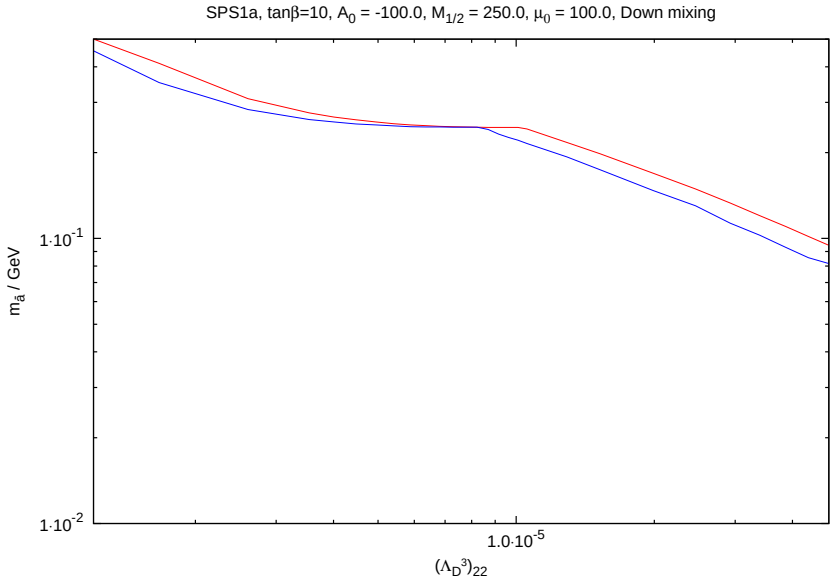

(a)

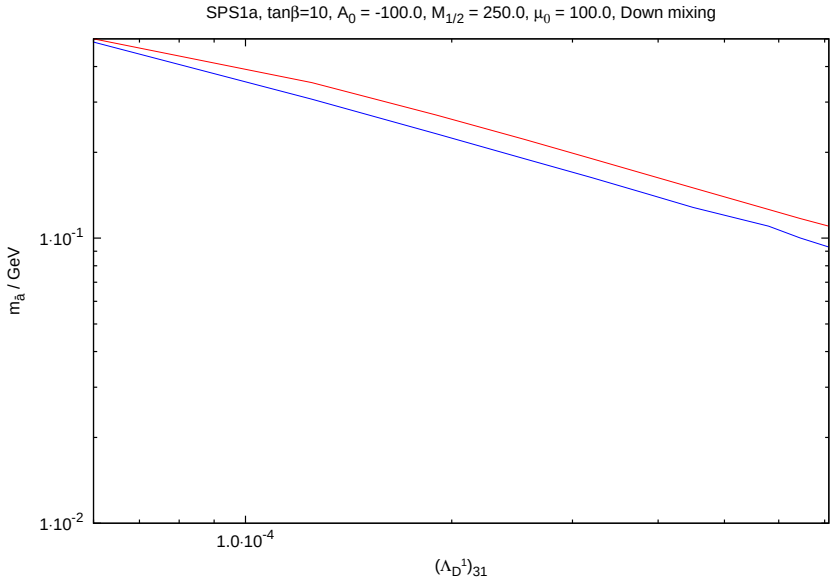

(b)

Figure E.5: A contour plot of the axino mass as a function of $\not{R}_p$ coupling $(\mathbf{\Lambda}_{D^3})_{22}$ (upper figure) $[(\mathbf{\Lambda}_{D^1})_{31}$ lower figure] and T_{R} - implcit on the z-axis. The analysis is performed at the benchmark point SPS1a with the parameter space values as shown on the top of the figure. The red (blue) line indicates the upper (lower) axino mass for a given $(\mathbf{\Lambda}_{D^3})_{22}$ $[(\mathbf{\Lambda}_{D^1})_{31}]$ value where the condition $\Omega_{\tilde{a}} = \Omega_{\mathrm{DM}}$ is satisfied. The behaviour of the lines is due to different boundary conditions of the reheating temperature as well as the BRs, see the text for details. This results are obtained for a PQ breaking scale of $f_{\mathrm{PQ}} = 10^{11}$ GeV. Note that the small kinks at the blue line are due to numerical artefacts and have no significance.

Bibliography

[1] S. L. Glashow, J. Iliopoulos and L. Maiani, Phys. Rev. D **2** (1970) 1285.

[2] S. Weinberg, Phys. Rev. Lett. **19** (1967) 1264.

[3] M. Drees, arXiv:hep-ph/9611409.

[4] S. P. Martin, arXiv:hep-ph/9709356.

[5] I. J. R. Aitchison, arXiv:hep-ph/0505105.

[6] J. E. Kim, Phys. Rept. **150** (1987) 1.

[7] C. Jarlskog, *CP Violation: Advanced Series on Directions in High Energy Physics Vol. 3*, World Scientific Publishing (1989).

[8] R. D. Peccei and H. R. Quinn, Phys. Rev. Lett. **38** (1977) 1440.

[9] R. D. Peccei and H. R. Quinn, Phys. Rev. D **16** (1977) 1791.

[10] S. Weinberg, Phys. Rev. Lett. **40** (1978) 223.

[11] F. Wilczek, Phys. Rev. Lett. **40** (1978) 279.

[12] G. G. Raffelt, Lect. Notes Phys. **741** (2008) 51 [arXiv:hep-ph/0611350].

[13] H. P. Nilles, Phys. Rept. **110** (1984) 1.

[14] G. Bertone, D. Hooper and J. Silk, Phys. Rept. **405** (2005) 279 [arXiv:hep-ph/0404175].

[15] E. W. Kolb and M. S. Turner, Front. Phys. **69** (1990) 1.

[16] J. A. Peacock, *Cosmological Physics*, Cambridge University Press (1999).

[17] P. Schneider, *Extragalactic Astronomy and Cosmology*, Springer Verlag (2006).

[18] D. N. Spergel *et al.* [WMAP Collaboration], Astrophys. J. Suppl. **170** (2007) 377 [arXiv:astro-ph/0603449].

[19] E. Aprile *et al.* [XENON100 Collaboration], arXiv:1005.0380 [astro-ph.CO].

[20] R. Bernabei *et al.* [DAMA Collaboration], Eur. Phys. J. C **56** (2008) 333 [arXiv:0804.2741 [astro-ph]].

[21] The CDMS collaboration has reported in Ref. [90] that two events with a probability of 20 % were observed. This probability is small but not zero which leads to the interpretaion of the CDMS collaboration that this "cannot be interpreted as significant evidence for WIMP interactions, but we cannot reject either event as signal", see Ref. [90].

[22] C. E. Aalseth *et al.* [CoGeNT collaboration], arXiv:1002.4703 [astro-ph.CO].

[23] K. G. Begeman, A. H. Broeils and R. H. Sanders, Mon. Not. Roy. Astron. Soc. **249** (1991) 523.

[24] L. Covi, J. E. Kim and L. Roszkowski, Phys. Rev. Lett. **82** (1999) 4180 [arXiv:hep-ph/9905212].

[25] L. Covi, H. B. Kim, J. E. Kim and L. Roszkowski, JHEP **0105** (2001) 033 [arXiv:hep-ph/0101009].

[26] L. Covi and J. E. Kim, New J. Phys. **11** (2009) 105003 [arXiv:0902.0769 [astro-ph.CO]].

[27] L. Covi, L. Roszkowski and M. Small, JHEP **0207** (2002) 023 [arXiv:hep-ph/0206119].

[28] A. Brandenburg and F. D. Steffen, JCAP **0408** (2004) 008 [arXiv:hep-ph/0405158].

[29] H. B. Kim and J. E. Kim, Phys. Lett. B **527** (2002) 18 [arXiv:hep-ph/0108101].

[30] H. Baer, A. D. Box and H. Summy, JHEP **0908** (2009) 080 [arXiv:0906.2595 [hep-ph]].

[31] M. Dine, W. Fischler and M. Srednicki, Phys. Lett. B **104** (1981) 199.

[32] A. R. Zhitnitsky, Sov. J. Nucl. Phys. **31** (1980) 260 [Yad. Fiz. **31** (1980) 497].

[33] H. K. Dreiner, arXiv:hep-ph/9707435.

[34] E. J. Chun, J. E. Kim and H. P. Nilles, Phys. Lett. B **287** (1992) 123 [arXiv:hep-ph/9205229].

[35] B. C. Allanach, A. Dedes and H. K. Dreiner, Phys. Rev. D **69** (2004) 115002 [Erratum-ibid. D **72** (2005) 079902] [arXiv:hep-ph/0309196].

[36] B. C. Allanach *et al.*, in *Proc. of the APS/DPF/DPB Summer Study on the Future of Particle Physics (Snowmass 2001)* ed. N. Graf, Eur. Phys. J. C **25** (2002) 113 [arXiv:hep-ph/0202233].

[37] S. P. Martin and M. T. Vaughn, Phys. Rev. D **50** (1994) 2282 [Erratum-ibid. D **78** (2008) 039903] [arXiv:hep-ph/9311340].

[38] B. C. Allanach, A. Dedes and H. K. Dreiner, Phys. Rev. D **60** (1999) 056002 [arXiv:hep-ph/9902251].

[39] B. C. Allanach and M. A. Bernhardt, arXiv:0903.1805 [hep-ph].

[40] F. Zwicky, *"Spectral displacement of extra galactic nebulae,"* Helv. Phys. Acta. **6**, 110-127 (1933).

[41] F. Zwicky, *"On the masses of nebulae and clusters of nebulae,"* Ap.J. **86** 217-246 (1937).

[42] We will not go to much into detail of the power of Gravitational lensing and its possibilities to detect DM. Instead we refer the reader to Ref. [43] for detailed introduction to this topic.

[43] Schneider, P., Ehlers, J. and Falco, E.E., *"Gravitational Lenses"*, Springer Verlag (1993).

[44] A. C. Fabian and S. W. Allen, arXiv:astro-ph/0304020.

[45] Note that Eq. (2.2) holds only for point like masses or lenses respectively. If we have an extended source we have to sum over the mass points and the according distances at which the source light is deflected.

[46] Edwin Hubble, *A Relation between Distance and Radial Velocity among Extra-Galactic Nebulae*, Proceedings of the National Academy of Sciences of the United States of America, Vol. 15, No. **3** (Mar. 15, 1929), pp. 168-173

[47] The value of the Hubble constant has been estimated with several different methods [17] yielding to the range $60\,\mathrm{kms}^{-1}\mathrm{Mpc}^{-1} \lesssim H_0 \lesssim 80\,\mathrm{kms}^{-1}\mathrm{Mpc}^{-1}$. Due to this uncertainty in H_0 cosmologists introduce a scaling factor h with $H_0 = h \cdot 100\,\mathrm{kms}^{-1}\mathrm{Mpc}^{-1}$. Throughout this thesis we will use the value $h = 0.72 \pm 0.03$ from the PDG group [48] which agrees with Ref. [18].

[48] C. Amsler *et al.* [Particle Data Group], Phys. Lett. B **667** (2008) 1.

[49] S. Weinberg, *Gravitation and Cosmology*, John Wiley & Sons (1972).

[50] A. A. Penzias and R. W. Wilson, Astrophys. J. **142** (1965) 419.

[51] D. J. Fixsen, E. S. Cheng, J. M. Gales, J. C. Mather, R. A. Shafer and E. L. Wright, Astrophys. J. **473** (1996) 576 [arXiv:astro-ph/9605054].

[52] Picture taken from COBE mission data, http://lambda.gsfc.nasa.gov/

[53] Picture taken from WMAP team, http://lambda.gsfc.nasa.gov/

[54] J. Dunkley *et al.* [WMAP Collaboration], Astrophys. J. Suppl. **180** (2009) 306 [arXiv:0803.0586 [astro-ph]].

[55] L. Bergstrom, Rept. Prog. Phys. **63** (2000) 793 [arXiv:hep-ph/0002126].

[56] F. D. Steffen, Eur. Phys. J. C **59** (2009) 557 [arXiv:0811.3347 [hep-ph]].

[57] E. W. Otten and C. Weinheimer, Rept. Prog. Phys. **71** (2008) 086201.

[58] B. Aharmim *et al.* [SNO Collaboration], Phys. Rev. C **81** (2010) 055504 [arXiv:0910.2984 [nucl-ex]].

[59] S. Abe *et al.* [KamLAND Collaboration], Phys. Rev. Lett. **100** (2008) 221803 [arXiv:0801.4589 [hep-ex]].

[60] E. J. Chun and A. Lukas, Phys. Lett. B **357** (1995) 43 [arXiv:hep-ph/9503233].

[61] T. Schwetz, M. A. Tortola and J. W. F. Valle, New J. Phys. **10** (2008) 113011 [arXiv:0808.2016 [hep-ph]].

[62] A. A. Belavin, A. M. Polyakov, A. S. Schwartz and Yu. S. Tyupkin, Phys. Lett. B **59** (1975) 85.

[63] A. M. Polyakov, Phys. Lett. B **59** (1975) 82.

[64] D. J. Gross, R. D. Pisarski and L. G. Yaffe, Rev. Mod. Phys. **53** (1981) 43.

[65] S. Weinberg, *Cambridge, UK: Univ. Pr. (1996) 489 p*

[66] We drop here a second valid motivation for Eq. (2.22). The Lagrangian in Eq. (2.22) can be also rewritten as total derivative. Following this argumentation we know from classical mechanics that such a term does not affect the Feynman rules and hence is in general not forbidden, see Ref. [65].

[67] J. E. Kim, Phys. Rev. Lett. **43** (1979) 103.

[68] M. A. Shifman, A. I. Vainshtein and V. I. Zakharov, Nucl. Phys. B **166** (1980) 493.

[69] S. J. Asztalos *et al.*, Phys. Rev. D **64** (2001) 092003.

[70] S. Andriamonje *et al.* [CAST Collaboration], JCAP **0704** (2007) 010 [arXiv:hep-ex/0702006].

[71] E. Zavattini *et al.* [PVLAS Collaboration], Phys. Rev. Lett. **96** (2006) 110406 [Erratum-ibid. **99** (2007) 129901] [arXiv:hep-ex/0507107].

[72] L. J. Rosenberg and K. A. van Bibber, Phys. Rept. **325** (2000) 1.

[73] E. Zavattini *et al.* [PVLAS Collaboration], Phys. Rev. D **77** (2008) 032006 [arXiv:0706.3419 [hep-ex]].

[74] E. Gildener, Phys. Rev. D **14** (1976) 1667.

[75] H. E. Haber and G. L. Kane, Phys. Rept. **117** (1985) 75.

[76] M. Drees, R. Godbole and P. Roy, *Hackensack, USA: World Scientific (2004) 555 p*

[77] S. Weinberg, *Cambridge, UK: Univ. Pr. (2000) 419 p*

[78] H. K. Dreiner, H. E. Haber and S. P. Martin, arXiv:0812.1594 [hep-ph].

[79] J. R. Ellis, G. B. Gelmini, J. L. Lopez, D. V. Nanopoulos and S. Sarkar, Nucl. Phys. B **373** (1992) 399.

[80] G. L. Kane, C. F. Kolda, L. Roszkowski and J. D. Wells, Phys. Rev. D **49** (1994) 6173 [arXiv:hep-ph/9312272].

[81] P. Gondolo, J. Edsjo, P. Ullio, L. Bergstrom, M. Schelke and E. A. Baltz, JCAP **0407** (2004) 008 [arXiv:astro-ph/0406204].

[82] G. Belanger, F. Boudjema, P. Brun, A. Pukhov, S. Rosier-Lees, P. Salati and A. Semenov, arXiv:1004.1092 [hep-ph].

[83] A. Djouadi, M. Drees and J. L. Kneur, JHEP **0603** (2006) 033 [arXiv:hep-ph/0602001].

[84] J. F. Arguin *et al.* [CDF Collaboration and D0 Collaboration and Tevatron Electroweak Workin], arXiv:hep-ex/0507091.

[85] D. N. Spergel *et al.* [WMAP Collaboration], Astrophys. J. Suppl. **148** (2003) 175 [arXiv:astro-ph/0302209].

[86] E. J. Chun and H. B. Kim, JHEP **0610** (2006) 082 [arXiv:hep-ph/0607076].

[87] D. Hooper and L. T. Wang, Phys. Rev. D **70** (2004) 063506 [arXiv:hep-ph/0402220].

[88] A. Strumia, JHEP **1006** (2010) 036 [arXiv:1003.5847 [hep-ph]].

[89] J. F. Navarro, C. S. Frenk and S. D. M. White, Astrophys. J. **462** (1996) 563 [arXiv:astro-ph/9508025].

[90] Z. Ahmed *et al.* [The CDMS-II Collaboration], arXiv:0912.3592 [astro-ph.CO].

[91] V. Sanglard *et al.* [The EDELWEISS Collaboration], Phys. Rev. D **71** (2005) 122002 [arXiv:astro-ph/0503265].

[92] J. I. Collar and D. N. McKinsey, arXiv:1005.0838 [astro-ph.CO].

[93] T. X. Collaboration, arXiv:1005.2615 [astro-ph.CO].

[94] S. D. Hunter *et al.*, Astrophys. J. **481** (1997) 205.

[95] W. B. Atwood *et al.* [LAT Collaboration], Astrophys. J. **697** (2009) 1071 [arXiv:0902.1089 [astro-ph.IM]].

[96] J. A. Coarasa [MAGIC Collaboration], J. Phys. Soc. Jap. Suppl. **77B** (2008) 49.

[97] U. B. de Almeida [on behalf of the H.E.S.S. Collaboration], arXiv:1006.4835 [astro-ph.HE].

[98] T. DeYoung [for the IceCube Collaboration], arXiv:0910.3644 [astro-ph.HE].

[99] S. Desai *et al.* [Super-Kamiokande Collaboration], Phys. Rev. D **70** (2004) 083523 [Erratum-ibid. D **70** (2004) 109901] [arXiv:hep-ex/0404025].

[100] D. Y. Akimov *et al.*, arXiv:1003.5626 [hep-ex].

[101] C. E. Aalseth *et al.* [CoGeNT Collaboration], Phys. Rev. Lett. **101** (2008) 251301 [Erratum-ibid. **102** (2009) 109903] [arXiv:0807.0879 [astro-ph]].

[102] J. Schmaler *et al.*, arXiv:0912.3689 [astro-ph.IM].

[103] M. C. Piro [on behalf of the PICASSO collaboration], arXiv:1005.5455 [astro-ph.IM].

[104] N. J. C. Spooner and P. Majewski [DRIFT II Collaboration], arXiv:0711.3341 [physics.ins-det].

[105] O. Adriani *et al.* [PAMELA Collaboration], Nature **458** (2009) 607 [arXiv:0810.4995 [astro-ph]].

[106] J. Chang *et al.*, Nature **456** (2008) 362.

[107] A. M. Brown and f. t. A. Collaboration, AIP Conf. Proc. **1178** (2009) 76 [arXiv:0908.1035 [astro-ph.HE]].

[108] S. L. Glashow, Nucl. Phys. **22** (1961) 579; S. Weinberg, Phys. Rev. Lett. **19** (1967) 1264.

[109] J. Wess and B. Zumino, Phys. Lett. B **49** (1974) 52.

[110] J. Wess and B. Zumino, Nucl. Phys. B **70** (1974) 39.

[111] S. Ferrara, J. Wess and B. Zumino, Phys. Lett. B **51** (1974) 239.

[112] A. Salam, J. Strathdee, Phys. Rev. D **11** (1975) 1521.

[113] S. Weinberg, Phys. Rev. D **26** (1982) 287.

[114] N. Sakai and T. Yanagida, Nucl. Phys. B **197** (1982) 533.

[115] S. Dimopoulos, S. Raby and F. Wilczek, Phys. Lett. B **112** (1982) 133.

[116] A. Y. Smirnov and F. Vissani, Nucl. Phys. B **460** (1996) 37 [arXiv:hep-ph/9506416].

[117] G. R. Farrar and P. Fayet, Phys. Lett. B **76** (1978) 575.

[118] H. K. Dreiner, C. Luhn and M. Thormeier, Phys. Rev. D **73** (2006) 075007 [arXiv:hep-ph/0512163].

[119] H. Dreiner, C. Luhn, H. Murayama, M. Thormeier, Nucl. Phys. B **795** (2008) 172 [arXiv:0708.0989 [hep-ph]].

[120] L. E. Ibanez, G. G. Ross, Phys. Lett. B **260** (1991) 291; L. E. Ibanez, G. G. Ross, Nucl. Phys. B **368** (1992) 3.

[121] Y. Grossman and H. E. Haber, Phys. Rev. D **59** (1999) 093008 [arXiv:hep-ph/9810536].

[122] R. Barbier *et al.*, Phys. Rept. **420** (2005) 1 [arXiv:hep-ph/0406039].

[123] H. K. Dreiner, C. Luhn, H. Murayama and M. Thormeier, Nucl. Phys. B **774** (2007) 127 [arXiv:hep-ph/0610026].

[124] H. K. Dreiner, J. Soo Kim and M. Thormeier, arXiv:0711.4315 [hep-ph].

[125] M. A. Bernhardt, S. P. Das, H. K. Dreiner and S. Grab, Phys. Rev. D **79** (2009) 035003 [arXiv:0810.3423 [hep-ph]].

[126] T. Banks and M. Dine, Phys. Rev. D **50** (1994) 7454 [arXiv:hep-th/9406132].

[127] H. Goldberg, Phys. Rev. Lett. **50** (1983) 1419 [Erratum-ibid. **103** (2009) 099905]; J. R. Ellis, J. S. Hagelin, D. V. Nanopoulos, K. A. Olive and M. Srednicki, Nucl. Phys. B **238** (1984) 453.

[128] J. R. Ellis, J. S. Hagelin, D. V. Nanopoulos, K. A. Olive and M. Srednicki, Nucl. Phys. B **238** (1984) 453.

[129] P. Minkowski, Phys. Lett. B **67** (1977) 421; R. N. Mohapatra and G. Senjanovic, Phys. Rev. Lett. **44** (1980) 912.

[130] H. K. Dreiner, S. Heinemeyer, O. Kittel, U. Langenfeld, A. M. Weber and G. Weiglein, Eur. Phys. J. C **62** (2009) 547 [arXiv:0901.3485 [hep-ph]]; D. Choudhury, H. K. Dreiner, P. Richardson and S. Sarkar, Phys. Rev. D **61** (2000) 095009 [arXiv:hep-ph/9911365].

[131] L. J. Hall and M. Suzuki, Nucl. Phys. B **231** (1984) 419.

[132] E. Nardi, Phys. Rev. D **55** (1997) 5772 [arXiv:hep-ph/9610540].

[133] A. Abada and M. Losada, Nucl. Phys. B **585** (2000) 45 [arXiv:hep-ph/9908352].

[134] M. Hirsch, M. A. Diaz, W. Porod, J. C. Romao and J. W. F. Valle, Phys. Rev. D **62** (2000) 113008 [Erratum-ibid. D **65** (2002) 119901] [arXiv:hep-ph/0004115].

[135] S. Davidson and M. Losada, JHEP **0005** (2000) 021 [arXiv:hep-ph/0005080].

[136] J. E. Kim and H. P. Nilles, Phys. Lett. B **138** (1984) 150.

[137] G. F. Giudice and A. Masiero, Phys. Lett. B **206** (1988) 480.

[138] H. K. Dreiner and M. Thormeier, Phys. Rev. D **69** (2004) 053002 [arXiv:hep-ph/0305270].

[139] H. P. Nilles and S. Raby, Nucl. Phys. B **198** (1982) 102.

[140] J. E. Kim, Phys. Lett. B **136** (1984) 378.

[141] E. J. Chun, Phys. Lett. B **348** (1995) 111 [arXiv:hep-ph/9411290].

[142] see explanation in [25] page 11 and private communication Dreiner/Covi.

[143] K. Tamvakis and D. Wyler, Phys. Lett. B **112**, 451 (1982).

[144] J. F. Nieves, Phys. Rev. D **33**, 1762 (1986).

[145] K. Rajagopal, M. S. Turner and F. Wilczek, Nucl. Phys. B **358** (1991) 447

[146] T. Goto and M. Yamaguchi, Phys. Lett. B **276**, 103 (1992).

[147] H. K. Dreiner and H. Pois, arXiv:hep-ph/9511444.

[148] V. D. Barger, M. S. Berger, R. J. N. Phillips and T. Wohrmann, Phys. Rev. D **53** (1996) 6407 [arXiv:hep-ph/9511473].

[149] B. de Carlos and P. L. White, Phys. Rev. D **54** (1996) 3427 [arXiv:hep-ph/9602381].

[150] A. F. Kord, JHEP **0812** (2008) 005.

[151] I. Jack, D. R. T. Jones and A. Pickering, Phys. Lett. B **426** (1998) 73 [arXiv:hep-ph/9712542].

[152] K. Agashe and M. Graesser, Phys. Rev. D **54** (1996) 4445 [arXiv:hep-ph/9510439].

[153] The explicit form of the μ and κ parameter can be found in Ref. [35] Appendix B.

[154] H. K. Dreiner, M. Kramer and B. O'Leary, Phys. Rev. D **75** (2007) 114016 [arXiv:hep-ph/0612278].

[155] H. K. Dreiner, G. Polesello and M. Thormeier, Phys. Rev. D **65** (2002) 115006 [arXiv:hep-ph/0112228].

[156] The reason for the different bounds is due to the fact the in Ref. [35] an older version of the program `Softsusy` was used. As boundary condition the sum of the neutrino masses was applied. With the now more improved `Softsusy3.0` version we obtain the different values.

[157] T. P. Cheng and L. F. Li, *Oxford, Uk: Clarendon (1984) 536 P. (Oxford Science Publications)*

[158] D. Bailin and A. Love, *Bristol, Uk: Hilger (1986) 348 P. (Graduate Student Series In Physics)*

[159] J. F. Gunion and H. E. Haber, Nucl. Phys. B **272** (1986) 1 [Erratum-ibid. B **402** (1993) 567].

[160] N. Fornengo, A. Riotto and S. Scopel, Phys. Rev. D **67** (2003) 023514 [arXiv:hep-ph/0208072].

[161] K. Y. Choi, L. Roszkowski and R. Ruiz de Austri, JHEP **0804** (2008) 016 [arXiv:0710.3349 [hep-ph]].

[162] S. Hannestad, Phys. Rev. D **70** (2004) 043506 [arXiv:astro-ph/0403291].

Publications

The publication:

- *Embedding the DFSZAxino in mSUGRA with RParity Violation,* Herbi K. Dreiner and Branislav Poletanović

is in preparation and will be published within the next weeks.